The Design of a Microfabricated Air Electrode for Liquid Electrolyte Fuel Cells

Fritz Pierre, Jr.

S.B., Massachusetts Institute of Technology (2000)

**Submitted to the Department of Mechanical Engineering
In partial fulfillment of the requirement for the degree of**

Doctor of Philosophy

at the

MASSACHUSETTS INSTITUTE OF TECHNOLOGY

September 2007

Signature redacted

Signature of Author _____
Department of Mechanical Engineering
August 24, 2007

Signature redacted

Certified by _____
Ernest Cravalho
Professor, Department of Mechanical Engineering

Signature redacted

Accepted by _____
Lallit Anand
Chairman, Department Committee on Graduate Studies

The Design of a Microfabricated Air Electrode for Liquid Electrolyte Fuel cells

by

Fritz Pierre, Jr.

Submitted to the Department of Mechanical Engineering
on August 24, 2007 in Partial Fulfillment of the
Requirements of the Degree of Doctor of Philosophy in
Mechanical Engineering

ABSTRACT

In this dissertation, the microfabricated electrode (MFE) concept was applied to the design of an air electrode for liquid electrolyte fuel cells. The catalyst layer of the electrode is envisioned to be fabricated by using a microfabricated die to apply a three-dimensionally patterned macro-texture upon a microporous carbon matrix. The resulting dual porosity structure consists of an array of cylindrical holes that are formed from the die and micropores present in the carbon matrix. The holes are used for gas transport while the micropores are saturated with a liquid electrolyte for ion transport. The catalyst is loaded into the microfabricated structure by electrodepositing thin catalyst films within the cylindrical holes.

In this dissertation, three issues concerning the design of the MFE were investigated: 1) identification of the best material to use for the microporous carbon matrix, 2) the study of electrokinetic parameters of electrodeposited Pt films, and 3) the study of oxygen transport behavior within a Pt film supported on the surface of a microporous carbon matrix.

Two types of polymer-bonded carbon materials have been identified as suitable materials for the carbon matrix. They are carbon black particles bonded into a microporous matrix either by polytetrafluoroethylene (PTFE) fibrils or by polyethersulfone (PES), which is a soluble polymer in common solvents. Experiments and modeling have indicated that these materials will allow the microfabricated catalyst layer to have an effective ionic conductivity that is 4 to 5 times greater than the conventional catalyst layer.

Rotating disk electrode experiments on electrodeposited Pt films in 0.5 M sulfuric acid show that these films have an oxygen reduction reaction mass activity that is 2.5 times greater than that of Pt particles supported on carbon black. Furthermore, oxygen gain experiments on electrodeposited Pt films supported on a microporous membrane indicate that these films experienced no oxygen transport losses in air, up to a current density of 130 mA/cm^2. These results strongly support the use of thin catalyst film technology in catalyst layers of fuel cells.

The experimental results presented this dissertation were used to develop a half-cell model of the MFE in concentrated phosphoric acid. The results of the model suggest that the MFE is capable of producing a current density 3.5 times greater than that of the conventional electrode. It is believed that such potential improvements in the performance of the air electrode support continued efforts to fabricate and test the MFE design concept presented in this dissertation.

Thesis Supervisor: Ernest G. Cravalho
Title: Professor of Mechanical Engineering

Acknowledgments

"I can do all thing through Christ which strengtheneth me."
Phillipians 4:13

I begin by recognizing that Jesus Christ made this doctoral thesis possible.

I thank Professor Ernest G. Cravalho, my advisor, who provided me the opportunity to pursue my doctoral studies at MIT. He began believing in me when I was a sophomore in college and remained supportive during the most challenging times of my doctoral studies.

I thank my committee members: Professor John G. Brisson, II and Professor Yang Shao-Horn. Professor Brisson was kind to provide me with several teaching assistant positions while I completed my work. Professor Shao-Horn allowed me the use of her lab space; without which many of my experiments would not have been possible.

I thank my friends. I am extremely grateful for their support, encouragement, and advice. I am especially grateful for my friends in the Fuel Cell and Cryogenic labs over the years: Derya, Franklin, Gunaranjan, Joanie, Justin, Matt, Rory, Sophie, Theresa, and Wayne. Over the years, they made old Building 41 tolerable. They made MIT a great place to work. My thanks also extend to students in the EEL Lab, especially G.J. and Simcha, who helped me with my SEM pictures that are presented in this dissertation. I thank my very best friends during my graduate years at MIT: Andre, Ayanna, Danielle, Denzil, Eric, Jeremy, Sean, and Todd. They made MIT fun and made me smile during the hardest of times.

I thank my family: my mom, sister, aunts, uncles, and cousins. I also thank my in-laws. They never stopped praying for and encouraging me.

Lastly, but certainly not the least, I thank my wonderful, beautiful wife Mrs. Brandice Pierre. Throughout my time at MIT, she helped me to become a better student, man, and husband. She kept me centered and focused. Without her strength, fearless support, patience, and love, I would not be the person I have become today. To her, I dedicate this dissertation.

To Brandice

Table of Contents

List of Figures

List of Tables

Acronyms

AFC	Alkaline Fuel Cell
BCP	Breakthrough Capillary Pressure
CE	Counter Electrode
CK	Carmen-Kozeny
CV	Cyclic Voltammetry
DCDPS	4,4'-dichlorodiphenyl sulfone
DHDPS	4,4'-dihydroxydiphenyl sulfone
DPS	Double Potential Step
DRIE	Deep Reactive Ion Etching
GDL	Gas Diffusion Layer
IBP	Initial Breakthrough Pressure
KIMM	Korea Institute of Machinery & Materials
LSV	Linear Sweep Voltammetry
MCFC	Molten Carbonate Fuel Cell
MEA	Membrane Electrode Assembly
MFE	Microfabricated Electrode
MIT	Massachusetts Institute of Technology
MPL	Microporous Layer
MTL	Microsystems Technology Lab
NHE	Normal Hydrogen Electrode
NMP	N-methyl-2-pyrrolidone (NMP)
NSTF	Nanostructured Thin Film

OCP	Open Circuit Potential
ORR	Oxygen Reduction Reaction
PAFC	Phosphoric Acid Fuel Cell
PBI	Polybenzimidazole
PCE	Porous Carbon Electrode
PEMFC	Proton Exchange Membrane Fuel Cell
PES	Polyethersulfone
PMMA	Polymethylmethacrylate
Pt/C	Platinum Particles Supported on Carbon Black
PTFE	Polytetrafluoroethylene
RBP	Repeating Breakthrough Pressure
RDE	Rotating Disk Electrode
RE	Reference Electrode
RF	Resorcinol-Formaldehyde
RRDE	Rotating Ring Disk Electrode
SCE	Saturated Calomel Electrode
SEM	Scanning Electron Microscopy
S-H	Scharifker and Hills
SOFC	Solid Oxide Fuel Cell
SPS	Single Potential Step
SPS-S	Single Potential Step with Seed Layer
TFCE	Thin Film Carbon Electrode
UME	Ultramicroelectrode

UTC	United Technology Company
WE	Working Electrode
XRD	X-Ray Diffraction

Chapter 1

Introduction

1.1 Motivation

In the 21st century, the practical attainment and conversion of energy will play an increasingly important role in the continued improvement of mankind's standard of living. However, fossil fuels, which were responsible for the remarkable technological advancements of the past two centuries, are now seen by many to have disadvantages that call into question a continued dependence on them. The adverse effects of fossil fuel combustion on the environment are now well known. For example, scientists now see global warming as a real threat, and if not addressed, will have catastrophic effects on our environment. Furthermore, a growing number of knowledgeable scientist and engineers believe that the continued widespread use of certain fossil fuels will eventually result in a depletion of the reserves of these fuels in this century.

On the dangers of the continued use of fossil fuel, there is no middle ground. For some experts, the disadvantages of fossil fuels are so great that they foresee a future in which the energy security of nations is ensured through forced energy savings as well as armed conflicts. More optimistic views consider the positive effects of new technologies leading to better utilization of fossil fuels, renewable energy forms, and atomic energy [1]. In this spirit, the fuel cell is seen as a technology that has the potential to help with the world's energy needs of the future. This technology has been known for over 160 years. Sir William Robert Grove demonstrated the first operating fuel cell in 1839. The

technology is now in its fourth cycle of attempts to penetrate the energy market. In the past, fuel cells had proven themselves to be too complex, too expensive, and too unreliable to compete with the simple oxidation of fuels in power plants and combustion engines [1]. However, in this present cycle, the outlook for the implementation of the technology is much more favorable. It now appears that the technological, political, and market conditions are appropriate for the introduction of fuel cell into the global energy market in one form or another.

Fuel cells convert hydrogen or hydrocarbon fuels directly into electricity. No other energy-generation technology offers the combination of benefits that fuel cells do. In addition to low or zero emissions, benefits include high efficiency and reliability, multi-fuel capability, site flexibility, durability, scalability, and ease of maintenance. Since fuel cells operate silently, they reduce noise pollution, and the waste heat from a fuel cell can be used to provide hot water or space heating for a home or office.

At present, despite vast amounts of capital dedicated to R&D, only a few commercial applications can be found. The production cost of fuel cells remains too high for them to contend with traditional power sources, such as batteries and combustion engines, without significant market drivers. Lowering cost is, therefore, an important task for the emerging fuel cell industry. The economy-of-scale effects in production will lead to cost reductions. Yet, this alone will not enable fuel cells to reach their target cost. Reductions must also come by improved fabrication techniques, development of new materials, and more efficient use of existing materials. In particular, cost saving can be realized in low temperature fuel cells, such as proton exchange membrane fuel cells (PEMFC) and phosphoric acid fuel cells (PAFC), by more efficient use of the materials

that make up their electrodes. This can be accomplished by improving the electrode structure to allow for improved catalyst utilization and the reduction in mass-transport losses particularly at high current densities.

1.2 Research Objectives

The performance of low temperature fuel cells, like proton exchange membrane fuel cells (PEMFC) and phosphoric acid fuel cells (PAFC), is largely controlled by the microstructures that make up the catalyst layer of the air/oxygen electrode. In state-of-the-art fuel cells, the catalyst layer is formed by conventional thin-film fabrication techniques. These techniques include the rolling, printing, or spraying the catalyst ink onto a gas backing layer or onto an electrolyte membrane. Conventional fabrication techniques provide little control over the geometry and distribution of microstructures within the catalyst layer. For this reason, conventional fuel cell electrodes suffer from low catalyst utilization and contain microstructures that are not optimal for transport of reactants and products. An ideal electrode is limited solely by the rate of the electrochemical reaction.

In this dissertation, microfabrication is introduced as a new method for constructing electrodes that addresses the limitations posed by existing fabrication techniques. The advantage of microfabrication comes from the technique's ability to provide greater control over the geometry and distribution of the microstructures that make up the catalyst layer of the electrodes. This added control allows for a more efficient use of the catalyst at the desired operating conditions of the fuel cell.

Microfabrication techniques are currently being used in research labs to fabricate micro-scale fuel cells [2, 3, 4]. In these designs, microfabrication techniques are used to construct micro-scale flow channels for the cell and/or the auxiliary components of the fuel cell system. The techniques are not used to fabricate the electrode itself. Prinz's research group at the Rapid Prototyping Laboratory at Stanford University has proposed the use of microfabrication to apply a three-dimensionally patterned macro-texture upon the microporous electrodes of polymer exchange membrane fuel cells[5, 6]. Prinz's group is the only other known research group who has proposed using microfabrication to construct the electrode itself.

In this research, the microfabricated electrode concept was applied to the design of an air electrode for liquid electrolyte fuel cells. The catalyst layer of the electrode is envisioned to be fabricated by using a microfabricated die to shape, either by casting or embossing, a porous carbon matrix into the reverse pattern of the die. The resulting dual-porosity layer consists of an array of cylindrical holes (10 to 50 μm in diameter) that were formed due to the pattern transfer and the "micropores" (pore size < 1 μm) of the carbon matrix.[1] The cylindrical holes are used for gas transport while the micropores are saturated with a liquid electrolyte for ion transport. The catalyst (Pt or Pt alloy) is loaded into the microfabricated structure by depositing thin catalyst films on the surfaces of the cylindrical holes. These films are less than 50 nm thick, and they should have a high density of triple-phase boundaries.

The objectives of the research presented in this dissertation were: 1) to propose a design for an air electrode that can be fabricated using existing microfabrication

[1] In the lexicon of porosimetry, micropores refer to pore sizes < 2 nm, mesopores to pore sizes from 2 to 50 nm and macropores to pore sizes > 50 nm. However, in this dissertation, micropores refer to the pores of the electrode that are < 1 μm and macropores refer to the microfabricated cylindrical holes.

technologies and 2) to evaluate if such an electrode has the potential to improve the performance of liquid electrolyte fuel cells. To accomplish these objectives, the research was divided into four major areas of study. These research areas are discussed below.

1. Identification of the best material to use for the porous carbon matrix of the catalyst layer.

Two types of polymer-bonded carbon materials were identified as materials that may be suitable for the catalyst layer matrix, the polytetrafluoroethylyne (PTFE) bonded membrane and the polyethersulfone (PES) bonded membrane. These materials were formed into thin membranes in order to characterize them. The properties of the materials that would directly affect the performance of the catalyst layer were measured. These property values were used in a 1-D electrode model to simulate the performance of the microfabricated electrode and optimize its structure.

The actual fabrication of the microfabricated catalyst layer was beyond the scope of the research presented in this dissertation. Preliminary work in this area was conducted by our colleague Dr. Chang Rae Lee at the Korea Institute of Machinery & Materials (KIMM). Some the results of his work are described briefly in Appendix A and Appendix B.

2. Measurement of the electrokinetic parameters of electrodeposited Pt films.

In the microfabricated electrode design, the catalyst is deposited as thin films in the catalyst layer rather than highly dispersed catalyst particles. The use of thin catalyst films in the catalyst layer is an essential characteristic of the microfabricated electrode design. Unfortunately, the kinetic data of the oxygen reduction reaction (ORR) on electrodeposited Pt films are scarce in the literature. In this part of the research, the

electrodeposition of thin Pt film on glassy carbon was studied. The electrokinetic parameters of these Pt films were measured using the rotating disk electrode technique and voltammetry.

The mass activity of the Pt film is the parameter that will most affect the microfabricated electrode design. The results of this work allow for an assessment of this important parameter.

3. Measurement of oxygen transport within the Pt film supported on a porous matrix that is saturated with electrolyte.

In the microfabricated electrode design, the catalyst is deposited as thin films in the belief that such films will lead to a significant reduction oxygen transport losses within the active region of the electrode. In this part of the research, Pt films were electrodeposited on the porous carbon membranes. The specific areas of these films were measured for different electrodeposition techniques. The oxygen transport characteristics within the deposited films were studied by conducting oxygen gain experiments on the Pt films.

4. Simulation of electrode performance.

The experimental results from research areas (1), (2), and (3) were incorporated into a 1-D model of a microfabricated electrode operating as the cathode in a phosphoric acid fuel cell. The model was used to optimize the geometry of the catalyst layer and predict the performance of the air-fed cathode operating at the typical conditions of state-of-the-art phosphoric acid fuel cells.

1.3 Thesis Organization

The main body of this dissertation comprises of 8 chapters. In Chapter 2, a survey of existing fuel cell technology and a brief review of the electrochemistry underlying fuel cells are provided. A more detailed discussion on fuel cell technology and fundamentals can be found in the following recommended books [1, 7, 8] and review articles [9, 10, 11, 12,]. For readers that are familiar with the basics of fuel cell technology and fundamentals, Chapter 2 may be skipped without loss of continuity with the remaining chapters of this dissertation.

In Chapter 3, a review of fuel cell electrode design methodology and a description of the state-of-the-art in electrode design for low temperature fuel cells are provided. The advantages and disadvantages of these electrodes are discussed and some published novel fabrication techniques employed to improve the electrode performance are introduced. Chapter 3 concludes with Section 3.4, which provides the description and discussion of the microfabricated electrode design concept of this research.

In chapters 4, 5, and 6, the experimental work of this dissertation is presented. The details and results of the preparation and characterization of the polymer-bonded membranes are presented in Chapter 4. The experimental procedures and results of the study of Pt electrodeposition on glassy carbon and the study of the ORR on these deposited films are given in Chapter 5. Lastly, in Chapter 6, the experimental procedures and results of the study of Pt films electrodeposited on the polymer-bonded membranes and the study of oxygen transport within these films are presented. These three chapters can be read in any order. However, the reader may find it helpful to review the electrodeposition sections of Chapter 5 before reading Chapter 6.

In Chapter 7, the 1-D model of the microfabricated air electrode is developed. The predictions of the model for various catalyst layer geometries are presented. Chapter 7 concludes with recommendations for an optimal electrode design. In Chapter 8, a summary of the research results presented in this dissertation as well as recommendations for future research possibilities are given.

References

[1] K. Kordesch and G. Simader, *Fuel Cells and Their Applications*, VCH Publishers, New York, 1993.

[2] K. Shah, W.C. Shin, and R.S. Besser, "A PDMS micro proton exchange membrane fuel cell by conventional and con-Conventional microfabrication techniques", *Sensors and Actuators B*, Vol. 97, p. 157, 2004.

[3] S.S. Hsieh, J.K. Kuo, C.F. Hwang, and H.H. Tsai, "A novel design and microfabrication for micro PEMFC", *Microsystems Technologies*, Vol. 10, p. 121, 2004

[4] R. O'Hayre, PhD Thesis, Department of Material Science and Engineering, Stanford University, 2004

[5] S.J. Lee, S. Cha, R. O'Hayre, A. Chang-Chien, and F.B. Prinz, "Miniature fuel cells with non-planar interface by microfabrication", *Proceeding of Electrochemical Society – Power sources for the new millennium*, pp. 67-76, 2000.

[6] S.J. Lee, S. Cha, Y. Liu, R. O'Hayre, and F.B. Prinz, "High power-density polymer-electrolyte fuel cells by microfabrication", *Proceeding of Electrochemical Society*, Spring 2000.

[7] A.J. Appleby and F.R. Foulkes, *Fuel Cell Handbook*, Van Nostrand Reinhold, 1996.

[8] J. Newman and K.E. Thomas, *Electrochemical Systems*, Third Edition, John Wiley & Sons, Inc., Hoboken, New Jersey, 2004.

[9] L. Carrette, K.A. Friedrich, and U. Stimming, "Fuel Cells: Principles, Tyes, Fuels, and Applications", *CHEMPHYSCHEM*, Vol. 1, p. 162, 2000.

[10] G.J.K Acres, "Recent advances in fuel cell technology and its applications", *Journal of Power Sources*, Vol. 100, p. 60, 2001.

[11] B.C.H. Steele, "Material science and engineering: The enabling technology for the commercialization of fuel cell systems", *Journal of Material Science*, Vol. 36, p. 1053, 2001.

[12] A.Z. Weber and J. Newman, "Modeling Transport in Polymer-Electrolyte Fuel Cells", Chem. Rev. Vol. 104, p. 4679, 2004.

Chapter 2

A Brief Review of Fuel Cell Technology

2.1 What is a fuel Cell

A fuel cell is an electrochemical device that continuously changes the chemical energy of a fuel and oxidizer to electrical energy by a process involving an invariant electrode-electrolyte system. Its operation is similar to that of a battery since chemical energy is directly converted to low voltage DC electricity. However, unlike a battery, fuel cells do not use chemicals that form part of their structure or are stored within their structure as the source of chemical energy. Instead, the reactants are supplied from an external source. For this reason, a fuel cell will continue to operate as long as the fuel and oxidizer are supplied and the products of the electrochemical reaction are removed from the cell.

Figure 2-1 illustrates the basic components and operation of a fuel cell. The components include two manifolds, a porous negative electrode (anode), a porous positive electrode (cathode), and an electrolyte that separates the two electrodes. The reactant gases are distributed via the manifolds. One manifold directs the fuel, typically hydrogen, to the anode while the other directs the oxidizer (air or oxygen) to the cathode. The fuel is electrochemically oxidized on the anode surface, and the oxidizer is electrochemically reduced on the cathode surface. Both electrodes are designed to be a thin, porous structure with a large surface area that provides the reactants with numerous reaction sites and an efficient means of accessing them.

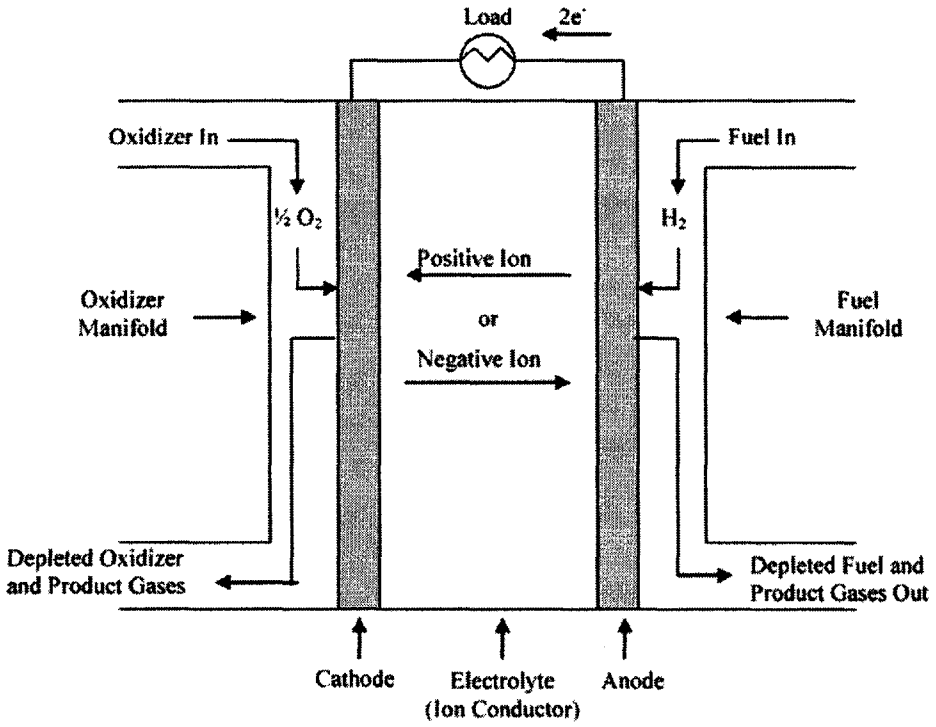

Figure 2-1: Fuel cell diagram

The ions created by the electrochemical reactions flow between the anode and cathode through the electrolyte. The type of fuel cell determines the type of ions produced and transported through the electrolyte. If the electrolyte is a cation conductor, positive ions are produced at the anode and migrate to the cathode. For the case of anion conductor, negative ions are produced at the cathode and are transported via the electrolyte to the anode. Like the electrodes, the electrolyte region is constructed to be as thin as possible in order to minimize the length of the path traveled by the ions and, hence, minimize the resistive losses associated with ion transport. The electrolyte must also be impermeable to both the reactants and the electrons produced at the anode. This assures that the maximum number of electrons is made to flow through the external load before getting to the cathode where they reduce the oxidizer.

Most, but not all, fuel cells use both gaseous fuel and oxidizer. Hydrogen is the preferred fuel because of its high reactivity in the oxidizing environment of the anode. Hydrocarbon fuels can be used, but they are typically reformed into hydrogen and other components prior to entering the fuel cell for lower temperature fuel cells (< 220°C) and within the fuel cell for higher temperature fuel cells (> 600°C). Direct electrochemical oxidation of hydrocarbons is problematic even at high temperatures since carbon deposits tend to form on the catalytic surface. Alcohols, such as methanol and ethanol, are currently being investigated as possible fuels that can be directly introduced into the anode without a reforming process. These fuels can be used in either a liquid or a gaseous phase. Since the activity of these alcohols is much lower than that of hydrogen, they have thus far found limited application. Due to their high activity, Borohydrides (MBH_4, where M is Li, Na, or K) have emerged as a promising alternative to carbon-based fuels. These fuels, at present, are only suitable in alkaline fuel cells since borohydrides are unstable at low pH values. In the cathode, oxygen is the preferred oxidizer because of its availability in the atmosphere. One company, Neah Power Systems, uses peroxide as the oxidizer in their portable fuel cell [1].

A single fuel cell, such as that illustrated in Figure 2-1, is capable of producing only 0.5 to 1 volts under operating condition. For this reason, fuel cell designs link together many individual cells in series to produce a more useful voltage. The most popular method for connecting cells in series is the stack configuration. Figure: 2-2 illustrates a fuel cell stack. This stack can then be configured in series and/or in parallel with other fuel cell stacks to further tailor the voltage, current, and power produced. The

number of individual cells contained within one stack is typically greater than fifty and varies significantly depending on the type of fuel cell [2].

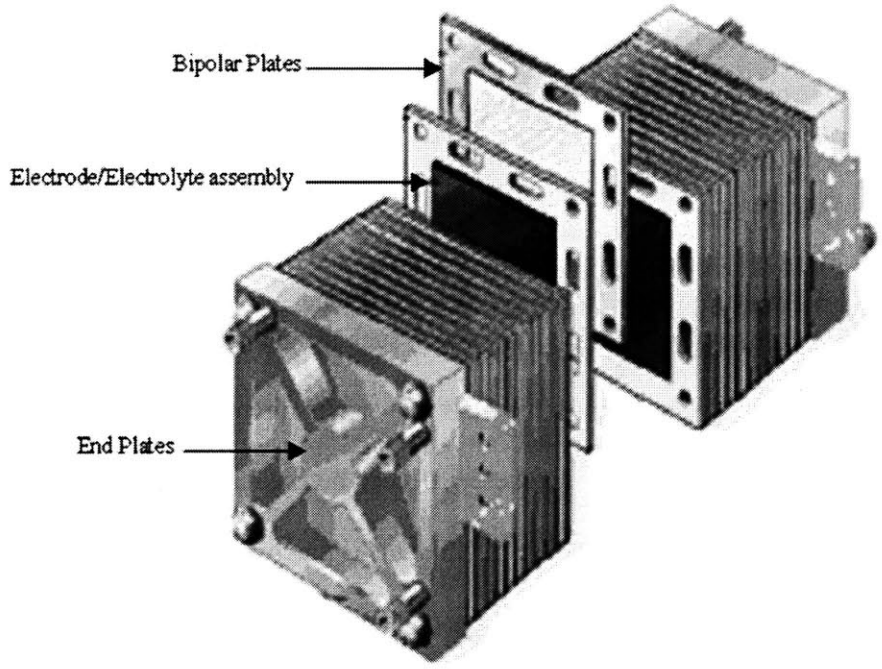

Figure: 2-2: Fuel cell stack

In a stack configuration each electrode is in electrical contact with the adjacent electrode via the bipolar plate as shown schematically in Figure 2-3. In addition to the electrode/electrolyte assembly itself, the bipolar plate is the most important component of the fuel cell stack. It performs several functions, each crucial to the proper operation of the stack. Each bipolar plate acts as a current collector for both the anode and cathode in contact with it. It also provides the electrical series connections between cells, and it physically separates the oxidizer flow of one cell from the fuel flow of the adjacent cell. The flow channels of the bipolar plates serve as distribution pathways for the fuel and oxidizer. Often these flow channels have complex configurations in order to distribute the fuel or oxidizer uniformly over the face of the electrode. The typical width of each

channel is 1mm or less. The performance of the cell tends to increase with a decrease in the width of the channels [2].

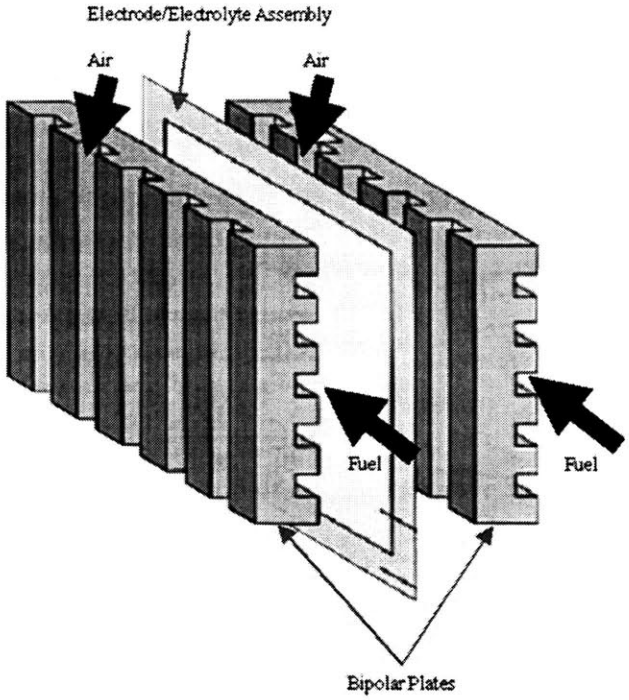

Figure 2-3: Fuel cell assembly with bipolar plates

In liquid electrolyte fuel cells, the electrolyte originally in the electrodes and matrix evaporates over time. This leads to a reduction in the performance of the fuel cell stack over the lifetime of the fuel cell system. The evaporation problem was solved by replacing the impermeable bipolar plates with porous bipolar plates. The porous bipolar plates store excess electrolyte in some of their pores. During the long-term operation of the stack, capillary forces slowly drive the electrolyte from the pores of the bipolar plates to the pores of the electrodes and matrix as the electrolyte evaporates. In 1979 the so-called "ribbed substrate" design, shown in Figure 2-4, was introduced by United Technologies. The ribs are formed on the reactant gas side of the electrode backing. An electrode is directly applied on the non-ribbed (flat) side of the substrate. The ribbed

substrate is a dual-porosity structure that has its small pores filled with electrolyte and its large pores providing the gas channels needed for the rapid diffusion of the reactants to the electrode. An impermeable flat graphite sheet serves as the gas separator plate contacting the substrate ribs for the anode and cathode of adjoining cells. The combination of the anode and cathode ribbed substrates and a separator plate comprises one bipolar plate. The ribbed substrate design allows for five-fold increase in effective electrolyte volume compared to the case where no electrolyte is stored in the bipolar plates [3].

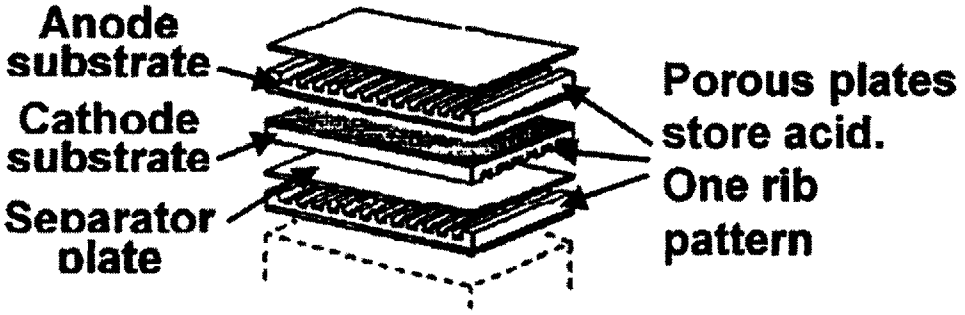

Figure 2-4: UTC's "ribbed substrate" stack design [3]

2.2 Types of Fuel Cells

Five principle types of fuel cells are currently in various stages of commercialization or are undergoing research, development, and demonstrations: solid oxide fuel cells (SOFC), molten carbonate fuel cells (MCFC), phosphoric acid fuel cells (PAFC), alkaline fuel cells (AFC), and proton exchange membrane fuel cells (PEMFC). These fuel cells types are characterized by their electrolyte, though the operation is fundamentally the same from one type to another. Figure 2-5 shows the electrochemical reactions that occur in each of these fuel cells.

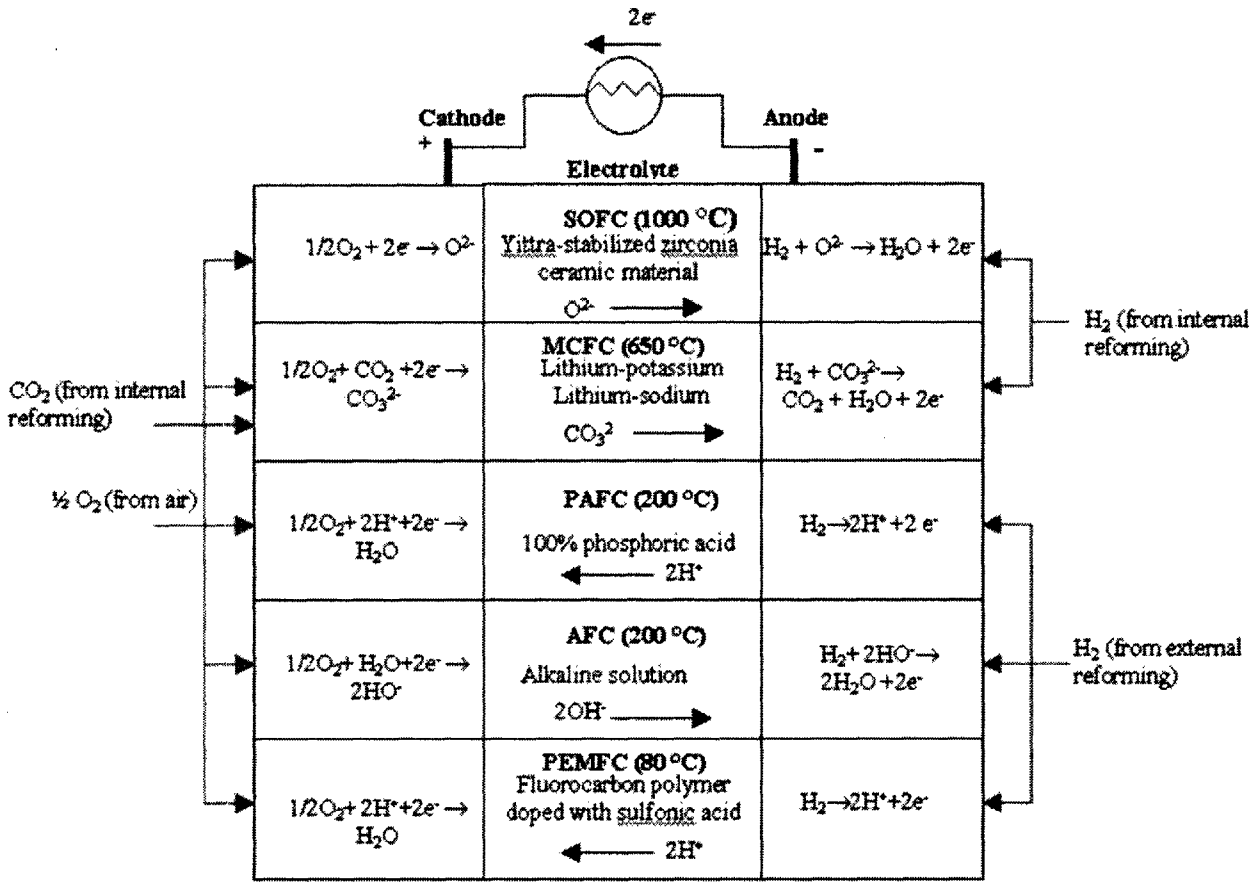

Figure 2-5: Types of fuel cells

2.2.1 High Temperature Fuel Cells (> 600°C):

The high temperature fuel cells, SOFC and MCFC, are seen as the most appropriate type of fuel cell for large power generation (> 200 kW). Their high operating temperatures allow easier and less complicated fuel reforming compared to the low temperature cells. Reforming can also take place in the fuel cell itself, where waste heat from the electrochemical reaction is directly available for the conversion of the fuel to hydrogen. Internal reforming typically leads to a significant increase in plant efficiency and decrease in system cost. Furthermore, the high temperature operation makes expensive catalyst unnecessary, and carbon monoxide is sufficiently oxidized at those

temperatures that it is considered a fuel and not a poison to the catalyst. These fuel cells are also well suited for applications where high quality waste heat is needed in industrial cogeneration.

Solid Oxide Fuel Cells:

The SOFC operates at high temperatures, ~ 500 – 1000°C, with an electrolyte comprising a ceramic oxygen conductor. The most common electrolyte currently used in SOFC is ZrO_2 (zirconia) doped with 8-10 mole-% of Y_2O_3 (yttria). At high temperatures, O^{2-} ions move across the electrolyte via vacant lattice sites. Since there is no liquid phase within the cell, pore flooding is not a problem and there is no electrolyte migration problem under cell operating conditions. The solid electrolyte is also very stable.

Molten Carbonate Fuel Cells:

The MCFC operates at high temperatures, ~ 650°C, with an electrolyte comprising a mixture of molten carbonates (M_2CO_3, M: Li, Na, K). The liquid electrolyte is held within a mixture of ceramic particles that form the electrolyte matrix. The MCFC relies on a balance of capillary pressures to establish the electrolyte interfacial boundaries in the porous electrodes and to keep the matrix flooded. Electrolyte management, that is, the control over optimum distribution of molten carbonate electrolyte within the cell components, is critical for achieving high performance and endurance with MCFCs [4].

2.2.2 Low Temperature Fuel Cells (< 220°C):

These types of fuel cells appear best suited for mobile and light-duty residential applications because of their relatively fast start up times and compact size. Their low

operating temperatures make corrosion and sealing problems much more manageable than those problems in the high temperature fuel cells.

Due to their low temperatures, the electrochemical kinetics are slow in these fuel cells. For this reason, an expensive catalyst, like Pt, is required in both electrodes. In the case of AFCs, non-noble metal electrocatalysts are feasible since the electrochemical reactions are more rapid in an alkaline electrolyte than an acid electrolyte. However, Pt remains the catalyst of choice in most AFC electrodes. In most applications, the electrodes of these fuel cells are formed with carbon black particles that are bounded into a porous network with the aid of a polymer binder. Teflon is used as a binder in certain regions of the electrode to provide appropriate electrolyte and/or liquid water management. The carbon black particles act as high surface area supports for the catalyst nano-particles (2 nm-10 nm). Keeping the catalyst particles size in the range of 2 – 10 nm allows for high catalyst mass activity which lowers required catalyst loading.

Phosphoric Acid Fuel Cells:

The PAFC operates at medium temperatures, ~ 150 - 220°C, with a liquid electrolyte comprising concentrated phosphoric acid. The electrolyte is retained in a microporous (~ 1μm) silicon carbide matrix, and it is at a concentration of approximately 100% H_3PO_4. Phosphoric acid offers many advantages as a fuel cell electrolyte. It has excellent thermal, chemical, and electrochemical stability at the operating conditions of the fuel cell. It also has a relatively low vapor pressure at temperatures above 150 °C. Other inorganic acids such as $HCLO_4$, H_2SO_4, and HCl were evaluated in laboratory-scale fuel cells. Compared to H_3PO_4, these acids have lower chemical stability and higher vapor pressure, and therefore are not acceptable at high temperatures (~ 150 -

220°C). Phosphoric acid does have some serious disadvantages. Among them are poor ionic conductivity near room temperature, low oxygen solubility, and lower oxygen kinetic rates compared to other acids. Despite these disadvantages, no alternative acid has been identified that offers any significant advantages over phosphoric acid.

Thus PAFC was the first to be commercialized for terrestrial applications. It is well suited for medium-scale cogeneration, such as office building and schools. Although the PAFC design currently represents the largest installed base of fuel cells worldwide, current development interest in this type of fuel cell has waned since they are now seen to be less promising than PEMFC. However, the phosphoric acid doped polybenzimidazole (PBI) membrane fuel cell, a hybrid between the PAFC and solid membrane fuel cell, is presently being considered as a higher temperature alternative to the PEMFC. The electrodes in this type of fuel cell are very similar to those of the PAFC since a portion of the phosphoric acid within these electrodes is in the liquid phase.

Alkaline Fuel Cells:

The AFC operates at low to medium temperatures, ~ 60 - 220°C, with a liquid electrolyte comprised of hydroxyl ions. Potassium hydroxide is the most common alkaline solution used in these fuel cells. Oxygen reduction kinetics is more rapid in alkaline electrolytes than in acid electrolytes; consequently, these fuel cells can operate satisfactorily with the use of non-noble metal electrocatalysts. A major disadvantage of AFCs is that alkaline electrolytes form carbonates in the presence of CO_2. For this reason, AFCs have traditionally been considered for specialized application where pure H_2 and O_2 are utilized. For example, this type of fuel cell was first used in the Apollo space crafts where pure H_2 and O_2 were available from the propulsion system of the spacecraft.

A number of fuel cell developers now believe the carbonate problem can be managed by using CO_2 scrubbers, non-carbon containing fuels (i.e. the borohydrides), and/or circulating the electrolyte. They are developing AFCs for portable power and vehicle applications [5, 6]. For portable power, the use of borohydrides as fuels is particularly promising.

Proton Exchange Membrane Fuel Cells:

The PEMFC operates at low temperatures, ~ 60 - 80°C, and is equipped with an ion exchange polymer membrane (fluorinated sulfonic acid polymer or other similar polymer). The PEMFC has the highest power density among all fuel cell types and is simple in its construction. For these reasons and its fast start up time, it is now seen as a prime candidate for use in vehicles and as the power source for portable electronic equipment such as cell phones, laptops and cameras.

Water management in the cell is critical for efficient performance of these fuel cells. The PEMFC must operate under conditions where the byproduct water does not evaporate much faster than it is produced because the membrane must be hydrated to effectively conduct the protons. At the same time, the presence of too much liquid water must also be avoided. Excess water can flood the electrode and limit the transport of reactant gas to the catalytic sites of the electrode. The importance of water management is demonstrated by performance gains of the UTC Power's PEMFC. The UTC Power engineers attribute the significant improvement in their PEMFC performance in recent years to mostly improved water management techniques. PEMFC systems run at a maximum of 80°C because operation above that temperature requires too much system support for adequate membrane hydration. Also, current proton exchange membranes

have glass transition temperatures in the range of 80-120°C and are thus subject to creep and hole-formation at temperatures in that range. Unfortunately, this low operating temperature restricts CO concentrations to values lower than 5 ppm in some PEMFC applications. The CO poisoning problem is one of the major reason why higher temperature alternatives to the PEMFC, like the PBI system mentioned above, are being aggressively sought after.

2.3 Advantages of Fuel Cells

It is now evident that fuel cells can play an important role in the energy conversion paradigms of the 21st Century. The technology offers enormous potential in a wide variety of applications ranging from stationary power plants with power levels on the order of tens of megawatts, to mobile power sources for cell phones and laptop computers with power levels on the order of watts.

In mobile applications, such as energy sources for vehicles and small appliances, fuel cells offer many of the same advantages as batteries, namely, noiseless, non-polluting, and vibration-free operation. For these reasons, they are natural candidates for use as battery replacements since they offer additional advantages of being much lighter in weight than batteries and not being energy storage devices that require recharging after use or disposal after they have reached the limit of their functional lives. Fuel cells take advantage of the high energy density of fossil fuels compared with the conventional low energy density associated with the chemicals within batteries. In electric vehicle applications, for example, refueling could be done in a manner similar to that of today's

gasoline vehicles, rather than by the slow recharging, which is required in battery powered electric vehicles.

In the case of stationary applications, fuel cells have the potential to operate with energy conversion efficiencies that far exceed other means of energy conversion. Since the fuel cell does not have any moving parts it does not suffer the energy losses characteristic of mechanical devices (friction, thermal losses, etc.), such as the diesel engine. More importantly, by converting chemical energy directly to electrical energy, fuel cells avoid the high entropy generating process of vigorous and spontaneous combustion found in heat engines. Fuel cells allow chemical energy to be released in a more controlled fashion, and for this reason, they are more efficient than conventional power generation systems. Figure 2-6 shows the efficiencies possible with the typical systems used to generate electrical power. Current combined cycle (gas turbine and steam turbine) technology (efficiency of 60%) is not included on Figure 2-6. Fuel cells have the advantages of being one and half to three times more efficient than gasoline, diesel, steam, and gas turbine systems and also being able to operate at high efficiencies over a wide range of powers. If the high temperature fuel cells are combined with gas turbines in a combined-cycle operation, the system can have efficiencies as high as 75%. In addition to the high electrical efficiencies, fuel cell units are well suited for thermal energy recovery. Cogeneration can add up to 40% more overall efficiency to the unit, making it a very cost effective way to supply both electricity and heat in the form of steam or hot water to a user [7].

When fueled with hydrogen, fuel cells are virtually pollution free which results in a significant advantage over other energy conversion devices powered from conventional

fossil fuels. For the hydrogen-oxygen fuel cell, water is the only product of the oxidation process. Even when fossil fuels are employed, fuel cells are more environmentally benign than heat engines since reforming of the fuel produces less pollution than combustion. Since fuel cell power sections have no moving parts and no explosive combustion, they are relatively quiet systems. These advantages, combined with the high efficiencies, continue to drive the development of fuel cells for large power plants, distributive energy generation, and mobile applications.

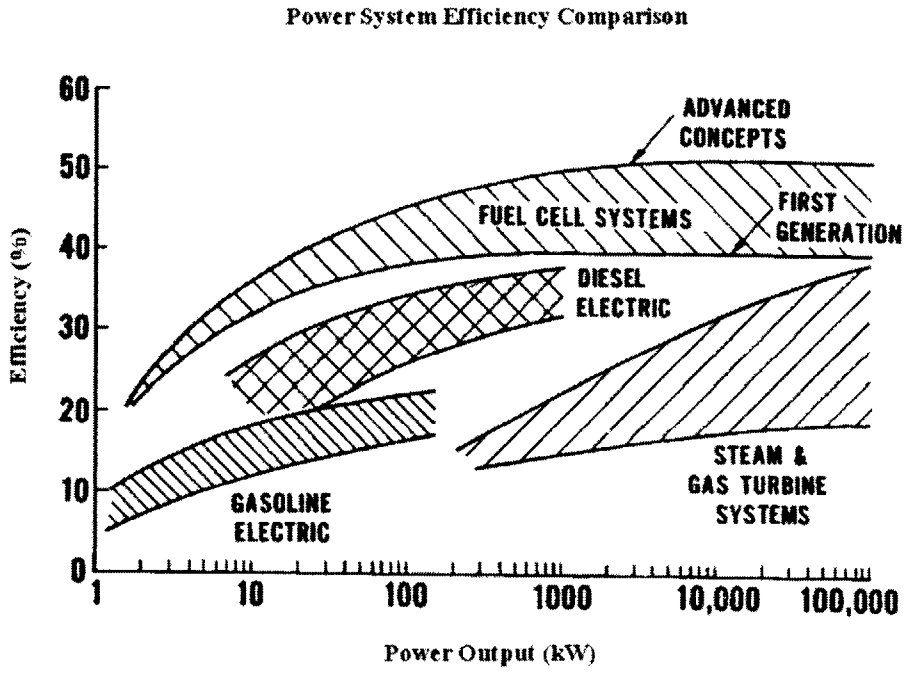

Figure 2-6: A comparison of the efficiency of power systems [7]

2.4 Disadvantages of Fuel Cells

Although fuel cells hold many advantages over conventional energy conversion devices, their high cost (dollars/kilowatt) has prevented their wide spread acceptance in

the energy market. The current cost of fuel cells ranges from $4500 /kW to $1000/kW [8]. The high cost renders them non-competitive in view of market demands. It is estimated that fuel cells cost must be reduced to $800/kW for stationary applications and $40/kW for vehicle applications in order to compete with existing technologies [8]. Continuing efforts to reach these cost reduction goals are the major thrust behind current research and development projects.

The cost of a fuel cell is inextricably linked to its performance. For example, the efficiency of the entire fuel cell system determines the fuel savings for the system over its operational life. If a fuel cell power plant has an efficiency that is significantly higher than other competing and less expensive modes of energy conversion, future fuel savings might more than compensate for its initial high capital cost. In the mid 1990's, United Technologies estimated that a 200 kW fuel cell operating at 40% efficiency and at a cost of $1500/kW would yield positive returns to the end user within the 5 year operation life of the system [7]. Recent studies in our laboratory have shown that payback period can be even shorter depending upon the market price of electricity [9].

The current density (mA/cm^2), another characteristic of fuel cell performance, affects the overall size of the cell; that is, at a given voltage, the overall current requirement of the cell is met by adjusting the planar area of the electrodes. Therefore, a fuel cell with a higher current density will be smaller in size for a given current output. Since the components that make up the fuel cell stack, i.e. the electrodes charged with precious catalyst, the bipolar plates, and the electrolyte, contribute a significant amount to the cost of the system, a reduction in their required size would significantly lower the cost of the system.

The performance of fuel cells has improved significantly over the years; however, it is still far from its theoretical limit. In addition to the engineering problem of materials, stacking, cooling and gas distribution, there are kinetic, charge transport, and mass transport problems within the fuel cell that limit its performance. The next two sections provide a brief review of the thermodynamics and rate dependent processes within the fuel cell.

2.5 Thermodynamics of Fuel Cells

2.5.1 Control Volume Analysis

The operation of a fuel cell can be represented schematically by the control volume in Figure 2-7. As illustrated, electrical work is extracted from the cell by the action of the load. A fuel cell is just like any other energy conversion device/system in that its performance can be assessed by the principles of thermodynamics. Treating the fuel cell as a black box and applying the steady flow energy equation with the assumption of negligible change of kinetic energy and potential energy to the control volume gives

$$\dot{Q}_{CV} - \dot{W}_{CV} + \sum_i (\dot{n}_i h_i)_{in} - \sum_i (\dot{n}_i h_i)_{out} = 0 \tag{2.1}$$

where $\dot{Q}_{CV}$ and $\dot{W}_{CV}$ are the rate of heat transfer into the control volume and the rate of work transfer out of the control volume, respectively. $\dot{n}_i$ *and* h_i are the molar flow rate and partial molar enthalpy of species i, respectively. The entropy balance for the control volume can be written as

$$\frac{\dot{Q}_{CV}}{T} + \sum_i (\dot{n}_i s_i)_{in} - \sum_i (\dot{n}_i s_i)_{out} + \dot{S}_{gen} = 0 \tag{2.2}$$

where s_i is the partial molar entropy of species i, $\dot{S}_{gen}$ is the rate entropy is generated in the control volume, and T is the temperature of the boundary of the control volume. It is equivalent to the temperature of the cell.

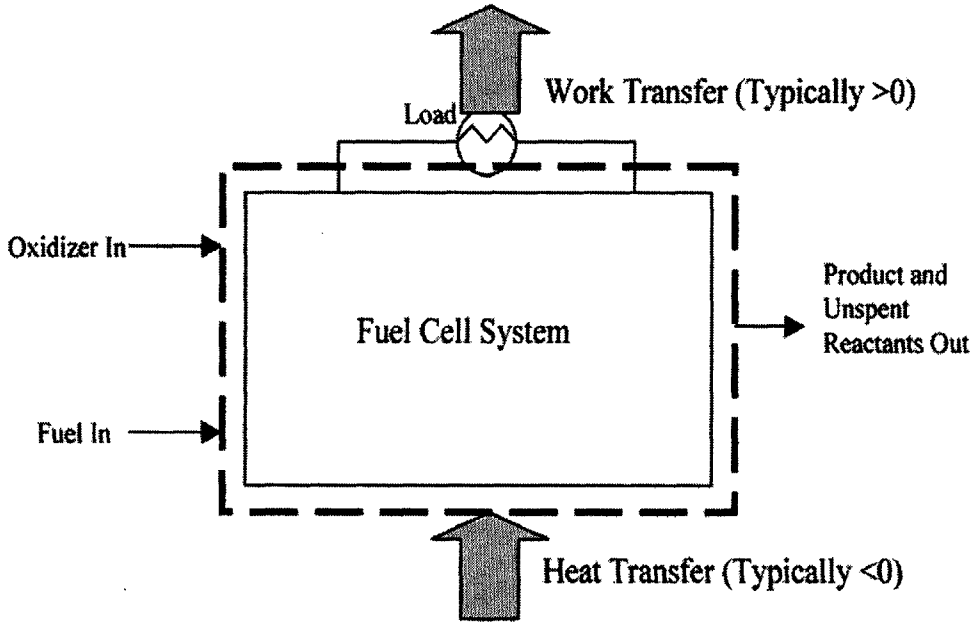

Figure 2-7: Control volume boundary of fuel cell

Combining Equations (2.1) and (2.2) with the assumption that the temperature of the inlet and outlet streams are the same and equal to T, yields

$$\dot{W}_{CV} = -\left[\sum_i (\dot{n}_i \mu_i)_{out} - \sum_i (\dot{n}_i \mu_i)_{in}\right] - T\dot{S}_{gen} \tag{2.3}$$

Using the activity, a_i, to define the chemical potential, μ_i,

$$\mu_i = \mu_i^0 + RT \ln a_i \tag{2.4}$$

μ_i^o is the chemical potential of pure species i at the cell temperature and a pressure of 1 bar. R is the ideal gas constant. Equation (2.3) can be rewritten in a more useful form:

$$\dot{W}_{CV} = -\left[\sum_i \left(\dot{n}_i \mu_i^0\right)_{out} - \sum_i \left(\dot{n}_i \mu_i^0\right)_{in}\right] - \bar{R}T \ln\left(\frac{\prod_i (a_i)_{out}^{n_i}}{\prod_i (a_i)_{in}^{n_i}}\right) - T\dot{S}_{gen} \tag{2.5}$$

The terms in the bracket of Equation (2.5) are the sum of chemical potential of the pure substance *i* at temperature *T* and a pressure of 1 bar. Values for the standard chemical potentials for various compounds can be obtained from the Chemistry WebBook at the National Institute of Standards and Technology website: http://webbook.nist.gov/chemistry/. Equation (2.5) applies generally to all energy conversion systems where the inlet and outlet streams are equal to the temperature of the system. If the inlet and outlet gases are model as ideal, then the activity in Equation (2.5) is equal to the partial pressure, p_i,of its respective gas in bars:

$$a_i = p_i \tag{2.6}$$

Now if we consider the classical example of a hydrogen-oxygen fuel cell. The net chemical reaction occurring in this cell is

$$H_2 + \frac{1}{2}O_2 \rightarrow H_2O \tag{2.7}$$

If we specify the fuel steam as pure hydrogen, the oxidizer stream as pure oxygen, and the product stream as pure water, then Equation (2.5) reduces to

$$\dot{W}_{CV} = -\dot{n}_{H_2}\Delta G_{rx}^0 + \dot{n}_{H_2} RT \ln\left(\frac{a_{H_2}\sqrt{a_{O_2}}}{a_{H_2O}}\right) - T\dot{S}_{gen}$$

where (2.8)

$$\Delta G_{rx}^0 = \mu_{H_2O}^0 - \mu_{H_2}^0 - \frac{1}{2}\mu_{O_2}^0$$

ΔG_{rx}^0 is the standard Gibbs energy for reaction (2.7), and is related to the equilibrium constant of the reaction by, $-\Delta G_{rx}^0 = RT \ln K(T)$. The product $T\dot{S}_{gen}$ is the lost work

associated with the irreversibilities of the fuel cell system. For an isothermally operated cell, its magnitude is a function of the three loss mechanisms within a fuel cell. These loss mechanisms are generally described as activation losses, ohmic losses, and mass transport losses. A review of these loss mechanisms is given in Section 2.6 of this chapter.

The maximum power of a fuel cell system is obtained when entropy generation is zero. Therefore, the maximum power this hydrogen fed fuel cell can generate is given by

$$\dot{W}_{CV} = -\dot{n}_{H_2}\Delta G^0_{rx} + \dot{n}_{H_2} RT \ln\left(\frac{a_{H_2}\sqrt{a_{O_2}}}{a_{H_2O}}\right) \tag{2.9}$$

In the case when the inlet gases and the exiting water are at standard condition, the maximum power is

$$\dot{W}_{CV(\max)} = -\dot{n}_{H_2}\Delta G^0_{rx} \tag{2.10}$$

where $\Delta G^0_{rx} = -237.3 kJ/mol$ if water exits the fuel cell in the liquid phase. Without further information concerning the structure of the fuel cell system, Equations (2.5), (2.8), (2.9), and (2.10) are about as much information as the control volume analysis can provide.

In the above analysis, no mention is made about the inner makeup of the fuel cell. The analysis is valid for a fuel cell system consisting of one cell or multiple cells arranged in series and/or parallel. However, the ideal voltage and current of the fuel cell system cannot be discerned without providing information about how the cells are connected and how the reactants and products are distributed within the cells. In Section 2.5.3, the reversible potential for an air electrode exposed to a uniform concentration of reactants and products is derived.

2.5.2 Efficiency of Fuel Cell System

Fuel Cells and Heat Engines:

One of the major advantages of fuel cells over other energy conversion systems is their high efficiency. This fact has prompted many to make statements such as "fuel cells are not heat engines, and thus their efficiencies are not limited by the Carnot efficiency" [10]. This statement fails to point out, from a thermodynamic point view, the fundamental difference between fuel cells and heat engines. Furthermore, the statement is misleading since it seems to imply that a reversibly operated fuel cell is a better energy converter than a reversibly operated heat engine. Of course, this cannot be true. Fuel cells and heat engines are both constrained by the same maximum efficiency. The limit is established by the second law of thermodynamics, and neither of the energy converters is able to break it [11].

An ideal fuel cell and externally reversible heat engine are illustrated in Figure 2-8.

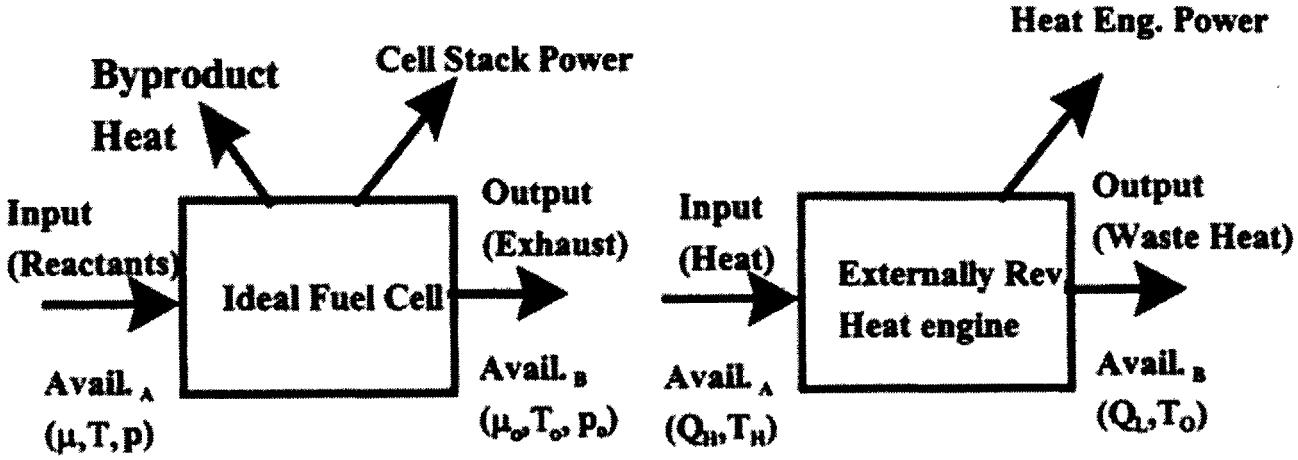

Figure 2-8: Reversible fuel cell and reversible heat engine [12]

If both systems are supplied energy flows with the same availability, A, and the waste streams availability, B, is zero, then both systems must have the same work. This is necessarily the case since the maximum work is a property. It does not depend on the path of the energy conversion process.

Figure 2-8 shows the major difference between a fuel cell and heat engine. A fuel cells receives its availability in the form of a chemical fuel, while a heat engine receives it in the form of heat. The heat for heat engines is often obtained by combustion of a chemical fuel. The combustion process is inherently irreversible. Thus, for an ideal fuel cell and an ideal heat engine receiving the same availability in the form of a chemical fuel, the lower performance of the heat engine is solely due to the combustion process, which can reduce the availability by as much as 40%. However, it should be clear that there is no inherent link between the Carnot efficiency and the combustion irreversibility [12].

Efficiency Definition:

In the case of the fuel cell, there are many possible definitions for the efficiency. Since fuel cells use materials that are usually burned to release their energy, it make sense to compare the electrical energy produced by the fuel cell to the heat release by complete combustion of one mole of the fuel at constant temperature and pressure. Thus, an efficiency can be defined as

$$\eta_f = \frac{\text{electrical energy produced per mole of fuel}}{\text{heat release for complete combustion of 1 mole of fuel}} \tag{2.11}$$

The quantity sometimes used to represent this heat release is the standard heat of reaction, ΔH_{rx}^0. It can be calculated by using the standard heat of formation, $\Delta h_{f,i}^0$, of the compounds taking part in the reaction:

$$\Delta H_{rx}^{0} = \sum_{i} v_i \Delta h_{f,i}^{0} \tag{2.12}$$

where v_i is the molar stoichiometric multiplier for the compounds in the reaction.

For fuels where the precise fuel composition is not known, the standard heat of reaction cannot be determined theoretically. The heating value, Q_{HV}, of the fuel is then measured directly. It is defined as the magnitude of the heat of reaction at constant pressure or alternatively at constant volume at a standard temperature for complete combustion of unit mole (or mass) of fuel:

$$\begin{aligned} Q_{HV_P} &= -(\Delta H)_{P,T_0} \\ Q_{HV_V} &= -(\Delta U)_{V,T_0} \end{aligned} \tag{2.13}$$

For typical fuels the difference between the heating value at constant pressure and constant volume is small [13].

Both ΔH_{rx}^{0} or Q_{HV_P} can be used to quantify the heat released during the complete combustion of a fuel. The former is calculated while the latter is obtained experimentally. When the heating value is measured at standard pressure, the difference between Q_{HV_P} and ΔH_{rx}^{0} is small. For this reason, they are often used interchangeably with little error [13].

For the burning of hydrogen fuel the heat of reaction is equal to

$$\Delta H_{rx}^{0} = -285.84\, kJ / mole \tag{2.14}$$

at $T = 25^{o}C \; and \; P = 1\,\text{bar}$, and with the product water existing as a liquid. For a fuel cell operating under these conditions, the maximum electrical energy it can produce is given by Equation (2.9). Thus, the maximum possible efficiency of the fuel cell is

$$\eta_f = \frac{\Delta G^0_{rx}}{\Delta H^0_{rx}} = 0.83 \tag{2.15}$$

Practically the electrical efficiency of the cell will be less than this value due to irreversibilities in its operation. The rate processes that lead to these irreversibilities in the fuel cell are discussed in Section 2.6.

2.5.3 Reversible Electrode Potential

The control volume analysis leads to expressions for the maximum possible power of an isothermally operated fuel cell. The implementation of a practical fuel cell depends upon the voltage at which this power is available. In order to gain further insight about the operation of the fuel cell, the arrangement of the cell's components and distribution of reactants and products within the cell must be examined. In this section, the condition of the cathode of a fuel cell at thermodynamic equilibrium is reviewed.

The potential of an electrode is defined or measured with respect to a reference electrode. This reference electrode can be imagined to be or actually placed near the reaction site in order to define or measure the potential difference between the electrode and the reference electrode. From a theoretical standpoint, the most common type of electrode is the normal hydrogen electrode. The normal hydrogen electrode is a Pt metal electrode exposed to hydrogen at the same temperature and in the same electrolyte as the solution in contact with the working electrode. Although the electrolyte of the working electrode and reference electrode are the same, the species dissolved in the electrolyte may differ. The potential difference between the working electrode and the reference electrode, U, is given by

$$U = \frac{\mu_{e^-}^{r} - \mu_{e^-}^{w}}{F} \tag{2.16}$$

where F is Faraday's constant, $\mu_{e^-}^{w}$ and $\mu_{e^-}^{r}$ are the electrochemical potential of electrons in the working electrode and in the reference electrode, respectively. The above equation assumes that the working electrode and the reference electrode are of identical composition. Generally speaking this is not true since the electrodes can be made from different materials. However, for most electrode materials, the error involved in making this assumption is negligible.

The electrochemical reaction in thermodynamic equilibrium at the reference electrode is

$$H_2 = 2H^+ + 2e^- \tag{2.17}$$

Thus, the electrochemical potential of the electrons in the reference electrode is equal to

$$\mu_{e^-}^{r} = \frac{\mu_{H_2}}{2} - \mu_{H^+}^{r} \tag{2.18}$$

where $\mu_{H^+}^{r}$ and μ_{H_2} are the electrochemical potential of protons and hydrogen molecules in the electrolyte phase of the reference electrode, respectively. The electrochemical reaction assumed to be in thermodynamic equilibrium at the cathode is

$$4H^+ + 4e^- + O_2 = 2H_2O \tag{2.19}$$

The electrochemical potential of the electrons in the cathode is equal to

$$\mu_{e^-}^{w} = \frac{\mu_{H_2O}}{2} - \frac{\mu_{O_2}}{4} - \mu_{H^+}^{w} \tag{2.20}$$

where $\mu^{w}_{H^+}, \mu_{O_2}$, and μ_{H_2O} are the electrochemical potential of protons, oxygen molecules, and water in the electrolyte phase of the working electrode, respectively. Combining Equations (2.18) and (2.20) with Equation (2.16) gives

$$FU = \frac{\mu_{H_2}}{2} + \frac{\mu_{O_2}}{4} - \frac{\mu_{H_2O}}{2} + \left(\mu^{w}_{H^+} - \mu^{r}_{H^+}\right) \tag{2.21}$$

Generally, the composition of the electrolyte phases of the reference electrode and working electrode differ. The two phases are often separated by a microporous frit that reduces diffusion of species from one phase to the other. Since the phases are of different composition, the term in parentheses in Equation (2.21) has a finite value. This value divided by Faraday's constant is known as the junction potential. The junction potential cannot be measured, but it can be estimated numerically using transport equations. Reference [14] provides a good introduction in the treatment of junction potential. In this dissertation, junction potentials are assumed to be negligible. With this assumption and the assumption that hydrogen, oxygen and water are ideal gases in the gas phase, Equation (2.21) reduces to what is known as the Nernst equation

$$U = U_{rev} = U^{\theta} + \frac{RT}{2F} \ln\left(\frac{P_{H_2}\sqrt{P_{O_2}}}{P_{H_2O}}\right) \tag{2.22}$$

where P_i is the pressure of species i in bars, R is the ideal gas constant, T is the absolute temperature, and U^{θ} is the standard cell potential, where the standard state for each species is 1 bar at the temperature T. U^{θ} has a value of 1.229 V at $T = 25^{o}C$. The P_{H_2} term could have been excluded from the above equation since the reference electrode is often assumed to be at the standard condition.

In general, the reversible thermodynamic potential, U_{rev}, depends on the temperature of the cell, the pressure and composition of the inlet and outlet streams, and how the cells are electrically connected to each other. Figure 2-9 shows its dependence on temperature. The ideal fuel cell potential decreases with increasing temperature, but usually the opposite is true for the actual fuel cell efficiency due to the accelerated electrochemical reaction kinetics at higher temperatures.

Equation (2.22) gives the reversible potential of the oxygen/air cathode. The actual potential of the cathode is much less than the value given by this equation due to the irreversibilities occurring in the cathode. These irreversibilities are explained in the next section. For further discussions on the thermodynamics of electrodes, references [14, 15, 16] are recommended.

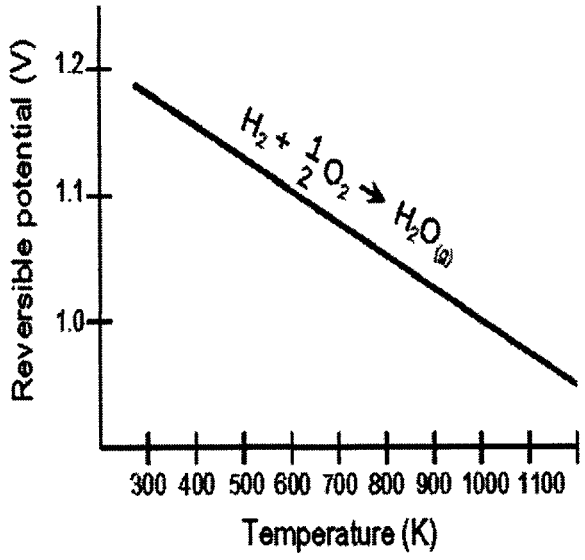

Figure 2-9: The dependence of reversible fuel cell potential on temperature [17].

2.6 Performance of Fuel Cells

The maximum potential of an oxygen electrode is given by Equation (2.22). At standard conditions its value is 1.229 V. Unfortunately, due to irreversibilities in the operation of the electrode, its potential when current is drawn from the electrode is much lower than this value. In the lexicon of the field of electrochemistry, these irreversibilities are interchangeably referred to as polarizations, overpotentials, or overvoltages. The performance of an electrode is most often reported in the form of a polarization curve. Such a curve is shown in Figure 2-10.

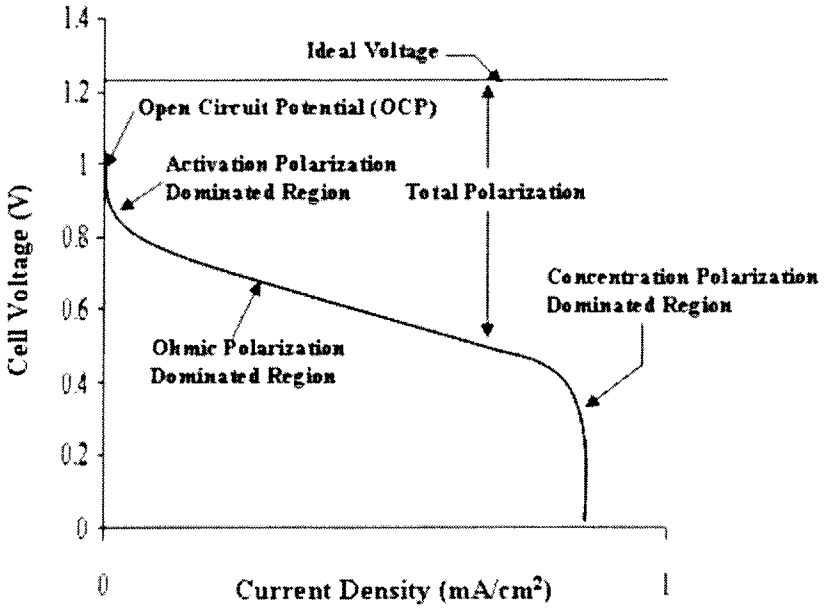

Figure 2-10: Fuel cell performance curve

It contains the typical characteristics of an air or oxygen electrode operated at temperature less than 250°C. The initial drop in the potential of the electrode is due to activation polarization. The activation polarization is the additional potential needed to drive the reaction from its equilibrium state. Even when no current is drawn from the electrode, its potential is measured to be around 1V. This potential drop is associated

with the activation polarization. The cause of this initial potential drop at the OCP is explained in Section 2.6.1.

As the current is increased, the performance curve becomes approximately linear. In this region, the losses are predominately due to ohmic polarization. The ohmic losses are mainly due to the transport losses associated with the migration of ions from the reference electrode to the reaction sites. In some cases, ohmic losses due to electron flow in the layers of the electrode and contact resistances can be important under certain operating conditions and cell configurations. Although the linear region is referred to as the ohmic polarization region, it is important to note the value of the slope does depend significantly on the activation polarization of the cell and the transport losses associated with uncharged species.

At high current densities, the concentration of reactants can decrease or the concentration of products can increase at the reaction sites. These effects act to reduce the rate of the reaction. In the region referred to as the concentration polarization region, this form of polarization dominates. In cathodes for low temperature fuel cells, the causes of concentration polarization are usually the transport limitations of oxygen and/or liquid water. The limiting current behavior seen in Figure 2-10 occurs when the concentration of a reactant goes to zero at all the reaction sites. This behavior can occur if a thin electrolyte film blankets the catalyst particles of the electrode. Since the permeability of oxygen is low in the electrolyte phase, the film can impose a limit on the rate of oxygen transport to the reaction sites. When liquid water is present, it too can blanket the catalyst particles or saturate the pores of the gas diffusion layer. Both of these effects can limit the rate of oxygen transport to the reaction site.

In the following sections, some of the equations used to model these loss mechanisms are given.

2.6.1 Activation Polarization

Chemical reactions involve energy barriers which must be overcome by the reacting species. The energy barrier is called the "activation energy" and it results in an activation polarization. Thus, the activation polarization may be regarded as the extra potential energy necessary to reduce the energy barrier of the rate-determining step of the reaction to a value such that the electrode reaction proceeds at the desired rate.

For a single step electrochemical reaction involving the transfer of one electron,

$$O + e^- \rightarrow R \tag{2.23}$$

the reaction kinetics is normally modeled by the well known Bulter-Volmer equation [15]

$$i = i_o \left\{ \exp\left[\beta \frac{F\eta}{RT} \right] - \exp\left[-(1-\beta) \frac{F\eta}{RT} \right] \right\} \tag{2.24}$$

where η is the overpotential, β is the symmetry factor, and i_o the exchange current density. The symmetry factor is defined for a single step reaction. It is related to the shape of the free-energy barrier and to the position of the activated complex along the reaction coordinate. Its value must be between 0 and 1 and it is commonly assumed to have a value of 0.5. The exchange current density is the forward and reverse electrode reaction rate at the equilibrium potential. A high exchange current density implies a high electrochemical reaction rate.

The overpotential is given by

$$\eta = \Phi_s - \Phi_l - U^{ref} \tag{2.25}$$

where Φ_s and Φ_l are the electrical potential of the metal (solid phase) and electrolyte (liquid phase), respectively. U^{ref} is the reference potential. Its value is determined using the Nernst equation (Equation (2.22)).

The Bulter-Volmer equation is strictly applicable only for an elementary reaction involving the transfer of single electron. For a multi-step reaction, the Bulter-Volmer equation is replaced with an equation similar in form:

$$i = i_o \left\{ \prod_i^a \left(\frac{P_i}{P_i^{ref}} \right)^{\sigma_i} \exp\left[\alpha_a \frac{F\eta}{RT} \right] - \prod_i^c \left(\frac{P_i}{P_i^{ref}} \right)^{\sigma_i} \exp\left[-\alpha_c \frac{F\eta}{RT} \right] \right\} \tag{2.26}$$

where α_a and α_c are the anodic and cathodic transfer coefficients, respectively. Their values can be strongly dependent on potential and temperature. P_i and P_i^{ref} are the partial pressure and reference partial pressure for species i respectively. σ_i is the reaction order for species i either for the anodic reaction, a, or the cathodic reaction, c. The values for $\alpha_a, \alpha_c, and\ \sigma_i$ are obtained experimentally or they are obtained theoretically by postulating a reaction mechanism and calculating their values. Equation (2.26) is used for a nearly reversible multi-step reaction, such as the hydrogen oxidation reaction.

The oxygen reduction reaction (ORR), on the other hand, is slow and represents the principal irreversibility for the oxygen electrode. Due to its sluggishness, the ORR is best modeled with a truncated form of Equation (2.26):

$$i = -i_{o,ORR} \left(\frac{P_{O_2}}{P_{O_2}^{ref}} \right) \exp\left[-\alpha_c \frac{F\eta}{RT} \right] \tag{2.27}$$

This equation is known as a Tafel equation. A linear fit on a Tafel plot of overpotential versus the log of the current density yields the Tafel slope, b', in V/decade.

$$b' = 2.3\frac{RT}{\alpha_c F} \tag{2.28}$$

The value of the transfer coefficient in dilute electrolytes has been shown to be

$$\alpha_c \approx cT \tag{2.29}$$

where the constant c has a value of 1 or 0.5 [18, 19, 20]. In concentrated phosphoric acid at temperatures above 130 °C, $\alpha_c \approx 1$. Equation (2.27) shows that the ORR has a first order dependence with respect to oxygen partial pressure.

Open Circuit Potential (OCP):

Figure 2-10 shows that the OCP of the oxygen electrode is far from the reversible potential. This initial drop in the electrode potential from its thermodynamic value is observed for reactions that are extremely sluggish. The ORR is such a reaction. At the OCP both oxidation and reduction reactions are occurring on the electrode surface. Since electrons are transferred from the sites on the electrode where the oxidation reaction is occurring to sites where the reduction reaction is occurring, no external current is required. At the typical OCP of 1 V, oxygen reduction accounts for the cathodic current. The anodic current is due to oxidation and dissolution of the Pt electrocatalyst, corrosion of carbon, and oxidation of impurities. The OCP is a mixed potential. It represents the potential where the total rate of the cathodic reactions is equal to the total rate of the anodic reactions. If we take the total anodic current to be i_{mix} and set it equal to the cathodic current given by Equation (2.27), the open circuit potential is given by

$$U_{OCP} = U^{ref} - \frac{RT}{\alpha_c F}\ln\left(\frac{i_{mix}}{i_o A_{pt}}\right) \tag{2.30}$$

where A_{Pt} is the roughness factor of the electrode. Equation (2.30) shows that a lower exchange current density leads to a lower open circuit potential.

2.6.2 Ohmic Polarization

Ohmic losses occur because of resistance to the flow of ions in the electrolyte and resistance to the flow of electrons through the electrode materials. The transport of electrons is govern by Ohm's law,

$$\vec{i}_s = -\kappa \vec{\nabla} \Phi_s \tag{2.31}$$

where $\vec{i}_s$ is the current flux due to electron flow and κ is the conductivity of the solid electrode. The subscript s denotes solid phase. The transport equation for the flow of ions is generally more complex than Ohm's Law. For example, in an infinitely dilute solution, the transport of ions is modeled using the Nernst-Plank equation,

$$\vec{N}_i = C_i \vec{v} - D_i \left[\vec{\nabla} C_i + z_i C \left(\frac{F}{RT} \right) \vec{\nabla} \Phi_l \right] \tag{2.32}$$

where $\vec{N}_i$ is the molar flux of species i. C_i is the local concentration of the ion with binary diffusion coefficient with the solvent of D_i and charge of z_i (also referred to as ion's valence). $\vec{v}$ is the velocity of the solution. Φ_l is the local potential of the solution. It is defined as the potential of a particular reference electrode in equilibrium with the electrolyte. The subscript l denotes liquid or electrolyte phase. The current flux due to ion flow, $\vec{i}_l$, is given by

$$\vec{i}_l = F \sum_{i=1}^{n} z_i \vec{N}_i \tag{2.33}$$

Combining this equation with Equation (2.32) gives

$$\vec{i}_l = -F\sum_{i=1}^{n} z_i D_i \vec{\nabla} C_i - \sigma\vec{\nabla}\Phi_l + F\vec{v}\sum_{i=1}^{n} z_i C_i$$
$$\sigma = \frac{F^2}{RT}\sum_{i=1}^{n} z_i^2 D_i C_i \tag{2.34}$$

where σ is the electrical conductivity of the electrolyte.

Applying Gauss's Law to a differential volume in the electrolyte phase, we get the Poisson's equation,

$$\vec{\nabla}\cdot\vec{E}_l = \nabla^2\Phi_l = -\frac{F}{\varepsilon}\sum_{i=1}^{n} z_i C_i \tag{2.35}$$

where $\vec{E}_l$ is the electric field in the electrolyte phase and ε is the dielectric constant, which is assumed to be uniform in the electrolyte phase. The proportionality constant in this equation is Faraday's constant divided by the dielectric constant. The value of this proportionality constant is very large ($1.392\times10^{16} V\cdot cm/mol$ for a relative dielectric constant of 78.303). Thus, a very large gradient in the electric fields is needed to allow for a modest separation of charge. In electrochemical systems, such gradients in electric field are only found 1 to 10 nm from phase or material boundaries. For typical electric fields in the bulk of the electrolyte, the difference in concentration between the cations and anions is on the order of 10^{-11} M. This is a negligibly small number compared to the concentration of the electrolyte (20 to 10^{-5} M). For this reason, the constraint given by the Poisson's equation is almost always replaced with the condition of electroneutrality,

$$\sum_{i=1}^{n} z_i C_i = 0 \tag{2.36}$$

in the bulk of the electrolyte.[1]

The condition of electroneutrality can be combined with Equation (2.34) to give

$$\vec{i}_l = -F\sum_{i=1}^{n} z_i D_i^{eff} \vec{\nabla} C_i - \sigma^{eff} \vec{\nabla} \Phi_l \tag{2.37}$$

The superscript *eff* is added to the diffusion coefficients and conductivity to denote that these properties in a porous medium are modified from their bulk values (see Equation (2.40)). Equation (2.37) indicates that current can flow as a result of concentration gradients or gradients in the electrolyte potential in the electrolyte phase. In an electrolyte with uniform composition, the above equation reduces to Ohm's law,

$$\vec{i}_l = -\sigma^{eff} \vec{\nabla} \Phi_l \tag{2.38}$$

It can be shown that Ohm's law is also applicable in a concentrated solution of uniform composition [14].[2]

2.6.3 Concentration Polarization

Concentration losses result from the resistance of the flow of reacting species to the reacting sites or product species away from the reacting sites. In the case of reactants, the concentrations of these species are lower at the reacting sites compared to their values at OCP. In the case of products, their concentrations are greater at the reacting sites compared to their values at OCP. Both these effects reduce the overall rate of the reaction (see Equation (2.26)). Thus, a higher overpotential is needed to compensate for

---

[1] It should be made clear that Possion's equation and the condition of electroneutrality cannot be used together. Doing so would imply Laplace's equation for the potential, $\nabla^2 \Phi_l = 0$, which is an unnecessary constraint that may be inconsistent with the constraints given by Equations (2.32) to (2.34).

[2] In concentrated solutions, multicomponent diffusion effects must be considered. Additionally, the true driving force for ion transport, the gradient in electrochemical potential, must be used and not the gradient in concentration and potential as given in Equation (2.32). For an excellent introduction to ion transport in dilute solutions and concentrated solutions, the reader is directed to reference [13].

the transport limitations. Any reactant or product, including electrons and ions, can lead to concentration polarization. However, in fuel cells, the most common cause of concentration polarization is resistance to the transport of oxygen to the active sites.

Concentration polarization can occur over the entire current range of the cell. It can have a strong effect on the value of the slope of the linear region of the performance curve. In Figure 2-10 the region labeled concentration polarization represents the current values when the concentration of one or more of the reactants approaches zero at the reaction sites. In liquid electrolyte fuel cells, this mass transfer limitation occurs as a result of the thin electrolyte films that cover the catalyst particles. In PEMFCs, the limiting current behavior is normally due to the flooding of the porous electrode by water, which greatly impedes the ability of oxygen to diffuse within the porous medium.

In an air electrode, oxygen is first transported in the gas filled pores of the electrode. It then dissolves in the electrolyte and diffuses to the active sites. The multicomponent diffusion of gases in the pores can be modeled using the following equation [21]:

$$\vec{\nabla} P_i = \frac{P_i}{RT}\left(\frac{RT}{P_G} - \frac{mw_i}{\rho}\right)\vec{\nabla} P_G + \sum_{j \neq i}^{n} \frac{RT}{P_G D_{i,j}^{eff}}\left(P_i \vec{N}_j - P_j \vec{N}_i\right) - \frac{RT}{D_{K,i}^{eff}} \vec{N}_i \qquad (2.39)$$

where P_G is the total pressure of the gas, mw_i is the molecular weight of species i, and ρ is the mass density of the gas. $D_{i,j}^{eff}$ is the effective binary diffusion coefficient between species i and j. By the Onsager reciprocal relationship, $D_{i,j}^{eff} = D_{j,i}^{eff}$. The superscript eff denotes that the diffusion coefficients are corrected for the porosity, ε, and tortuosity, τ, for gas transport in the electrode,

$$D_{i,j}^{eff} = \frac{\varepsilon}{\tau} D_{i,j} \tag{2.40}$$

$D_{K,i}$ is the effective Knudsen diffusion coefficient of species i. Using the kinetic theory of gases to express the mean free path of the molecule, the Knudsen diffusion coefficient is given by

$$D_{K,i} = \frac{2r_K}{3}\left(\frac{8RT}{\pi mw_i}\right)^{\frac{1}{2}} \tag{2.41}$$

where r_K is the pore radius. Since the porous electrode contains a pore size distribution, and average radius is used in Equation (2.41).

Equation (2.39) is written shorthand for n independent equations (an equation for each species that makes up the gas mixture). These equations can be summed up to give Darcy's law for assumed Stokes flow in the porous medium,

$$\vec{v} = \frac{k}{\mu}\vec{\nabla} P_G \tag{2.42}$$

where μ and κ are the viscosity and effective gas permeability of the gas phase, respectively. In this equation, $\vec{v}$ is specifically the mass average velocity. It is given by

$$\vec{v} = RT\frac{\sum_i^n mw_i N_i}{\sum_i^n mw_i P_i} \tag{2.43}$$

The addition of Darcy's Law as a separate equation reduces the number of independent equations given by (2.39) to $n-1$.

For the porous electrodes used in fuel cell applications, the gas permeability is often high enough that the total gas pressure can be assumed to be uniform throughout the electrode. Under this condition, Equation (2.42) is replaced with

$$\nabla P_G = 0$$
$$P_G = \text{constant} \tag{2.44}$$

and Equation (2.39) reduces to

$$\vec{\nabla} P_i = \sum_{j \neq i}^{n} \frac{RT}{P_G D_{i,j}^{eff}} \left(P_i \vec{N}_j - P_j \vec{N}_i \right) - \frac{RT}{D_{K,i}^{eff}} \vec{N}_i \tag{2.45}$$

Equation (2.45) is the familiar Stefan-Maxwell equation with the addition of an extra term to account for Knudsen diffusion. This equation is written shorthand for $n-1$ independent equations. In this dissertation, Equation (2.45) is used to model gas transport in the electrode.

The concentration of the reacting gases, such as oxygen, in the electrolyte phase is on the order of 10^{-3} to 10^{-4} M. For this reason, the pseudo-binary diffusion assumption is used to model the transport of these species in the electrolyte phase. The flux of the species is given by

$$\vec{N}_i = C_i \vec{v} - D_i \vec{\nabla} C_i \tag{2.46}$$

For 1-D diffusion with no motion of the electrolyte, the limiting current, i_{lim}, for oxygen reduction on a planer electrode can be easily shown to be

$$i_{\text{lim}} = \frac{4FC_{O_2}^{o} D_{O_2}}{\delta} \tag{2.47}$$

where δ is the diffusion length of oxygen from the bulk solution, with an oxygen concentration of $C_{O_2}^{o}$, to the surface of the electrode.

References

[1] http://www.neahpower.com/technology

[2] J.M.J Blomen and M.N. Mugerwa, Editors, *Fuel Cell Systems*, New York, NY, 1993.

[3] K.V. Kordesch and J.C.T. Oliveira, "Fuel Cells", *Ullmann's Encyclopedia of Industrial Chemistry*, Vol. A 12, pp. 55-83, 1989.

[4] H.R. Kunz, "Transport of Electrolyte in Molten Carbonate Fuel Cells", *J. Electrochem. Soc.*, Vol. 134, p. 105, 1987.

[5] E. De Geeter, M. Mangan, S. Spaepen, W. Stinissen, and G. Vennekens, "Alkaline Fuel Cells for Road Traction", *J. Power Sources,* Vol. 80, P. 207, 1999.

[6] S.C. Amendola, P. Onnerud, M.T. Kelly, P.J. Petillo, S.L. Sharp-Goldman, and M. Binder, "A Novel High Power Density Borohydride-Air Cell", *J. Power Sources*, Vol. 84, p. 130, 1999.

[7] P. Gallagher, M.S. Thesis, Mechanical Engineering Department, Massachusetts Institute of Technology, Cambridge, MA, 1995.

[8] G. Cacciola, V. Antonucci, and S. Freni, "Technology Up date and New Strategies on Fuel Cells", *J. Power Sources*, Vol. 100, p. 67, 2001.

[9] S. Tarud, M.S. Thesis, Mechanical Engineering Department, Massachusetts Institute of Technology, Cambridge, MA, 2004.

[10] Y.A. Cengel and M.A. Boles, *Thermodynamics: An Engineering Approach*, 2nd Edition, McGraw-Hill, New York, 1994.

[11] A.E. Lutz, R.S. Larson, and J.O. Keller, "Thermodynamic Comparison of Fuel Cells to Carnot Cycle", *Int. J. Hydrogen Energy*, Vol. 27, p. 1103, 2002.

[12] C. Haynes, "Clarifying reversible efficiency misconceptions of high temperature fuel cells in relation to reversible heat engines", *J. Power Sources*, Vol. 92, p. 199, 2001.

[13] J.B. Heywood, Internal Combustion Engine Fundamentals, McGraw-Hill, New York, 1988.

[14] J. Newman and K.E. Thomas, *Electrochemical Systems*, Third Edition, John Wiley & Sons, Inc., Hoboken, New Jersey, 2004.

[15] A.J. Bard and L.R. Faulkner, Electrochemical Methods: *Fundamentals and Applications*, John Wiley & Sons, Inc., New York, New York, 2001.

[16] E. Gileadi, *Electrode Kinetics for Chemists, Chemical Engineers, and Material Scientist*, Wiley-VCH, New York, NY, 1993.

[17] J.H. Hirschenhofer, D.B. Stauffer, R.R. Engleman, and M.G. Klett, *Fuel Cell Handbook*, 4th Edition, U.S. Department of Energy, Morgantown, WV, 1998.

[18] U.A. Paulus, T.J. Schmidt, H.A. Gasteiger, and R.J. Behm, "Oxygen reduction on a high-surface area Pt/Vulcan carbon catalyst: a thin-film rotating ring-disk electrode study", *J. Electroanal. Chem.*, Vol. 495, p. 134, 2001.

[19] E. Yeager, M. Razaq, D. Gervasio, A. Razaq, and D. Tryk, "The Electrolyte Factor in O_2 Reduction Electrocatalysis", in *Structural Effects in Electrocatalysis and Oxygen Electrochemistry*, D. Scherson, D. Tryk, M. Daroux, and X.Xing, Editors, Proc. Vol. 92-11, Pennington NJ: The Electrochem. Soc. Inc, p. 440, 1992

[20] J.C. Huang, R.K. Sen, and E. Yeager, "Oxygen Reduction on Platinum in 85% Orthophosphoric Acid", *J. Electrochem. Soc.* Vol. 126, p.786, 1979.

[21] A.Z. Weber, PhD Thesis, Chemical Engineering Department, University of California, Berkeley, Berkeley, CA, 2004.

Chapter 3

Review of Electrode Designs and Presentation of Microfabricated Electrode Design Concept

3.1 Membrane Electrode Assembly

3.1.1 Introduction

In its most basic form, a fuel cell consists of two electrodes, an anode and a cathode, that are separated from each other by an electrolyte layer. In this dissertation this electrode-electrolyte assembly will be referred to as the membrane electrode assembly (MEA) for both solid polymer and liquid electrolyte fuel cells. In polymer electrolyte fuel cells, the three layers of the MEA are typically fabricated individually and then pressed together at high temperature and pressure. In liquid electrolyte fuel cells with an immobile electrolyte, the electrolyte matrix material is typically coated or sprayed on the catalyst side of cathode and/or anode. A MEA is pictured in the schematic of a single cell shown in Figure 3-1. The MEA is typically sandwiched in between two flow field plates that are often mirrored to make bipolar plates as discussed in Section 2.1.

As shown in Figure 3-1, the electrode is the component of the MEA that span from the surface of the electrolyte layer to the gas channel of the bipolar plate. An effective electrode is one that optimizes the transport of all reactants and products to and from the electrochemically active regions of the electrode.

The three required transport processes are:

1. Ion transport from the electrolyte layer to the catalyst sites in the catalyst layer, or from the catalyst site to the electrolyte layer;
2. Electron transport from the current collector to the catalyst (or opposite direction in case of the anode); and
3. The reactant gas transport to the active sites in the catalyst layer and product gas to the gas channels. At temperatures below 100 C, liquid water permeation to the gas channels.

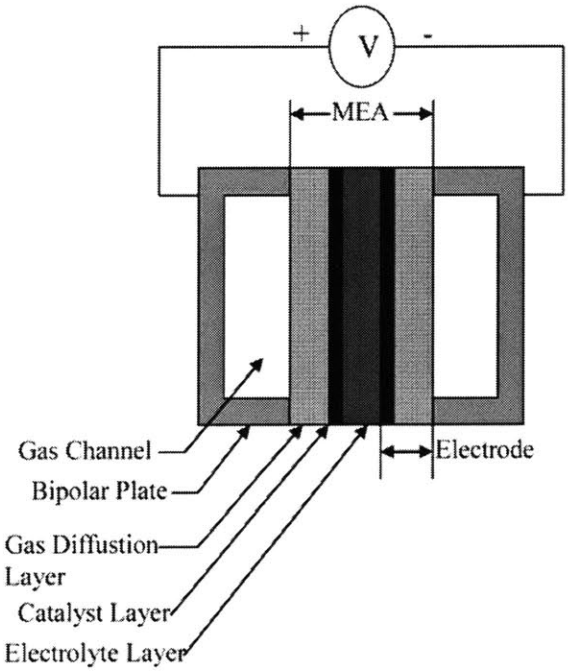

Figure 3-1: Schematic of a typical membrane electrode assembly (MEA)

Unfortunately, there is no single phase or material that is capable of effectively transporting electrons, gases, and ions. Therefore, three separate phases are required in the catalyst layer: an ion conducting media, electron conducting media, and gas pores. The goal of electrode fabrication is the optimal distribution of these three phases in the catalyst layer in order to reduce transport losses [1]. The intimate intersection of the

three phases at the catalyst particles is known as the triple phase boundary. A high density of these triple-phase boundaries is vital for the effective operation of the fuel cell.

3.1.2 Catalyst Layer

The catalyst layer is in direct contact with the electrolyte layer and the gas diffusion layer. It is the most important region of the electrode since it is in the catalyst layer that the electrochemical reactions occur. The catalyst layer should be extremely thin. For this reason, it is often not designed to be a freestanding sheet. It is typically applied in an ink form to the electrolyte layer or the gas diffusion layer. In either case, the objective is to place the catalyst particles in the catalyst layer within close proximity to both the gas phase and the electrolyte phase.

Ideally, the catalyst layer is an infinitely thin region within the electrode where all reactants can be transported to the reaction sites free of any transport limitations under the operating conditions of the fuel cell. However, the slow kinetics of some electrochemical reactions dictates the use of a large amount of high surface area catalyst in order for the fuel cell to generate practical power densities. This catalyst requirement results in a "thick" catalyst layer where the increased diffusion lengths can cause the reactions to fall under diffusion control.

With pure hydrogen as the fuel, the reaction at the anode is fast when a suitable catalyst, such as Pt, is used and carbon monoxide poisoning of the catalyst is avoided. The low catalyst requirement at the anode results in a thin catalyst layer that can be easily fabricated into a structure that is free of any significant overpotentials. Thus, in an optimally fabricated fuel cell, the anode does not significantly contribute to the losses within the cell. On the other hand, the oxygen reduction reaction (ORR) is slow even on

the best known catalysts, Pt and Pt alloys. Consequently, the cathode needs a high Pt loading in order to generate practical power densities. The high catalyst requirement makes fabrication of an optimal cathode difficult.

For the above reasons, the proposed microfabricated concept is applied to the design of a superior performing cathode catalyst layer. A well fabricated catalyst layer is thin (< 150 μm), but remains a porous structure activated by the presence of a suitable amount of high-surface area catalyst. Most, if not all, of the catalyst particles are in electronic contact with both the remainder of the electronically conducting structure of the electrode and with a continuous electrolyte network to provide an ionic path for ion transport to or from the electrolyte layer of the cell. Finally, since reactant gases are transported fastest in the gas phase, the catalyst layer has a network of gas pores that minimizes the diffusion length between the gas phase and the active catalyst particles that are within the electrolyte phase.

3.1.3 Gas Diffusion Layer

The major component of the gas diffusion layer (GDL) is the free-standing porous carbon sheet. The sheet is either a carbon paper or a carbon cloth material. The choice of carbon paper or cloth depends on the fuel cell type and operating conditions. In either case, the sheet serves as the structural support of the GDL. In certain GDL designs, a polytetrafluoroethylene-bonded (PTFE-bonded) carbon black sublayer is deposited on the catalyst side or on both sides of the carbon sheet. The thickness of this sublayer range from 15 to 100 μm [1]

The GDL has many roles. It ensures that the reactants effectively diffuse to the catalyst layer by allowing the gases to uniformly distribute within it as the gases diffuse

from the gas channel to the catalyst layer. Secondly, the GDL is the electrical conductor that transports electrons to and from the catalyst layer. Thus, a GDL with high conductivity is desired. To improve mass transport of the gases, GDLs can be made more porous at the cost of increased electrical resistance. This is often justified since resistive losses within the diffusion layer have a second order affect on the performance of the cell even at high (80% to 90 %) porosity [2].

Another important function of the gas diffusion layers in an MEA is management of the liquid phase within the cell. The GDL is rendered hydrophobic with PTFE to ensure that most of the pores in the carbon sheet do not become clogged with liquid electrolyte or water. A saturation of the GDL with liquid would prevent rapid gas diffusion necessary at high current densities. However, PTFE needs to be applied to GDL with careful measure since it is not an electric conductor and it reduces the porosity of the GDL. The optimal amount of PTFE in GDL ranges from 20wt% to 50wt% depending on fuel cell type and the operating conditions of the cell [2].

Unlike the catalyst layer, the GDL does not differ substantially between liquid electrolyte fuel cells and PEMFCs. The differences that do exist, such as the amount of PTFE loading, desired pore size, and desired porosity, result from the type of the liquid that the GDL needs to effectively manage. The particular aspects of the gas diffusion layer for liquid electrolyte cells and for the PEMFC are briefly discussed in Sections 3.2.1 and 3.3.2. .

3.2 Electrode Design for Liquid Electrolyte Fuel Cells

3.2.1 Porous Carbon Electrode (PCE) Technology

The phosphoric acid fuel cell (PAFC) and the alkaline fuel cell (AFC) are the two types of liquid electrolyte fuel cells in various stages of development and commercialization. The PTFE-bonded porous carbon electrode (PCE) is commonly used in these types of fuel cells. Figure 3-2 is a schematic of a specific porous carbon electrode design for a PAFC [3]. The electrode consists of three layers: (1) a gas diffusion layer, (2) a gas diffusion sublayer, and (3) a catalyst layer.

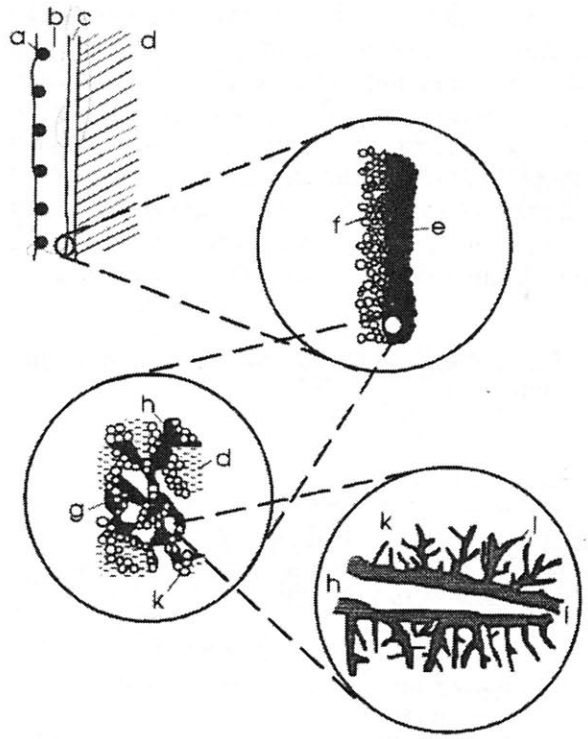

Figure 3-2: Polymer-bonded electrode: a) gas side, b) hydrophobic backing layer, c) catalyst layer, d) electrolyte, e) PTFE-bonded catalyst support, f) diffusion sublayer, g) PTFE particle, h) gas channels, I) electrolyte film, K) catalyst, l) micro- and mesopores. Figure from reference [3]

It is customary when a sublayer is present to refer to the gas diffusion backing layer as the backing layer and the sublayer as the microporous layer (MPL). The backing layer, which is fabricated from carbon paper, contacts the gas channels. It serves as the current collector and provides the main structural support for the other layers. The MPL consists of a mixture of uncatalyzed carbon black and PTFE. It is rendered highly hydrophobic by having a high content of PTFE (40-70 wt%) that is sintered at temperatures well above its glass transition temperature [2]. The MPL provides a porous barrier that prevents penetration of electrolyte through the electrode, while at the same time providing for rapid gas permeation. Furthermore, it provides a suitable surface to deposit the catalyst layer. With its smaller pore size than the carbon paper, it prevents catalyst particles from penetrating deep into the backing layer where they can be rendered inactive. The catalyst layer contains the electrocatalyst supported on carbon black, as well as a lesser amount of PTFE (30-50 wt%) [4]. In some electrode designs, the catalyst layer may also contain wet-proof carbon black in order to further increase gas channels within the layer [5]. The thickness of the catalyst layer is limited to values less than 100 μm [3].

In the PCE technology, a catalyst ink is sprayed, spread, rolled, or printed onto the GDL. The solid components of the ink are Pt nanoparticles (2-5 nm in size) supported on carbon black particles (30-50 nm in size) and colloidal PTFE. The former is referred to as Pt/C. After depositing the ink, the liquid is evaporated leaving behind a solid mixture of carbon agglomerates and PTFE particles. The average size of these agglomerates is crucial to the performance of the catalyst layer. When the applied ink is baked at temperatures above 300°C, the PTFE sinters and binds the carbon agglomerates. During the sintering processes, the PTFE wets parts of the catalyst structure on a random basis.

The region in between the carbon agglomerates that have become wetted by PTFE will be hydrophobic, producing gas pores for rapid reactant gas transport. As a result of PTFE's high viscosity at its sintering temperatures, it is unable to wet the spaces in between the individual carbon particles. The size of these pores range from 30 to 100 nm. The regions that are not covered by a PTFE film after sintering are the hydrophilic regions of the catalyst layer. These regions are flooded with the electrolyte and serve as the ion conducting path to or from the electrolyte layer of the MEA.

The catalyst ink must be properly mixed, aged, and combined with the right amount of wetting and sizing agents to adjust the agglomeration of the carbon–PTFE mixture [6]. Slight variations from optimal catalyst ink conditions often lead to a mixture with large aggregates of Pt/C of varying dimensions in a random admixture with PTFE [2]. The resulting performance of a catalyst layer formed with this uneven mixture is usually unacceptably low. Furthermore, the sintering of the PTFE must be controlled carefully to arrive at a repellant, but not overly wet proofed, catalyst layer. The careful control and balance that must be achieved with the materials that makeup the ink, its application to the GDL, and its heat treatment for optimal electrode fabrication are the reasons why electrode fabrication is often referred to as a "black art". Indeed, the exact PCE electrode fabrication recipes for most fuel cell developers remain guarded trade secrets [2].

Liquid electrolyte fuel cells have the added challenge of immobilizing the electrolyte. For this reason, all porous structures within the MEA must be optimized to minimize liquid movement, which leads to flooding, weeping, and bubbling [7]. All of these processes hinder the formation of the three-phase contact, which is crucial for the

successful operation of the fuel cell. PCE rely on the combination of hydrophobic (PTFE) and hydrophilic phases within the MEA to help properly distribute the electrolyte. In the PAFC design, micron-sized silicon carbide particles are bonded by a modest amount of PTFE (< 10 wt%) to form the electrolyte matrix layer [3]. The silicon carbide matrix houses the electrolyte and serves as an electrical insulator between the two electrodes. In the production of a MEA, the SiC ink is applied on one or both of the electrodes. The MEA is then compressed when mounted into the stack in order to ensure low contact resistance.

3.2.2 Advantages and Disadvantages of PCE Design

PCE holds several advantages over previous types of electrode designs. The most important of which is that it allows for an order of magnitude reduction in Pt loading compared to its predecessor that used unsupported Pt black [2]. Secondly, once the appropriate preparation conditions are determined, the MEA containing the PCE is relatively simple to construct. The major components of the MEA, the carbon materials, the PTFE, and the SiC particles, can all be processed by methods which have been available since the very beginning of fuel cell development. These processes could be adjusted to the demands of the fabrication of the fuel cell components in relatively short time [3].

Although the PCE performs better than its predecessors, the technology still suffers from low catalyst utilization and poor oxygen and proton transport at normal operating current densities. Engineers generally believe the commercially required operating condition for PAFC cathode is about 0.75 to 1 A/cm^2 at a potential of 700 mV/cell [3]. The existing porous electrode designs allow for losses that prevent the

cathode from reaching this performance level. Typically PAFC cathodes operate at a range of 100-500 A/cm^2 at a potential of 700-600 mV/cell.

As was previously mentioned, the PTFE particles distribute themselves in a random fashion in the catalyst layer. For this reason, the network of gas channels and wetted carbon agglomerates are also distributed randomly. A percentage of the supported Pt particles find themselves in locations where they are electrically isolated and therefore inactive. The Pt particles on the carbon supports may be isolated because they are not in electronic contact with the GDL and/or they may be isolated because they are not in ionic contact with the electrolyte layer. The ratio between the amount of active Pt (that is, Pt particles in both ionic and electronic contact with the electrolyte and GDL, respectively) to the total amount of Pt in the electrode is the catalyst utilization value. The typical catalyst utilization values for PCEs are around 50%-60% [8]. These Pt utilization levels are tolerated because numerous gas channels are required for rapid transport of oxygen. Reducing the percentage of PTFE used in the mixture can increase the Pt utilization value of the cell by increasing the amount of Pt particles wetted by the electrolyte. However, this reduction in PTFE content often leads to excessive flooding of the catalyst layer and a detrimental reduction in the rate of reactant gas transport to the catalyst particles.

Within the active region of the PCE cathode, carbon black particles form agglomerates that are about 1 to 4μm in diameter [8]. Figure 3-3, which includes a schematic of the catalyst layer, illustrates the carbon agglomerates [9].

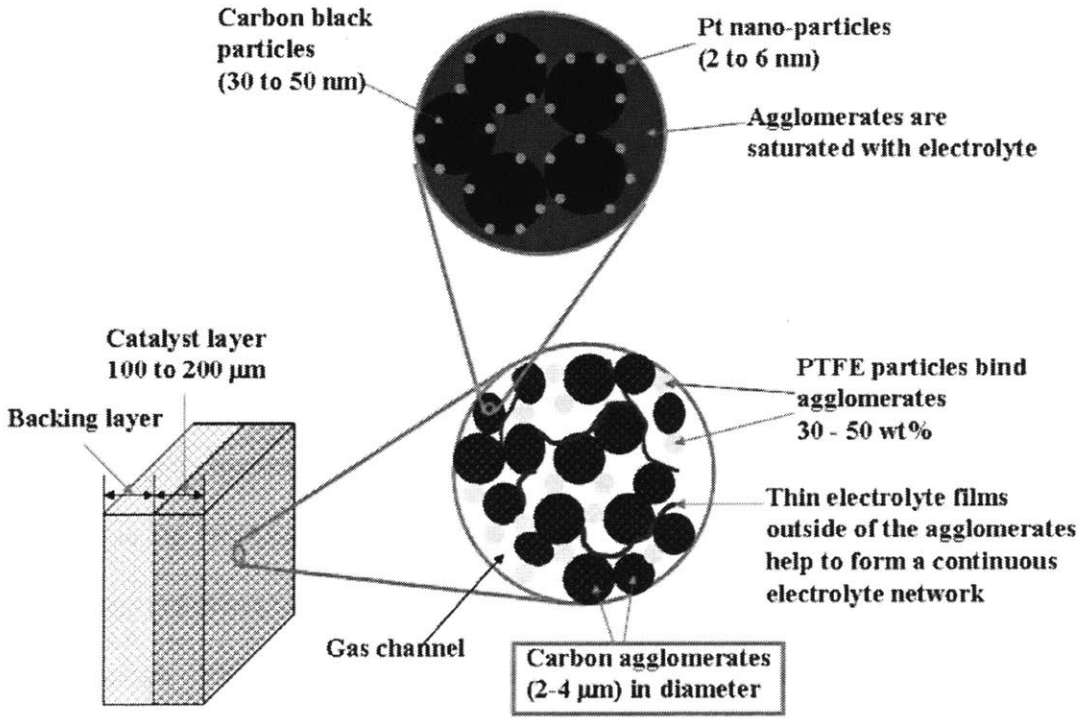

Figure 3-3: Illustration of carbon agglomerates within catalyst layer of PCE [9]

These agglomerates are saturated with the liquid electrolyte. As a result of the extremely low permeability of oxygen within the electrolyte, the concentration of oxygen diminishes within the inner regions of the agglomerate during the operation of the cell.[1] Since the Pt particles within the agglomerates are exposed to a lower concentration of oxygen, the rate of the ORR is reduced on their surface. The resulting concentration overpotential seriously reduces the performance of the cathode.

The concentration overpotential can be reduced by decreasing the size of the agglomerates. One way to effectively decrease the size of the agglomerate is to increase the PTFE content of the catalyst layer. Chan *et al.* studied the effects that the PTFE

[1] The permeability of oxygen in most liquid electrolytes is between 10^{-11} to 10^{-12} $mol/(s \cdot cm)$

content had on the agglomerate size and the effective ionic conductivity of a PAFC catalyst layer [10]. Table 3-1 is a list of their results.

PTFE (Wt%)	Agglomerate Radius (μm)	Effective Conductivity (bulk: 0.6 S/cm)	Current Density: 0.7 V (mA/cm^2)
20	40	0.11	200
30	4.8	0.057	275
40	**1.2**	**0.036**	**290**
50	0.32	0.009	190

Table 3-1: The effects that PTFE content has on agglomerate radius, effective conductivity and electrode performance. The agglomerate radius and effective ionic conductivity were obtained by fitting the performance curve to flooded agglomerate model [10].

The maximum electrode performance was obtained for a PTFE content of 40 wt%. Increasing the PTFE content beyond this point caused excessive ohmic loss caused by a low saturation of the catalyst layer with the electrolyte. At a PTFE content of 40 wt%, the ionic conductivity of the catalyst layer was about 0.036 S/cm. This conductivity value is about 17 times less than the bulk conductivity of the electrolyte. The fact that the gas and electrolyte phases are randomly distributed within the catalyst layer results in a highly tortuous path for ion transport and consequently an extremely low effective ionic conductivity (see Figure 3-3). At PTFE content of 40%, a PAFC half-cell model predicts that the performance lost due to ion transport limitations is about equal to the performance lost due to oxygen transport limitations in the agglomerates.

A half-cell model for the state-of-the-art PCE for a PAFC was presented by Fuller et al. [11]. We programmed this model into MATLAB using most of the parameters provided by Fuller *et al.* except for the volumetric exchange current density. The value for volumetric exchange current density used in the MATLAB program was $ai_o = 3.5 \times 10^{-3} A/cm^3$, which represented the activity of Pt/C. Figure 3-4 shows the performance curve of the porous carbon electrode and the ideal electrode operating in air at 1 bar and at a uniform temperature of 204 °C.[2]

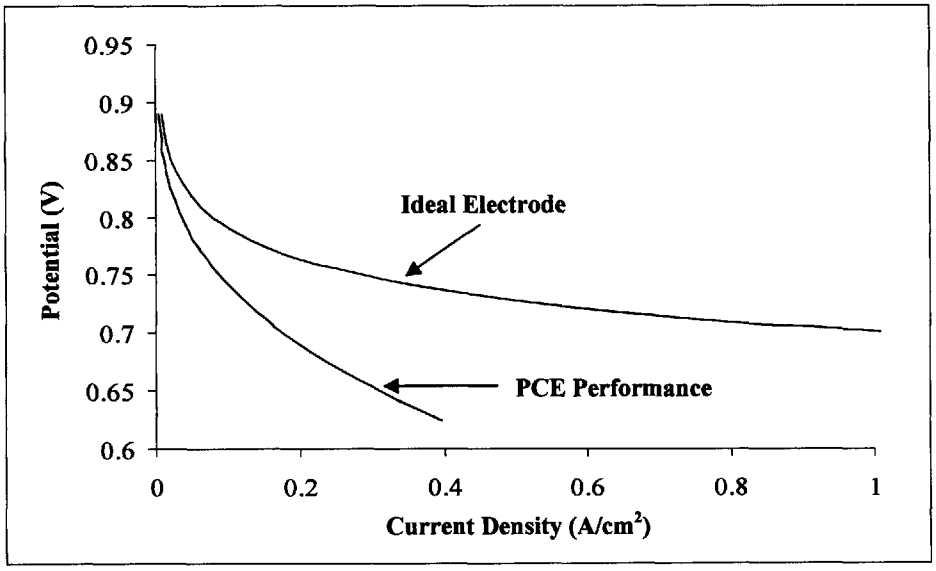

Figure 3-4: Simulated performance curve of air-electrode for PAFC. Parameters of the model were obtained from referenced [11]. The ideal electrode performance curve is simply the Tafel plot. Ideal electrode operates only under kinetic control.

Figure 3-4 shows that at the typical operating potential of the cell of 0.7 V, the current density of the electrode is approximately 17% of the ideal electrode which is operating strictly under kinetic control and at 100% catalyst utilization. Furthermore, the transport limitations of the PCE prevent the operation of the electrode at 25 to 50 mV lower

[2] A specific transport limitation is eliminated by multiplying the diffusion coefficient or conductivity by a factor of 10^6. The ideal performance curve is obtained by multiplying all diffusion coefficients and conductivities in the model by a factor of 10^6.

potentials where significant gains in current density and power density are theoretically possible. The graphs suggest that there is ample room for improvements in the performance of the air electrode in PAFC. Increasing the current density and power density of individual cells means that the size and number of cells can be reduced for a given electrical output of the stack. Reducing the size of the PAFC stack can lead to lower cost and greater system reliability. While higher current and power densities raise other issues, such as thermal and liquid electrolyte management, these issues can be managed with modified stack designs.

3.2.3 Two Improved PCE Fabrication Concepts

Several groups have sought to improve on the PCE technology by altering the fabrication techniques to allow for more control over the geometry and distribution of the structures that make up the catalyst layer. Two different concepts, which are relevant to the microfabricated electrode concept, are presented in this section.

Watanabe *et al.* claimed to develop a catalyst layer with 100% catalyst utilization by replacing the conventional catalyst ink with a dry solid mixture consisting of hydrophobic un-catalyzed carbon black particles and hydrophilic catalyzed carbon black particles [12, 13]. The uncatalyzed carbon particles were made hydrophobic by premixing them with PTFE in a colloid mill. The catalyzed carbon particles were made more hydrophilic by treatment in hot nitric acid and heat treatment in an air oven. The catalyst layer was formed by pressing the powder at room temperature followed by hot-pressing at 360 °C for 3 seconds under 5 kg/cm^2. The powder was hot-pressed for only 3 seconds to ensure that PTFE did not wet the hydrophilic particles.

Watanabe *et al.* reported that their catalyst layer fabrication technique lead to a significant improvement in the performance of the cathode compared to the conventional PCE. First, the formed catalyst layer had a higher catalyst utilization than the conventional PCE because the required hydrophobic regions of the layer did not contain Pt particles. Second, this catalyst layer reduced ohmic losses because the hydrophilic carbon particles helped make the ion path less tortuous. More recently Shim *et al.* refined the earlier work of Watanabe by improving on the method by which the hydrophobic carbon particles where formed [14].

Katz *et al* used a post-catalyzation techniques to enhance Pt utilization [15]. A post-catalyzation technique involves loading catalyst layer with the catalyst after its structure has been formed. The post-catalyzation method is advantageous since it may provide one with greater control over the distribution of the catalyst. In one embodiment of the invention by Katz et al., a solution containing a Pt salt was impregnated into a preformed catalyst layer. The solvent was a mixture of water and an alcohol. After impregnation, the alcohol portion of the solvent was evaporated in such a way that the remaining Pt salt solution was only found in hydrophilic regions of the catalyst layer. The Pt salt in solution was then reduced to Pt nanoparticles supported on the carbon via a chemical oxidation-reduction reaction. In a second embodiment of their invention, an anodic potential was applied to the electrode to selectively wet the electrode with a solution containing the Pt salt. Pt nanoparticles were then formed on the wetted carbon particles using a chemical oxidation-reduction reaction. The electrodes formed using both post-catalyzation methods had near 100% catalyst utilization values. Numerous researchers and fuel cells developers have sought to use post-catalyzation techniques to

improve the performance of the catalyst layer. Most notable are the groups who have used electrodeposition to deposit Pt or Pt alloys in the catalyst layer. Electrodeposition is often the preferred loading technique since the applied current or voltage provides additional control over the Pt particle size and distribution.

Both of the fabrication concepts discussed in this section demonstrate that PCE performance can increase significantly by using methods that allow greater control over structures within the catalyst layer. The novel electrode concept presented in Section 3.4 takes this concept a step further by directly microfabricating some of the micro-structures within the catalyst layer.

3.3 Electrode Design for Polymer Electrolyte Fuel Cells

3.3.1 Thin Film Carbon Electrode (TFCE) Technology

The catalyst layer for polymer electrolyte fuel cells (PEMFC) is formed using thin-film methods. For the purposes of this chapter, the electrodes formed with these methods will be referred to as thin-film carbon electrodes (TFCE). Wilson, in his 1993 patent, was the first to describe an effective thin-film technique for fabricating a PEMFC catalyst layer [16]. In this method, the hydrophobic PTFE traditionally used to bind the catalyst layer is replaced with perfluorosulfonate ionomer (Nafion). Nafion is the ion conducting phase of the cell. Nafion is not as strong a binder as PTFE and it does not impart the same degree of beneficial hydrophobicity to the catalyst layer as PTFE. Nonetheless, replacing the PTFE with the ion-conducting polymer, greatly improves both the effective ionic conductivity of the catalyst layer and the catalyst utilization [17].

A procedure for forming a thin-film catalyst layer on the polymer membrane, as described by Wilson in his 1993 patent [16], is as follows:

1. Combine 5% solution Nafion dissolved in a solvent and 20wt% Pt/C support catalyst in a ratio of 1:3 Nafion/catalysts.
2. Add water and glycerol to weight ratios of 1:5:20 carbon-water-glycerol. The glycerol is added to the mixture in order to improve the paintability of the mixture.
3. Mix solution with ultrasound until the catalyst is uniformly distributed and the mixture is adequately viscous for coating.
4. Ion-exchange the Nafion membrane to Na+ form by soaking it in NaOH, then rinse and let dry. This ion-exchange was done in order to improve the resiliency of the Nafion in the heat treatment phase.
5. Apply the catalyst ink to one side of the membrane by a painting method. Two coats are typically required for adequate catalyst loading.
6. Dry the membrane in a vacuum with the temperature of the approximately 160°C.
7. Repeat Steps 5 and 6 for the other side of the membrane.
8. Ion-exchange the assembly to the protonated form by lightly boiling the MEA in 0.1 M H_2SO_4 and rinsing in de-ionized water.
9. Place carbon paper/cloth against the film and produce a gas diffusion layer.

Wilson *et al.* also described a method in which the catalyst layer is applied using a transfer printing method [17]. In this method, the catalyst layer is first cast onto a PTFE blank, heat-treated to remove the solvents, and then the catalyst layer is decaled on to the membrane. This method reduces the high temperature exposure of the polymer membrane and is generally easier to do in a research laboratory. Directly casting the catalyst layer on the membrane leads to higher performing electrodes than Wilson's method. The improvement is due to the better ionic connection between the membrane and the ionomer in the catalyst layer [18]. Several research groups have published slight variations in the thin-film electrode fabrication method. The details of these methods can be found in their respective publications [19, 20, 21, 22].

Figure 3-5 is a schematic of the thin-film catalyst layer. The layer has typical thickness between 10-25 $\mu g/cm^2$ depending on Pt/C and Nafion loading and fabrication

procedure. Several research groups have reported that the optimum Nafion loading in the thin-film catalyst layer is about 33% of the total catalyst weight [22, 23, 24]. This translates to a Nafion volume fraction of approximately 25%. When the Nafion loading is increased beyond 33% the electrolyte films that cover the Pt/C particles are too thick. These films impede oxygen diffusion to the Pt particles and increase the contact resistance between carbon particles.

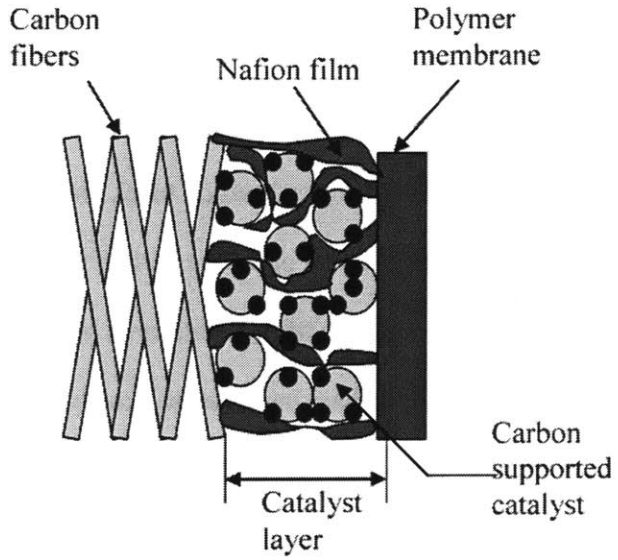

Figure 3-5: Schematic of a electrode for a PEMFC

3.3.2 Gas Diffusion Layer

More so than the GDL in liquid electrolyte fuel cell, the GDL in PEMFC electrode has a major impact on electrode performance. Therefore, any PEMFC electrode design must provide an optimal GDL or the fuel cell performance will suffer significantly.

In the PEMFC, the membrane needs to be sufficiently hydrated in order to conduct protons. However, the MEA cannot be overly flooded with water since that

would impede reactant gas transport. In typical PEMFC designs, the GDL plays an important role in water management within the MEA. The GDL must allow the appropriate amount of water vapor to reach the membrane in order to keep the membrane humidified. At the same time, the GDL must act to remove liquid water produced at the cathode to prevent flooding.

Microporous Layer (MPL):

In MEA designs, it is now common practice to form the GDL of the cathode as a composite of a hydrophobic carbon paper or cloth and a microporous hydrophobic sublayer, the MPL. The MPL lies in between the carbon sheet and the cathode catalyst layer. It is made from a mixture of uncatalyzed carbon black and PTFE. An appropriate amount of PTFE is added and sintered to wet proof the carbon particles and bind them into a continuous porous network. The role of this additional layer is to improve the transport mechanisms across the porous backing layer and catalyst layer interface, and to enhance water management [1]. Cathodes with an MPL typically show better water management characteristics and the performance of the cell is improved over the entire performance curve [25].

The method by which the MPL improves water management in the cell is still being debated. Qi and Kaufman speculated that the improved water management is caused by the microporosity of the sublayer [26]. They suggest that stable water particles may not be able to form in such small and hydrophobic pores of the MPL. For this reason, the MPL is less likely to flood. Qi and Kaufman conclusion, however, is inconsistent with fact that the smallest pores of the MPL are free of PTFE and therefore hydrophilic. A more plausible explanation for the enhanced water management is that

the MPL increases the flow of liquid water back towards the membrane (away from the cathode GDL) [27, 28]. Therefore, the saturation of cathode GDL is lower. Since the permeability of oxygen in the cathode GDL is much lower than the permeability of hydrogen in the anode GDL, increasing liquid flow towards the anode is beneficial to the overall cell performance.

The MPL is partially hydrophobic and it has an average pore size that is much smaller than that of the backing layer. These two factors make the permeation of liquid water through the MPL difficult. In order for water to flow through MPL, a high liquid water pressure is needed at the MPL/catalyst layer interface. This liquid pressure is high enough to overcome the hydraulic resistance of the membrane. Thus, some of the liquid water that crossed the membrane from the anode by osmotic drag is pushed back towards the anode by the high hydraulic pressure at the MPL/catalyst interface.

3.3.3 Advantages of TFCE Technology

In the early 1990's, the PEMFC electrode designs were principally of the PCE type originally developed for liquid electrolyte fuel cells. In the PCE technology, the polymer electrolyte is loaded into the PTFE bound catalyst layer by impregnating it with a Nafion solution. The TFCE is now the electrode design of choice since it has been found to operate at almost twice the power density of PCE catalyst layers [28]. The better performance of the TFCE design over the PCE is attributed to its higher catalyst utilization and its more effective proton transport characteristics. The catalyst utilization of TFCE is about 35% to 45% depending on ionomer loading, while that of at TPCE range from 10% to 22% at optimal ionomer loading [28]. In the TFCE catalyst layer, the Nafion ionomer is uniformly distributed. This is not the case for the PCE catalyst layer.

It is difficult to obtain a uniform distribution of the Nafion within the PCE catalyst layer by impregnating it with the ionomer solution. For this reason, the effective conductivity of the PCE is less than that of the TFCE catalyst layer.

3.3.4 Novel Catalyst Layer Fabrication Concepts

Microfabrication Application:

Prinz's research group at the Rapid Prototyping Laboratory at Stanford University has proposed the use of microfabrication to apply a three-dimensionally patterned macro-texture upon the microporous electrodes of PEMFCs [29, 30]. The structure proposed by Prinz et al. is similar to the microfabricated electrode structure proposed in this dissertation (see Section 3.4.1). The design of their microfabricated fuel cell is shown in Figure 3-6.

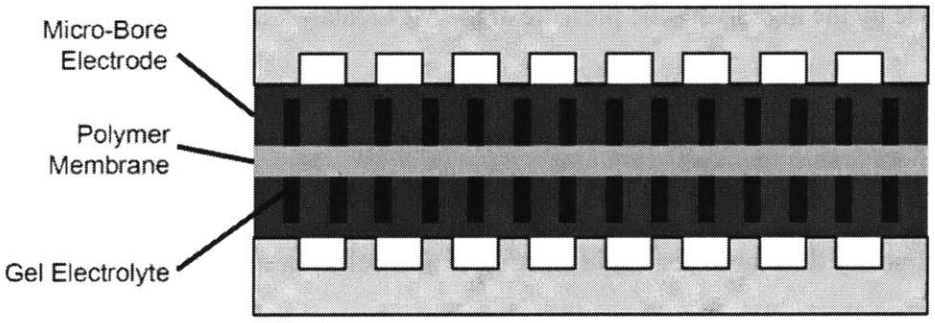

Figure 3-6: Micro-bore electrodes with gel electrolyte [29]. Figure not drawn to scale.

In the Prinz design, a polymer electrolyte membrane separates the electrodes in a manner similar to conventional design. However, the catalyst layer of the electrodes is made much thicker than that of conventional design. To improve ion transport within the catalyst layer, micro-bore cavities (25 to 100 μm in diameter), filled with an acid gel, are present throughout the catalyst layer. Prinz et al. predicted that the additional catalytic area per geometric area of the electrode available for reaction can be enhanced

dramatically if the bores can be made very small with tight spacing, for example, square bores 50 μm wide with bore-to-bore spacing of 50 μm.

Thin Film Technology Application:

The TFCE technology suffers from durability problems associated with the electrochemical corrosion of the carbon support and loss of Pt surface area due to Pt particle agglomeration and dissolution at high potentials [31, 32, 33]. 3M is currently developing a non-conventional catalyst layer that attempts to solve the electrodes durability problems by depositing Pt as thin films on a non-carbon surface. The 3M technology is briefly described here since the novel electrode design presented in this dissertation also proposes the deposition Pt as thin films within the catalyst layer.

In 3M's nanostructured thin film (NSTF) electrode design concept, Pt catalyst is vacuum deposited as thin film onto an ultra thin nanostructured film of oriented crystalline organic whiskers. These organic whiskers are formed by vacuum depositing a crystalline organic pigment material, N,N-di(3,5-xylyl)perylene-3,4:9,10 bis(dicarboximide), onto a substrate. The deposited material has little or no overt structure until it is annealed in a vacuum between 200 and 300°C. At those temperatures the pigment material undergoes a unique conversion to vertically oriented nanostructured whiskers. Figure 3-7 contains side and top SEM images of the whiskers [34]. The whiskers have an aspect ratio (length to width) controllable in the range of 20-50. The number of whiskers per unit area range from 3 to 5 billion whiskers/cm^2. For example, for a pigment film that was deposited 150 nm thick, the thermally formed whiskers led to a geometric surface-area enhancement of about 10-15 cm^2 (total area) per cm^2 (planar) [35]. This additional area is beneficial to Pt deposition since it allows Pt to be deposited

as ultra thin films (low loading per total area) without sacrificing overall Pt loading per planar area. As will be discussed in Section 3.4, the novel electrode design of this dissertation uses a microfabricated catalyst layer to increase the surface area for Pt deposition over the planar area of the electrode.

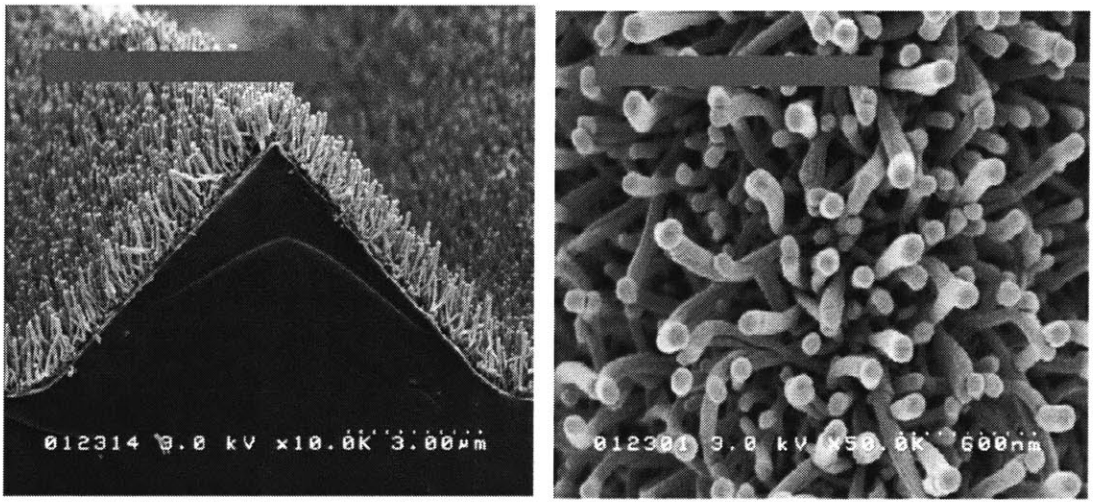

Figure 3-7: SEM images of typical NSTF catalyst as fabricated on microstructured catalyst transfer substrate, seen (left) in cross-section with original magnification of x10,000, and (right) in top view with original magnification of x50,000 [34].

To form the MEA the catalyst/whisker nanostructured film is transferred from the original substrate to the surface of the ion exchange membrane in much the same way as the transfer printing method described by Wilson. Figure 3-8 is an SEM image of the nanostructured film transferred onto the membrane.

The resulting catalyst layer differs for the TFCE technology in four major ways. First, Pt is distributed within the catalyst layer as a thin film rather than dispersed nanoparticles. The specific area of the Pt films is 10 m^2/g [34]. This value is about 8 to 7 times lower than the specific area of dispersed Pt nanoparticles. However, Debe *et al.*, using the RDE technique, have found that the NSTF Pt film catalyst has a specific activity 5 to 10 times greater than that of high surface area dispersed Pt/C [36]. Thus, the

higher specific activity of the thin Pt films compensates for the lower specific area. In the work presented in Chapter 5 of this dissertation, the specific activity of electrodeposited Pt is also measured to be higher than that of dispersed Pt. Furthermore, Debe *et al.* have found that the NSTF Pt catalysts are much more resistant than Pt/C catalyst to permanent loss of surface area due to Pt agglomeration and dissolution [34]. The electrodes were tested under high voltage cycling (0.6-1.2 V) at high temperatures, at high potentials (1.5 V), and hundreds of accelerated stop/start cycles.

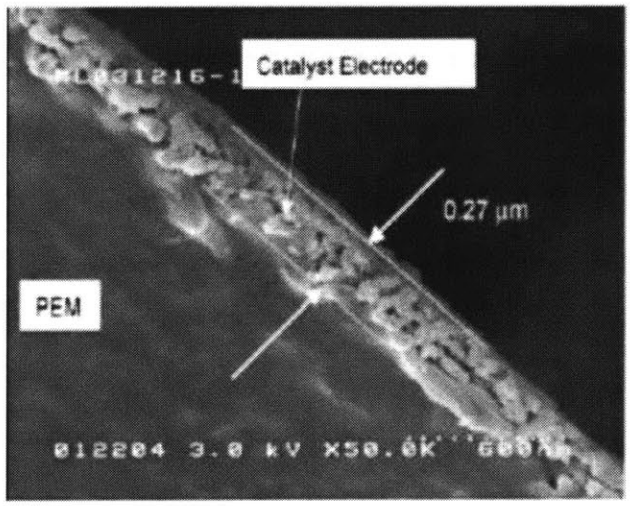

Figure 3-8: SEM image of an NSTF catalyst electrode layer after transfer to the surface of the PEM. The image shows the catalyst layer thickness is less than 0.3 µm.

Under the voltage cycling, the sputtered Pt film lost only 30 % of its original specific area of 10 m^2/g for 3000 cycles. The area lost for the film quickly stabilized at 32% for over 7226 cycles. For the Pt/C supported catalyst, the area lost was more than 95% of its original specific area of 192 m^2/g. This area lost did not appear to stabilize. In both the case of the Pt film and the supported Pt, the loss of specific surface area is primarily the result of the growth of Pt grain size, but the Pt/C XRD grain sizes increase significantly more than the Pt film grain sizes.

The NSTF catalyst layer also differs from the TFCE catalyst layer since it only contains the Pt as the electronically conducting phase. Based on experiments, the Pt films appear more than capable of supporting the current produced at the cell [35]. Additionally, there is no ionomer in the catalyst layer. Apparently the thin nature of this catalyst layer (300 nm) makes ionomer unnecessary for proton transport over the distance of the layer. Adsorbed surface hydrogen species are highly mobile on precious metal surfaces with diffusion coefficients of the order of $10^{-4} - 10^{-3}$ cm^2/sec [37, 38]. Therefore, protons may be transferred to the active sites principally by surface diffusion. The absence of carbon in the catalyst contributes to the overall increase in the durability of the electrode. The NSTF MEA lifetime is 10 to 20 times longer than that of the conventional electrode [34]. In the TFCE catalyst layer, carbon corrosion is known to severely reduce the performance of the cell during accelerated durability testing [31].

3.4 Microfabricated Electrode for Liquid Electrolyte Fuel Cells

3.4.1 Novel Electrode Design Concept of this Dissertation

The microfabricated electrode (MFE) design consists of three layers: (1) a hydrophobic backing layer, (2) a highly hydrophobic microporous layer (MPL), and (3) the microfabricated catalyst layer. The backing layer, like that of the PCE, is fabricated from hydrophobic carbon paper. Its main function is to serve as a current collector and to aid in the uniform distribution of gas to the MPL. A highly hydrophobic MPL is added to the backing layer. Similar to the MPL in PEMFC technology, the MPL in this design is made from carbon black and 30 to 40 wt% of sintered PTFE that acts to bind the carbon

particles and make the layer highly hydrophobic. The role of the MPL is to improve the backing layer's gas distribution and electrolyte repelling properties. Unlike the conventional electrode for PAFCs, neither the backing layer nor the MPL are designed to store electrolyte. Only the anode and the anode bipolar plate will store the electrolyte.

The catalyst layer is a microfabricated dual porosity structure. Specifically, it is a porous matrix (with "micropores" in the order of one micron or less) on which an array of closely packed cylindrical holes is fabricated (see Figure 3-9).

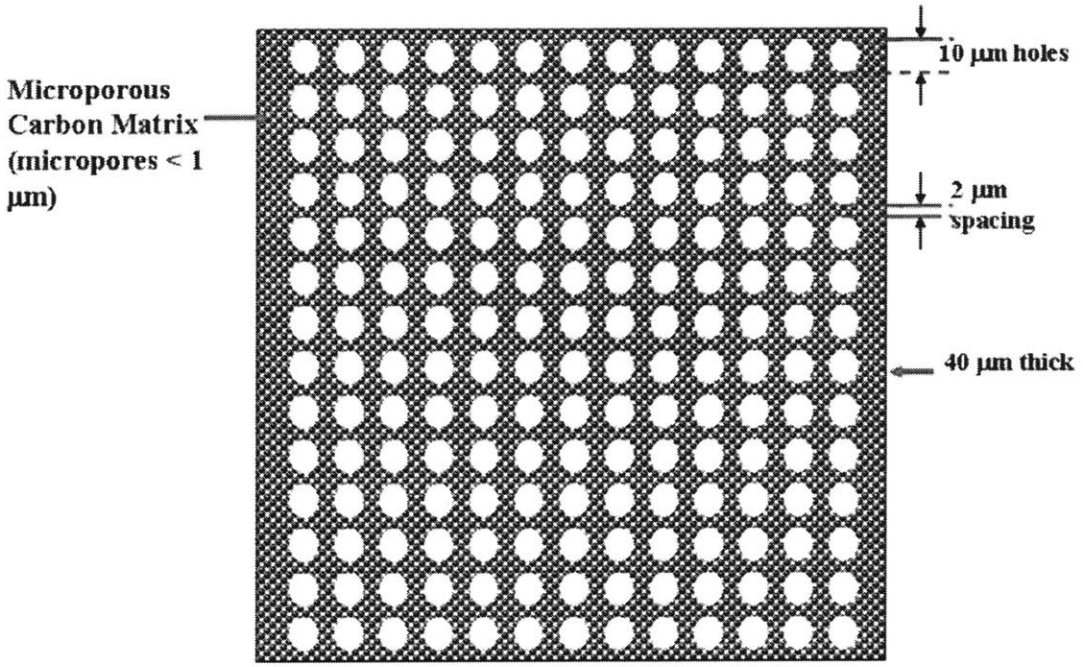

Figure 3-9: Front view of MFE catalyst layer. The porous carbon matrix can be made from carbon black bonded with a polymer. Although this figure suggests that the cylindrical holes go all the way through, they do not (see Figure 3-10).

The microfabricated holes need not be identical in the dimensions. They need only be significantly larger than the micropores of the catalyst layer matrix and the electrolyte filled pores of the anode and the anode bipolar plates. Depending on the effectiveness of the microfabrication process, the cylindrical holes can have a diameter as small as 5 microns.

Figure 3-10 illustrates the MFE design concept along with the other layers that make up a MEA. The MPL is not drawn for clarity.

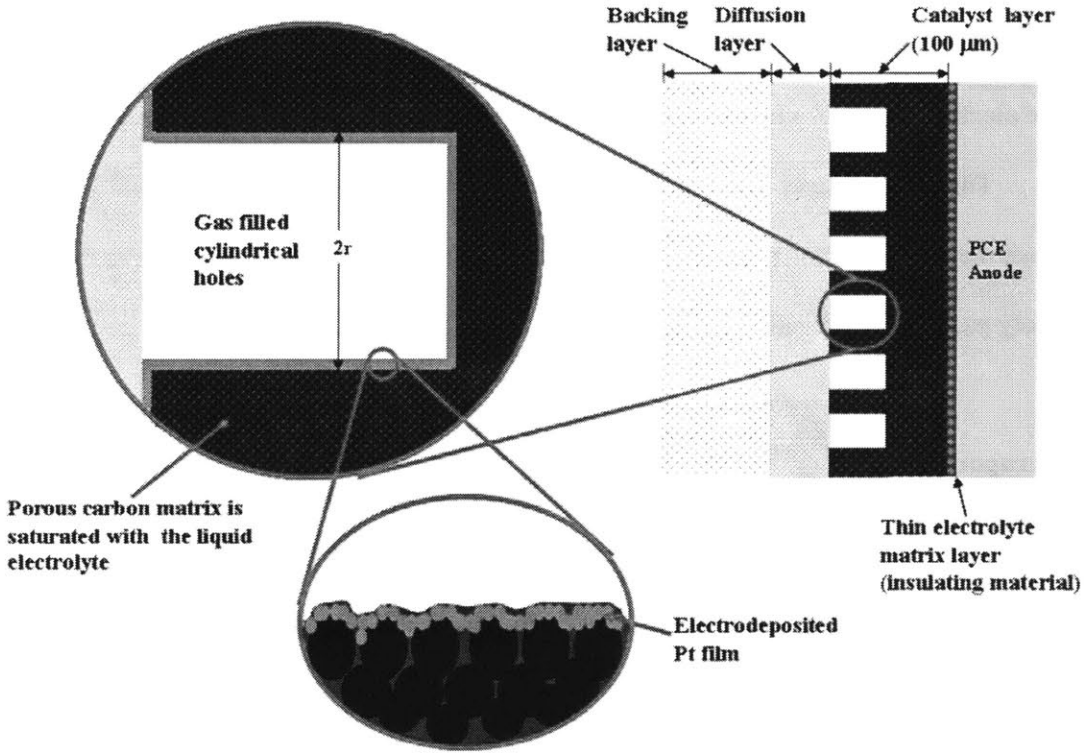

Figure 3-10: Side view of MFE design concept along with other cell components. Illustration is not drawn to scale.

Figure 3-10 shows that the catalyst layer matrix material is saturated with electrolyte and that it makes up most of the electrolyte matrix region of the cell. A thin silicon carbide layer (or some other insulting material) is placed in between the catalyst layer matrix and anode to prevent shorting of the electrodes. The silicon carbide layer can be extremely thin since the gas separating and high bubbling pressure requirements of the electrolyte matrix are fulfilled by the catalyst layer matrix. The catalyst layer matrix has the smallest pores among the porous regions of the cell. Therefore, capillary pressures will insure that it remains flooded with the electrolyte. Depending on the coating process, the silicon

carbide layer can be as thin as 10 μm, which is much thinner than the 100 to 50 μm thickness of conventional silicon carbide layers.

Pt loading is done after the catalyst layer has been fabricated. Pt is deposited as a ultra thin film (Pt loading between 20 to 100 $\mu g/cm^2$) by either physical vapor deposition or, more preferably, by electrodeposition onto the surface of the cylindrical holes. The magnified view in Figure 3-10 illustrates the Pt film. For loading by electrodeposition, one way to allow for the preferential deposition of Pt onto the surface cylindrical pores is to use a "pore-blocking" agent. The pore-blocking agent saturates the pores of the catalyst layer matrix and prevents Pt particles from depositing into the micropores during electrodeposition. Concentrated phosphoric acid, which solidifies at 45 °C in the presence of many nucleation sites, is an ideal pore-blocker when the electrode is used in a phosphoric acid fuel cell.

Certain polymer-bonded carbon materials show significant contact angle hysteresis for aqueous solutions. The contact angle hysteresis causes a dry matrix to act as if it is highly hydrophobic and a water saturated matrix to act as if it is highly hydrophilic. This fortuitous dual-wetting property implies that a MFE catalyst layer made with this type of material can have its cylindrical holes filled with an aqueous deposition solution while having the micropores of the catalyst layer matrix remain completely dry without the use of a pore-blocking agent. Only a slight liquid pressure would be needed to fill the 5 μm or greater diameter holes with the deposition solution. The micropores of the matrix would remain dry since a higher pressure is needed to force the deposition solution into these pores. Two types of polymer-bonded carbon materials

are recommended for the MFE concept. They are described in detail in Chapter 4. Both materials have this dual-wetting property.

The Pt catalyst is loaded as a thin film, 10-50 nm thick, in order to minimize the required diffusion length of oxygen in the electrolyte. The thin catalyst film is an essential characteristic of the MFE electrode concept. Earlier designs considered the uniform distribution of Pt nanoparticles throughout the catalyst layer matrix. Such a design would make the loading of the catalyst layer simple for a polymer-bonded matrix since the matrix can be made from carbon black particles preloaded with Pt nanoparticles. Despite this advantage, simulations of this MFE design concept indicated that a catalyst layer with a hole-to-hole spacing of less than 1 micron is required for modest improvement in electrode performance. This requirement would make fabricating the catalyst layer extremely challenging. For example, a catalyst layer with a hole diameter of 5 μm and hole-to-hole spacing of 1 μm, the thickness of the catalyst layer needs to be more than 100 μm thick for optimal fuel cell performance. Fabricating such a catalyst layer would require a die with poles that have a length to diameter ratio of more than 20.

The dual porosity of the catalyst layer provides the mechanism by which the liquid-gas interface stabilizes close to the deposited Pt. For example, the liquid-gas interface can be actively control by applying a slight overpressure of the air to force liquid electrolyte out of the cylindrical holes. The micropores of the catalyst layer matrix, however, remain saturated due to the high capillary pressure needed to remove the electrolyte from these pores. Also, the liquid-gas interface can be passively stabilized at the deposited film by designing the cell in such a way that the cylindrical holes are the largest pores in the cell. In this way, capillary forces of the smaller pores in the cell will

insure that the cylindrical holes do not flood. For cylindrical holes with diameters of 10 μm or greater, this should not be difficult to accomplish. However, the electrolyte storage regions of the cell may have to be specially designed to ensure that their pore sizes are sufficiently smaller than the diameter of the cylindrical holes. In PAFC applications, the migration of the electrolyte towards the anode at high current densities assists in keeping the cylindrical holes free of the electrolyte. This phenomenon is discussed further in Chapter 7.

Figure 3-11 shows the transport paths for reactants and products in a MFE of an acid-type cathode.

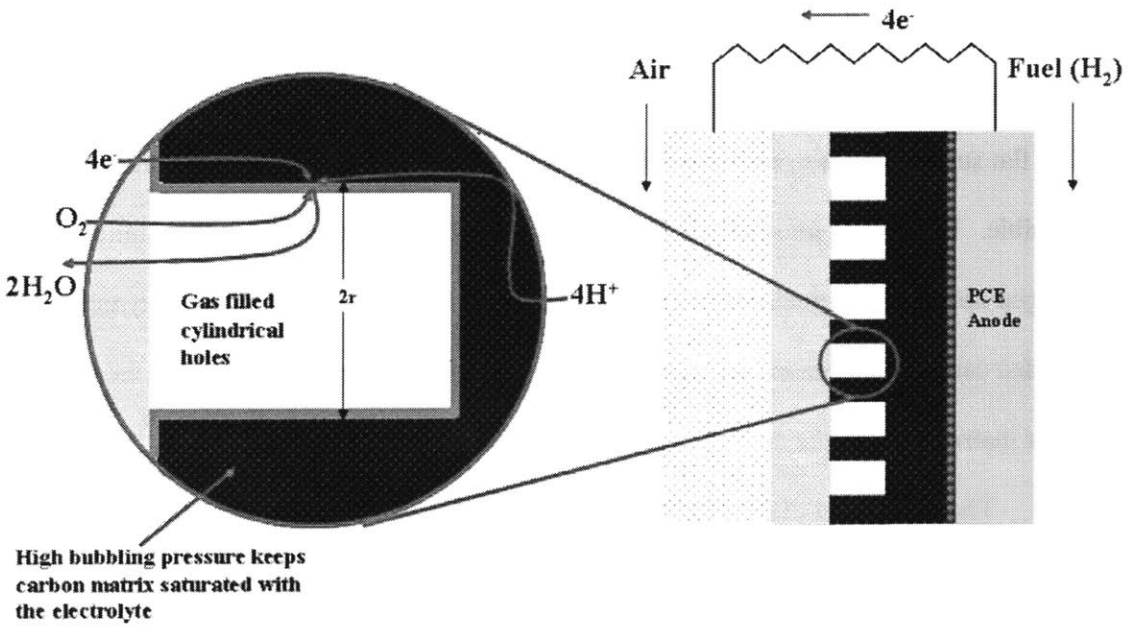

Figure 3-11: Transport in MFE catalyst layer of an acid-type fuel cell

In the catalyst layer, oxygen is primarily transported in the gas filled cylindrical holes. It dissolves in the electrolyte that saturates the catalyst film and diffuses to the reaction sites. The electrons are conducted in the solid regions of the catalyst layer matrix and protons are conducted in the electrolyte-filled micropores of the catalyst layer. For fuel cells

operating above 100°C, water product is primarily transported as vapor as shown in Figure 3-11.

3.4.2 Advantages of Microfabricated Electrode Design

The MFE has several potential advantages over the conventional PCE for liquid electrolyte fuel cells.

1. The MFE design allows for the deposition of the catalyst as thin films. Thus, the required diffusion length of oxygen in the electrolyte is minimized since oxygen only needs to diffuse, in the electrolyte, within the very thin catalyst film. Oxygen is primarily transported in the gas phase where its permeability is approximately five orders of magnitude greater than its value in most electrolytes. Thin Pt films, when deposited on Vycor glass, have been shown to have excellent oxygen transport characteristics [39, 40]. The flat surface and the microporosity (pore size < 50 nm) of Vycor glass makes this possible. The results presented in Chapter 6 of this dissertation suggest that similar oxygen transports characteristics are possible for Pt films deposited on the polymer-bonded carbon membranes described in Chapter 4. These membranes are the catalyst layer matrix without the array of cylindrical holes.

2. The deposition of the catalyst as thin films can also lead to a reduction in the thickness of the catalyst layer. In PCE technology, the 10 wt% Pt particles supported on carbon black is used.[3] One way to decrease the thickness of the catalyst layer, for an equivalent Pt loading per planer area of the electrode, is to use a higher wt% of Pt. However, a higher wt% increases the Thiele modulus of the agglomerate for oxygen transport. Simulations have predicted a reduction in cell performance with an increase

[3] 10 wt% is the percent weight of Pt to the total weight of Pt and carbon.

wt%.[4] In the case of the MFE, the catalyst layer can be made thin by reducing the spacing and the diameter of the holes. Also, the Pt loading within the holes can be increased to reduce the thickness of the catalyst layer. The results presented in Chapter 6 of this dissertation suggest that increasing the thickness of the Pt film by increasing the loading does not lead to an increase in oxygen transport overpotential.

3. The ordered and controllable macro-texture of the catalyst layer makes the uniform deposition of the catalyst film possible. It is envisioned that the catalyst will be electrodeposited onto the surface of the cylindrical holes. Electrodeposition has several advantages including the ability to uniformly distribute the catalyst along vertical sidewalls. The macro-textured patterned shown in Figure 3-9 and Figure 3-10 makes it much easier to apply potential or current modulations to help deposit the catalyst uniformly within the holes.

The controllable macro-texture also makes it easier to optimize the catalyst layer. For a given operating condition of the cell, a catalyst layer with the optimal hole-to-hole spacing, with optimal Pt loading within the cylindrical holes, and with optimal catalyst layer thickness can be fabricated.

4. The catalyst utilization is expected to be 100% for the MFE. This is significantly better than the 60% catalyst utilization for the PCE of a PAFC. The specific area of a Pt film is expected to be in the range of 30 to 5 m^2/g. These values are significantly lower than the 80 m^2/g value for Pt/C supported catalyst. The higher specific activity of the Pt film should partially compensate for the difference in specific area. In the work presented in Chapter 5 of this dissertation, the higher specific activities of the

[4] In these simulations the specific area and specific activity of Pt was assumed to be constant regardless of wt%. New technology exists so that the wt% of Pt can increase without the significant loss of area. E-TEK sells such Pt/C catalyst under the name HP Platinum.

electrodeposited Pt films were found to more than compensate for their lower specific area. In 0.5 M sulfuric acid at room temperature, the mass activities of the electrodeposited Pt film were about 2.5 times greater than that of Pt/C supported catalyst (for further details see Chapter 5). Whether or not similar improvements in activity for Pt films would occur in other electrolytes, such as concentrated phosphoric acid, is uncertain. The chemistry of hot concentrated phosphoric acid is different from dilute sulfuric acid. Nonetheless, the factors that may be contributing the improved activity of electrodeposited films, such as the presence of more favorable crystal facets, lattice compression, and surface defects, should also positively affect the activity of the catalyst in phosphoric acid.

Interestingly, the MFE may provide a new paradigm for mass activity improvements of the catalyst. The Pt activity results presented in Chapter 5 suggest that Pt or Pt alloy can be deposited as thin films in order to enhance mass activity rather than the heavily studied supported catalyst technology.

5. As discussed in Section 3.3.4, the thin catalyst film technology may improve the catalyst layer durability by reducing the rate of active area loss over the lifetime of the cell. For the thin catalyst films, the catalyst "particles" are already sintered. Thus, changes in the grain size that may occur over the life of the cell will not significantly affect the specific area of the film [35].

6. As shown in Figure 3-11, the regions for gas transport and ion transport in the catalyst layer of the MFE are separated throughout the thickness of the catalyst layer. This configuration should lead to a more direct path for ion, electron, and gas transport in the catalyst layer. In contrast, Figure 3-3 shows that these paths are uniformly disturbed

throughout the catalyst layer of the PCE. In the PCE, finely disturbed gas channels are necessary for rapid oxygen transport. However, the channels lead to an extremely tortuous path for ion transport. In an optimized PCE catalyst layer, its tortuosity for proton transport is between 4 and 5.

The effective ionic conductivity of the MFE catalyst layer, $\sigma_{CL,eff}$, is expected to be given by

$$\sigma_{CL,eff} = \sigma_b \left(\frac{\varepsilon}{\tau} \right) \varphi \tag{3.1}$$

where σ_b is the intrinsic conductivity of the electrolyte and φ is the volume fraction of the catalyst layer that is the microporous region (or catalyst layer matrix region). ε and τ are the catalyst layer matrix porosity and tortuosity, respectively. They are expected to be similar in value to porosity and tortuosity of the microporous membranes that will be presented in Chapter 4. Ionic conductivity testing of these polymer-bonded membranes indicates that $\tau \approx 1$ for polymer wt% less than 40 wt%.

For a fully saturated catalyst layer matrix, the product $\varepsilon\varphi$ is the electrolyte volume fraction of the catalyst layer. The MFE is expected to have a value of 0.40 to 0.30 for the electrolyte volume fraction. These values are comparable to the electrolyte volume fraction of the PCE catalyst layers. However, a comparison of the ionic tortuosities suggests that the effective conductivity of the MFE catalyst layer will be 4 to 5 times greater than that of the PCE catalyst layer.

7. In PCE technology, the presence of PTFE in the catalyst layer prevents the flooding of the layer. Unfortunately, the hydrophobicity of PTFE degrades overtime and the performance of the cathode slowly decreases as the electrolyte content of the catalyst

layer increase. In the catalyst layer of the MFE, the three-phase interface is maintained by the dual-porosity of the catalyst layer and pressure differentials.[5] Electrodes using graded porosities to maintain the three-phase interface have shown better long-term stability of that interface than PTFE-bonded electrodes [2].

3.4.3 Fabrication of MFE Catalyst Layer

It is envisioned that the microfabricated catalyst layer and some other layers of the cell will be fabricated in a process similar to what is illustrated in Figure 3-12.

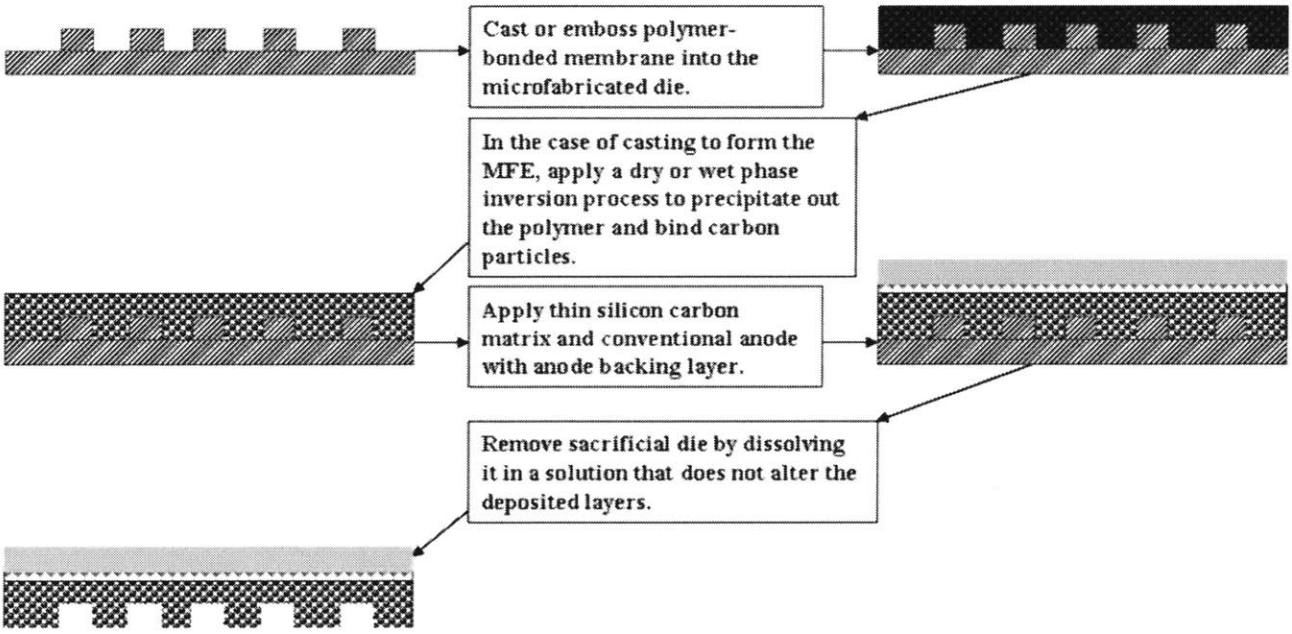

Figure 3-12: Illustration of one possible fabrication process for MFE

In the case of casting to form the MFE, the slurry is cast onto the microfabricated die as shown in the figure. The slurry undergoes a dry or wet phase inversion process to precipitate out the polymer that bonds the carbon particles. A wet phase inversion process is preferred over a dry phase inversion process since it usually leads to a more

[5] The pressure differential may not be necessary if all the hydrophilic pores of the cell are smaller in diameter than the cylindrical holes.

porous structure. Membranes formed by casting tend to be brittle. For this reason, the silicon carbide matrix and anode are placed on top of the catalyst layer. The backing layer of the anode provides the major structural support for the layers. In the case of MFE catalyst layer that is formed by embossing, the embossed membrane is flexible and free-standing. Therefore, the sacrificial die can be removed without adding the anode. The most challenging and costly step of the MFE fabrication process is the production of the catalyst layer die. The catalyst layer die must contain features that are on the micron scale and have these features uniformly replicated on the scale of tens to hundreds of centimeters. The large difference in these relevant scales poses the biggest technical hurdle to the application of the MFE concept.

There are several microfabrication techniques available that can fabricate a die with the required high aspect ratios. Among them are: (1) deep reactive ion etching (DRIE) of silicon, (2) photolithography with plasma etching of the photoresist SU-8, and (3) microembossing of polymers, such as polymethylmethacrylate (PMMA). DRIE was used to produce the dies use in MFE fabrication work done at the Korean Institute of Machine and Materials (KIMM). Appendix A and B contain brief review of the work done at KIMM. Figure 3-13 is an SEM image of the silicon die. DRIE of silicon was chosen for this preliminary work since the technique was available at KIMM's facilities. However, such dies are impractical for the actual MFE fabrication method since the technique is not suitable for high-throughput manufacturing of the die. For a sacrificial die, as shown in the process outline in Figure 3-12, the high cost of repeatedly fabricating the die would make the MFE concept cost prohibitive.

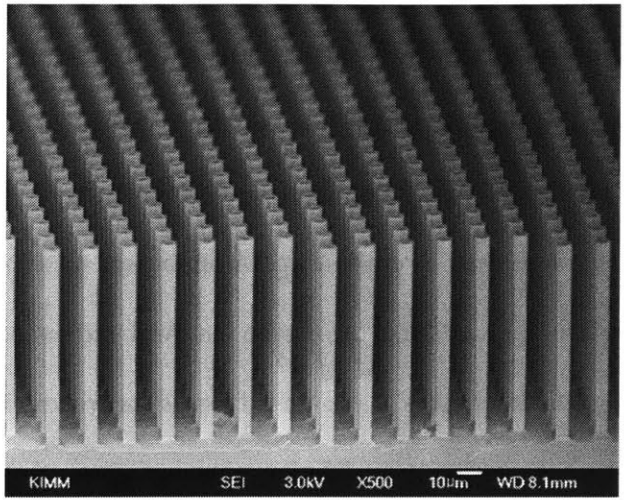

Figure 3-13: Silicon die made by deep reactive ion etching

SU-8 is a popular negative photoresist that has found many applications for many years in micromachining and other microelectronic applications. The exposed and subsequently thermally cross-linked portions of the SU-8 film become insoluble to liquid developers. SU-8 is capable of forming high aspect ratio structures with near vertical sidewalls as a result of its high optical transmission above 360 nm. Figure 3-14 provides two examples of array of high aspect ratio poles that are formed from SU-8. Image (a) is an SEM image of the cylindrical poles fabricated by Prof. Kim's group at the Micro & Nano Systems Laboratory at MIT [42]. Their processes could be modified to produces an array with smaller pole-to-pole spacing.

Forming the die using a photoresist, such as SU-8, results in many of the same disadvantages as DRIE of silicon. Most notably, the process is a low volume process, the capability of the process to uniformly replicate the pattern over a large area is questionable, and the process will most likely be expensive.

Microembossing of a polymer, such as PMMA, is one of the more promising methods to form the die. The technique is suitable for a high-throughput manufacturing.

For example, Avery Dennison Company is developing their microreplication technology that uses a roll-to-roll process to produce precession structures in polymeric substrates continuously and at low cost [41].

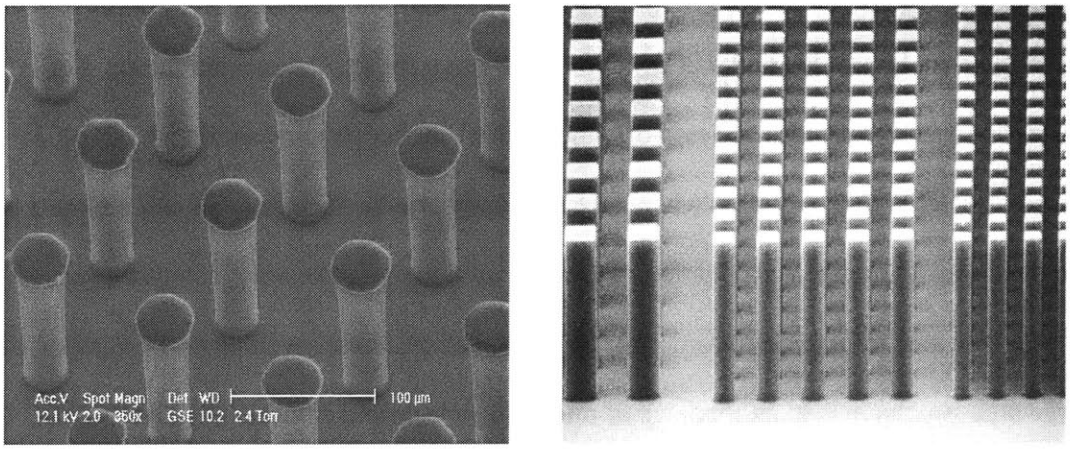

(a) (b)

Figure 3-14: (a) Image of "nanocandles" produced by Prof. Kim's group here at MIT. Nanocandles are 20 µm in diameter and 110 µm in height. SU-8 2075 with oxygen plasma etching was used to fabricate nanocandles [42]. (b) Image of square poles with a square dimension of 10 µm and a height of 50 µm. SU-8 2000 was used to make these poles [43].

The company claims that wide web widths are possible; therefore, the patterning can occur over a large area. Figure 3-15 is an SEM image of one such pattern produced by the microreplication technology.

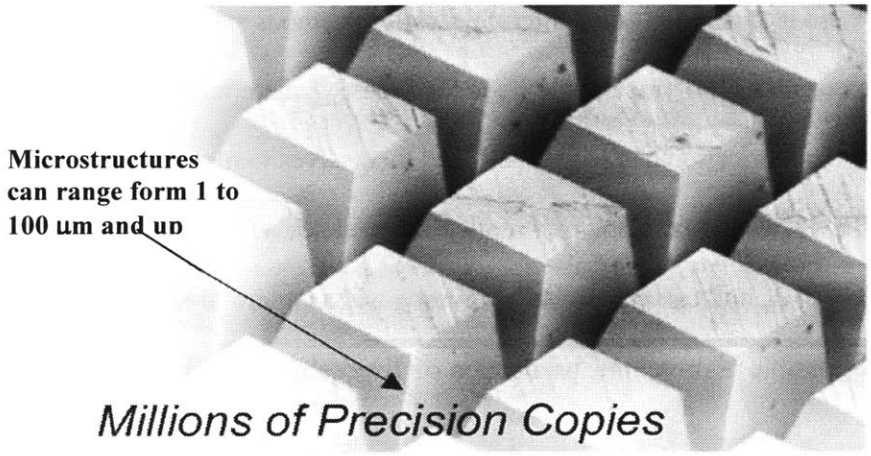

Figure 3-15: SEM of pillars formed by the microreplication process of the Avery Dennison Company [41].

The formed microstructures can range from 1 to 100 μm and up.

Concluding Remarks:

A complete survey of microfabrication techniques capable of forming the die is beyond the scope of this dissertation. However, it suffices to say that Microfabrication techniques are improving and will continue to improve for the foreseeable future. For example, macroelectronics and microfluidic device fabrication are specific microfabrication research areas where advances may provide technologies and methods for the cheap and reliable production of the dies used to make the MFE catalyst layer.

The area of macroelectronics (or large-area electronics) involves the production of large area structures that are made up of micro-size electronic devices [44]. At present, the most visible application of macroelectronics is flat-panel displays. In this application, the transistors are on the scale of 10 μm, but the total surface area of the display can be as large as 600 m^2! The need to make cheaper and more reliable flat-panel displays as well as new applications in the areas of paper-like displays and thin-film solar cells are fueling intensive research in this area of microfabrication.

In the field of microfluidics, especially with respect to its application in the life sciences, there is a need for novel microfabrication methods which use substrates other than silicon or glass. Polymers, as a the main structural material, offer a possible solution to many of the fabrication challenges and lend themselves to mass fabrication of microfluidic devices. Many polymer replication methods such as hot embossing, injection molding, and casting are being investigated as microfabrication methods that may make possible high-volume production of disposable microfluidic devices.

References

[1] S. Litster and G. McLean, "PEM fuel Cell Electrodes", *J. of Power Sources*, Vol. 130, p. 61, 2004.

[2] A.J. Appleby and F.R. Foulkes, *Fuel Cell Handbook*, Van Nostrand Reinhold, 1996.

[3] K. Kordesch and G. Simader, *Fuel Cells and Their Applications*, VCH Publishers, New York, 1993.

[4] N. Giordano *et al.* "An investigation of the effects of electrode preparation parameters on the performance of phosphoric acid fuel cell cathodes," *J. Electrochimica Acta*, Vol. 35, pp. 1411-1421, 1990.

[5] M. Watanabe, M. Tomikawa, and S. Motoo, " Preparation of a high performance gas diffusion electrode", *J. Electroanal. Chem.,* Vol. 182, p. 193, 1985.

[6] K. Kordesch, S. Jahangir, and M. Schautz, "Engineering concepts and technical performance of oxygen-reducing electrodes for batteries and electrochemical pocesses", *J. Electrochimica Acta*, Vol. 29, p. 1589, 1984.

[7] K. Kinoshita, *Electrochemical Oxygen Technology*, John Wiley & Sons, 1992.

[8] H.R. Kunz and G.A. Gruver, "The catalytic activity of Pt supported on carbon for electrochemical oxygen reduction in phosphoric acid", *J. Electrochem. Soc.* Vol. 122, p. 1279, 1975.

[9] S.R. Choudhury, M.B. Deshmukh, and R. Rengaswamy, "A Two-Dimensional Steady-State Model for Phosphoric Acid Fuel Cells (PAFC)", *J. Power Sources*, Vol. 112, p. 137, 2002.

[10] D.S. Chan and C.C. Wan, "Effect of structure on porous gas-diffusion electrodes for phosphoric acid fuel cells", *J. Power Sources*, Vol. 50, p. 261, 1994.

[11] T.F. Fuller, F.J. Luczak, and D.J. Wheeler, "Electrocatalyst Utilization in Phosphoric Acid Fuel Cells", *J. Electrochem. Soc.*, Vol. 142, p. 1752, 1995

[12] M. Watanabe, M. Tomikawa, and S. Motoo, "Preparation of a high performance gas diffusion electrode", *J. Electroanal. Chem.* Vol. 182, p. 193, 1985.

[13] M. Watanabe, K. Makita, H. Usami, and S. Motoo, "New preparation method of a high performance gas diffusion electrode working at 100% utilization of catalyst clusters and analysis of the reaction layer", *J. Electroanal. Chem.* Vol. 197, pp. 195-208, 1986.

[14] J.C. Shim and J.S. Lee, "Development of electrode structure and analysis of electrode pore distributions in phosphoric acid fuel cells", *Materials Chemistry and Physics* Vol. 63, pp. 133-138, 2000.

[15] M. Katz and A. Kaufman, *Method for catalyzing a fuel cell electrode and an electrode so produced*, US Pat. No. 3,979,227 (1976).

[16] M.S. Wilson, *Membrane catalyst layer for fuel cells*, US Pat. No. 5,234,777 (1993).

[17] M.S. Wilson, J.A, Valerio, and S. Gottesfeld, "Low Pt loading electrodes for polymer electrolyte fuel cells fabricated using thermoplastic ionomers", *Electrochimica Acta*, Vol. 40, p. 355, 1995.

[18] Z. Qi, and A. Kaufman, "Enhancement of PEM fuel cell performance by steaming or boiling the electrode", *J. Power Sources* Vol. 109, p 227, 2002.

[19] V.A. Paganin, E.A. Tecianelli, and E.R. Gonzalez, "Development and electrochemical studies of gas diffusion electrodes for polymer electrolyte fuel cells", *J. Appl. Electrochem.* Vol. 26, p. 297, 1996.

[20] E. Guzlow and T. Kaz, "New results of PEFC electrodes produced by the DLR dry prepartion technique", *J. Power Sources*, Vol. 106, p. 122, 2002.

[21] E. Gulzow *et al.* "Dry layer preparation and characterization of polymer electrolyte fuel cell components", *J. Power Sources*, Vol. 86, p. 352, 2000.

[22] Z. Qi, and A. Kaufman, "Low Pt loading high performance cathodes for PEM fuel cells", *J. Power Sources*, Vol. 113, p. 37, 2003.

[23] E. Passalacqua *et al.* "Nafion content in the catalyst layer of polymer electrolyte fuel cells: effect on structure and performance", *Electrochimica. Acta*, Vol. 46, p. 799, 2001.

[24] S. Gamburzev and A.J. Appleby, "Recent progress in performance improvement of the proton exchange membrane fuel cell (PEMFC)", *J. Power Sources* Vol. 107, p. 5, 2002.

[25] Z. Qi, A. Kaufman, "Improvement of water management by micro-porous sublayer for PEM fuel cells", *J. Power Sources*, Vol. 109, p. 38, 2002.

[26] Z. Qi, and A. Kaufman, "Low Pt loading high performance cathodes for PEM fuel cells", *J. Power Sources*, Vol. 113, p. 37, 2003.

[27] U. Pasaogullari, C.Y. Wang, and K.S. Chen, "Two-Phase Transport in Polymer Electrolyte Fuel Cells with Bilayer Cathode Gas Diffusion Media", *J. Electrochem. Soc.*, Vol. 152, p. A1574, 2005.

[28] A.Z. Weber and J. Newman, "Effects of Microporous Layers in Polymer Electrolyte Fuel Cells", *J. Electrochem. Soc.* Vol. 152, p. A677, 2005.

[29] S.J. Lee, S. Cha, R. O'Hayre, A. Chang-Chien, and F.B. Prinz, "Miniature fuel cells with non-planar interface by microfabrication", *Proceeding of Electrochemical Society – Power sources for the new millennium*, pp. 67-76, 2000.

[30] S.J. Lee, S. Cha, Y. Liu, R. O'Hayre, and F.B. Prinz, "High power-density polymer-electrolyte fuel cells by microfabrication", *Proceeding of Electrochemical Society*, Spring 2000.

[31] D. Stevens, M. Hicks, and J. Dahn, "Ex-situ and In-situ Stability Studies of PEMFC Catalysts: Effect of Carbon Type and Humidification on the Degradation of the Carbon", *J. Electrochem. Soc.* Vol. 152, p. A2309, 2005.

[32] P.J. Ferreira, G.J. la O', Y. Shao-Horn, D. Morgan, R. Makharia, S. Kocha, and H. Gasteiger, "Instability of Pt/C Electrocatalysts in Proton Exchange Membrane Fuel Cells: A Mechanistic Investigation", *J. Electrochem. Soc.*, Vol. **152**, p. A2256, 2005

[33] R.M. Darling and J.P. Meyers, "Mathematical Model of Platinum Movement in PEM Fuel Cells", *J. Electrochem. Soc.* Vol. 152, p. A242, 2005.

[34] M.K. Debe, A.K. Schmoeckel, G.D. Vernstrom, and R. Atanasoski, "High Voltage Stability of Nanostructured Thin Films Catalysts for PEM Fuel Cells", *Journal of Power Sources*, Vol. 161, p. 1002, 2006.

[35] M.K. Debe, "Novel Catalyst, Catalyst Support and Catalysts Coated Membrane Methods," *Handbook of Fuel Cells – Fundamentals, Technology and Applications*, W. Vielstich, H.A. Gasteigher, A. Lamn, Editors, Vol. 3, John Wiley & Sons, 2003.

[36] M.K. Debe, "Advanced catalyst and membrane technology with enhanced performance and durability for automotive requirements", in: Proceedingcs of the 4th International Fuel Cell Workshop 2005, Kofu, Japan, September 22-24, 2005, p. 62.

[37] L. Su and B.L. Wu, "Investigation of surface diffusion and recombination reaction kinetics of H-adatoms in the process of the hydrogen evolution reaction (her) at Au electrodes", *J. Electroanal. Chem.* Vol. 565, p. 1, 2004.

[38] M.V. Arena, E.D. Westre, D.E. Brown, J. Kutzner, "Surface-Diffusion of Hydrogen on a Stepped Ru (001) Surface", *Surface Science*, Vol. 325, p. 151, 1995.

[39] B. Cahan, PhD Thesis, Chemical Engineering Department, University of Pennsylvania, Philadelphia, PA, 1968.

[40] A.J. Asher and J.S. Batzold, in From Electrocatalysis to Fuel Cells, G. Sandstede, Editor, pp. 223-230, 1972.

[41] http://www.reflectives.averydennison.com/

[42] S.C. Kim, "Assembly of Nanotubes: a Mechanical Way", Presentation, April 8th, 2005, Department of Mechanical Engineering, MIT.

[43] http://www.microchem.com/products/pdf/SU8_2-25.pdf

[44] Z. Suo, J. Vlassak, and S. Wagner, "Micromechanics of Macroelectronics", *China Particuology*, Vol. 3, p. 321, 2005.

Chapter 4

The Preparation and Characterization of Polymer-Bonded Microporous Membranes

4.1 Introduction

The proposed catalyst layer is a dual porosity structure with 10 to 50 μm cylindrical holes microfabricated within a microporous matrix. The materials that form this matrix are crucial to the performance of the catalyst layer. The microporous matrix must have pores that are less than 1 μm. This pore size allows for a significant range of capillary pressures capable of expelling the liquid electrolyte from the cylindrical pores while the pores of the matrix remain flooded. The matrix must be electrically conductive and must have a high porosity so that the electrolyte saturated matrix has a high ionic conductivity and a high liquid permeability. The matrix must also have good mechanical properties and be chemically resistant to the reducing environment of the cathode.

Carbon black and graphitized carbon have been shown to be effective and inexpensive materials used to construct the electrodes of fuel cells. For this reason, carbon is the preferred material for the microfabricated catalyst layer. In this work, two types of carbon-based materials were considered for the matrix material: (1) carbon aerogel monoliths and (2) polymer-bonded carbon black membranes. These materials were formed into porous membranes to test their fitness for the catalyst layer matrix. The membranes were examined for their porosity, liquid uptake, breakthrough pressures, ionic and electronic conductivities, liquid permeability, and mechanical properties.

Carbon Aerogel:

The carbon aerogel membrane is a microporous carbon monolith made from the carbonization of resorcinol-formaldehyde polymer. The details of carbon aerogel preparation and properties are given in Appendix B. The carbon aerogel membranes prepared in this work proved to be too brittle when they were thinner than 300 μm. Also, the aerogels shrunk significantly during the drying and carbonization process. These facts made aerogel membranes very difficult to work with. All attempts at microfabricating a carbon aerogel catalyst layer failed (see Appendix B). For this reason, the carbon aerogel monolith is *not* believed to be a suitable material to form the microfabricated catalyst layer.

Polymer-Bonded Membrane:

Two types of polymer-bonded membranes were prepared and characterized in this work, the polytetrafluoroethylyne (PTFE) bonded membrane and the polyethersulfone (PES) bonded membrane. For both of these types of membranes, a furnace carbon black was used as the carbon material. In the case of the PTFE-bonded membranes, PTFE particles were sheared into fibrils that intertwined to bond the carbon particles. In the case of the PES-bonded membranes, the PES polymer is soluble and a mixture of the polymer, carbon black, and solvent underwent a phase inversion process to form the membranes. The details and results of the preparation and characterization of these membranes are provided in this chapter.

Nafion and polybenzimidazole (PBI) are two other types of polymers that are commonly used in fuel cell technologies. These polymers were not studied in this work. Nafion has the advantage of being a good proton conductor. For this reason, a high

volume fraction of this polymer as a binder for the carbon particles would be less detrimental to the matrix's ionic conductivity compared to a high volume fraction of the non-proton conducting PTFE and PES polymers. However, Nafion is a very brittle polymer when cast from solution [1, 2]. This brittleness is attributed to poorly developed morphology of the crystalline fluoropolymer regions and ionic clusters of the recast films [3]. Furthermore, Nafion, a perflourosulfonate ionomer, is not melt-processable because of side chain entanglement and ionic interactions between the functional groups [4]. Thus, Nafion cannot be sintered to improve the bonding between it and the carbon particles. The brittleness of Nafion and the fact that it is not a thermoplastic indicate that Nafion will not be a mechanically strong binder for the catalyst layer matrix. Nafion is also much more expensive than PES or PTFE. For these reasons, Nafion is not considered to be suitable binder for the catalyst layer matrix.[1]

PBI is also a good proton conductor when it is doped with sulfuric or phosphoric acid [5, 6]. However the mechanical properties of PBI are poor at high doping levels. For this reason, PBI is not a suitable binder for the catalyst layer matrix considering that the matrix will be flooded with an electrolyte.

[1] Lee did work with Nafion as a binder for carbon black particles, He showed that it can be used to bind carbon into the microfabricated catalyst layer structure. However, a high volume fraction of the polymer is needed. Some of the results of Lee's work are given in Appendix A.

4.2 Membrane Preparation and Observations

4.2.1 PTFE-Bonded Microporous Membranes

Background:

PTFE and other fluoropolymers have long been used as binders for the flooded electrodes used in batteries and double-layer capacitors. Flooded electrodes are typically created by mixing a carbon powder with a polymer and a lubricant. The resulting mixture is then subjected to high shear forces in order to fibrillize the binder particles. In typical applications, a ram or screw extruder is used to produce the high shear forces for this process. The fibrils intertwine to eventually form a matrix which acts to support and bind the particles. The extrudent is then calendered to the desired thickness. The numerous patents that describe this method of forming electrodes differ principally in the tool used to fibrillize the polymer [7, 8, 9, 10]. Recently, Mitchell *et al.* patented a process that uses a jet mill to fibrillize the polymer [10]. Their process has an advantage in that no lubricants are needed during the fibrillization of the polymer. When lubricants are utilized in the manufacture of electrodes for capacitors, the operating lifetime, as well as the maximum operating voltage, may be reduced as the result of undesirable chemical interactions that can occur between residues of the lubricant and the electrolyte.

The electrode-forming methods described above use fluoro-polymer resins. The diameter of these resins ranges from 20 to 500 μm. The polymer particles, when fibrillized, create a support matrix where the spacing between fibrils is on the order of microns [7]. This matrix is suitable for binding particles into a flat sheet. In the proposed microfabricated catalyst layer, the particles must be sufficiently bonded together so that cylindrical holes, ranging from 10 to 20 μm in diameter and with a hole-

to-hole spacing of 2 to 5 μm, can be formed by micro-embossing the membrane. Such a membrane needs a high density polymer matrix with inter-fiber spacing on the scale of hundreds of nanometers or less. In order to process such a dense matrix, PTFE dispersions are needed instead of resins. The size of the polymer particles in a dispersion ranges from 50 to 500 nm [11].

Membranes with the desired high density matrix were fabricated. The membranes were characterized and a decision about their suitability for the catalyst layer was made. No attempts were made to develop a process that is optimal in terms of energy, time, and cost.

Preparation of Membranes:

The procedure for preparing PTFE-bonded membranes is as follows:

Step 1. Mix 0.5 g of carbon black (Vulcan XC72 carbon black or Vulcan XC72R carbon black) with 90 mL of water (5.6 mg/mL of water).

Step 2. Sonicate the mixture at maximum power for 10 minutes (50 watt sonicator).

Step 3. Use a syringe to add PTFE (Teflon® PTFE 30 from DuPont) solution into the carbon/water mixture drop by drop. PTFE wt% used: 5wt, 10wt, 15wt, 20wt, and 25 wt%. PTFE wt% is the ratio of the mass of PTFE to the total mass of carbon black and PTFE.

Step 4. Sonicate the mixture at maximum power for 15 minutes

Step 5. Boil the excess water until only the water saturated dough is left in the beaker. Use a stainless steel spoon/spatula and swirl the beaker in a circular motion to roll the water saturated carbon/PTFE dough into a tight ball.

Step 6. Dry the carbon/PTFE dough in an air oven at 120°C for 24 hours to remove water in pores.

Step 7. Using a razor blade, cut a 1-2 mm slice from the dough. Saturate slice with isopropanol for 2-4 minutes. Using two polished aluminum plates (mirror finish), press dough in between the plates under an initial

pressure of 17.2 bar (1021 kg from the press) to form a thin membrane. Release from the press when the load drops from 1021 kg to range of 680 kg to 454 kg. The resulting membrane thickness ranges from 250 μm to 50 μm.

Step 8. Dry membrane in an air oven at 120°C for 30 minutes. Then, heat-treat the membrane in an air oven at 280°C for 30 minutes to decompose the surfactant that was in the PTFE dispersion.

Two types of carbon black were used to make the membranes, Vulcan XC72 and Vulcan XC72R.[2] XC72 is the pelleted form of the carbon black. XC72R is the fluffy form. These two carbon blacks are made using the same manufacturing process except for the final step. In that final step, XC72 undergoes an additional compaction process to form pellets. The compaction process involves wetting the XC72R powder with water and running it through a system that uses centrifugal forces to compact the powder.[3] The end product is carbon black particles aggregated into spherical pellets as large as 1 mm. XC72 and XC72R have densities of 0.262 g/cm^3 and 0.096 g/cm^3 respectively. The XC72 pelleted carbon black is usually desired over the XC72R fluffy carbon black since the former is much easier to work with than the latter. XC72 is the most widely used carbon black in fuel cell applications [12]. However, VC72R has recently been used to form the hydrophobic microporous layers in PEMFCs [13].

In step 1, the carbon black particles were mixed with a large amount of water (5.6 mg/mL of water) to ensure high dispersion of the carbon black and PTFE particles [14]. The larger the water content in this recipe, the more time consuming and energy intensive the process is for making the membrane. However, no attempts were made to determine

[2] Vulcan XC72 and Vulcan XC72R are the Cabot product name for a type of oil furnace black. In the remainder of this chapter, "Vulcan" will be excluded from the product name of these carbon blacks.
[3] This information was obtained from a phone conversation with a Cabot technician.

the minimum amount of water that would sustain both an adequate dispersion of the solids and fibrilization of the PTFE particles.

XC72R carbon black was used to make some of the PTFE-bonded membranes in hopes that it would produce membranes with a higher porosity than membranes formed from XC72 carbon black. However, XC72R proved much harder to work with than XC72. For example, water was unable to wet the XC72R carbon. The extremely low-density powder quickly floated to the water-air interface when 90 mL of water was added to the beaker. In this condition, the carbon black particles could not be dispersed when sonicated. Since isopropanol spontaneously wets the XC72R powder, attempts were made to first wet the powder with 10 mL of isopropanol before pouring water into the beaker. This additional step did allow the powder to be wetted with water, then sonicated, and ultimately formed into membranes. However, the membranes did not have good mechanical properties. SEM pictures revealed that PTFE fibers were not uniformly distributed throughout the membrane. The addition of isopropanol adversely interacted with the nonionic surfactant, used in the PTFE dispersion to stabilize the particles. This interaction caused some of the PTFE particles to coagulate. No attempts were made to wet the XC72R powder with a lower amount of isopropanol to limit the alcohol's effect on the stability of the dispersion.

The XC72R powder was properly wetted with water by first pouring a small of amount of water into the beaker containing the powder (about 2 to 3 mL of water). A stainless steel spoon/spatula was used to pat the water into the powder. This procedure was repeated until the powder turned to a thick paste. At this point, the remaining amount of the 90 mL of water was added to the beaker without having the carbon black

float to the top. This was a time consuming process, but it proved effective in producing strong XC72R/PTFE membranes.

Step 2 involved the initial sonication of carbon black particles. It was used to disperse the carbon particles and to reduce most of the carbon black particles to their primary agglomerate size of 200 nm to 1 μm. This step also released all the gas bubbles that were trapped in the carbon aggregates, thus fully wetting the carbon particles with water. After the initial sonication the PTFE dispersion was added (Step 3).

In step 4, high shear forces produced by cavitation were used to turn the 50 to 500 nm particles of PTFE into fibrils with lengths greater than 1 μm. During the boiling step, step 5, some of the solid components of the mixture were loosely held together and seen floating on top of the boiling water as a thin layer. When most of the water was boiled off, the carbon/PTFE mixture laid at the bottom of the beaker as a loosely connected, water saturated sheet. At this point, a spoon was used to collect the solid mixture and press it against the walls of the beaker in order to expel excess water. The beaker remained on the hot plate in order to boil off the excess water that was pressed out of the mixture. The resulting dough was then rolled into a tight ball by swirling the beaker in a circular motion and by periodically placing the beaker on the hot plate to boil off excess water.

Observations:

Figure 4-1 for shows the dough after it was rolled up. Step 4 was crucial to the formation of the membranes. A Carbon/PTFE/water mixture that was not sonicated did not form a solid mixture with sufficient polymer bonds that it could be pressed together

and then rolled up into a tight ball. The rolled dough shown in Figure 4-1 can be held and pressed without breaking into pieces or cracking.

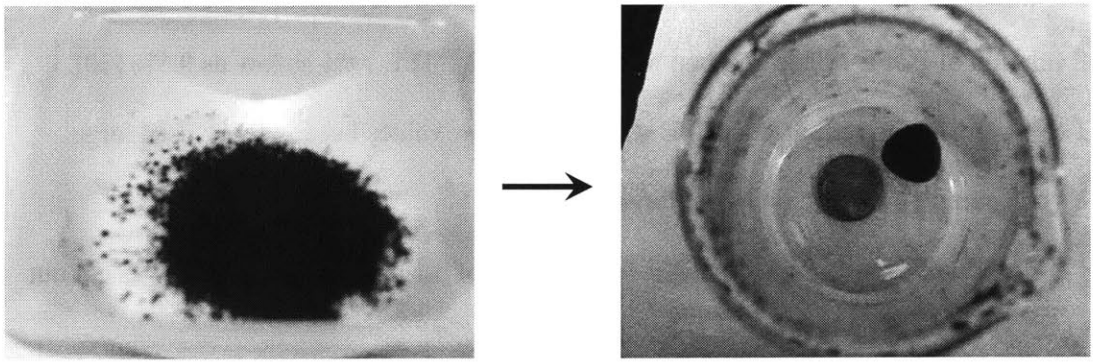

XC72 carbon black **Rolled dough after step 5**

Figure 4-1: Carbon black powder and dough

At the end of step 5, water accounted for 80 to 90% of the dough's mass. Drying the dough in an air oven caused it to uniformly shrink to approximately 65% of its original volume. For PTFE contents greater than 5 wt%, the amount of PTFE did not noticeably change the amount of shrinkage the dough experienced when dried. Doughs with 5 wt% of PTFE appeared to shrink less than the others, and they sometimes formed large cracks when air dried. The latter observation is probably an indication that 5 wt% is close to the minimum amount of PTFE that can be used in this process.

Larger particles and aggregates can be bonded with lower amounts of PTFE than smaller particles and aggregates. This fact was observed when doughs formed with 5 wt% PTFE and XC72R were pressed to form membranes. The resulting membranes were not mechanically strong. They often tore during the pressing process. In contrast, membranes made with XC72 and 5 wt% PTFE did not tear during the pressing process. The difference between the two membranes is the average size of the carbon aggregates. The average size of the aggregates of XC72R is smaller than that of XC72. For this reason, to have the same mechanical strength, a higher polymer content (a denser PTFE

matrix) is needed to bind XC72R particles than is needed for XC72 particles. The amount of carbon-carbon bonds clearly affects the overall strength of the membrane. Mitchell *et al.*, using a more complicated dry fibrillization process, reported the formation of PTFE-bonded carbon membranes with PTFE wt% as low as 0.5% [10]. They were able to reduce the PTFE wt% to such low values because they used large carbon particles to form their membranes.

Figure 4-2 is a SEM picture of the surface of a 1 mm thick slice that was cut out from a 15 wt% dough. The slice has not been pressed.

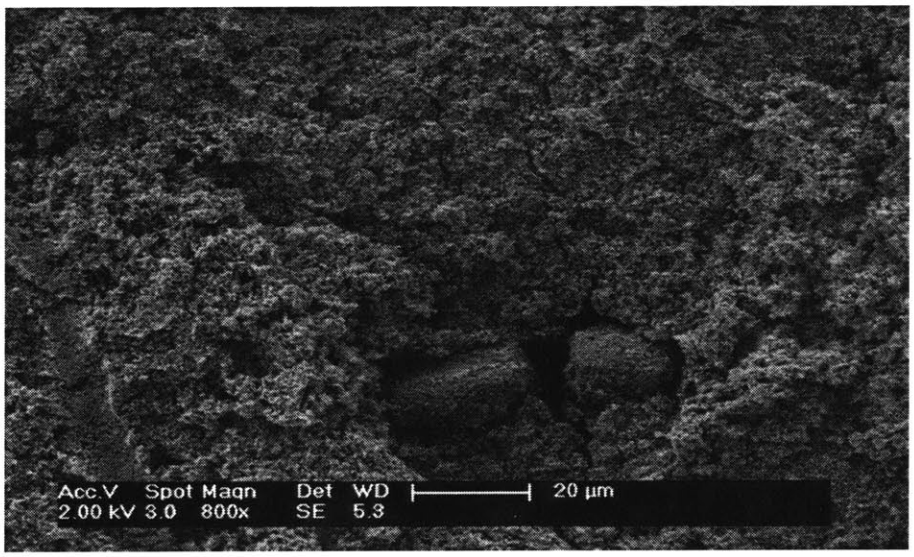

Figure 4-2: SEM image of the surface of a slice from the dough (XC72/15 wt% PTFE)

The SEM picture shows an uneven surface with visible cracks and large aggregates of carbon. Figure 4-3 is a SEM picture of the surface of a 15 wt% PTFE-bonded membrane. The surface of the membrane went from a rough surface, similar to what is shown in Figure 4-2, to a relatively smooth and compact surface by pressing the membrane at a modest pressure of 17.2 bar. Isopropanol, added in step 7, acted as a lubricant that allowed the carbon particles and aggregates to easily slide between each other. Additives,

such as alcohols, are often used as lubricants in the extrusion processes used to form PTFE-bonded membranes on the industrial scale [7, 8, 9]. After pressing the membrane, the aluminum plates were separated from each other. If the membrane remained attached to one of the plates, it was allowed to dry. As the isopropanol evaporated, the membrane spontaneously peeled off of the aluminum plate.

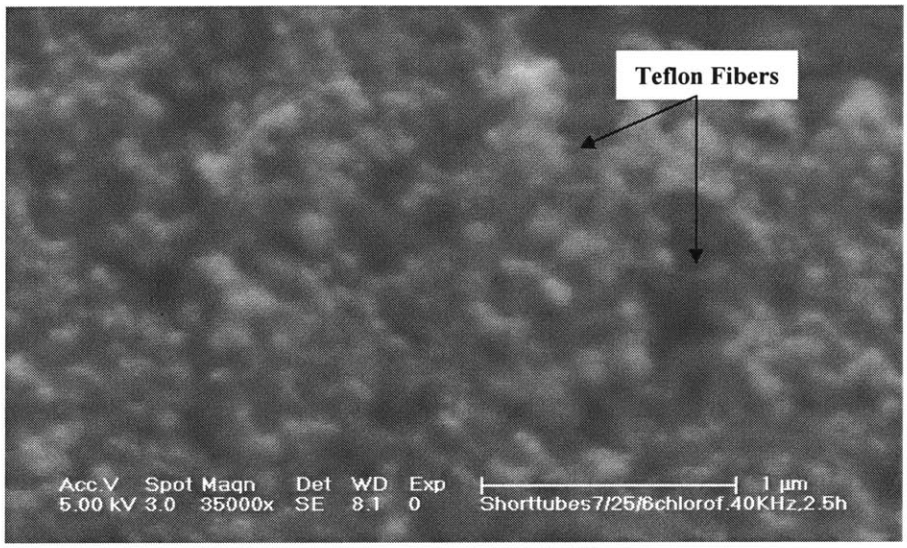

Figure 4-3: SEM image of the surface of a 15 wt% PTFE-bonded membrane

Figure 4-3 shows that the surface of the membrane appears denser than the porosity measurements of 70 to 80% would suggest (see Section 4.4.1). One reason the membrane appears dense is because a significant fraction of the pore volume of the membrane is found in pores which are less than 30 nm in diameter. These are the pores formed between the primary particles of the carbon black. They are not visible at the magnification of SEM picture. Another reason is because of the alignment of the carbon aggregates at the surfaces of the membrane. During the pressing process, carbon aggregates near the aluminum plates are forced to align themselves in a compact fashion in order to form a flat surface. As a result of this, the surfaces of the PTFE-bonded

membranes are probably less porous than the interior portion of the membrane. The dense surface of the PTFE-bonded membrane is not a membrane skin in the traditional sense (see Section 4.2.2), but it is referred to as one in this chapter. A membrane skin is beneficial for preferential catalyst loading on the surface of the membrane. High surface area means more nucleation sites for catalyst deposition. On the other hand, the membrane skin may significantly lower the overall permeability and ionic conductivity of the membrane.

Figure 4-4 shows SEM images of the surface of membranes with 5, 10, and 15 wt% of PTFE. The carbon aggregate of the 5 wt% membrane appears stretched apart. This may be due to the way the aggregates aligned themselves during the pressing process. At 5 wt% of PTFE, there may not have been a sufficient amount of PTFE fibrils to tightly bind the aggregates. Thus, during the pressing process, the aggregates moved further apart from each other than they would have in the presence of greater amounts of fibrils. Another possibility is that the aggregates and fibrils stretched apart while the membrane was handled. The PTFE fibrils make the membranes elastic to a certain degree. A low fibril density renders the membrane more susceptible to permanent deformation when it is stressed. The SEM picture of the 5 wt% membrane is possibly showing evidence of a deformed membrane. The series of pictures in Figure 4-4 clearly show that these effects decrease with an increase in the PTFE wt%. They also show that the porosity of the membrane surfaces decrease with an increase in the PTFE wt%. The porosity of the entire membrane decreases with an increase in PTFE wt % (see Section 4.4.1). However, the SEM pictures of the surface of membranes with a 20 and 25 wt% of PTFE were not significantly different from that of membranes with 15 wt% of PTFE.

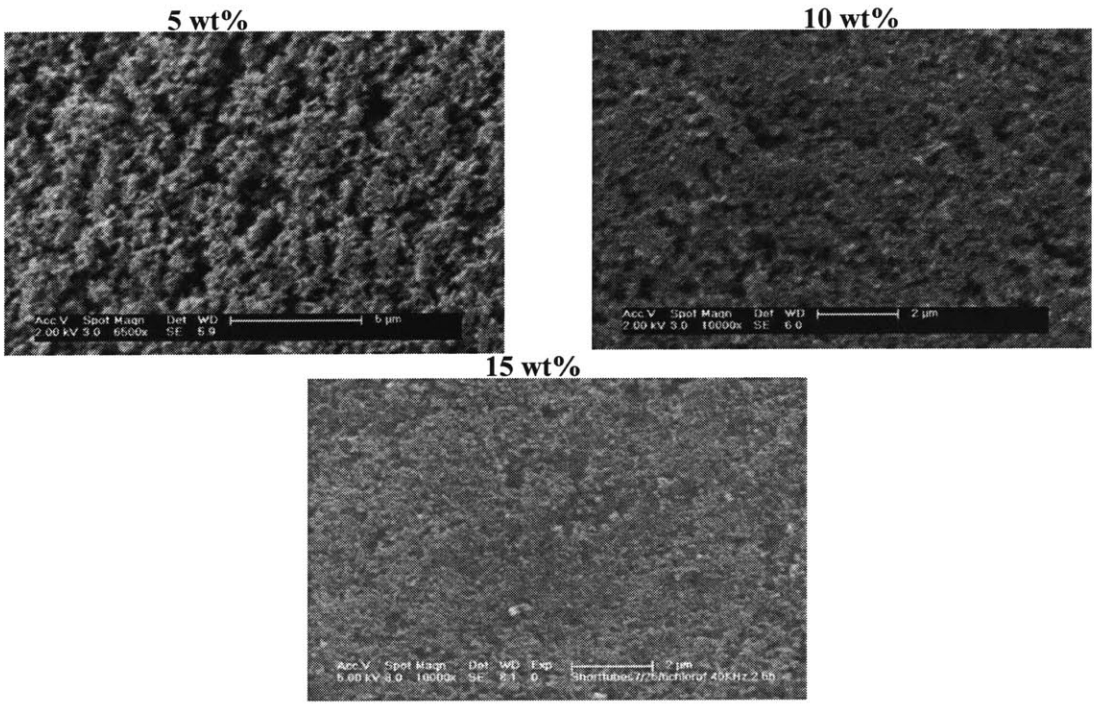

Figure 4-4: SEM images of the surface of membranes with 5, 10, and 15 wt% PTFE

Figure 4-5 is a picture of a dry membrane. All membranes formed with 10 wt% PTFE or higher were mechanically strong and flexible both in their dry and water saturated states. The membranes seemed more flexible when they were saturated with water. In both their dry and water saturated states, the membranes had a low-shedding surface. When a Q-tip was lightly brushed over the surface of the membranes, only a small amount of carbon particles were seen to be removed from the surface of the membranes. A low-shedding surface is a good indication that the carbon aggregates are tightly bonded together by the polymer fibrils.

Water did not spontaneously imbibe into any of the prepared PTFE-bonded membranes. A membrane of each polymer wt% was prepared and left floating on top of deionized water in a beaker. After more than a week, the membranes were removed from the beaker and a napkin was used to remove excess water on the surface of the

membranes. None the membranes prepared in this fashion showed a significant difference between their original mass and their mass after floating on top of water. In order to saturate the membranes with water, isopropanol is used as an intermediary liquid. The detailed procedure for saturating the membranes with water is given in Section 4.3.1.

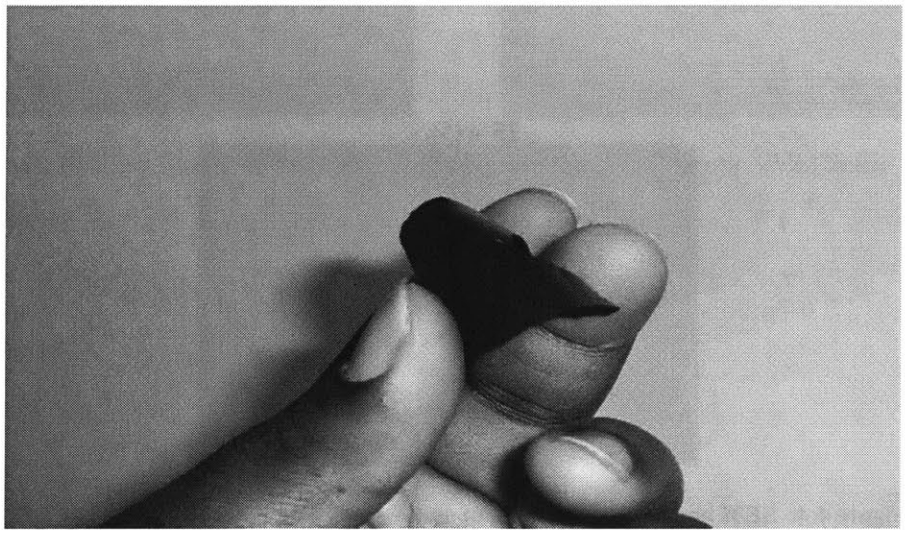

Figure 4-5: Flexible PTFE-bonded membrane

When water droplets were placed on the surface of the membranes, the droplets either stuck to the surface of the membrane or rolled off. No portion of the droplets appeared to penetrate the membrane. Water droplets stuck to the surface of the 5 and 10 wt% membranes. When these membranes were submerged underwater, a portion of the membrane's surface remained wet with water. In contrast, membranes prepared with 15 wt% PTFE and higher appeared to remain completely dry after being submerged in water. Water droplets rolled off the surface of these membranes, which indicates a contact angle near 180°. These observations prove that the PTFE content had a strong effect on the hydrophobicity of the membranes' surface. In future work, the sessile drop technique should be used to obtain the contact angle of these water droplets.

4.2.2 PES-bonded Microporous Membranes

Background:

PES is an amorphous engineering thermoplastic. Its synthesis involves the nucleophilic substitution of 4,4'-dichlorodiphenyl sulfone (DCDPS) with 4,4'-dihydroxydiphenyl sulfone (DHDPS) in a dipolar aprotic solvent such as diphenyl sulfone, sulfolane, and N-methyl-2-pyrrolidone (NMP) [15]. Dephenyl sulfone is the preferred solvent. The repeat structure of PES is shown in Figure 4-6.

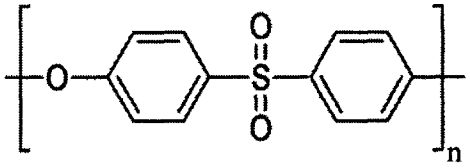

Figure 4-6: Polyethersulfone fundamental repeating unit [15]

It consists of repeated phenyl, sulfone, and ether groups. The SO_2 linkage is the sulfone group, and the oxygen linkage is the ether group. Broad chemical resistance, hydrolysis resistance, constant use temperature of 200°C, and high mechanical strength are the key properties that are due to the sulfone group presence in the polymer. The ether linkages provide chain flexibility and the wholly aromatic structure [16]. Both the sulfone and ether groups are corrosion resistant to concentrated phosphoric acid and alkaline solutions. PES has been tested and found to be stable in concentrated phosphoric acid at temperatures up to at least 191°C [17]. The wholly aromatic structure improves the thermal properties of PES compared to those of the closely related polysulfone polymer. The glass transition temperature of PES is 223°C. The polymer is mildly hydrophilic. A cast non-porous membrane of PES was found to have an advancing contact angle of about 66°, measured by using a 36 cm horizontal beam comparator [18]. Water does not

spontaneously imbibe into porous PES membranes. These membranes must be specially treated to make them spontaneously imbibe water [19, 20, 21]. PES is soluble in polar solvents such as NMP and N,N-dimethylformamide and non-polar solvents such as dichloromethane. It is soluble in and reacts with concentrated sulfuric acid.

PES has found extensive use as a polymer in electronic components, medical devices, and photographic accessories. Its use is favored in applications where repeated sterilization in an autoclave is required. The largest application area of PES is in the filtration membrane field, which accounts for 20% of the total PES market [15].

PES filtration membranes are generally made by using a wet phase inversion technique. In this method, a casting solution made up of PES and a suitable solvent is formed into a thin film. The film is then submerged under a solution containing a specific concentration of a non-solvent to precipitate the polymer into a porous membrane. The solvent has a greater affinity for the non-solvent than for the polymer. For this reason, when the non-solvent comes into contact with the PES/solvent mixture, the solvent dissolves in the non-solvent and the polymer precipitates around the trapped liquid solution. The liquid solution (solvent and non-solvent) acts as the pore-former. When a strong non-solvent is used in this process, such as water, more of the PES precipitates out near the initial interface of the film and non-solvent [22]. This phenomenon can lead to an asymmetric polymer membrane where the pores of the membrane enlarge gradually from its surface through its interior structure. When an extremely strong non-solvent is used, a membrane skin is formed [22, 23]. In membrane science, the termed "skinned" usually refers to a membrane structure where the surface pores are much smaller than the interior pores. The typical thickness of the skin is on the

order of 5% or less of the total membrane thickness. Unlike the asymmetrical membrane, the transition to the much larger interior pores is abrupt. The skin can have a dramatic effect on the properties of the membrane. For example, the flow through skinned membranes is generally controlled by the size of the pores in the skin layer and is independent of the total membrane thickness.

Greenwood *et al.* patented a technique that produced skinless and essentially symmetrical PES microporous membranes [22]. The technique involved adding a lower aliphatic glycol to both the solvent and non-solvent solutions to reduce the rate of polymer precipitation relative to the rate of mixing of the solvent and non-solvent. In the limit of a very fast mixing and very slow precipitation of the polymer, the film approaches a uniform solution composition before precipitation commences. When the polymer then precipitates out, it does so at a uniform rate throughout the film. In one formulation Greenwood *et al.* used a casting solution containing, by weight, 63% triethylene glycol, 27% NMP, and 10% PES. The mixture was coagulated in a bath which initially contained 90% triethylene glycol and 10% water. With this type of mixture composition, the PES precipitated out of solution at a much slower rate than the rate of the mixing of the solvent and non-solvent liquids. As a result, the membrane's porosity and pore size were essentially uniform throughout the thickness of the membranes.

PES has been used as a binder in fuel cell applications dating back to 1987. Trocciola *et al.* of United Technologies patented a process where PES was used as the binder for the silicon carbide (SiC) matrix of a PAFC instead of the traditional PTFE binder [17]. They claimed that the PES binder is hydrophilic and, for this reason, it could

be used in proportionally larger amounts than PTFE without rendering the matrix unwettable to the electrolyte. The PES-bonded matrix was reported to be stronger, more wettable, and have a higher bubble pressure compared to a PTFE-bonded matrix. The PES matrix was formed by dissolving PES in dichloromethane and mixing the solution with SiC. The mixture was spread onto a sheet and dried at room temperature. The dried layer was broken up into flakes and chopped in a blender to form a fine powder. The powder was then mixed with water, polyethylene oxide, and Triton X-100 and stirred overnight. The polyethylene oxide was added to the mixture in order to make the PES more hydrophilic [21]. The mixture was finally coated on a gas diffusion electrode, dried, and heat treated to remove the surfactant and sinter PES binder. Recently, Yoon *et al.* used PES to bind SiC whiskers in order to form a PAFC matrix [24, 25]. Their process involved dissolving the PES in either dichloromethane or NMP. The slurry was either cast on one electrode or on both the anode and cathode. The slurry was then dried and heat treated.

Cabasso *et al.* prepared a gas diffusion layer for a PEMFC using PES to bind the carbon black particles [26]. The porosity of the gas diffusion layer decreased in the direction of the reactant gas diffusion. In one embodiment of their technology, the diffusion layer was formed using a wet phase inversion process where the carbon/PES slurry was coagulated in the presence of a strong non-solvent solution. The preferred non-solvent was water. When a mixture was used, water and alcohol or water and salt were the preferred mixtures. Suitable alcohols include ethanol, isopropanol, and methanol. Suitable salts include LiCl, $LiNO_3$, and $NaNO_3$. The use of a strong non-solvent led to the desired asymmetrically porous membrane.

Generally, the wet phase inversion process produces membranes that have a higher porosity than membranes formed by evaporating the solvent (dry phase inversion process). For this reason, a wet phase inversion process, similar to that of Cabasso *et al.*, was used to prepare the PES-bonded membranes in this work. Since a symmetric membrane is desired, the solvent and non-solvent solutions had a composition similar to the solutions used by Greenwood *et al.* to produce symmetric PES membranes. The detailed procedure for the fabrication of a PES-bonded is provided below.

Preparation of Membrane:

The procedure for preparing PES-bonded membranes is as follows:

Step 1. Mix 0.125, 0.167, 0.214, 0.269, or 0.333 g of PES (Radel® A Polyethersulfone from Solvay Advance Polymers), which corresponds to 0.20, 0.25, 0.30, 0.35, 0.40 wt% of PES based on the total mass of carbon/PES mixture respectively, with 2 g of NMP and 4.6 g of triethylene glycol. Stir mixture with a magnetic PTFE coated bar until all the polymer resins have dissolved. Mixture has no floating particles and has a yellowish tint.

Step 2. Add 0.5 g of Vulcan XC72 carbon to the solution. Stir mixture with a stainless steel spatula/spoon for 5 minutes. Sonicate mixture for 10 minutes at maximum power. Repeat stirring and sonicating until mixture is uniform and is a pourable slurry.

Step 3. Use an X-Acto knife to remove a 6.5 cm by 1.7 cm rectangular cutout from adhesive back PTFE sheets (each sheet is 50 μm thick and has a dimension equal to that of the glass slide, 7.5 cm to 2.5 cm). Stack sheets on the glass slide to the desired thickness of the casting slurry. The glass slide with stacked PTFE sheets is the casting die for the membrane.

Step 4. Using a stainless steel spoon/spatula, place a portion of the slurry on glass side. Use a razor blade to spread slurry into a thin film and to remove excess slurry. The depth between the razor blade and top surface of the glass slide is set by the PTFE sheets.

Step 5. Carefully place an oven dried Toray carbon paper (6.5 cm by 1.7 cm) on top cast slurry. Gently press on the carbon paper to ensure that a small portion of the slurry penetrates the pores of the paper.

Step 6. Coagulate the slurry by submerging carbon paper, slurry, and glass plate into a precipitation bath (90% triethylene glycol and 10% water) for 15 minutes. The glass plate and membrane is then submerged in 100% triethylene glycol for 15 minutes to remove to remove any residual solvent.

Step 7. Used an X-Acto knife to separate the PES-bonded membrane/carbon paper composite from the glass slide. The composite is dried in a vacuum oven at 100°C for 24 hours and then heat treated at 300°C to sinter the PES.

Observations:

The solid content of the slurry was observed to be an extremely important parameter for the formation of the membrane. The solid content is defined as the ratio of the combined mass of the carbon black and PES to the total mass of the slurry. A low solid content slurry produced membranes that formed visible cracks during the vacuum drying process. In some cases, the membrane fragmented into many small pieces on the carbon paper when it was dried in a vacuum oven. On the other hand, a high solid content made it difficult to mix the contents into a uniform slurry. This condition also made it difficult to cast the slurry as a thin film. These observations suggest that there is a limited solid content range for the slurry where it can be effectively cast into a membrane. The observations also point to a possible challenge in any future work to fabricate the catalyst layer by casting this slurry on a microfabricated die. A low solid content slurry is favored in order to have it completely penetrate the die. Lee demonstrated that a XC72/Nafion solution slurry with a solid content of 13.6 % can be cast into the microfabricated catalyst layer (see Appendix A). The solid contents used in the preparation of the PES-bonded membranes are less than or equal to 11.2 %. However,

the slurries prepared in this work were more viscous than the slurries prepared by Lee due to the presence of the viscous triethylene glycol.

Attempts were made to prepare membranes without a Toray carbon paper support. These membranes proved to be extremely fragile and easily broke when they were handled. Only unsupported membranes with a thickness of 500 μm or greater were mechanically strong enough to be used in electronic conductivity experiments (see Section 4.3.5). The PES-bonded membrane/carbon paper composite had suitable mechanical properties. The composites were not flexible. Nonetheless, the composites could be handled and tested for their properties without the membrane cracking. Membranes with 25 wt% of PES or higher had a surface that appeared optically smooth. These membranes have a low-shedding surface. When a Q-tip was lightly brushed over them, no carbon particles were seen on the Q-tip. When the membranes were not heat treated (step 7), a small amount of carbon did shed off of the membranes' surface when a Q-tip was lightly brushed over them. This observation indicates that the heat treatment step helped to improve the strength of the carbon/polymer bonds. A sintered PES binder coats the carbon particles more effectively.

Figure 4-7 shows SEM pictures of the surface of membranes prepared with different polymer content. The 20 wt% membrane did not show visible cracks. However, under SEM, large and numerous mud cracks were observed on these membranes. Membranes with higher PES wt% did not show mud cracks to the degree observed on the 20 wt % membrane. The membranes with 20 wt% of PES do not to have sufficient amounts of polymer to prevent them from forming cracks when they were dried. As the polymer content increased, the size and number of cracks visible under SEM decreased.

Membranes with a 30 wt% of PES and higher had no surface cracks. This trend is different from what was observed on microporous membranes prepared by spraying a XC72/PTFE ink on a carbon paper. In the case of these membranes, the number and size of cracks increased with an increase in polymer content [27].

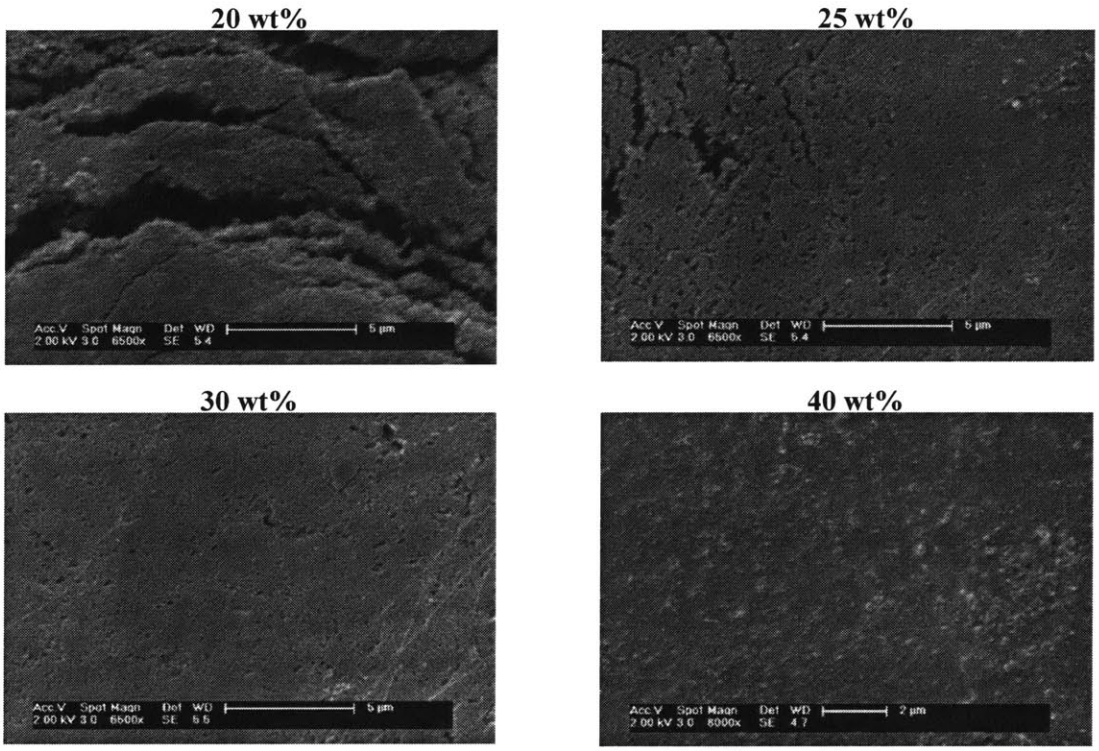

Figure 4-7: SEM images of PES-bonded membranes with 20, 25, 30, 40 wt% of PES

Similar to the PTFE-bonded membranes, the surface of the PES-bonded membranes appear to have a porosity much lower than the porosity measurements suggest (see Section 4.4.1). Again, this observation is partially due to the fact that a certain percentage of the pores are not visible under SEM. Another reason is that the membranes appear to have a skin on the surface that was in contact with the glass slide. The membrane skins appear denser and have a smaller average pore size with higher polymer content. The observed membrane skins are not the type associated with the use

of a strong non-solvent. Such membranes would have their pore size decreasing towards the carbon paper backing with a possible skin formation at the interface of the membrane and carbon paper. Instead, the slurry appears to interact with glass plate in such a way that a skin forms on that surface. The glass plate may have provided a high density of nucleation sites for the precipitation of the polymer. Thus, more of the PES precipitates out near the surface of the glass plate than in the bulk of the film. Similar skin formation was observed when resorcinol-formaldehyde (RF) polymers were cast on glass and Lexan (see Appendix B). In the case of the RF polymer, Petricievic *et al.* attributed the observed skin to the catalytic influence of the mold surface during the gelation process [28]. The enhanced catalysis improves RF deposition, leading to denser structures with smaller pores than the bulk RF skeleton. Cabasso *et al.* also observed this type of skin formation when they coagulated a slurry of polyvinylidene and Pt supported on carbon black on a glass substrate [29]. They attributed the presence of the membrane skin to the way the glass interacted with the polymer carbon mixture. No further explanation was provided. A similar phenomenon is probably causing the skin formation in the PES-bonded membranes of this work.

The wettability of the PES-bonded membranes was tested by using the same method used for the PTFE-bonded membranes. Like the PTFE-bonded membrane, water did not spontaneously imbibe into any of the prepared membranes. The intrinsic contact angles of water with carbon black and PES are 45° and 66°C respectively. Thus, the average contact angle of the membrane should be between these values. It is well known that in order for a liquid to penetrate a porous structure, the intrinsic contact angle of the liquid with solid often needs to be much lower than 90°. That is, a critical contact angle

exists which is required for the spontaneous imbibition of the wetting phase for a given system [30]. The intrinsic contact angle between water and the membrane is apparently not lower than the critical value needed for the membrane to take in water. This phenomenon is discussed further in Section 4.4.2. In the filtration membrane field, hydrophilic membranes[4] are often desired. There are several patents that describe methods of increasing the hydrophilic property of PES membranes [19, 20, 21]. None of these techniques were examined in this work.

4.3 Experimental Procedure

4.3.1 Porosity

The porosity of each carbon-polymer membrane composition was measured using two different methods. The mass of the dry membrane, m_{dry}, was measured in both methods. For method 1, the membrane was saturated with a liquid, either water or hexane, and then the mass of the wet membrane was measured, m_{wet}. For a fully saturated membrane, the volume fraction of the liquid is equal to the porosity of the membrane. Thus, if we assume that the membrane is fully saturated, the porosity, ε, is given by

$$\varepsilon = \frac{\dfrac{m_{wet} - m_{dry}}{\rho_l}}{\left(\dfrac{m_{dry}\left(1-x_p\right)}{\rho_c}\right)+\left(\dfrac{m_{dry}x_p}{\rho_p}\right)+\left(\dfrac{m_{wet}-m_{dry}}{\rho_l}\right)} \tag{4.1}$$

[4] Hydrophilic membranes are defined as membranes that can spontaneously absorb water.

where ρ_c, ρ_p, and ρ_l, are the densities of carbon, the polymer, and the saturating liquid respectively. x_p is the mass fraction of the polymer in the carbon-polymer solid mixture. For the membranes that were supported on Toray carbon paper, the mass of the dry and the wet carbon paper was subtracted from the measured values to obtain the desired mass of the wet and the dry membrane.

For method 2, the thickness of the dry membrane was measured using a digital caliper. The thickness was measured at five locations along the 1.5875 cm diameter membrane. The average of these measured thicknesses was taken to be the thickness of the membrane. The porosity is given by

$$\varepsilon = \frac{A \cdot l_{avg} - \left(\frac{m_{dry}(1-x_p)}{\rho_c}\right) - \left(\frac{m_{dry} x_p}{\rho_p}\right)}{A \cdot l_{avg}} \tag{4.2}$$

where l_{avg} is the average thickness of the membrane and A is the area of the membrane. For the membranes that were supported on Toray carbon paper, the thickness of the paper was subtracted from the measured values to obtain the thickness of the membranes. It is known that a portion of the membrane penetrates the pores of the carbon paper. However, this effect is ignored.

Saturating Membranes with Water:

Liquid water does not spontaneously imbibe into any of the membranes tested. In order to saturate the membranes with water, they were first saturated with isopropanol. The low surface tension of isopropanol allows for all the pores of a membrane to be filled with it. Other alcohols, such as acetone and ethanol, can be used instead of isopropanol. A syringe was used to add droplets of isopropanol onto the dry membranes. Once the

membranes appeared saturated with isopropanol, they were submerged under it for 24 hours. During this period, the smallest pores of the membranes were allowed to fill with the isopropanol. Since isopropanol is soluble in water, the isopropanol that filled the pores of the membranes was then exchanged with water by simply submerging the membrane in a beaker filled with deionized water for 24 hours. The beaker was refilled with fresh water once or twice during the 24 hour period.

4.3.2 Breakthrough Capillary Pressure and Saturation

The breakthrough capillary pressure is the difference in pressure between the nonwetting and the wetting fluid that corresponds to the incipient formation of a continuum of the nonwetting phase through a pore network. It does not correspond to either the capillary pressure of the largest pores on the exterior of the sample or the capillary pressure at the near zero saturation of the wetting fluid. The penetration of a nonwetting phase into networks of capillaries with randomly distributed pore sizes will result in breakthrough at a capillary pressure corresponding to some intermediate pore size [30].

The microporous region of the microfabricated catalyst layer should ideally be completely flooded with the electrolyte at all operating conditions of the cell. However, pressure gradients can develop in the catalyst layer that might affect its saturation. For this reason, the breakthrough capillary pressure and the saturation of the microporous membrane at this pressure are important properties of the membrane since they are direct measures of the microporous region's ability to remain flooded with the wetting phase.

The breakthrough capillary pressure was measured for each membrane using a half-cell apparatus fabricated in the laboratory. A schematic of the apparatus is shown in Figure 4-8.

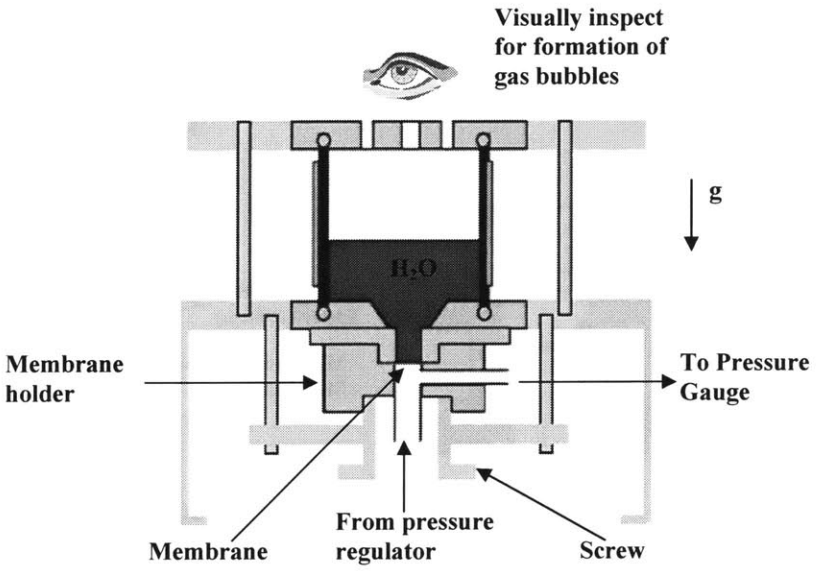

Figure 4-8: Schematic of half-cell apparatus for breakthrough pressure experiments

A water-saturated membrane was placed within the half-cell apparatus in the manner illustrated in Figure 4-8. The top side of the membrane was in contact with a column of water with a hydrostatic head of no more than 5 cm. The bottom side of the membrane was in contact with nitrogen gas, the nonwetting fluid. Water was chosen as the wetting fluid rather than an electrolyte for safety reasons.

A more detailed schematic of the membrane holder is illustrated in Figure 4-9. The holder is made entirely of PTFE. The holder consists of two separate components: the main body that houses the membrane and the cap. As shown in the Figure 4-9, the membrane was sandwiched between two Kalrez® washers that helped prevent nitrogen gas from leaking through the sides of the membrane housing. Nitrogen gas was able to leak only when its pressure reached the membrane's breakthrough pressure. At this

pressure, the nitrogen gas leaked through the membrane. Two 190 μm thick Toray carbon papers saturated with water were placed on the liquid water side of the membrane to keep the membrane rigid up to a nitrogen pressure of 4.2 bar. The two parts of the membrane holder are held together by a large screw that presses the membrane holder between the screw and the main body of the half-cell (see Figure 4-8).

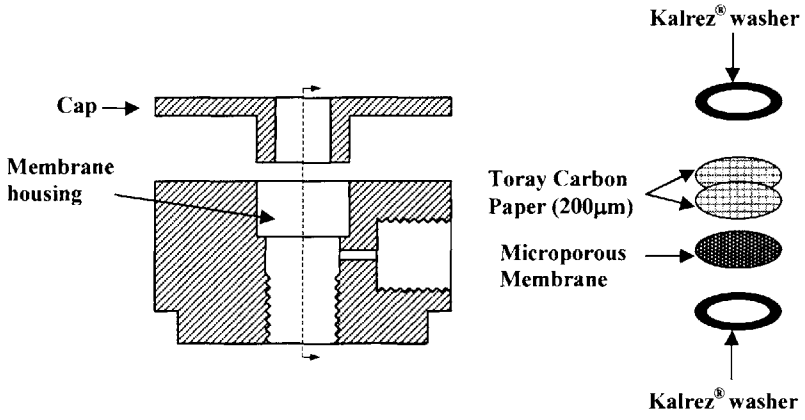

Figure 4-9: Schematic of half-cell membrane holder

During the experiment, the pressure of the nitrogen gas was increased in 0.07 bar intervals using a nitrogen tank pressure regulator. The pressure of the gas was measured using a differential pressure gauge located downstream of the electrode holder. During the experiment, a valve located after the pressure gauge was closed and prevented the flow of nitrogen. For each 0.07 bar increase in the pressure of nitrogen, the liquid side of the membrane was visually inspected for 30 seconds to see if any gas bubbles formed on the membrane. The pressure leading to a continuous production of bubbles was taken to be the initial breakthrough capillary pressure.

After the initial breakthrough pressure was reached, the pressure of the gas was dropped to zero gauge pressure by lowering the pressure of the regulator and opening the valve to exhaust the excess nitrogen. The pressure was held at zero gauge pressure for 30

seconds. Then the experiment was repeated. The new bubbling pressure was taken to be the repeating breakthrough capillary pressure. Its value was always lower than the initial breakthrough pressure. For all membranes tested, no change in the breakthrough pressure was observed beyond the second experiment.

After the last breakthrough pressure experiment was completed for a membrane, water was first removed from the liquid compartment of the cell before reducing the nitrogen gauge pressure to zero. This was done to keep the amount of water in the membrane equal to its value at the repeating breakthrough capillary pressure. The membrane was then carefully removed from the half-cell apparatus and its mass was measured. The saturation of the membrane at the breakthrough capillary pressure, S_{BP}, is given by

$$S_{BP} = \left(\frac{\dfrac{m_{wet,BP} - m_{dry}}{\rho_l}}{\left(\dfrac{m_{dry}\left(1-x_p\right)}{\rho_c}\right) + \left(\dfrac{m_{dry}x_p}{\rho_p}\right) + \left(\dfrac{m_{wet,BP} - m_{dry}}{\rho_l}\right)} \right) \frac{1}{\varepsilon} \tag{4.3}$$

where $m_{wet,BP}$ is now the mass of the membrane after breakthrough pressure experiment.

4.3.3 Permeability

The permeability of a porous medium, k, is defined by Darcy's law in much the same way that the electronic conductivity and thermal conductivity of a material is defined by Ohm's law of electricity and Fourier's law of heat conduction respectively. Darcy's law in differential form is

$$\vec{v} = -\left(k/\mu\right)\vec{\nabla}P \tag{4.4}$$

where $\vec{v}$ is the filter velocity defined as the differential volumetric flow rate divided by the differential face area, μ is the dynamic viscosity of the fluid, and P is the pressure of the fluid. Effects due to body forces, such as gravity, are omitted in the above equation. The rationale behind Equation (4.4) is that the porous medium is imagined to be subdivided into a network of small blocks, and Darcy's law is applied to each block. The size of each block must be small enough to approximate $\vec{v}, \mu, P,$ and k with constant values within each block, but also large enough for Darcy's law in its macroscopic form to apply in each block [30]. Fluid motion on the scale of the pores of the porous medium is governed by the Navier-Stokes equation. Nevertheless, on the macroscopic scale, Darcy's law is always applicable when the unsteady and inertia terms in the Navier-Stokes equation are negligible for the fluid flow in the pores (Stokes flow) [31]. Both Matheron in 1966 [32] and Whitaker in 1969 [33] have given a formal proof of this. Appropriate assumptions about the statistical nature of the geometry of the porous medium have to be introduced to go from the Stokes flow on the "microscopic" scale to Darcy's law on the macroscopic scale. These assumptions are used to obtain a single parameter, the permeability. Thus, in Darcy's law, $\vec{v}$ and P are not the actual velocity and pressure of the fluid at a point within the porous medium. Rather, they are a statistical average velocity and pressure.

The permeability for each of the membranes was measured using a simple falling-head permeameter fabricated in the laboratory. Figure 4-10 is a picture of the permeameter. A neoprene gasket was placed between the brass cap and the top part of the membrane holder to prevent leaks between them. The entire membrane holder and brass cap were fastened together by four 12.7 cm long stainless steel bolts. The bolts and

nuts were most effectively tightened by using a flat head screw driver to turn the bolt while holding the nut in place by hand. This technique sufficiently fastened the membrane holder to prevent leaking while not significantly deforming the membrane. A 0.635 cm OD 0.3175 cm ID Kel-F tube was attached to the brass cap by a 1/4 inch brass tube fitting (Swagelok). The height of the top end of the tube was measured to be 47.87 cm from the membrane. The tube was graduated at 2 cm intervals. Each line was labeled in sequential number order with line 1 located 2 cm from the top end of the tube.

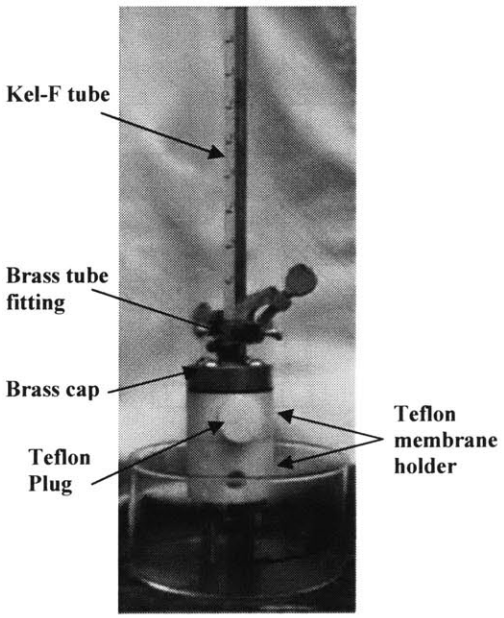

Figure 4-10: Picture of the falling-head permeameter

Figure 4-11 is a schematic of the top and bottom parts of the membrane holder and the brass cap. As illustrated in Figure 4-11, the membrane was placed in the membrane housing with two Kalrez® washers that acted to prevent water from leaking out of the membrane housing. The two water-saturated Toray carbon papers acted to keep the membrane from deforming under the weight of the water column. The inner area of the washers was 1 cm^2. Thus, the liquid flow area of the membrane was assumed

to be 1 cm^2. The carbon papers did not affect the measured permeability of the microporous membrane since its permeability is 3 to 4 orders of magnitude greater than the permeability of the membranes. Likewise, the flow resistance of the tube and other parts of the permeameter are negligible compared to that of the membrane.

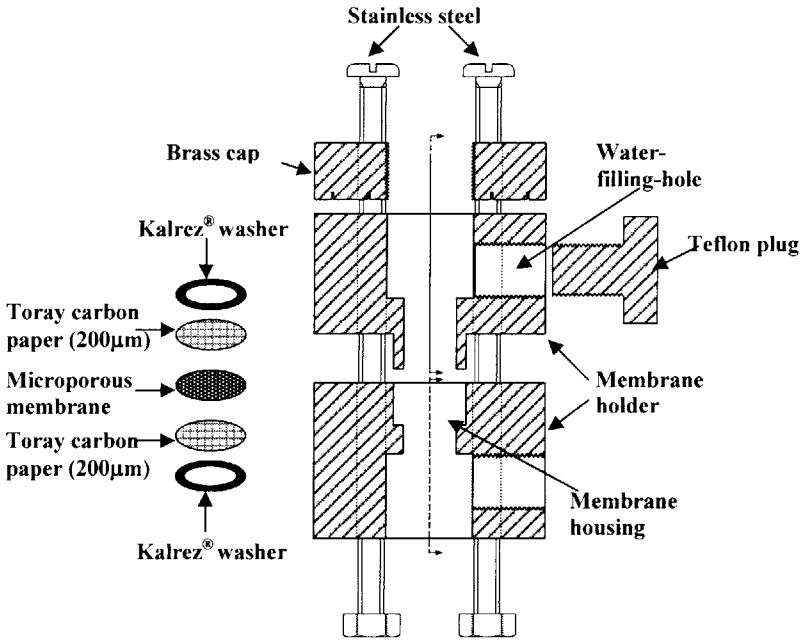

Figure 4-11: Schematic of the membrane holder of the permeameter

Each permeability experiment began with the water-saturated membrane properly placed and sealed in the membrane holder. The permeameter was then laid at a slight angle relative to the lab table. The top part of the membrane holder and tube were filled with liquid water. The Teflon plug was then used to close off the water-filling-hole. The permeameter was then placed upright as shown in Figure 4-10. A finger was used to seal the top end of the tube which prevented water from flowing through the membrane until the finger was removed. Care was taken ensure that the entire tube was vertically aligned with the membrane holder before any water was allowed to flow through the membrane.

When the water-air interface crossed the first or second line, a digital stop watch was started. The time it takes for the water-air interface to cross the other lines drawn on the tube was recorded. A plot of $\ln(h/h_o)$ vs. t, where h and h_o are the water height above the membrane at time $t = t$ and $t = 0$ sec, respectively, yields a straight line for Darcian flow. The permeability is calculated from

$$k = \frac{A_{tube}\mu_w l_{avg}}{A_m \rho_w g}\left(\frac{-\ln(h/h_o)}{t}\right) \tag{4.5}$$

where A_{tube} is the inner area of the graduated tube, ρ_w and μ_w are the density and dynamic viscosity of water, respectively, l_{avg} is the thickness of the membrane, A_m is the liquid flow area of the membrane ($A_m = 1 cm^2$), and g is the acceleration due to gravity. The term in the parentheses in Equation (4.5) is the slope of the $\ln(h/h_o)$ vs. t plot. It is calculated by applying a least squares linear regression to the data.

4.3.4 Ionic Conductivity

The microporous region of the catalyst layer is flooded with the electrolyte in order to provide a continuous path for ion transport either to or from the reaction zones of the catalyst layer. The theoretical model of the microfabricated catalyst layer suggests that the ionic conductivity of the electrolyte-filled microporous region is the membrane parameter that most affects the performance of the cell. Obtaining an accurate measure of the ionic conductivity of the various carbon-polymer membrane compositions is, therefore, extremely important.

The ionic conductivity of the carbon-polymer membranes was measured using a conductivity cell fabricated in the laboratory [34]. An illustration and picture of the

experimental setup are given in Figure 4-12. The conductivity cell consisted of two compartments separated by the membrane housing. Each contained a Pt electrode 50 μm thick and 2.54 cm in diameter and contained a saturated calomel reference electrode (SCE). During the experiments, both compartments were filled with 3.7 M sulfuric acid. Solartron's 1287A potentiostat was used to apply constant currents between the two Pt foils and to measure the potential difference between the two reference electrodes.

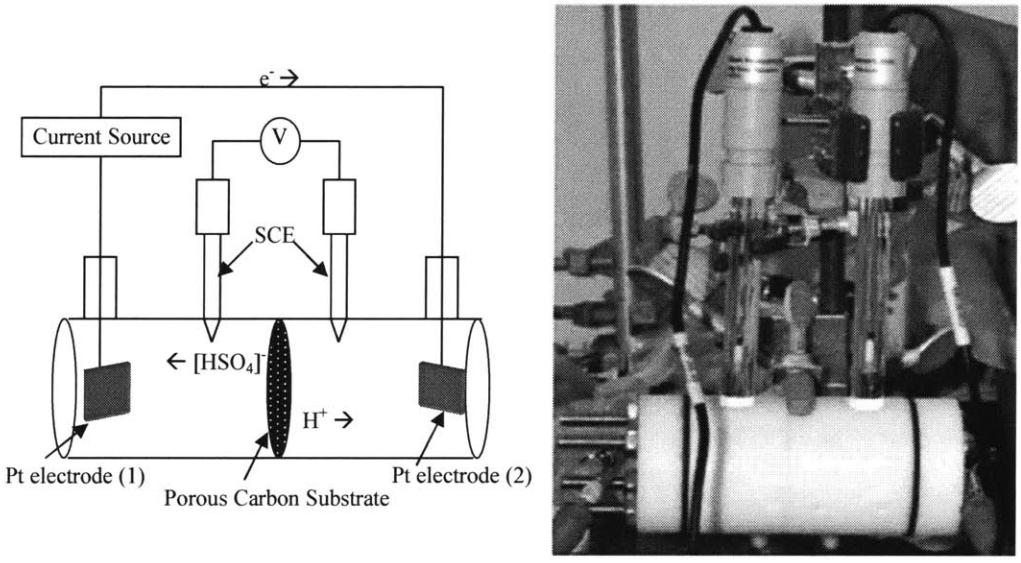

Figure 4-12: Schematic and picture of ionic conductivity experimental setup

During the operation of the conductivity cell, electrons flow from left to right. The positive current flows in the opposite direction. Protons migrate from the left compartment to the right compartment, and sulfate ions migrate in the opposite direction. Pt electrode (1) generates protons by catalyzing the reaction

$$2H_2O \rightarrow 4H^+ + O_2 + 4e^- \tag{4.6}$$

Pt electrode (2) is a catalyst for the following two reactions that converts protons into water and hydrogen:

$$4H^+ + O_2 + 4e^- \rightarrow 2H_2O \tag{4.7}$$

$$4H^+ + 4e^- \rightarrow 2H_2 \qquad (4.8)$$

Since the transport of oxygen within the electrolyte is limited, the evolution of hydrogen is the most the dominant reaction on the Pt electrode (2). At high current values ($i > 1A$), gas bubbles were seen escaping from both reference electrode openings. For this reason, currents higher than 1 A were not used in this experiment. The sulfate anions, which migrate to the left compartment of the cell, do not react. Instead, they keep an equivalent amount of protons from migrating to the right compartment in order that charge neutrality is maintained in both compartments. Therefore, during the experiment, the concentration of the electrolyte increases in the left compartment and decreases in the right. The effects of this phenomenon on the experiment are discussed in Section 4.4.4.

Figure 4-13 is a more detailed schematic of the all-Teflon conductivity cell. In each compartment, the Pt foil was placed between the end of the compartment and the compartment's cap. A 1.91 cm diameter area of the Pt foil was exposed to the electrolyte. The electrolyte was prevented from leaking between each compartment and its cap by using a neoprene gasket with OD of 5.08 cm and ID of 2.54 cm. As shown in Figure 4-13, the microporous membrane was sandwiched between two Kalrez® washers that acted to prevent the electrolyte from leaking out of the membrane housing. The Kalrez washers had a void area of 1 cm^2. For all membranes thinner than 300 μm, the membrane was also placed in between two 100 um thick Teflon sheets. Each Teflon sheet had a concentric hole of diameter 0.5 cm^2. The sheets acted to reduce the area where the current flowed within the membrane. The lower conductivity area increased the potential drop across the membrane and made it easier to measure the ionic conductivity of thin, highly porous membranes $\left(A_m \approx 0.20 cm^2\right)$. The components of the

conductivity cell are held together by four 12.7 cm long stainless steel bolts and nuts that were lightly fastened in the manner described in Section 4.4.3 in order to prevent the membrane from significantly deforming.

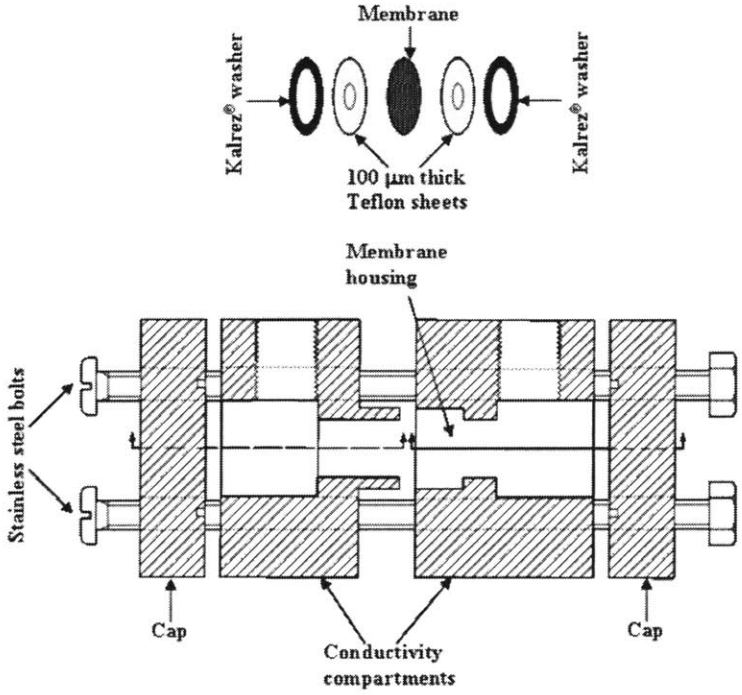

Figure 4-13: Schematic of the conductivity cell

The membrane was saturated with 3.7 M (31 wt%) sulfuric acid by soaking a water-saturated membrane in 3.7 M sulfuric acid for more than 24 hours. Measuring the ionic conductivity of the cell involved applying a constant current between the two Pt electrodes and measuring the resulting potential drop between the two saturated calomel reference electrodes. The procedure was repeated for 6 to 10 current values. A plot of potential vs. current yielded a straight line, where the slope of the line was the resistance of the cell, R. The effective ionic conductivity of the electrolyte saturated membrane, σ_{eff}, is calculated by using the relation

$$\sigma_{eff} = \frac{l_{avg}}{A_m \left(R_M - R_{base} \right)} \tag{4.9}$$

where R_M and R_{base} are the resistance of the cell with a porous membrane and the resistance without a porous membrane respectively.

The measurements were done differently for the membranes that were supported on Toray carbon paper. In those cases, R_{base} was measured with a plain, electrolyte-saturated Toray paper in between the Teflon sheets. R_M was measured with the plain Toray paper removed and the membrane supported on Toray paper now in between the Teflon sheets. The conductivity calculated using Equation (4.9) is solely the effective conductivity of the polymer-bonded membrane. It is not the conductivity of the combination of the membrane and Toray paper support. This method for calculating the ionic conductivity of a supported membrane assumes that the conductivity of the Toray paper support is the same as that of the plain Toray paper. This assumption may not be completely valid since carbon black particles are expected to penetrate the Toray paper and possibly change its ionic conductivity. Nevertheless, nothing was done to compensate for this possible source of experimental error.

To test the accuracy of the conductivity cell, the resistance of the cell with membrane, R_m, was obtained with the membrane replaced by a Teflon sheet identical to the ones illustrated in Figure 4-13. The conductivity calculated using Equation (4.9), is approximately equal to the reported values for the intrinsic conductivity of sulfuric acid at room temperature [35]. This result suggests that possible sources of experimental error, such as errors due to fringe field effects, did not prevent an accurate measurement of conductivity.

4.3.5 Electronic Conductivity

The electronic conductivity of the membranes was measured using the four-point experiment. All measurements were made using the DFP-02 advance model (Silicon Valley labs, Saratoga, CA). Figure 4-14 is a picture of this four-point conductivity instrument. The probes are spaced 0.2 cm from each other. The 1.5875 cm diameter dry membrane was placed flat on the base of the conductivity instrument. The center of the membrane was closely aligned with the halfway point between the two potential probes. Only the weight of the probe frame was used to maintain contact between the four probes and the membrane.

Measurement of the electronic conductivity of the dry membrane involved applying a constant current between the two current probes and measuring the potential drop between the potential probes. The Solartron's 1287A potentiostat was again used to apply the current and measure the potential difference. The measurements were made for 10 current values from 1 to 10 mA at 1 mA intervals. A plot of current vs. potential yielded a straight line. The slope of the line, s_κ, was applied to the following equation to calculate the electronic conductivity of the membrane, κ_M:

$$\kappa_M = \frac{s_\kappa}{l_{avg}} \times f\left(\frac{D}{s}\right) \tag{4.10}$$

where D is the diameter of the membrane and s is the spacing between the potential probes. The function, f, accounts for the effects the edges have on the potential field. For a sample with a diameter much greater than the potential probe spacing, the value of this function goes to $f = \ln 2/\pi$. For the diameter of the membranes used in these

experiment, $D = 1.588\,cm$, and a probe spacing of $s = 0.2\,cm$, the value of the function f is calculated to be $f = 0.25189$ [36].

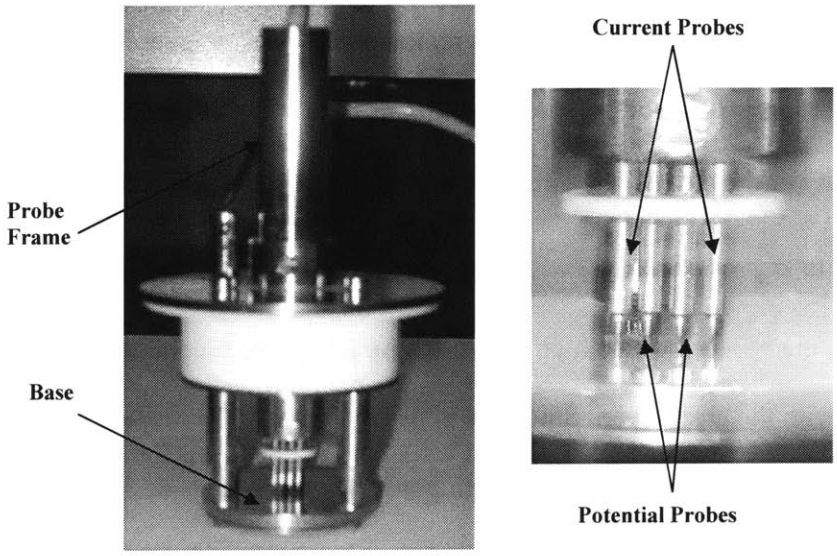

Figure 4-14: Pictures of the four-point electronic conductivity tester

The electronic conductivity of PES-membranes supported on Toray carbon paper was difficult to measure. The in-plane electronic conductivity of Toray carbon paper is reported to be $\approx 172\,S/cm$ [37]. This value is about two orders of magnitude greater than the electronic conductivity of the polymer-bonded membranes. For this reason, it was difficult to resolve the conductivity of the membrane by first measuring the conductivity of a Toray carbon paper and then measuring the conductivity of the membrane with carbon paper support. In order to measure the electronic conductivity of the PES-membranes, unsupported membranes with a thickness of about 500 μm were fabricated. Thick membranes were used to keep them from cracking while being handled and when under the weight of the probe frame. The electronic conductivity of PES-membrane supported on carbon paper is not expected to be much different than that of the unsupported membrane.

4.4 Results and Discussion

4.4.1 Porosity

The porosity of the microporous region of the catalyst layer is expected to affect the transport parameters of the species within its pores. For example, the ionic conductivity of the electrolyte within the this region, σ_{eff}, is related to its bulk value, σ_b, according to $\sigma_{eff} = (\varepsilon / \tau) \times \sigma_b$, where τ is the tortuosity of the microporous region [38]. Generally, membranes with a high porosity have a high ionic conductivity when it is saturated with the electrolyte. Since ion transport is one of the more limiting rate processes within the catalyst layer, a high porosity membrane is desired.

The bulk porosity of each of the polymer-bonded membranes was determined using two different methods. Method 1 involved weighing the sample before and after saturating it with a liquid. Method 2 involved measuring the volume of the dry membrane. The porosity values measured when hexane or water was used as the wetting fluid did not differ significantly. For this reason, the data presented in this section only include porosity values measured with water saturated membranes. Figure 4-15 is a plot of the porosity of the PTFE-bonded and PES-bonded membranes at varying polymer wt%. For each polymer wt%, the porosity of four or five membranes was measured. Each data point in Figure 4-15 is the average value of these measured porosities.

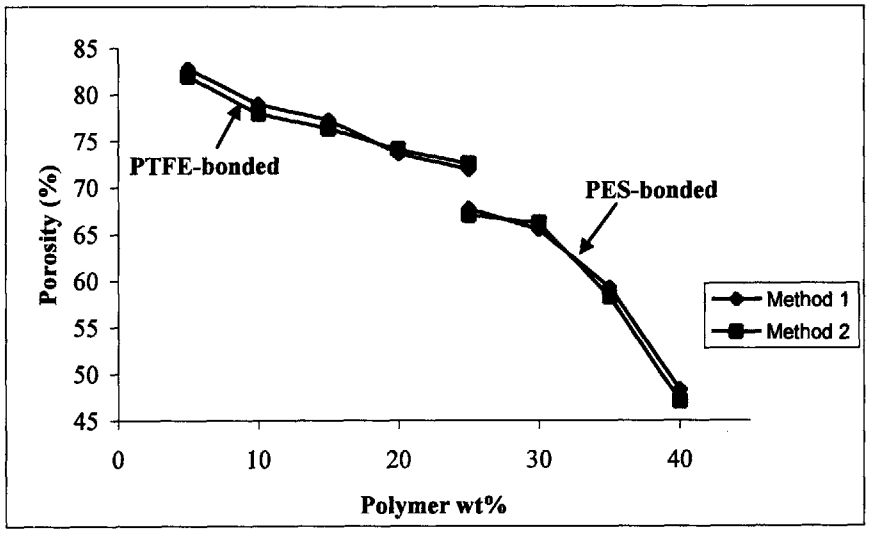

Figure 4-15: Plots of the porosity of polymer-bonded membranes made from XC72 carbon black verses their polymer wt%

The plot shows that the porosities measured, using the two methods, are in very good agreement for all polymer wt%. This result is an indication that the water saturation method, described in Section 4.3.1, fully saturates the membrane with water. If a membrane was not fully saturated, Method 2 would give a higher porosity value than Method 1. However, for most of the polymer wt%, Method 1 results in the slightly higher porosity value. This trend might be due to a slight swelling of the membranes when they are saturated with water. A swollen membrane holds more liquid volume than its dry void volume. The difference between the two methods is still within the experimental error. Thus, either method can be used to effectively measure the porosity of the membrane.

The high porosity of the PTFE-bonded membranes proves that water acted as a good pore-former during the preparation of the dough. It also proves that these pores did not collapse during either the air drying of the dough or the pressing step to form the thin membrane. As Figure 4-16 shows, the porosity of the PTFE-bonded membranes

decreased approximately linearly with an increase in polymer wt%. The slope of the line is gradual. Increasing the PTFE wt% from 10 to 25 wt% only reduces the porosity from 80 to 72%.

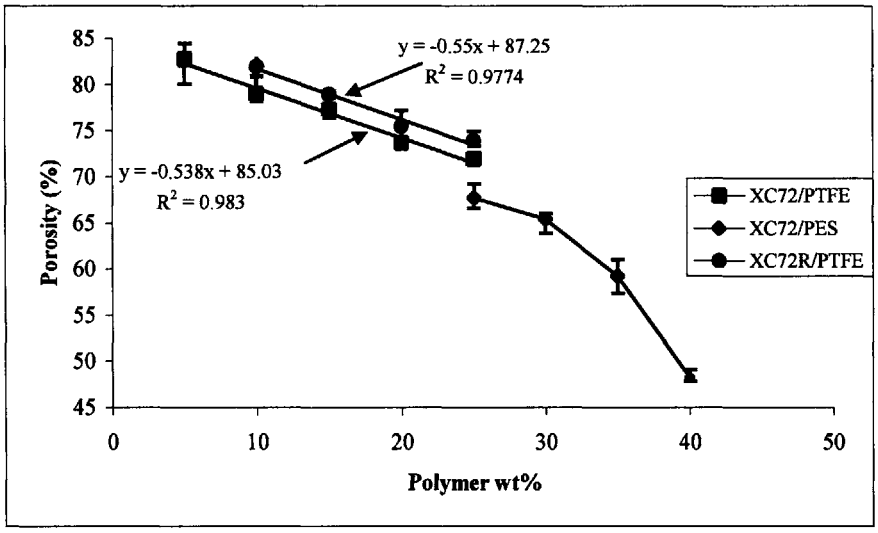

Figure 4-16: Plots of the porosity of the PTFE-bonded membranes made with XC72 and XC72R carbon black. Plot of the porosity of PES-bonded membranes made with XC72 carbon black.

It is not surprising that the porosity decreased with an increase in PTFE content. As previously discussed, SEM pictures showed that the average size of the pores near the surface of the membranes decreased as the PTFE content increased from 5 to 15 wt%. This observation is most likely a result of more PTFE fibrils binding the carbon aggregates closer together. The interior pores of the membranes may have similarly been affected by the increase in the PTFE content. The smaller pores of the membrane result in a less porous structure.

The reduction in carbon black content also contributed to the measured reduction in porosity. The size of the primary carbon particles of XC72 and XC72R is about 30 nm in diameter. The particles bond to each other by weak van der Waal's forces to form primary agglomerates that are highly porous. These agglomerates are the building blocks

of the porous membrane. Replacing the low density, highly porous agglomerates with non-porous PTFE fibers can lead to a linear reduction in the porosity of the membrane. The observed linear relation between porosity and PTFE wt% suggests that this is the primary reason for the reduction in porosity of the PTFE-bonded membranes. The porosity of the membrane is given by

$$\varepsilon = \frac{\upsilon_c - \left(1/\rho_{s,avg}\right) + \left(\upsilon_p - \upsilon_c\right)x_p}{\upsilon_c + \left(\upsilon_p - \upsilon_c\right)x_p} \tag{4.11}$$

where υ_c and υ_p are the specific volume of the carbon agglomerates and the specific volume of the PTFE matrix respectively. The specific volume of carbon agglomerates is the sum of the specific volume of carbon, $\left(1/\rho_c\right)$, and the specific pore volume of the agglomerates. Similarly, the specific volume of the PTFE matrix is the sum of the specific volume of PTFE, $\left(1/\rho_p\right)$, and the specific pore volume of the PTFE matrix. $\rho_{s,avg}$ is the average density of the solid phase of the membrane. It is given by

$$\rho_{s,avg} = \left(\frac{1-x_p}{\rho_c} + \frac{x_p}{\rho_p}\right)^{-1} \tag{4.12}$$

The density of carbon is about equal to the density of PTFE. For this reason, the average density can be approximated as $\rho_{s,avg} \approx \rho_c$. If the second term in the denominator of Equation (4.11) is neglected and the specific volumes are assumed to be constant, Equation (4.11) reduces to a linear relation between porosity and the polymer mass fraction (or polymer wt%):

$$\varepsilon = \left(1 - \frac{1}{\rho_c \upsilon_c}\right) + \left(\frac{\upsilon_p}{\upsilon_c} - 1\right)x_p \tag{4.13}$$

This equation is used along with the linear regression result for the XC72/PTFE membranes (see Figure 4-16) to calculate the specific volumes of the agglomerates and PTFE matrix, $\upsilon_c = 3.34 cm^3/g$ and $\upsilon_p = 1.54 cm^3/g$. The calculated specific volume of the agglomerates is slightly higher than previously reported value of $2.240 cm^3/g$ [27]. The specific volume of the PTFE matrix is greater than the specific volume of the solid PTFE fibrils themselves. Therefore, the matrix contributes to the overall porosity of the membrane. This result is not surprising. A membrane made only of PTFE that is formed by fibrillizing the polymer particles is expected to be porous. In the case of membranes prepared by sintering the PTFE and not fibrillizing it, the specific pore volume of the PTFE was found to be essentially zero [27].

The porosity of PTFE-bonded membranes made with XC72R carbon black, which is the non-compacted form of the furnace black, was not significantly higher than those prepared with XC72 carbon black. Considering the added difficulty of working with the non-compacted form of carbon black, the slight increase in the porosity of the membrane does not justify its use.

In contrast to the PTFE-bonded membranes, the PES-bonded membranes experienced a rapid reduction in porosity with an increase in polymer content. As shown in Figure 4-16, the slope of the curve is not constant. Instead, it increases with an increase in the PES content. This trend suggests that more than one factor is acting to reduce the porosity of the PES-bonded membrane. First, the porosity of the polymer binders is not greater than that of the carbon agglomerates. Thus, similar to the PTFE-bonded membrane, replacing the agglomerates with the less porous PES binder reduced the porosity of the membrane. Second, the increase in the solid content of the slurry

reduces the porosity of the membrane. The wet phase inversion process promotes the formation of pores between the solid contents of the carbon-PES slurry. The carbon-polymer bonds form around the trapped solvent and non-solvent. Thus, the liquid phase acts as a pore-former. Since the amount of liquid in the slurry was not altered, increasing the PES wt% meant an increase in the overall solid content of the slurry and a reduction in the percentage of the pore-forming liquid. In the polymer condensing phase inversion process, a higher solid content results in a polymer membrane that has smaller pores and is less porous [22]. A similar effect occurs here with the PES-bonded membranes as the polymer content increased. finally, as seen in the SEM pictures in Figure 4-7, increasing the polymer content reduced the amount of cracks observed on the surface of the membrane. These cracks, although undesired, contributed to the overall porosity of the membrane.

4.4.2 Breakthrough Capillary Pressure (BCP) and Saturation

The electrolyte saturated microporous regions of the catalyst layer also act as gas barriers preventing the mixing of oxygen in the cathode with the fuel in the anode. A mixing of gases, in sufficient quantities, would lead to a catastrophic failure of the cell. The microporous regions must have a high breakthrough capillary pressure (BCP) to ensure that the mixing of gases cannot occur at any operating conditions of the cell.

The saturation of the membrane at the BCP is expected to be the same regardless of the wetting fluid. Thus, the BCP for one wetting fluid, $P_{BCP,1}$, is related to that of another wetting fluid, $P_{BCP,2}$, by

$$P_{BCP,2} = \left(\frac{\sigma_2 \cos\theta_2}{\sigma_1 \cos\theta_1} \right) P_{BCP,1} \tag{4.14}$$

where σ_2 and θ_2 are the surface tension and contact angle of fluid 2, and σ_1 and θ_1 are the surface tension and contact angle of fluid 1 [39]. All BCP experiments were conducted with water as the wetting fluid. The experimental results, with water as the wetting fluid, can be combined with Equation (4.14) to estimate the BCP in the microporous regions of the catalyst layer with an electrolyte as the wetting fluid.

Initial Breakthrough Capillary Pressure(IBP):

Figure 4-17 is a plot of the initial breakthrough capillary pressures (IBP) and repeating breakthrough capillary pressures (RBP) of the PTFE-bonded and PES-bonded membranes. Excluding the 25 wt% PTFE-bonded membrane, the measured BCPs of all the other membranes were greater than 0.7 bar. The required BCP for the electrolyte matrix within the state-of-the-art PAFC is about 0.21 bar [40].

The PTFE-bonded membrane experiences a maximum in the BCP between 10 and 15wt% of PTFE. This observed maximum is a result of the competing effects associated with increasing the PTFE content within the membrane. As discussed in earlier sections, increasing the PTFE content probably led to a decrease in the average pore size and porosity of the membrane. These structural changes in the membrane act to increase the capillary pressure required for bubbling. On the other hand, increasing the PTFE content also makes the pores of the membrane more hydrophobic. The contact angle of water on smooth PTFE is reported to be 110° [41]. A higher average contact angle acts to reduce the capillary pressure at a given saturation [30]. These competing effects offset each other at the maximum IBP and RBP of the PTFE-bonded membranes.

For some of the 25 wt% of PTFE membranes tested, the RBP was less than 0.07 bar. Bubbling of the nitrogen gas occurred at the slightest increase in gas pressure. At this amount of PTFE, the hydrophobicity of the membrane is at level where it is difficult for water to sufficiently reenter the pores of the membrane after the IBP. Thus, BCP experiments for PTFE-bonded membranes suggest that the PTFE content of the microporous membrane should be less than 25 wt%, with an optimum value between 10 wt% to 15 wt%, in order to ensure that the micropores remain flooded with the electrolyte.

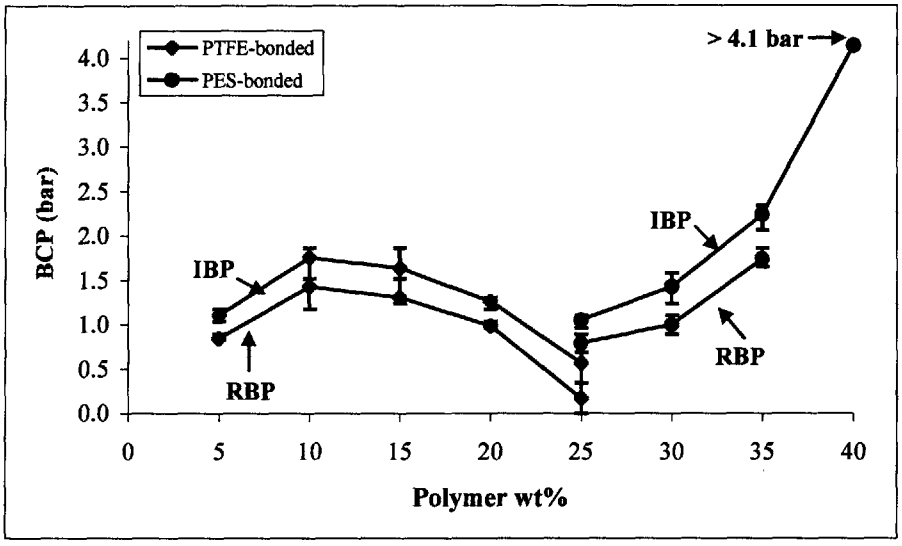

Figure 4-17: Initial breakthrough pressure (IBP) and repeating breakthrough pressure (RBP) of polymer-bonded membranes saturated with water.

Figure 4-17 shows that there was no maximum BCP measured for the PES-bonded membranes. The BCP continuously increased with an increase in the PES content. At a PES content of 40 wt%, the BCP exceeded 4.1 bar. Higher capillary pressures were not attainable since 4.1 bar was the maximum pressure of the nitrogen regulator used in the experiment. Pressures in excess of 2.8 bar appeared to cause some visible changes to the surface of the membranes.

The advancing contact angle of water on a smooth PES surface is about 66° [18]. This value is within the range of reported contact angles for carbon (45° to 80°). Unlike PTFE, increasing the PES content did not significantly increase the hydrophobicity of the membrane. There is no effect that acts to reduce the BCP as the PES content is increased. However, increasing the PES content led to membranes with lower porosities, smaller pores, and less surface cracks. All these factors act to increase the BCP of the membrane. For these reasons, the IBP and RBP continuously increased as the PES content increased.

Contact Angle Hysteresis:

Liquid water did not noticeably imbibe into any of the prepared membranes. Nonetheless, once liquid water was made to saturate the membrane, the measured BCP indicated that the water was now behaving as a wetting fluid. This change in the wetting behavior of a fluid is commonly observed with compact powders. For example, in porous PTFE plugs, suction (positive capillary pressure) is needed for displacement of liquid, with an intrinsic contact angle of 108°, by air [42].

The imbibition of liquid water into the microporous membrane depends on the advancing contact angle, while its drainage depends on the receding contact angle. It is well documented that, for many solid-liquid contacts, the receding contact angle is significantly lower than the advancing contact angle. Some of the causes of contact angle hysteresis are contamination of either liquid or solid, surface roughness, chemical heterogeneity, behavior of sorption layers, and molecular reorientation. Morrow measured the advancing and receding contact angles of internally roughened tubes of PTFE [43]. He found very significant contact angle hysteresis at the rough surface. A fluid with an intrinsic contact angle of 100° had an advancing contact angle of about 160°

and a receding contact angle of about 60° on the rough PTFE surface. For low surface energy solids, such as PTFE, the difference between advancing and receding contact angles, measured on a smooth surface, are very small. Benziger *et al.* measured the surface contact angles of carbon paper and cloth using the Whilemy plate technique [44]. Toray carbon paper was measured to have and advancing contact angle of 115° with water and a receding contact angle of 35°. This contact angle hysteresis explains why dry Toray carbon paper floated on top of water and did not fully saturate with water. In this work, Toray paper was saturated with water the same way the polymer-bonded membranes were saturated with water. Contact angle hysteresis provides a good explanation for the observed difference in the water wetting behavior between the dry and water-saturated polymer-bonded membranes. The contact angle of water in contact with the carbon particles near the surface of the membrane is greater than 90°, while the receding contact angle of water in the pores is less than 90°. This difference in wetting behavior was not a characteristic of carbon aerogel membranes. Water spontaneously saturated these membranes (see Appendix B).

Repeating Breakthrough Capillary Pressure (RBP):

For both the PTFE-bonded and PES-bonded membrane, the RBP followed the same trend as the IBP, except that the RBP values were about 20% to 30% less than the IBP values. The fact that the RBP is not zero, for most of the membranes, indicates that pores that were partially drained of water at the IBP were able to spontaneously take in water when the pressure was lowered to zero gauge pressure. Therefore, spontaneous imbibition of liquid water is possible in the case of a partially saturated membrane, but it is not possible in an oven-dried membrane. One possible reason for this behavior may

have to do with differences in the chemical properties of the dry and previously wetted surface. For example, water in the pores can cause the detachment of hydrophobic organic molecules from the particles [45]. Thus, when the water is drained, the surface of the pore is less hydrophobic and can now spontaneously take in water. Another possible reason is that the contact angles of water in the pores are lower than the contact angle on the rough surface of the membrane. It has been observed that the contact angle on a rough surface, measured by the Sessile drop method, can be much higher than the intrinsic contact angle [46]. In the case of a dry membrane, water must first penetrate the surface of the membrane before wetting the internal pores. A contact angle of greater than 90° at the membrane surface would prevent this from occurring. However, in the case of a partially flooded membrane the internal capillary forces can drive the flooding of the dried pores since the pores that remained flooded provide a path for the permeation of water from the surface of the membrane. Regardless of the reasons, the high RBP is a fortuitous result. It suggests that the electrolyte can remain wetting to the micropores even after the liquid has been removed from the pores by a positive capillary pressure.

Several of the membranes that were tested were dried in an air oven (100°C for 24 hours), saturated with water, and retested. In all cases the IBP and RBP did not differ by more than 0.07 bar from their original measured values. This result proves that the RBP is not lower than the IBP because of some irreversible structural changes in the membrane. Rather, it is most likely due to a change in the membrane's saturation after the IBP experiment. Water reentered the membrane after the IBP, but it did not fully saturate the membrane.

Saturation after RBP:

Figure 4-18 is a plot of the saturation of the membrane after the RBP. For both types of polymer-bonded membranes, the membranes remained more than 91% saturated after the breakthrough pressure. The saturation values did not change significantly with a change in the polymer wt%. This trend is consistent with the known fact that the percolation threshold for the non-wetting phase does not vary much with porosity [47]. Mercury-intrusion porosimetry measurements of carbon black particles bonded with a polymer usually reveals the presence of a bimodal pore structure [13]. The first group of pores is formed by the primary particles of the carbon black. The group typically has a narrow size distribution and has an average pore size of about the size of the primary particles. Recall that XC72 and XC72R have a primary particles size of around 30 nm. The second peak in the porosimetry data is associated with the pores formed by the carbon black aggregates. The average size of these pores can range from 200 nm to 1 μm. The high saturation values plotted in Figure 4-18 suggest that a significant amount of the porosity of the membranes is found in the primary pore distribution. Both Maja *et al.* [13] and Antolini *et al.* [27] determined from mercury-intrusion porosimetry measurements that the majority of the porosity of a PTFE-bonded microporous layer was found in the primary pore distribution.

The microporous regions of the microfabricated catalyst layer should be excellent at retaining the electrolyte. In modeling the catalyst layer region of the electrode, it was assumed that the microporous region remains fully saturated regardless of the capillary pressure (see Chapter 7). As long as the capillary pressure remains below the breakthrough capillary pressure, the error in making this assumption is small.

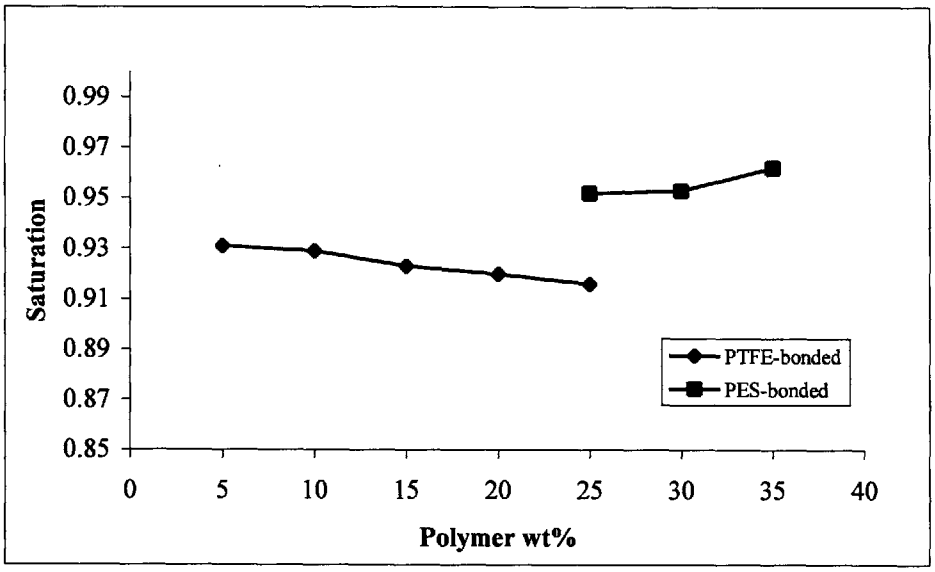

Figure 4-18: Saturation of polymer-bonded membranes after repeating breakthrough pressure

Implications for Catalyst Layer:

The dual wetting behavior of the polymer-bonded membranes is a favorable property. Electrodeposition is envisioned to be preferable for depositing the catalyst onto the surface of the microfabricated cylindrical holes of the catalyst layer. An aqueous based electrodeposition solution can be made to saturate these holes without wetting the micropores of the catalyst matrix. Thus, the catalyst can be preferentially deposited on the surface of microfabricated holes without the use of cumbersome pore blocking materials. The use of an alcohol, like isopropanol, as an intermediary for the saturation of the catalyst layer matrix with the electrolyte is a simple process. Once the matrix of has been properly saturated, the high breakthrough pressure ensures that the region will remain saturated at all operating conditions of the cell.

4.4.3 Permeability

Electrolyte Motion in PAFCs:

Liquid electrolytes are susceptible to motion resulting from the flow of current. For example, the electrolyte can move from the cathode to the anode of a cell in PAFCs. In concentrated phosphoric acid, about 98% of the current is carried by protons that migrate via the Grotthus proton switching mechanism [48, 49]. The remaining fraction of the current is carried by the phosphate anions, $H_2PO_4^-$. In PAFCs the anions migrate to the anode. There, in order to maintain electroneutrality, they associate themselves with protons that are generated at the anode. The net result of this migration of anions is the weeping of the electrolyte towards the anode. At high current densities, this can lead to a flooded anode. Flooding of an electrode causes severe concentration polarization and cell voltage instability.

At constant current, the motion of the electrolyte towards the anode continues until capillary forces or some other constraints outside of the cell lead to pressure gradients that drive the electrolyte back towards the cathode or out of the cell. If the electrolyte remains in the cell, the seepage velocity (or volume average) within the pores of the cell goes to zero at the steady state condition. In other words, the volume flux associated with the migration of the anion is balanced by the volume flux associated with the pressure driven flow of the electrolyte. The volume flux of the electrolyte is the mass average velocity. This phenomenon within the pores of the phosphoric acid cell is most simply modeled with the following equation:

$$(k/\mu)\vec{\nabla}P = \left(\frac{\bar{V}_{-}t_{-}}{F}\right)\vec{i} \tag{4.15}$$

where $\bar{V}_-$ and t_- are respectively the partial molar volume and the transference number with respect to the mass average velocity of the phosphate anion. $\vec{i}$ is the ionic current density and F is Faraday's constant. This equation assumes that the current flows purely by migration, the concentration of phosphoric acid is uniform, and the pressure driven flow of the electrolyte is governed by Darcy's law. Equation (4.15) indicates that the permeability of the electrolyte saturated regions of the cell can greatly affect the performance of the cell if its value is low. A cell with a low electrolyte permeability requires higher pressure gradients to move the electrolyte. High liquid pressure in the anode can lead to electrolyte flooding of its hydrophobic pores. Low liquid pressure in the cathode can reduce its electrolyte content well below the optimal value. Landsman *et al.* realized the importance of the electrode permeability [50]. They increased the permeability of their PAFC electrodes by mixing the traditional PTFE/catalyst floc with hydrophilic particles. Within the electrodes, the hydrophilic particles provided a more permeable path for electrolyte motion. The cells with the additional hydrophilic particles operated at higher potentials than the conventional electrodes at current densities ranging from 200 to 600 mA/cm^2. At 600 mA/cm^2 the cell with the conventional electrode had an unstable voltage. The unstable voltage was most likely due to anode flooding.

Permeability of Membranes and the Carmen-Kozeny Equation:

Figure 4-19 is a graph of $\ln(h/h_o)$ vs. t for 15 wt% PTFE-bonded membrane. All tested membranes produced similar looking curves. The curve is almost perfectly linear, which proves that the flow in the membrane is governed by Darcy's law. It also indicates that the simple method used to record the height of the fluid did not cause any noticeable scatter in the data.

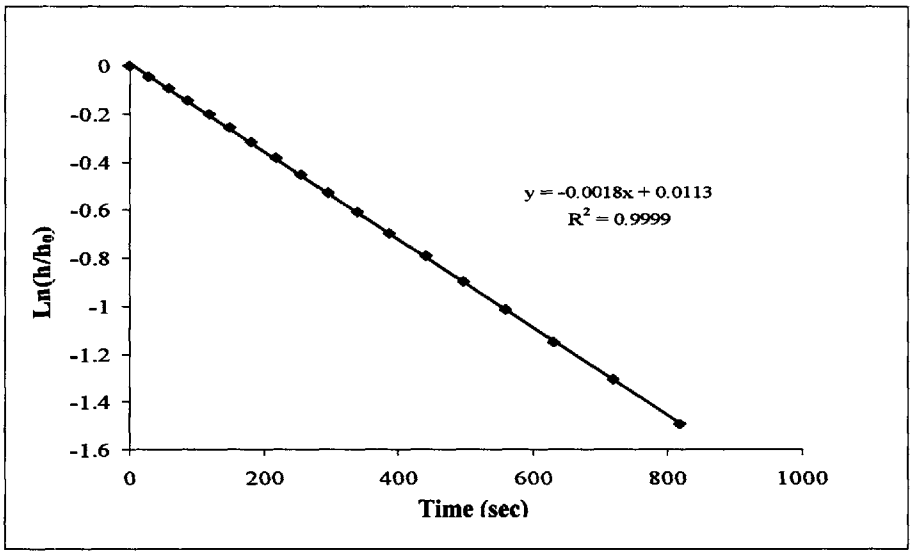

Figure 4-19: A plot $\ln(h/h_o)$ vs. t from the falling-head permeameter for a 15 wt% PTFE membrane (volume fraction: 77.8%)

In both Figure 4-20 and Figure 4-21, the measured permeability of the membranes are plotted verses their porosity for the PTFE-bonded and PES-bonded membranes respectively.

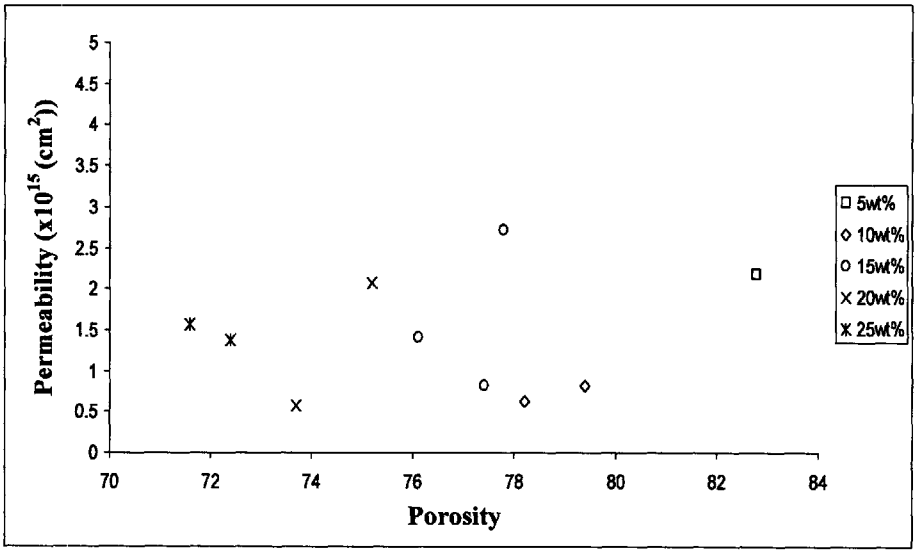

Figure 4-20: Permeability of PTFE-bonded membranes

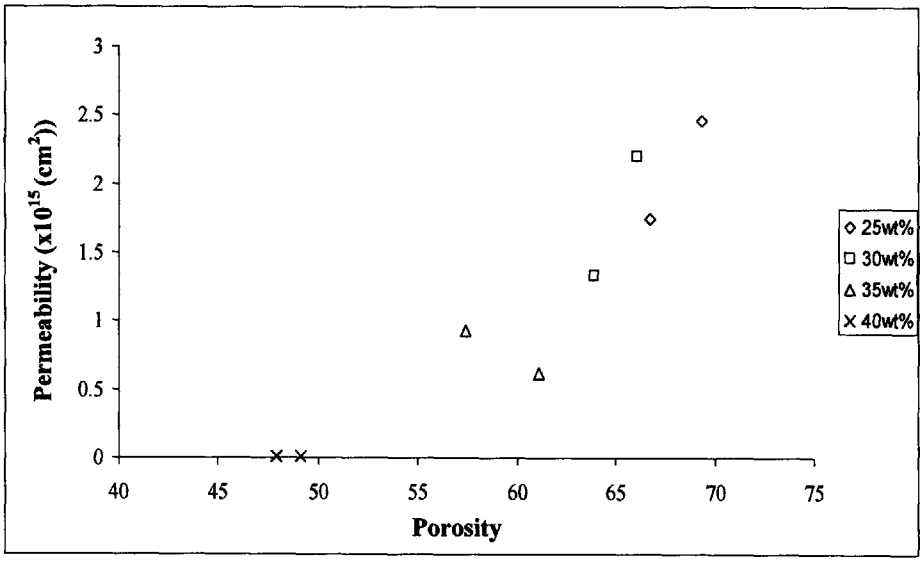

Figure 4-21: Permeability of PES-bonded membranes

The Carmen-Kozeny (CK) equation,

$$k_{CK} = \frac{\varepsilon^3 r_{avg}^2}{45(1-\varepsilon)^2} \tag{4.16}$$

where r_{avg} is the average pore radius, is often used to calculate the permeability of a porous medium [13]. It has recently been used in PEMFC models to give the liquid water permeability of the PTFE-bonded microporous layer of these cells [51, 52]. As shown on Figure 4-20, the permeability of PTFE-bonded membranes does not appear to be dependent on the porosity of the membranes. However, the Carmen-Kozeny equation predicts a strong relationship between permeability of a porous medium and the medium's porosity. In the case of the PES-bonded membranes, the permeability increased with an increase in porosity. However, it does not appear that the permeability depends on the porosity by the power law relationship given by the Carmen-Kozeny equation.

In the Kozeny theory, the porous medium is assumed to be an assemblage of channels of various cross-sections, but of a definite length [31]. The Navier-Stokes equations are solved simultaneously for all channels passing through a cross-section normal to the flow in the porous medium. The solution to the filter velocity, v, is a Hagen-Poiseuille type equation,

$$v = \frac{c\varepsilon D_H^2}{\mu} \tag{4.17}$$

where c is the Kozeny constant. It depends only on the shape of the cross-section. D_H is the hydraulic diameter. Kozeny originally defined the hydraulic diameter as

$$D_H = \frac{\varepsilon^2}{S} \tag{4.18}$$

where S is the specific surface area of the tube. Carmen modified the definition of the hydraulic diameter to

$$D_H = \frac{\varepsilon^2}{S_o(1-\varepsilon)^2} \tag{4.19}$$

where S_o is the specific surface exposed to the fluid; that is, the surface exposed to the fluid per unit volume of solid (not porous) material [53]. Carmen also set the value of the Kozeny constant to be $c = 1/5$. According to Carmen, this value gave the best agreement with experiments. If one defines the mean particle radius, r_{avg}, as the radius of the hypothetical sphere with the same S_o as the particle,

$$r_{avg} = 3/S_o, \tag{4.20}$$

and combine this definition with Equations (4.17) and (4.19), Equation (4.16) can be obtained.

The average permeability of PTFE-bonded and PES-bonded membranes are 1.42×10^{-15} cm^2 and 1.17×10^{-15} cm^2, respectively. The measured permeability of a PTFE-bonded membrane with a polymer content of 15 wt% and a porosity of 76.1% is 1.42×10^{-15} cm^2. For this permeability, Equation (4.16) estimates an average pore size of about 1 nm for the membrane. The average radius of the PTFE-bonded membranes is clearly much greater than this value. The polymer-bonded membranes showed the presence of a membrane skin at high polymer content. However, this skin cannot be the reason for the discrepancy between the measured permeability and the value predicted by the Carmen-Kozeny equation. Membranes with 5 to 10 wt% of PTFE, which had skins with visible pores at 10,000x magnification, had permeability values as low as the other membranes. The problem most likely lies with the Carmen-Kozeny equation.

The problems with using the Carmen-Kozeny equation as a means of calculating permeability of all porous medium have been well documented [31]. The Kozeny theory neglects certain aspects of the fluid flow in the porous medium. Most notable, the theory neglects the effects that large variations in the pore size of the medium will have on the permeability of the membrane. It also assumes that in a cross-section normal to the channel there is no tangential component of the fluid velocity. Therefore, the Kozeny theory neglects the influence of viscous flow in the constrictions and expansions of the pores. Both of these phenomena cause the permeability to be lower than what is predicted by the Carmen-Kozeny equation. In a porous medium with a bimodal distribution, like the polymer-bonded membranes of this work, these effects cannot be ignored.

In the polymer-bonded membranes, the fluid is expected to permeate in pores that are part of the primary (small pore size) and secondary (large pore size) distributions. Keeping with the channel geometry of the Kozeny theory, a significant change in pore size can be modeled by considering cylindrical channels which consist of an alternating sequence of segments of two different diameters, D_l and D_s (the subscript l denotes large pore and subscript s denotes small pores). By using the Hagen –Poiseuille equation for each segment, neglecting both the expansion and contraction losses, it can be shown that the bundle of permeability varies as follows [30]:

$$k = k_{CK} \frac{(1+y)^2 (1+yx)^2}{(1+yx^2)^3 (1+y/x^4)} \tag{4.21}$$

where $x = D_l / D_s$ and $y = l_l / l_s$. l_l and l_s are the aggregate lengths of the large and narrow segments respectively. In the polymer bonded membrane, the average pore size of the primary distribution is probably around 30 nm and the average pore size of the secondary distribution is approximated to be equal since more than 50% of the membrane porosity is expected to come from pores in the primary distribution. Thus, with $x = 10$ and $y = 1$, Equation (4.21) gives $k = 4.7 \times 10^{-4} k_{CK}$. Using this result and Equation (4.16), the average pore radius of the 15 wt % membrane is now calculated to be 42 nm. This is a more reasonable value for the average pore size of the membrane. However, it still represents a lower limit for the average radius value. It does not take into consideration the fact that the XC72 carbon black particles have a specific area greater than the value calculated assuming the particles are smooth spheres (see Equation (4.20)). XC72 has a specific area of 254 m^2/g [13], while the specific area for a smooth carbon

sphere with a diameter of 30 nm is 100 m^2/g. Therefore, if we multiply the average pore radius of 42 nm by the ratio of these specific areas, we get a more accurate approximation of the membranes average pore radius, $r_{avg} = 107\,nm$. This value is within the range expected for the average radius of PTFE-bonded microporous membranes [13, 27].

The common equations for permeability, such as the Carmen-Kozeny equation, are most appropriately applied to porous media with a narrow pore size distribution. They should not be used to find the permeability of the polymer-bonded carbon black membranes that typically have a bimodal distribution. Using these equations can result in a severe over-prediction of the membrane's permeability. In the above discussion, the Carmen-Kozeny equation was combined with the serial-type nonuniformity correction to calculate a permeability of the same order as those that were measured. However, this approach is not rigorous. There is a need for liquid permeability equations more suitable for porous media with a bimodal distribution like that of the polymer-bonded membranes of this work and microporous layers found in PEMFCs and PAFCs.

Microporous Gas Diffusion Layer (MPL) of PEMFC:

The microporous gas diffusion layer of PEMFC plays a crucial role in water management in these cells (see Section 3.32). The layer is typically located only in the cathode between the carbon paper or cloth backing layer and the catalyst layer. The MPL reduces flooding in the porous cathode and enhances water management in PEMFCs by increasing the back flow tendency of liquid water across the membrane towards the anode. The liquid permeability of this layer is one of the more important parameters that affect how well the MPL is able to repel water back towards the anode. Generally, MPLs

with a low permeability are better at repelling water since a high liquid pressure is required for water to permeate within it.

The falling head permeameter was used to measure the permeability of the GDL LT 1400-W gas diffusion layer from E-TEK. The layer consisted of one microporous layer on carbon cloth. The measured permeability of the MPL ranged from 2.08×10^{-15} to 2.23×10^{-15} cm^2. These values are only slightly higher than the permeability values measured for the PTFE-bonded membranes of this work. This result is not surprising. The PTFE-bonded membranes are expected to have properties similar to MPLs even though in the case of MPLs the carbon black particles are bonded by sintered, not fibrillized, PTFE. Figure 4-22 is an SEM image of the MPL. Its surface appears very much like that of the 10 wt% PTFE-bonded membrane seen in Figure 4-4. Unlike the PTFE-bonded membranes of this work, the MPL had a few cracks on its surface. This might explain the slightly higher permeability of the MPL compared to the PTFE-bonded membranes.

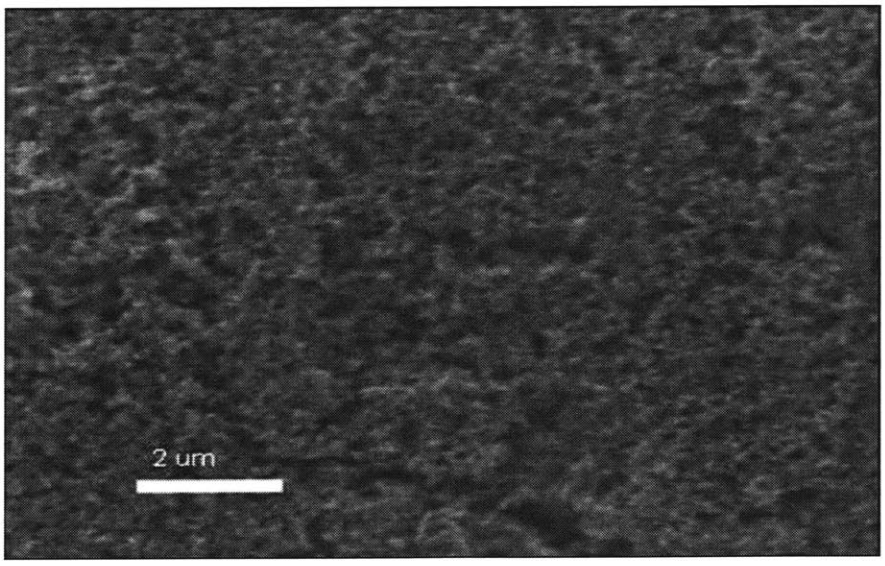

Figure 4-22: SEM image of the microporous layer of the GDL LT 1400-W layer from E-TEK

Recently, researchers have attempted to develop two-phase models for PEMFCs in order to better understand the role of the MPL in water management [51, 52, 54, 55]. An important parameter that these models produce is β, which is defined as the net flux of water from the anode to the cathode, $\dot{N}_{H_2O}$, per proton flux:

$$\beta = \frac{\dot{N}_{H_2O} F}{i} \tag{4.22}$$

where i_i is the current density in the membrane and F is Faraday's constant. Pasaogullari *et al.* [54] in their two-phase model calculated the permeability of the MPL from the empirical expression given by Rumpf and Gutte [56] for packed beds with a narrow range of size distribution,

$$k = \frac{\varepsilon^{5.5} r_{avg}^2}{22.4} \tag{4.23}$$

This expression gives a lower value for the permeability than the Carmen-Kozeny equation. However, the calculated permeability of $2.5 \times 10^{-12}\,\text{cm}^2$ is three orders of magnitude lower than the measured values. With this permeability value, the Pasaogullari *et al.* model predicted that the MPL had a small effect on water management at current densities above 0.4 A/cm^2. This conclusion contradicts experimental data which shows that the greatest difference in the performance of a cell with and without a MPL occurs at high current densities. The cathode is most susceptible to flooding at high current densities. In the Weber *et al.* model, the permeability of the MPL was a fitting parameter [55]. The model yielded a value of $1.6 \times 10^{-15}\,\text{cm}^2$ for the permeability of the MPL. At this value, the Weber *et al.* model had the MPL playing an important role in water management. At high current densities, the cell without a MPL had a $\beta \approx 0.2$

while with a MPL the value reduced to $\beta \approx -0.4$. This result means that three times more water is repelled back towards the anode with a MPL than without a MPL at high current densities. It is believed that the Weber *et al.* model is more consistent with experimental data of the PEMFC because it used a more accurate value for the permeability of the MPL.

The measured permeability values of this work support the results of Weber *et al.* model. Since water management is a major concern for PEMFC, there clearly needs to be more work in the areas of MPL property measurements and modeling.

4.4.4 Ionic Conductivity

Figure 4-23 shows the transient behavior of the potential during the application of a constant current between the two Pt electrodes.

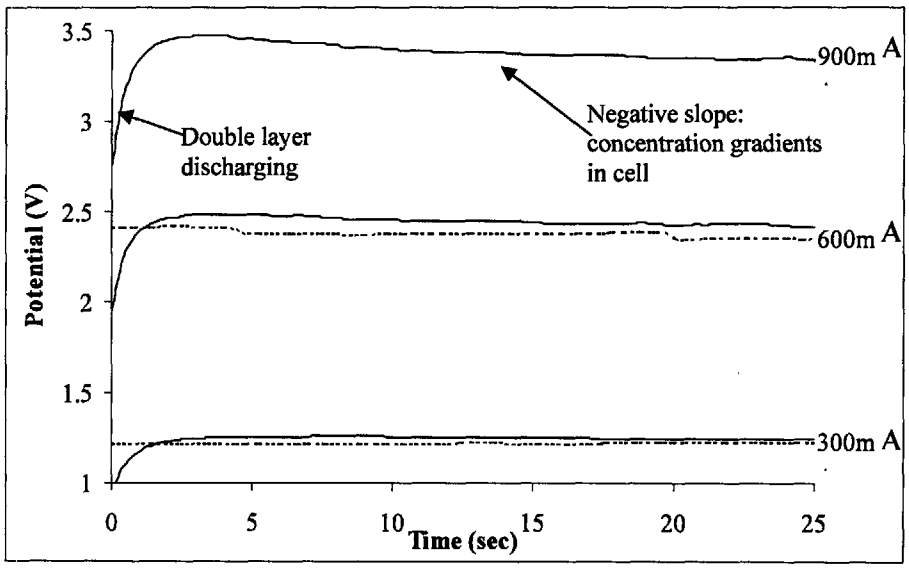

Figure 4-23: Potential vs. time plots for ionic conductivity experiments (solid line: with membrane, dash line: without membrane)

The initial rise in the potential is associated with the discharging of the ionic double layer of the membranes. Initially, some of the current is carried by the discharging double

layer. As this contribution to the current decreases, the potential increases. The discharging of the double layer essentially ends when the potential reaches its maximum value. The initial rise in potential was not observed when the conductivity cell contained a porous, all PES membrane or no membrane at all. In these cases, the potential stepped to its maximum value with a step in the current. Thus, the porous carbon membrane is the only element with a noticeable capacitance between the two reference electrodes. For currents $\leq 600\,\text{mA}$, the potential essentially reaches a steady state value after the initial rise in potential. For each current value, the value of the potential at 5 seconds was used to generate the potential vs. current plot. At higher current values, a negative slope was noticeable at times greater than 5 seconds. Figure 4-23 shows a plot for an applied current of 900 mA. The reduction in the potential after 5 seconds is visible. This behavior is believed to be due to the change in electrolyte concentration from one compartment to the other that was described in Section 4.3.4.

The effect that the change in electrolyte concentration has on the behavior of the potential can best be explained by introducing some of the equations that describe ion transport in an electrolyte. For the purposes of this discussion, we will assume that the 3.7 M sulfuric acid is a binary electrolyte and that it is sufficiently dilute such that the equations for an infinitely dilute solution are valid. The latter assumption is strictly not valid for 3.7 M sulfuric acid. However, the conclusions that are drawn from dilute solution theory are qualitatively consistent with those drawn from concentrated solution theory. Refer to reference [57] for the concentrated solution theory equations for ion transport. The molar flux, $\vec{N}_i$, for an ion in an infinitely dilute solution is given by the Nernst-Plank equation,

$$\vec{N}_i = C_i\vec{v} - D_i\left[\vec{\nabla}C_i + z_i C\left(\frac{F}{RT}\right)\vec{\nabla}\Phi_l\right] \tag{4.24}$$

C_i is the local concentration of the ion with binary diffusion coefficient with the solvent of D_i and charge of z_i (also referred to as the ion's valence). $\vec{v}$ is the velocity of the solution. Φ_l is the local potential of the solution. $F, R, \text{and } T$ are Faraday's constant ($\approx 9.6485\times10^4\ C/mol$), the ideal gas constant ($8.314\ J/(mol\cdot K)$), and the temperature of the solution, respectively. The ionic current density, $\vec{i}_l$, is given by

$$\vec{i}_l = F\sum_{i=1}^{n} z_i\vec{N}_i \tag{4.25}$$

Combining this equation with Equation (4.24) and assuming local electroneutrality in the electrolyte, $\sum_{i=1}^{n} z_i C_i = 0$, gives the relationship between the current density, concentration gradient, and potential gradient:

$$\begin{aligned}\vec{i}_l &= -F\sum_{i=1}^{n} z_i D_i\vec{\nabla}C_i - \sigma\vec{\nabla}\Phi_l \\ \sigma &= \frac{F^2}{RT}\sum_{i=1}^{n} z_i^2 D_i C_i\end{aligned} \tag{4.26}$$

where σ is the electrical conductivity of the electrolyte.[5] The first term on the right side of Equation (4.26) is referred to as the diffusion current and the other term is referred to as the migration current. For the sulfuric acid solution (a single binary electrolyte), Equation (4.26) reduces to

[5] The condition of electroneutrality is approximately observed in all solutions except in the thin double layer region near electrodes and boundaries. The thickness of this double layer is or the order of 1 to 10 nm. Therefore, it is reasonable to assume electroneutrality in the bulk of the solution. The electroneutrality condition is not a fundamental law of nature. It replaces the more correct constraint given the Poisson's equation. For the typical potential fields that occur in electrolyte solutions, Newman (pp. 286-288) showed by applying the Poisson's equation that the difference in concentration between the positive and negative ions is on the order of 1 x 10^{-11} M. Thus, the assumption of electroneutrality is very good [57].

$$\vec{i}_l = -F\left(D_+ - D_-\right)\vec{\nabla}C - \sigma\vec{\nabla}\Phi_l$$
$$\sigma = \frac{F^2}{RT}\left(D_+ - D_-\right)C \tag{4.27}$$

where C is the concentration of the electrolyte. In the absence of concentration gradients, Equation (4.26) and Equation (4.27) reduce to Ohm's law. In the conductivity experiment, the electrolyte conductivity is calculated assuming Ohm's law behavior. For this reason, the concentration gradient of the electrolyte should be as small as possible to accurately measure the conductivity. At current values higher than 600 mA, the rate at which the electrolyte concentration increases in the left compartment and decreases in the right compartment of the conductivity cell is sufficient to cause significant concentration gradients between compartments. The concentration gradients increase with time and point in the direction opposite current flow. Since the diffusion coefficient of protons is larger than that of the sulfate ions, the concentration gradients contribute to the positive flow of current. As time passes and the concentration gradients increase, more of the current is carried by diffusion rather than migration. Thus, the potential difference between the reference electrodes decreases over time. This phenomenon is an experimental artifact. For this reason, current values higher than 600 mA were not included in the potential vs. current plots. Higher current can be reached with larger conductivity cell compartments since large compartments will tend to reduce the rate of increase of the concentration gradients. Nevertheless, current values less than 600 mA provide adequate data points for the conductivity experiment.

Figure 4-24 shows the potential vs. current plot for 15 wt% PTFE-bonded membrane and the base condition of no membrane. All membranes produced similar looking curves. A least squares linear regression was done to both sets of data. Both

curves are almost perfectly linear, which indicates Ohm's law behavior for ion transport. Based on the linear regression, the open circuit potential (OCP) for the conductivity cell with the membrane and without the membrane are 0.0119 V and 0.0147 V respectively. These values are sufficiently close to the measured OCP of 0.013 V. When current values greater than 600 mA were included in the linear regressions the square of the correlation coefficient, R_P^2, only fell to values of around 0.9975. However, the OCPs obtained from these linear regressions were more than 3 times the measured OCP.

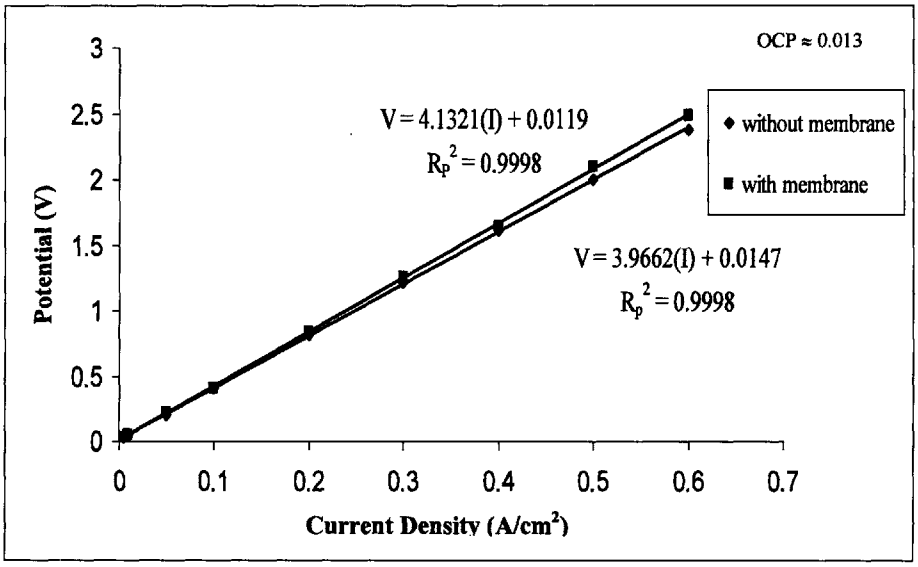

Figure 4-24: Potential vs. current plots from ionic conductivity experiment

Figure 4-25 is a graph of the effective ionic conductivity of the polymer-bonded membranes vs. their porosity. The solid line in the figure is a plot of the equation

$$\sigma_{eff} = \sigma_b \varepsilon \tag{4.28}$$

where σ_b is the bulk conductivity (or intrinsic conductivity) of the electrolyte. Its value was measured to be $\sigma_b = 0.735 S/cm$. This value is within 9% of the value reported in the literature of $0.804 S/cm$ for 3.7 M sulfuric acid [35]. The PTFE-bonded and the

PES-bonded membranes' conductivities follow this line very well. Only the PES-bonded membranes, with porosities of 49.1% and 47.9% have conductivities noticeably lower than the values given by Equation (4.28). The PTFE-bonded membrane data show more scatter than the data from the PES-bonded membranes. The measured conductivities for the PTFE-bonded membranes range from 5.5% higher to 8.6% lower than the values given by Equation(4.28).

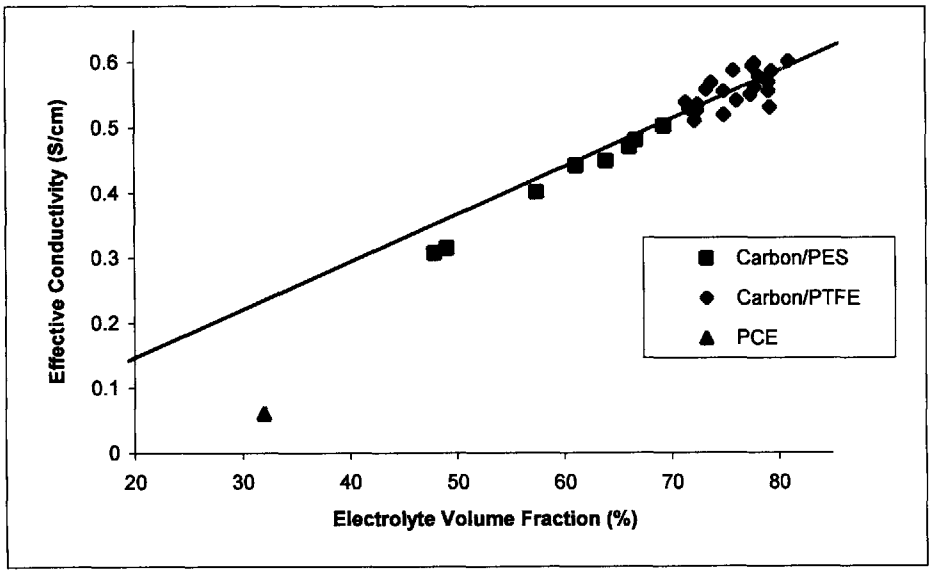

Figure 4-25: Effective ionic conductivity of polymer-bonded membranes

The reason for this scatter in data is not known. It may be due to a random experimental error. For example, the tightness of the conductivity cell's bolts may be different between membrane measurements. Since the PTFE-bonded membranes appear to be more compressible than the PES-bonded membranes, this source of error would affect the former more than the latter. Also, the average thickness of the membrane was used to calculate the conductivity of the membranes. The average thickness may be sufficiently different from the thickness at the center of the membrane where the current was flowing. No matter the reason, the scatter is small enough so as not to obscure the trend in the

conductivity data. The measured conductivities for the PES-bonded membranes are lower and within 5% of the values given by Equation (4.28) for membrane porosities greater than 0.57. This result suggests that the measured conductivity of plain Toray paper is a sufficiently accurate value for the conductivity of Toray papers used as supports for the PES-bonded membranes.

Recall that the conductivity of electrolyte in a porous medium is given by $\sigma_{eff} = (\varepsilon / \tau) \times \sigma_b$. Thus, the graph suggests that $\tau \approx 1$. The Bruggeman correlation is often used to relate the tortuosity to the porosity of a porous medium, $\tau = \varepsilon^{-0.5}$ [56]. The observed value of $\tau \approx 1$ is partially due to the high porosity of the measured membranes. It is also due to the primary size of the carbon black particles, which is about 30 nm. Relative to the thickness of the membranes, these particles are very small obstructions to a direct path for ion transport. It makes physical sense that the smaller the obstructions, the closer the porous medium tortuosity will be to a value of one. The conductivity values of carbon aerogel membranes with porosities similar to that of the PES-bonded membranes are about 18% lower than the values predicted by Equation (4.28). This is probably due to the larger size of the carbon aerogel particles. In the case of these membranes, the size of the carbon aerogel particles was found to be in the range of 100 nm to 1 μm (refer to Appendix B for carbon aerogel results). As the porosity of the PES-bonded membrane decreased below 57%, the tortuosity increased. The increase in tortuosity is partially due to the formation of membrane skin. The SEM picture of the 40 wt% PES-bonded membrane had a membrane skin with pore sizes that were not detectable at 8000x magnification (refer to Figure 4-7).

The high conductivity of the polymer-bonded membranes point to a major advantage that the microfabricated catalyst layer is expected to have over the conventional catalyst layer. The effective conductivity of the microfabricated catalyst is expected to be given by

$$\sigma_{CL,eff} = (\sigma_b \varepsilon)\varphi \tag{4.29}$$

Where φ is the fraction of the catalyst layer that is the microporous region, and ε is the porosity of the of the microporous region. A catalyst layer with 50% of its volume as the microporous region and with the microporous region made from 15 wt% PTFE with a porosity of $\varepsilon = 0.774$, the catalyst layer effective conductivity is predicted to be $\sigma_{CL,eff} = 0.284\, S/cm$ in 3.7 M sulfuric acid. This is 4.6 times the effective conductivity of the conventional electrode catalyst layer [58, 59].

4.4.5 Electronic Conductivity

Figure 4-26 is a typical current vs. potential curve generated from the four-probe electronic conductivity experiment. The curve is perfectly linear, with the square of the correlation coefficient equal to one. The line gives a current that is essentially zero when the potential is zero. These results are consistent with the electron transport following Ohm's law. Figure 4-27 is a graph of the electronic conductivity of the polymer-bonded membranes vs. their polymer wt%. All three of the membrane types showed an approximately linear relationship between conductivity and polymer wt%, with the conductivity decreasing as the polymer wt% increased. This result is not surprising. The carbon black particles are the electronic conductors within the membrane while the

polymer is an electronic insulator. Therefore, increasing the wt% of polymer should lead to a proportional reduction in the electronic conductivity of the membrane.

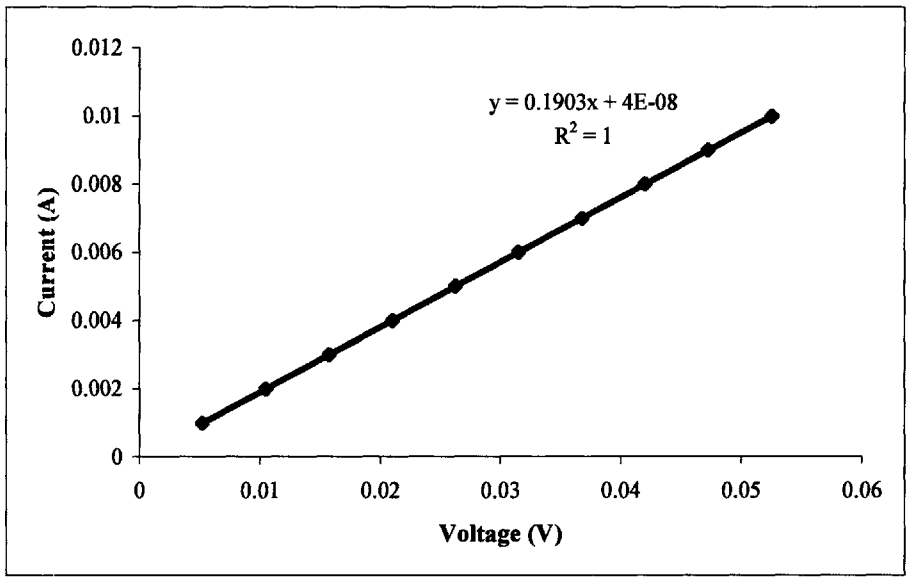

Figure 4-26: Current vs. potential plot from electronic conductivity experiment, 10 wt% PTFE-bonded membrane with XC72 carbon black

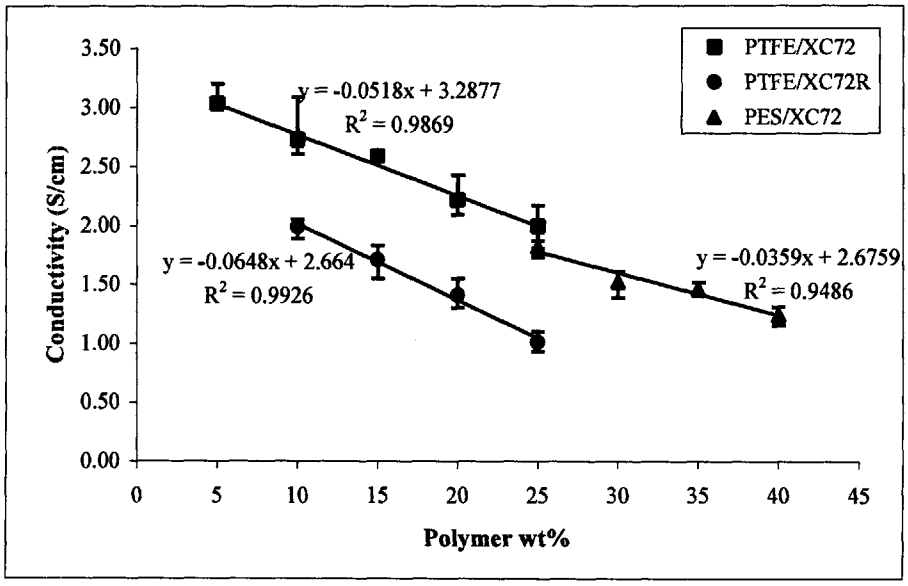

Figure 4-27: Effective electronic conductivity of polymer-bonded membranes

Figure 4-27 shows that the conductivity of the PTFE-bonded membranes with XC72 carbon black is significantly higher than that of PTFE-bonded membranes with XC72R.

Recall that the difference between XC72 and XC72R is that the former undergoes an additional compaction step. In membranes with XC72 carbon black, more of the carbon particles are bonded to each other by the weak van der Waals forces. This bond is stronger than the physical bonds caused by the PTFE fibers. The stronger carbon-to-carbon bonds in the XC72 carbon reduce the contact resistance between these carbon particles. Thus, the membranes with XC72 carbon have higher electronic conductivities than membranes with XC72R carbon black.

The electronic conductivity is the property that varied the most between membranes made from XC72 and XC72R. No measurable difference in the values and trends of the breakthrough capillary pressure and permeability were observed between these membranes. The porosity of the PTFE/XC72R membranes had, on average, a slightly higher value at a given PTFE wt% than the porosity of the PTFE/XC72 membranes. However, the higher porosity did not lead to an enhanced ionic conductivity beyond what is predicted by Equation (4.28). The significantly lower electronic conductivity at a given PTFE content for the XC72R membranes compared to that of XC72 membranes, suggests that the former should not be used to form membranes. The difficulty associated with working with XC72R in the preparation of membranes provides another reason why it should not be used over XC72 carbon black.

As shown in Figure 4-27, if the PTFE/XC72 membrane linear regression line was extended to the wt% values of the PES/XC72 membranes, the line would show good agreement with the PES-bonded membrane data. A least squares linear regression on both sets of data yields a line with an equation of

$$\kappa_M = -0.0534(wt\%) + 3.2826 \tag{4.30}$$

and the square of the correlation coefficient of $R_p^2 = 0.9784$. This result suggests that the proportionality constant relating polymer content to electronic conductivity is about the same for both types of polymer-bonded membranes.

The PTFE/XC72 linear regression line slightly over-predicts the conductivity for most of the polymer wt% of the PES-bonded membranes. This fact may be a result of the higher volume fraction of polymer for the PES-bonded membrane compared to the PTFE-bonded membrane at the same polymer wt%. The density of PES is about 1.37 g/cm^3 while the density of PTFE is 2.2 g/cm^3. This difference in volume fraction is significant and suggests a greater difference in conductivity between the two types of membranes than the results in Figure 4-27 and Equation (4.30) indicate. Although the higher volume fraction of polymer in the PES-bonded membrane leads to lower conductivity values, this effect may be compensated by the lower porosity of PES-bonded membranes and possibly stronger carbon-to-carbon bonds in these membranes compared to the PTFE-bonded membranes. Regardless, Equation (4.30) can be used to approximate the conductivity of both the PTFE-bonded and PES-bonded membranes made with XC72 carbon.

4.5 Conclusion

Porosity:

The porosity of the PTFE-bonded membranes ranged from 82.5 to 72% for a PTFE content between 5 and 25 wt%. The porosity decreased linearly with and increase in the PTFE content. The porosity of the PES-bonded membranes ranged from 66 to

47% for a PES content between 25 and 40 wt%. The porosity decreased faster as the PES content increased. This result was attributed to the fact that multiple factors contributed to the decrease in porosity with an increase in PES content.

Breakthrough Capillary Pressure:

Both the PTFE-bonded and PES-bonded membranes did not imbibe liquid water or electrolyte when they were oven dried. In order to saturate these membranes with liquid water or electrolyte, isopropanol was used as an intermediary fluid. Once saturated with water, the membranes had high breakthrough capillary pressures. Excluding the 25 wt% PTFE-bonded membrane, the measured breakthrough capillary pressures of all other membranes tested were greater than 0.7 bar. The hydrophobicity of the 25wt% PTFE-bonded membrane was such that the repeating breakthrough pressure was at times measured to be 0 bar. For this reason, this level of PTFE is not recommended for the membranes.

The dual wetting behavior of the polymer-bonded membranes is a favorable property. As presented in Chapter 6, the behavior was used to effectively electrodeposit Pt only on the surface of the membranes.

Permeability:

The average permeability of PTFE-bonded and PES-bonded membranes are $1.42 \times 10^{-15}\,\mathrm{cm}^2$ and $1.17 \times 10^{-15}\,\mathrm{cm}^2$, respectively. These values are much lower than the permeability values predicted by commonly used Carmen-Kozeny equation. The Carmen-Kozeny equation does not account for the bimodal distribution of the polymer-bonded membranes. The Carmen-Kozeny equation was combined with the serial-type nonuniformity correction to calculate permeability values of the same order as those that

were measured. This approach, however, is not rigorous. There is a need for liquid permeability equations more suitable for porous media with a bimodal distribution like that of the polymer-bonded membranes of this work and microporous layers found in PEMFCs and PAFCs.

Ionic Conductivity:

For most the polymer-bonded membranes tested, the effective ionic conductivity was found to be approximately equal to the bulk conductivity of the electrolyte times the porosity of the membrane. Thus, the tortuosity is approximately one for most of the membranes tested. These results point to a major advantage microfabricated catalyst layer is expected to have over the conventional catalyst layer design. It is possible that the effective ionic conductivity of the microfabricated catalyst layer will be more than 5 times that of the conventional catalyst layer.

Electronic Conductivity:

`The electronic conductivity of the polymer-bonded membranes made with XC72 carbon black ranged from about 3 to 1.25 S/cm for a polymer content between 5 and 40 wt%. The conductivity decreased approximately linearly with an increase in polymer content. PTFE-bonded membranes made with XC72R carbon black had electronic conductivities that were about 33 to 50% lower than the equivalent membrane made with XC72 carbon black. The electronic conductivity is the property that varied the most between membranes made from XC72 and XC72R. Considering the added difficulty associated with working with XC72R in the preparation of membranes, this fluffy-type of carbon black is not recommended for the polymer-bonded membranes.

Concluding Remarks:

The PTFE-bonded membranes have superior properties compared to the PES-bonded membranes. Thus, it is expected that a catalyst layer matrix made with PTFE-bonded carbon will perform better than that made from PES-bonded carbon. However, it has not yet been demonstrated that the viscoelastic property of the PTFE-bonded membrane makes the microembossing of this type of membrane possible. On the other hand, Dr. Chang Rae Lee has shown that carbon slurry (with dissolved polymer) can be cast on a microfabricated die to form the three-dimensional geometry presented in Section 3.4 (see Appendix A). Thus, the PES-bonded catalyst layer matrix may still be a better option.

Future work will involve working with the polymer-bonded membranes described in this chapter and microfabricated dies. The work should determine if such membranes can be formed into the catalyst layer of the microfabricated electrode.

References

[1] W.G. Grot, *Perflourinated ionomers, in Encyclopedia of Polymer Science and Engineerng*, John Wiley & Sons, New York, 1989.

[2] C.R. Martin, T.A. Rhoades, and J.A. Ferguson, "Dissolution of Perflourinated Ion Containing Polymers", *Anal. Chem.*, Vol. 54, p. 1639, 1982.

[3] R.B. Moore and C.R. Martin, "Procedure for Preparing Solution-Cast Perfluorosulfonate Ionomer Films and Membranes", *Anal. Chem.* Vol. 58, p. 2569, 1986

[4] S.H. Kwak, D.H. Peck, Y.G. Chun, C.S. Kim, and K.H. Yoon, "New Fabrication Method of the Composite Membrane for Polymer Electrolyte Membrane Fuel Cell", *J. New Mat. Electrochem. Systems*, Vol. 4, p. 25, 2001.

[5] O. Savadogo and B. Xing, "Hydrogen/Oxygen Polymer Electrolyte Membrane Fuel Cell (PEMFC) Based on Acid-Doped Polybenzimidazole (PBI)", *J. New. Mat. Electrochem. Systems*, Vol. 3, p. 345, 2000.

[6] L. Qingfeng, H.A. Hjuler, and N.J. Bjerrum, "Phosphoric Acid Doped Polybenzimidazole Membranes: Physiochemical Characterization and Fuel Cell Applications", J. App. Electrochem. Vol. 31, p. 773, 2001.

[7] G.A. Shia, *Battery Electrode and Method of Making*, U.S. Pat. No. 4,556,618 (1985).

[8] J.M. Bilhorn, *Method and Apparatus for Continuous Formation of Fibrillated Polymer Binder Electrode Component*, U.S. Pat. No. 4,976,904 (1990).

[9] I. Chi, G. Cintra, J. Golay, G. Heyn, and M.J. Sinclair, *Method of Making Batter*, U.S. Pat. No. 6,368,365 (2002)

[10] P. Mitchell, X. Xi, L. Zhong, and V. Hermann, *Electrode Impregnation and Bonding*, U.S. Pat. No. 7,102,877 (2006).

[11] DuPont, Teflon PTFE 20 Product Information Sheet, http://www2.dupont.com/Teflon_Industrial/en_US/assets/downloads/h03234.pdf

[12] A.J. Appleby and F.R. Foulkes, *Fuel Cell Handbook*, Krieger, Malabar, Florida, 1993.

[13] M. Maja, C. Orecchia, M. Strano, P. Tosco, and M. Vanni, "Effects of Structure of the Electrical Performance of Gas Diffusion Electrodes for Metal Air Batteries", *Electrochimica Acta*, Vol. 46, p. 423, 2000.

[14] H.G. Petrow and R.J. Allen, *Control of the Interaction of Novel Platinum-on-Carbon Electrocatalysts with Fluorinated Hydrocarbon Resins in the Preparation of Fuel Cell Electrodes*, U.S. Pat. No. 4,166,143 (1979).

[15] Nexant Chem. System, PERP Program – New Report Alert. March 2005.

[16] D. Lu, H. Zou, R. Guan, H. Dai, and L. Lu, "Sulfonation of Polyethersulfone by Chlorosulfonic Acid", *Polymer Bulletin*, Vol. 54, p. 21, 2005.

[17] J.C. Trocciola, J. Powers, and R.G. Martin, *Silicon Carbide Matrix for Fuel Cells*, U.S. Pat. No. 4,695,518 (1987).

[18] D.E. Suk, G. Pleizier, Y. Deslandes, and T. Matsuura, "Effects of Surface Modifying Macromolecule (SMM) on the Properties of Polyethersulfone Membranes, *Desalination*, Vol. 49, p. 303, 2002.

[19] M. Kraus, M. Heisler, I. Katsnelson, and D. Velazques, *Filtration-Membranes and Method of Making the Same*, U.S. Pat. No. 4,900,449 (1990).

[20] M.J. Witham and J.S. Johnson, *Non-Cracking Hydrophilic Polyethersulfone Membranes*, U.S. Pat. No. 6,465,050 (2002).

[21] L.M. Heijnen, *Membrane which comprises a blend of a polysulphone or a polyether sulphone and polyethylene oxide/polypropylene oxide substituted ethylene diamine*, U.S. Pat. No. 6,495,043 (2002).

[22] J.M. Greenwood, J.S. Johnson, and M.J. Witham, *Preparation of Polyethersulfone Membranes*, U.S. Pat. No. 6,056,903 (2000).

[23] I. Wang, *Highly Asymmetric Polyethersulfone Filtration Membranes*, U.S. Pat. No. 5,886,059 (1999)

[24] K.H. Yoon, J.Y. Choi, J.H. Jang, Y.S. Cho, and K.H. Jo, "Electrode/Matrix Interfacial Characteristics in a Phosphoric Acid Fuel Cell", *J. App. Electrochem.*, Vol. 30, p. 121, 2000.

[25] K.H. Yoon and B.D. Yang, "Preparation and Characterization of Matrix Retaining Electrolyte for a Phosphoric Acid Fuel Cell by Non-Volatile Solvent, NMP", *J. Power Sources*, Vol. 124, p. 47, 2003.

[26] I. Cabasso, Y. Yuan, and X. Xu, *Gas Diffusion Electrodes Based on Polyethersulfone Carbon Blends*, U.K. Pat. No. GB2316802A

[27] E. Antolini, A. Pozio, L. Giorgi, and E. Passalacqua, "Morphological Characteristics of Carbon/Polytetrafluoroethylene Films Deposited on Porous Carbon Support", *J. Mater. Sci.*, Vol. 33, p. 1837, 1998.

[28] R. Petricevic, M. Glora, A. Moginger, and J. Fricke, "Skin Formation on RF Aerogel Sheets", *J. Non-Cryst. Solids*, Vol. 285, p. 272, 2001.

[29] I. Cabasso, Y. Yuan, and X. Xu, *Gas Diffusion Electrodes Based on Poly(vinylidene Fluoride) Carbon Blends*, U.S. Pat. No. 5,783,325 (1998).

[30] F.A.L. Dullien, *Porous Media: Fluid Transport and Pore Structure*, Academic Press, New York, 1979

[31] A.E. Scheidegger, *The Physics of Flow Through Porous Media*, University of Toronto Press, Toronto, 1960

[32] G. Matheron, Rev. Inst. Franc. Petrole, Vol. 21, p. 1697, 1966.

[33] S. Whitaker, Ind. Eng. Chem. Vol. 61, p. 14, 1969.

[34] E. Agel, J. Bouet, and J.F. Fauvarque, "Characterization and use of Anionic Membranes for Alkaline Fuel Cells", *J. Power Sources*, Vol. 101, p. 267, 2001.

[35] D.D. Wagman, *The NBS Tables of Chemical Thermodynamic Properties: Selected Values for Inorganic and C1 and C2 Organic Substances in SI Units*, American Chemical Society and the American Institute of Physics for the National Bureau of Standards, New York, 1982.

[36] Am. Soc. Test. Mater., ASTM Standard, F723, Part 43.

[37] Toray Carbon Paper Data Sheet from Electrochem. Inc. http://www.fuelcell.com/techsheets/TORAY-TGP-H.pdf

[38] R.H. Perry and D.W. Green, *Perry's Chemical Engineers Handbook, 7th ed.*, pp 5-55, McGraw Hill, New York, 1997.

[39] J.T. Gostick, M.W. Fowler, M.A. Ioannidis, M.D. Pritzker, Y.M. Volfkovich, and A. Sakars, "Capillary Pressure and Hydrophilic Porosity in Gas Diffusion Layers for Polymer Electrolyte Fuel Cells", *J. Power Sources*, Vol. 156, p. 375, 2006.

[40] S. Dheenadayalan, R. Song, and D. Shin, "Characterization and Performance Analysis of Silicon Carbide Electrolyte Matrix of Phosphoric Acid Fuel Cell Prepared by Ball-Milling Method", *J. Power Sources*, Vo. 107, p. 98, 2002.

[41] C.W. Extrand and Y. Kumagai, "An Experimental Study of Contact Angle Hysteresis", *J. Colloid Interface Sci*, Vol. 191 p. 378, 1997.

[42] N.R. Morrow, *J. Can. Pet. Technol.* Vol. 10, p. 38, 1971.

[43] N.R. Morrow, *J. Can. Pet. Technol.* Vol. 15, p. 49, 1976.

[44] J. Benziger, J. Nehlsen, D. Blackwell, T. Brennan, and J. Itescu, "Water Flow in the Gas Diffusion Layer of PEM Fuel Cells", *J. Membr. Sci.*, Vol. 261, p. 98, 2005.

[45] M. Goebel, J. Bachmann, S.K. Woche, W.R. Fisher, and R. Horton, "Water Potential and Aggregate Size Effects on Contact Angle and Surface Energy", *Soil Sci. Soc. Am. J.*, Vol. 68, p. 383, 2004.

[46] M. Lazghab, K. Saleh, I. Pezron, P. Guigon, and L. Komunjer, "Wettability Assessment of Finely Divided Solids", *Powder Technology*, Vol. 57. p. 79, 2005.

[47] A.Z. Weber, R.M. Darling, and J. Newman, "Modeling Two-Phase Behavior in PEFCs", *J. Electrochem. Soc.*, Vol. 151, p. A1715, 2004.

[48] Th. Dippel, K.K. Kreuer, J.C. Lassegues, and D. Rodriguez, "Proton Conductivity in Fused Phosphoric Acid; A $^{1}H/^{31}P$ PFG-NMR and QNS Study", *Solid State Ionics*, Vol. 61, p. 41, 1993.

[49] D. Chin, and H.H. Chang, "On the Conductivity of Phosphoric Acid Electrolyte", *J. Applied Electrochemistry*, Vol. 19, p. 95, 1989.

[50] D.A. Landsman and P.A. Plasse, *High Current Acid Fuel Cell Electrodes*, U.S. Pat. No. 5,217,821 (1993).

[51] U. Pasaogullari and C.Y. Wang, "Two-Phase Transport and the Role of Micro-Porous Layer in Polymer Electrolyte Fuel Cells", *Electrochimica Acta*, Vol. 49, p. 4359, 2004.

[52] J.H. Nam and M. Kaviany, "Effective Diffusivity and Water-Saturation Distribution in Single- and Two-Layer PEMFC Diffusion Medium", *Int. J. Heat and Mass Transfer*, Vol. 46, p. 4595, 2003.

[53] P.C. Carman, *Flow of Gases Through Porous Media*, Butterworths, London, 1956.

[54] U. Pasaogullari, C.Y. Wang, and K.S. Chen, "Two-Phase Transport in Polymer Electrolyte Fuel Cells with Bilayer Cathode Gas Diffusion Media", *J. Electrochem. Soc.*, Vol. 152, p. A1574, 2005.

[55] A.Z. Weber and J. Newman, "Effects of Microporous Layers in Polymer Electrolyte Fuel Cells", *J. Electrochem. Soc.* Vol. 152, p. A677, 2005.

[56] M. Kaviany, *Principles of Heat Transfer in Porous Media*, Springer, New York, 1999.

[57] J. Newman and K.E. Thomas, *Electrochemical Systems*, Third Edition, John Wiley & Sons, Inc., Hoboken, New Jersey, 2004.

[58] D.S. Chan and C.C. Wan, "Influence of PTFE dispersion in the Catalyst Layer of Porous Gas-Diffusion Electrodes for Phosphoric Acid Fuel Cells", *J. Power Sources*, Vol. 50, p. 163, 1994.

[59] D.S. Chan and C.C. Wan, "Effect of Structure on Porous Gas-Diffusion Electrodes for Phosphoric Acid Fuel Cells", *J. Power Sources*, Vol. 50, p. 261, 1994.

Chapter 5

A Rotating Disk Electrode Study of the Oxygen Reduction Reaction on Thin Platinum Films Electrodeposited on Glassy Carbon.

5.1 Introduction

In the standard electrode design, Pt is deposited, in the form of highly dispersed nanoparticles (2 to 6 nm in diameter), on high surface area carbon black particles (Pt/C). The small particle size results in a Pt specific area as high as 120 m^2/g. In the proposed electrode design Pt is deposited as a thin film on a smooth porous substrate with Pt loadings up to 80$\mu g/cm^2$. Pt films deposited on smooth nonporous substrates are known to have specific areas only as high as 35 m^2/g. Furthermore, the specific area tends to decrease with an increase in the Pt loading [1]. Pt films deposited on a microporous substrate are not expected to have a specific area much different than that of films deposited on a nonporous substrate (see Chapter 6). The much lower specific area of a thin Pt films compared to Pt/C appears to be a major problem for the proposed fuel cell electrode. However, the specific area is not the only parameter that affects the mass activity of Pt.

It is now well known that the oxygen reduction reaction (ORR) is extremely sensitive to the size and structure of the Pt catalyst [2]. For example, a polycrystalline Pt disk in sulfuric acid has a specific activity that is three times greater than that of Pt/C [3]. The enhance activity of polycrystalline Pt over Pt/C is also observed for the ORR in

perchloric acid, which unlike sulfuric acid, is an electrolyte with a non-adsorbing anion. In perchloric acid, the ORR specific activity on polycrystalline Pt is ten times greater [4]. In both these cases, the higher activity of polycrystalline Pt is attributed to the lower adsorption of site-blocking species such as $HSO_{4(ad)}$ in sulfuric acid and $OH_{(ad)}$ in perchloric acid [5].

Thin Pt films, either from physical vapor deposition or electrodeposition, tend to have a morphology similar to polycrystalline Pt. For this reason, the ORR in these films may be similar to that of polycrystalline Pt and thus have the same enhanced activity. For example, the improved activity of Pt films was demonstrated by Poirier *et al.* who sputter deposited thin Pt films on glassy carbon substrate. They measured a maximum specific activity of 70 $\mu A/cm^2$ for the ORR on the sputtered films in sulfuric acid. This specific activity is much larger than the 5 $\mu A/cm^2$ reported in the work of Peuckert *et al.* for the ORR on Pt/C [6]. Recently, electrodeposited films have been shown to have enhanced reactivity compared to the bulk polycrystalline surface in a variety of practically important electrochemical processes, including oxygen reduction [7]. The enhanced activity may be related to the high volume density of grain boundaries in these films [*8*].

Electrodeposition is expected to be the method of choice for depositing thin Pt films within the microfabricated cylindrical holes of the catalyst layer. Electrodeposition has several advantages over other deposition techniques. It is capable of depositing Pt films uniformly within cylindrical holes. The pulse electrodeposition method can be used to effectively deposit a metal within high aspect ratio pores. Electrodeposition has been shown to produce Pt films with specific areas greater than 20 m^2/g, even for Pt films with

a loading as high as 100 $\mu g/cm^2$. Other deposition techniques, such as sputter deposition, produce films with much lower specific areas at this high Pt loading. Lastly, electrodeposition produces films with a high density of grain boundaries and other defects. A high density of defects is known to enhance several electrochemical reactions, including oxygen reduction.

The kinetic data of the ORR on electrodeposited Pt films are scarce in the literature. In the work presented in this chapter, Pt was electrodeposited on glassy carbon. Glassy carbon was chosen as the substrate because its surface activity for Pt deposition was expected to be similar to the surface activity for Pt deposition on the polymer-bonded membranes presented in Chapter 4. Also, glassy carbon is easily polished and electrochemically treated to produce reproducible surfaces. Cyclic voltammetry, linear sweep voltammetry, and scanning electron microscopy (SEM) were used to characterize the electrodeposited films. The rotating disk electrode (RDE) technique was used to measure the ORR on these Pt films in 0.5 M H_2SO_4. The kinetic data were compared with values reported in the literature for Pt/C.

To our knowledge, this is first reported RDE study of the ORR activity on electrodeposited Pt films. Others have used the RDE technique to study the ORR of physical vapor deposited Pt films in sulfuric acid [1] and potassium hydroxide [9]. In these works the activity of the Pt films was correlated with Pt loading. Recently, several research groups have used the RDE technique to study the ORR activity on Pt monolayers deposited by the galvanic displacement by Pt of electrodeposited less noble metal, such as Cu or Ag [10, 11, 12]. However, the morphology of these Pt films is very different than Pt films directly electrodeposited on the support surface. There is a need

for the study of the ORR on electrodeposited Pt films. The work presented in this chapter attempted to address this need. Considering the importance of the thin film technology to the catalyst layer design concept, this work also provided valuable information on the practicality of the thin Pt film from a mass activity perspective.

5.2 Theory and Background

5.2.1 The Kinetics of Oxygen Reduction Reaction (ORR) on Pt

Theory:

The electrochemical reduction of oxygen has been extensively investigated as a result of its enormous importance in fuel cell technologies and other applications. It has been well covered in symposium proceedings [13, 14], review articles [5, 15, 16], and books [17]. The ORR have been studied in the following electrolytes: H_3PO_4, H_2SO_4, $HClO_4$, HF, KOH, NaOH, and ion conducting membranes such as Nafion. The ORR has also been studied extensively on the following electrodes: Pt and Pt alloys, Carbon, Os, Pd, Ag, Au, Ir, Ru, and Rh. Pt and Pt alloys remain the catalysts with the highest activity for the ORR. Despite the considerable amount of work completed on the electrochemical reduction of oxygen on Pt in acid and alkaline electrolytes, the complete reaction mechanism (i.e. all intermediate steps) is still not clear.

Markovic *et al.* [5] state that a modified Wroblowa *et al.* reaction scheme is the most effective scheme to describe the reaction pathway by which oxygen is reduced on the Pt surface. The modified Wroblowa pathway is shown below [18]

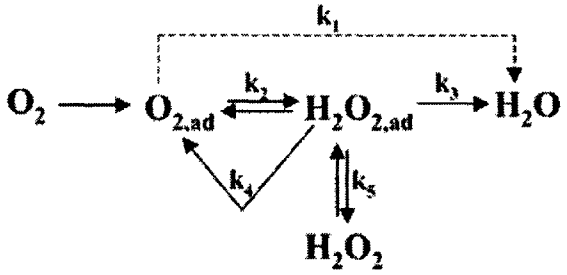

(5.1)

where k_i is the kinetic coefficient for reaction number i. Based on this reaction pathway, oxygen can be electrochemically reduced directly into water. This is referred to as the "direct" $4e^-$ reduction pathway. Oxygen can also be reduced into an adsorbed peroxide atom. The peroxide route is referred to as the series $2e^-$ reduction pathway. The adsorbed peroxide can be 1) electrochemically reduced to water, 2) chemically decomposed back to oxygen and hydrogen on the surface of the catalyst, or 3) it can desorb and diffuse into the bulk of the solution.

Markovic *et al.*, in recent studies of ORR on single crystal Pt electrodes and on supported Pt (Pt/C) and Pt alloy nanoparticles, have found that oxygen is either reduced to water or peroxide depending on the adsorbed species on the Pt surface [5]. The adsorbed species affect the reaction pathway by lowering the ratio of k_3 / k_5 (refer to Equation (5.1)). Assuming that only one of the pathways is dominant on the Pt surface (the direct or series pathway), Markovic *et al.* observations led them to conclude that the series pathway, via an adsorbed peroxide intermediate, is operative on Pt and Pt alloy catalysts.

Regardless of which pathway is dominant, the first step in the ORR is believed to be the adsorption of oxygen on the Pt surface,

$$O_2 + Pt \leftrightarrow Pt(O_2)_{ad} \tag{5.2}$$

This step is followed by an electrochemical step involving the transfer of one electron,

$$Pt(O_2)_{ad} + e^- \rightarrow Pt(O_2^-)_{ad} \tag{5.3}$$

The first electron transfer step is considered to be the rate determining step in the overall reaction.[1] With this assumption, the rate expression for the ORR can be written as [19, 20],

$$i = nFKP_{O_2}\left(1-\Theta_{OH}-\Theta_{ad}\right)^{x}\exp\left[\frac{-\beta FE}{RT}\right]\exp\left[\frac{-\gamma r\Theta_{OH}}{RT}\right] \tag{5.4}$$

where i is the current density, n is the total number of electrons transferred for the entire reaction, K is the chemical rate constant, P_{O_2} is the concentration of oxygen in the gas phase, Θ_{OH} is the coverage of hydroxyl atoms on the surface of the Pt catalyst, Θ_{ad} is the total coverage of the remaining adsorbed species on the Pt surface, x is either 1 or 2 depending on the site requirements of the adsorbates, β and γ are the symmetry factors (assumed to be 1/2), E is the applied potential, and r is a factor that gives the measure of the change of the energy of adsorption of oxygen containing species with their coverage. F, R and T are the Faraday's constant, the ideal gas constant, and the temperature, respectively.

Equation (5.4) shows the kinetic rate of oxygen reduction as being first order with respect to the pressure of oxygen in the gas phase. This is a more general kinetic equation than the ones that have oxygen reduction as being first order with respect to the concentration of oxygen in the electrolyte. The chemical potential of oxygen in the electrolyte phase is independent of the particular electrolyte, provided the electrolyte phase is in equilibrium with the gas phase.[2] Thus, unless the reaction is under transport

[1] The assumption that the first electron step is the rate determining step is not universally accepted. Yeager *et al.* [21] theorized that the rate determining step is the adsorption of oxygen onto the Pt catalyst surface. Under this theory, the dependence of the ORR on potential is due to the potential dependence of the standard free energy of activation of the transition state.

[2] From absolute rate theory, it is known that the rate of a reaction ultimately depends on the chemical potentials of the reacting species and the transition state.

control in the gas and/or electrolyte phases, the rate of oxygen reduction does not directly depend on the concentration of oxygen in the electrolyte. This explains why there is no corresponding drop-off in the rate of O_2 reduction on the Pt electrode between 0.1 and 10 M KOH even though the solubility of oxygen drops off by a factor of 10^{-2} from the dilute to the concentrated KOH [21].

The coverage of the ORR intermediates is assumed to be small under the reaction conditions [22]. Therefore, the reversible hydroxyl atoms adsorbed on the surface of Pt catalyst are not the ORR intermediates as was previously assumed [23]. They result from the reversible reaction

$$Pt + H_2O \leftrightarrow PtOH + H^+ + e^- \tag{5.5}$$

in acid electrolytes and the reversible reaction

$$Pt + OH^- \leftrightarrow PtOH + e^- \tag{5.6}$$

in alkaline electrolytes [22, 24]. These reversible forms of the adsorbed hydroxyl atoms suppress the ORR by blocking reaction sites, but they do not alter the reaction pathway (i.e. they do not lead to an increase the production of peroxide). OH_{ad} is assumed to be the only adsorbent whose coverage affects the Gibbs free energy of adsorption of oxygen atoms at potentials greater than 0.6 V. Hence, the argument in the second exponential term in Equation (5.4) only depends on Θ_{OH}. In dilute acid electrolytes, two Tafel slopes are often observed for the ORR on Pt, 60 mV/decade at potentials higher than 0.85 V and 120 mV/decade at potentials between 0.85 V and 0.6 V. The generally excepted reason for the change in the Tafel slope of the ORR is the change in the adsorption isotherm of the hydroxyl atoms. At high potentials (0.95 to 0.85 V), the adsorption of hydroxyl

atoms follows a Temkin isotherm[3] where the coverage of the adsorbents are linearly related to the potential,

$$\Theta_{OH} = \frac{FE}{r} \tag{5.7}$$

Under this condition, Equation (5.4) reduces to

$$i = nFKP_{O_2}\left(1-\Theta_{OH}-\Theta_{ad}\right)^x \exp\left[\frac{-FE}{RT}\right] \tag{5.8}$$

The inverse of the Tafel slope is approximately equal to

$$\frac{\partial \log i}{\partial E} = \frac{-F}{2.3RT} \tag{5.9}$$

where the derivative of $\left(1-\Theta_{OH}-\Theta_{ad}\right)^x$ is neglected since it is negligible compared to the derivative of the exponential term for Θ_{OH} less than 0.5. At a temperature of $T = 25^oC$, Equation (5.9) gives a Tafel slope of 59 mV/decade. At potentials less than 0.85 the adsorption of hydroxyl atoms follows a Lagmuir isotherm where the Gibbs free energy of adsorption of reversibly adsorbed oxygen containing atoms is constant $\left(r\Theta_{OH} \approx \text{constant}\right)$. Under this condition, Equation (5.4) reduces to

$$i = nFK'P_{O_2}\left(1-\Theta_{OH}-\Theta_{ad}\right)^x \exp\left[\frac{-FE}{2RT}\right] \tag{5.10}$$

where the inverse of the Tafel slope is approximately equal to

$$\frac{\partial \log i}{\partial E} = \frac{-F}{2.3\left(2RT\right)} \tag{5.11}$$

Hence, the Tafel slope doubles when the hydroxyl atom adsorption isotherm shifts from a Temkin isotherm to a Langmuir isotherm.

---

[3] The Temkin isotherm is derived by assuming that the energy of adsorption varies linearly with coverage. For this reason, r is a constant.

In concentrated electrolytes with strongly adsorbing anions such as HSO_4^- and $H_2PO_4^-$, the Tafel slope given by Equation (5.11) is observed over the entire potential range (0.95 to 0.6 V) [25]. This is a result of the high coverage of the electrolyte's anions, which suppress the reversible adsorption of the hydroxyl atoms [26].

In acid electrolytes, the Tafel slope increases at potentials lower than 0.6 V. The kinetic current appears to approach a limiting value. This limiting kinetic current value is thought to be due to a change in the ORR rate determining step to a reaction which is approximately independent of potential [27]. Kinetic potentials lower than 0.6 V are beyond the practical limits of fuel cells. For this reason, this kinetic regime has not been studied significantly.

Equation (5.9) and (5.11) indicate that the Tafel slope is proportional to the temperature. However, experimental measurements have repeatedly indicated that the Tafel slopes are invariant with temperature in acid electrolytes [3, 21, 27, 28]. That is, the Tafel slope is essentially equal to 60 mV/decade at low overpotentials and is equal to 120 mV/decade at high overpotentials independent of temperature. There is not a generally accepted model for the ORR that captures both the effects of the doubling of the Tafel slope and the anomalous lack of temperature dependence of Tafel slope. The independence of the Tafel slope with respect to temperature was one of the bases for Yeager *et al.* to surmise that the rate determining step for the ORR is the oxygen atom adsorption step [21]. They concluded that the Tafel slope is invariant to temperature because most of the potential dependence of the reaction rate is associated with the

potential dependence of the entropy of activation of the reaction rather than the simple change of the height of the potential energy barrier.[4]

Θ_{ad} is the total coverage of the remaining species on the Pt surface excluding the ORR intermediates and the hydroxyl atoms. These include, depending on the electrolyte, bisulfate atoms, phosphate atoms, and halides. It also includes hydrogen atoms when the potential is in the hydrogen adsorption/desorption range. In strongly adsorbing electrolytes, such as H_2SO_4 and H_3PO_4, the anions irreversibly adsorb onto the surface of the Pt and suppress the ORR kinetics. The sulfate or phosphate atoms inhibit reduction of molecular oxygen, most likely, by blocking the sites for oxygen adsorption on the Pt(111) facets. The activity of all three low-index Pt planes is significantly higher in the non-adsorbing perchloric acid than in sulfuric acid. This fact indicates that the adsorption of bisulfate anions affects the kinetics of the ORR on all three surfaces. However, the effects on the Pt(111) surface is particularly strong probably because of the strong adsorption of bisulfate anions from the symmetry match between the FCC Pt(111) face and the C_{3V} geometry of the oxygen atom of the sulfate anions [5]. For this reason, anion adsorption from phosphoric acid would be expected to exhibit similar structure sensitivity to that of sulfuric acid [29]. The similarity of the cyclic voltammetry of the Pt(111) surface in sulfuric acid and in phosphoric acid supports this hypothesis [30]. Bisulfate and phosphate atoms do not affect the pathway of the reaction, since when present they do not lead to greater peroxide formation [5, 29, 30]. The halides, such as chloride (Cl) and bromide (Br) atoms strongly inhibit the ORR. They strongly adsorb on all three low-

[4] The Gibbs free energy of the reaction is $\Delta G = \Delta H - T\Delta S$. The derivative with respect to potential is $\frac{\partial \Delta G}{\partial E} = \beta - aT$, where a is constant and equal to $\frac{\partial \Delta S}{\partial E}$.

index single-crystals of the Pt catalyst [20, 31,]. They also alter the reaction pathway of the ORR. At potentials less than 0.3 V, adsorbed hydrogen atoms, H_{upd}, lead to an increase in peroxide production on both the Pt(111) and Pt(100) surfaces. The adsorbed hydrogen atoms do not appear to affect the ORR pathway on the Pt(110) surface since no increase in peroxide production was observed for Pt(110) surface in the hydrogen adsorption/desorption region [24, 32].

The Effect of Pt Morphology on the Kinetics of the ORR:

One of the first public documents to report the dependence on the ORR kinetics on Pt morphology was a paper by Bregoli [2] of United Technologies. Figure 5-1, a copy of a graph from this paper, is given below.

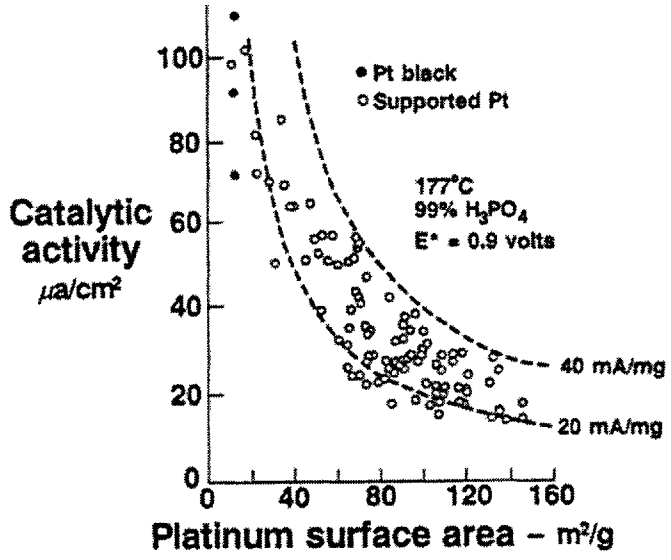

Figure 5-1: Catalytic activity of Pt nanoparticles versus the Pt specific area in concentrated phosphoric acid [2]

The mass activity of the Pt, $\bar{i}_{k,0.9V}$,[5], is the most technically relevant parameter due the high cost of Pt. It is related to the Pt specific area, SA, and Pt specific activity (i.e. the activity of the Pt per Pt area), $i_{k,0.9V}$, by the following equation:

$$\bar{i}_{k,0.9V} = i_{k,0.9V} \cdot SA \tag{5.12}$$

Figure 5-1 shows that in concentrated phosphoric acid the mass activity of Pt is essentially constant. Thus, the specific activity is inversely proportional to the specific area. This conclusion had enormous implications for the design of the phosphoric acid fuel cell (PAFC) cathodes. Typical dispersions of Pt nanoparticles produced particles with a specific area of 80 to 100 m^2/g. The results in Figure 5-1 indicate that increasing the particle dispersion beyond these values would not lead to higher performance. The results from the figure also suggest that, in PAFC cathodes, the growth of particles did not reduce the performance of the cell by reducing the kinetic current. Instead, particle growth leads to an increase in the local diffusion flux around the larger particles. This increase in the mass transport overpotential is one of the reasons for the reduction in cell performance over time.

References [33, 34, and 35] reported the measured dependence of mass activity to the crystallite size in concentrated phosphoric acid. Reference [6] did the same for the ORR in 0.5 M sulfuric acid at room temperature. Kinoshita [36] presented an excellent summary of these experimental works and also a review of thermodynamic analysis of how metal particles' shapes change with size. Kinoshita showed that the crystallite size dependence of the data fit a model which assumes: (1) the Pt particles are perfect cubo-

[5] In the subscript, k denotes that the current is only controlled by the ORR kinetics, the number denotes the potential at which the kinetic current was measured. The bar denotes current density per unit mass.

octohedral crystallites[6] and (2) that only the Pt(100) facets are active for the ORR. A picture of a cubo-octahedral crystallite is given in Figure 5-2.

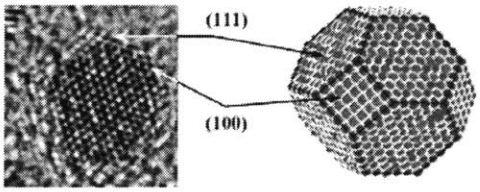

Figure 5-2: TEM image of Pt particle and an illustration of the cubo-octahedral shape [5]

Using the cubo-octahedral structure, Kinoshita calculated the total number of surface atoms from the (100) face normalized by the total number of atoms that make up the crystallite, MAD(100), and normalized by the total number of atoms on the surface of the crystallite, SAD(100). Figure 5-3 shows that SAD(100) and MAD(100) correlate very well with the specific activity data and mass activity data, respectively. The graphs were obtained from reference [36].

The particle size effect in the ORR is now generally accepted, especially after several recent studies [5, 24, 29, 32] with Pt single-crystal electrodes indicated that the structurally sensitive anion adsorption significantly changes the rates of the ORR. The differences in the coverage and adsorption strengths of these spectator species between Pt crystallographic orientations are believed to be the primary reasons for the strong structure dependence of the reaction rates of the ORR. The activity of the Pt(100) surface was observed to be more active by two orders of magnitude as compared to the Pt(111) surface [31]. The anomalously lower catalytic activity on the Pt(111) surface in sulfuric acid was reported to be attributed to the formation of a bidimensionally ordered adlayer

[6] The cubo-octahedral particles consist of eight octahedral (111) crystal faces and six cubic (100) crystal faces bounded by edge and corner atoms. Using the concept of localized metal bounds, the analysis of Romanowski suggests that the cubo-octahedral crystallite is the structure with the minimum surface energy among Pt crystallites [36]. TEM images of Pt particles supported on carbon black suggest that the majority of the Pt particles or cubo-octahedral crystallites.

of specifically adsorbed bisulfate anions that dramatically inhibit oxygen reduction. The measured activities the Pt(111) and Pt(100) single-crystals support the Kinoshita model, which assumed that only the Pt(100) facets are active for the ORR. In model calculations, a factor of 100 between the two facets is sufficient to fit the data [5].

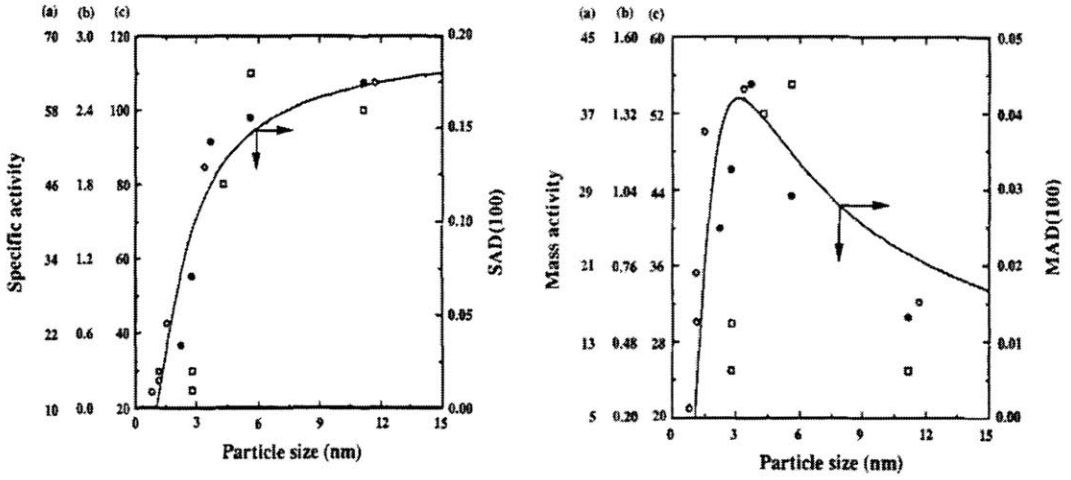

(A) (B)

Figure 5-3: Graph (A) superimposed plots of specific area for oxygen reduction and SAD(100) as function of particle size: (Solid line) SAD(100); (a) (shaded circles), 98% H_3PO_4 at 180°C [33,34]; (b) (open circles), 0.5 M H_2SO_4 at 25°C [6]; and (c) (open squares), 97% H_3PO_4 at 177°C. Graph (B) Superimposed plots of mass activity and MAD(100) as function of particle size: (Solid line) MAD(100); (a) (shaded circles), 98% H_3PO_4 at 180°C [33,34]; (b) (open circles), 0.5 M H_2SO_4 at 25°C [6]; and (c) (open squares), 97% H_3PO_4 at 177°C

The effects that Pt morphology has on the ORR are also observed in the significant difference in the ORR rates between dispersed Pt crystallites and bulk polycrystalline Pt. Table 5-1 lists some specific activities for the ORR for Pt/C and polycrystalline Pt in several electrolytes. The reasons for the differences in activity between the two types of Pt, in both strongly and weakly adsorbing electrolytes, are not as well studied as the reasons for the particle size effect on Pt/C. However, like the particle size effect, structure sensitive adsorption of site-blocking species is thought to be

one of the reasons for the observed difference in activity. This and other explanations are discussed further in Section 5.4.2.

Acid Solution	Dispersed Pt Specific Activity @ 0.9 V (mA/cm^2_Pt)	Polycrystalline Pt Specific Activity @ 0.9 V (mA/cm^2_Pt)
0.5 M H_2SO_4 (25 °C)	$5x10^{-4}$-0.005 [6], 0.012 [3]	0.04 [3]
Nafion/0.1 M $HClO_4$ (60 °C) [4]	0.16-0.31	2.77
5 mM $HClO_4$ (25 °C) [81]	0.005 – 0.011	0.05
96% H_3PO_4 (160 °C) [34]	0.03	0.09

Table 5-1: Specific activity of polycrystalline Pt compared to that of dispersed Pt nanoparticles

5.2.2 Electrochemistry of Pt Electrodeposition

Generally, there are four methods available for depositing Pt films on a substrate: (1) the collection of metal colloid particles from suspension onto a surface either by controlled adsorption or by electrophoresis, (2) chemical reduction of a Pt containing salt, acid, or base, (3) physical vapor deposition of Pt in a vacuum (4) electrodeposition of Pt from a Pt containing salt, acid, or base. Methods (1) and (2) are capable of depositing Pt with a high specific surface area (> 60 m^2/g) on a high surface area substrate like carbon black. However, when Pt is deposited as a film on a low surface area substrate, the Pt particles easily coalesce into large particles with low specific areas.

Physical vapor deposition techniques have been used extensively to deposit Pt films for fuel cell applications [37, 38, 39, 40]. Sputter deposition has been used to deposit thin Pt films on the gas diffusion layers [37,38] and on the membranes of PEMFCs [39,40]. Sputter deposition has several advantages. It is a commercialized technique for large area thin film coating applications, such as glass coating. The technique is cost competitive with other coating technologies. The sputter deposition of catalyst can also simplify cell fabrication, leading to manufacturing cost reductions [40].

The sputter deposition of Pt onto a low surface energy substrate follows an island growth mechanism. The Pt particles are initially separate, but they grow together into a continuous film as the loading increases. Phillips *et al.* investigated the growth morphology of ultra-thin Pt films sputtered onto glass substrates [41]. Their TEM results revealed the nucleation of individual islands of Pt on the SO_2 substrate. Island coalescence occurred at a loading of about 5 $\mu g/cm^2$. The coalescence of the islands at this low loading indicates a high density of Pt nucleation sites. This is one of the advantages of Pt sputter deposition. The energy barrier to the nucleation of Pt from the gas phase during sputter deposition is much lower than the energy barrier to the nucleation of Pt during electrodeposition. For this reason, sputter deposition is capable of depositing high specific area films $\left(\approx 30 m^2/g\right)$ on a low surface area substrate at low Pt loadings $\left(< 20 m^2/g\right)$. However, at higher Pt loadings, a large fraction of the Pt simply deposits on preexisting Pt sites and the specific area quickly decreases with an increase in the Pt loading.

Electrodeposition is uniquely capable of depositing Pt films with a high specific area on a low surface area substrate. During electrodeposition, the secondary nucleation phenomenon (i.e. the nucleation and growth of Pt particles on existing particles) produces Pt clusters that are made up of much smaller Pt crystallites. These Pt clusters have specific areas that are much greater than a smooth Pt particle of the same size. Figure 5-4 is a graph of the specific area of Pt films electrodeposited on glassy carbon versus the Pt loading. The data is taken from several references. The plots are compared with Pt films deposited by sputter deposition onto glassy carbon. Figure 5-4 shows that electrodeposition, under the right conditions, is capable of depositing Pt films with

specific areas greater than 20 m^2/g for Pt loadings as high as 160 $\mu g/cm^2$. In the case of sputter deposition, the specific area drops below 20 m^2/g at Pt loadings greater than 40 $\mu g/cm^2$. For this reason, electrodeposition should be the favored loading technique if high specific area at high Pt loadings is required.

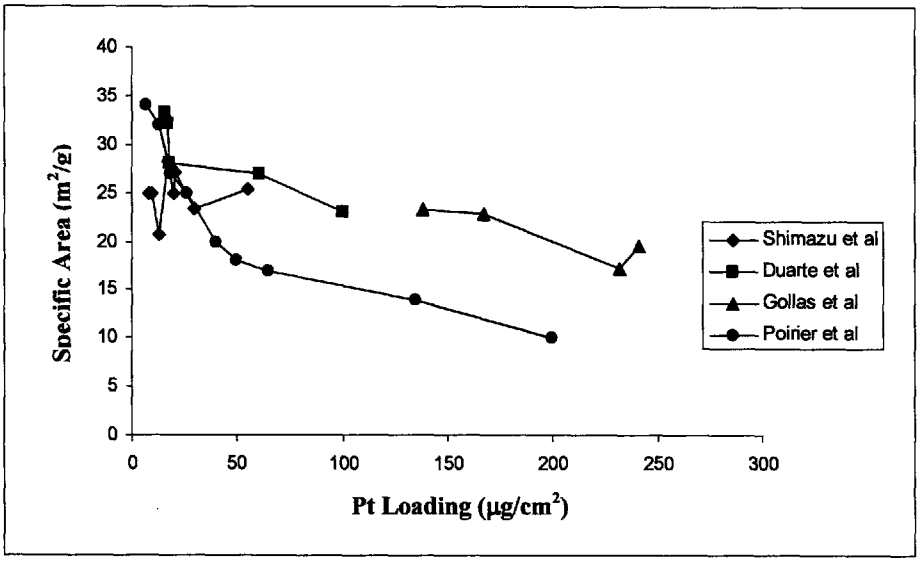

Figure 5-4: Plots of specific area of Pt films vs. Pt loading from various published references, Pt electrodeposited on glassy carbon: Shimazu *et al.* [42], Duarte *et al.* [43], and Gollas *et al.* [44]. Pt sputter deposited films: Poirier *et al.* [1]

Pt Electrodeposition from a $PtCl_6^{2-}$ containing solution:

The chloroplatinate ion, $PtCl_6^{2-}$, is the most widely used ion for the study of Pt electrodeposition in the laboratory. It is usually used in either its acid form, H_2PtCl_6, or in its salt form, K_2PtCl_6. The acid form readily absorbs water from the atmosphere and dissolves. This makes it difficult to work with. For this reason, it is not used in this work. $PtCl_6^{2-}$ is preferred over other Pt containing ions, such as $Pt(NH_3)_4^{2+}$ and $H_3Pt(SO_3)_2^-$, because it can be reduced to Pt at potentials greater than 0 V vs. the normal hydrogen electrode (NHE) [45]. At potentials lower than 0 V, hydrogen evolution quickly becomes

the dominant reaction. Hydrogen evolution causes a reduction in the Faradaic efficiency of the Pt deposition reaction and a reduction in secondary nucleation phenomenon. Secondary nucleation is crucial to producing films with a high specific area.

According to Fetham *et al.*, the electrodeposition of the chloroplatinate ion involves three reactions [46]:

$$PtCl_6^{2-} + 2e^- \rightarrow PtCl_4^{2-} + 2Cl^- \quad E^\circ = 0.726\,V_{NHE} \tag{5.13}$$

$$PtCl_6^{2-} + 4e^- \rightarrow Pt + 6Cl^- \quad E^\circ = 0.744\,V_{NHE} \tag{5.14}$$

and/or

$$PtCl_4^{2-} + 2e^- \rightarrow Pt + 4Cl^- \quad E^\circ = 0.758\,V_{NHE} \tag{5.15}$$

The corresponding standard redox potentials are taken from reference [47]. All three of these reactions involve the exchange of several electrons and the break of several Cl bonds. For these reasons, the reactions have low exchange current densities and display strong irreversibility.

Figure 5-5 is a cyclic voltammogram recorded on a graphite substrate in a 1 mM solution of H_2PtCl_6. The figure is from reference [48]. This voltammogram is a good representation of typical voltammograms measured on low surface energy substrates in a $PtCl_6^{2-}$ anion containing solutions. During the 1st cycle, the initial rise in the current is attributed to the reduction of $PtCl_6^{2-}$ (Pt(IV) for short) to $PtCl_4^{2-}$ (Pt(II) for short) given by Equation (5.13). Pt deposition on spontaneously formed Pt nuclei may have also contributed to the rise in the current. On glassy carbon, the spontaneous formation of Pt nuclei does not occur. Any rise in the current on this substrate is due to the reduction of Pt(IV) to Pt(II). Peak A in the cyclic voltammogram at 0.442 V vs. NHE (0.18 vs. SCE) can also be assigned to the reduction of Pt(IV) to Pt(II).

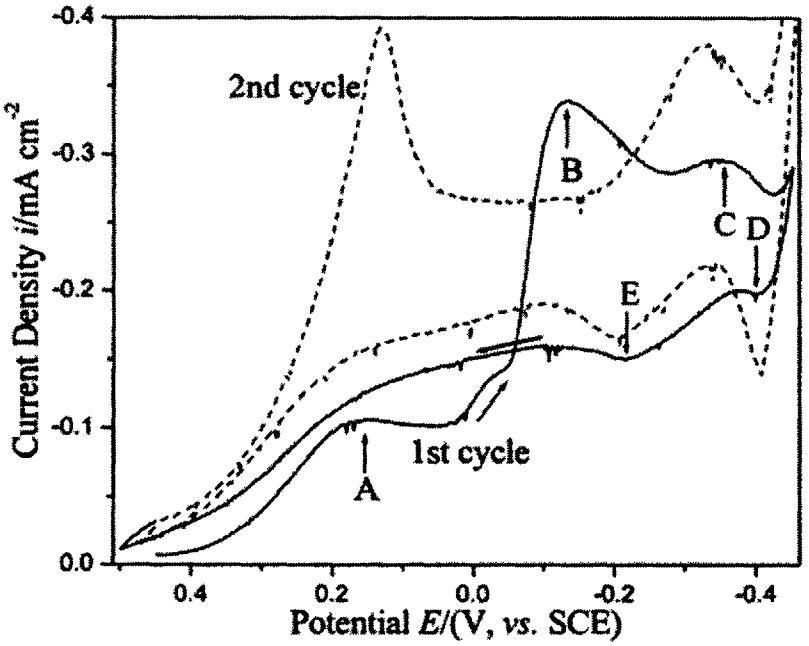

Figure 5-5: Cyclic voltammograms recorded on a graphite substrate in a 1 mM solution of H_2PtCl_6 [48]

At potentials greater than 0.250 V, Pt(II) undergoes a chemical conversion to Pt and Pt(IV) [49]. The disproportionation reaction is

$$2PtCl_4^{2-} \rightarrow Pt+PtCl_6^{2-}+2Cl^- \qquad (5.16)$$

Over time, a sufficient amount of Pt nuclei can form on the substrate and the electrochemical deposition of Pt on these nuclei becomes the dominant reaction. The overall reaction then shifts from a two electron reaction to a four electron reaction. At potentials between 0.250 and 0.200 V, this disproportionation reaction occurs along with Pt(II) and Pt(IV) reduction to Pt at defect sites on the substrate where nucleation of Pt occurs at lower voltages. The shoulder observed on the first cycle in Figure 5-5, next to the letter A, is probably due to this reaction.

The chemical pathway to Pt deposition can be inhibited in the presence of a chloride-containing supporting electrolyte. Lau and Hubbard have explained this effect

in terms of the inhibition of the formation of the Pt(II) complex due to the surface coverage of Cl^- [50]. Pt(II) would require the availability of several adjacent sites due to its planar geometry. Pt(IV) reduction to Pt is not inhibited to the same extent as a result of its octahedral structure, which requires only the availability of a single site

Peak B at -0.15 V (0.091 V vs. NHE) is attributed to the reduction of Pt(II) and Pt(IV) to Pt. Recently, Plyasova *et al.* deposited Pt on glassy carbon using the single potential step technique where the potential was stepped from the open circuit potential to the deposition potential [51]. They found that, for loadings between 100 and 200 $\mu g/cm^2$, a potential step to 0.100 V produced Pt films with the highest specific area. The reason for this optimal potential for deposition was attributed to the interplay between primary and secondary nucleation. Low potentials (high overpotentials) favor the nucleation of Pt on the glassy carbon substrate. A high density of primary nucleation sites results in Pt films with more numerous and smaller clusters of Pt crystallites. The specific area of the Pt film increases with a decrease in the size of the clusters. At high Pt loadings, secondary nucleation plays the more important role in affecting the specific area of the Pt film. The formation of new crystals on top of the particles formed from primary nucleation centers leads to Pt films with a higher specific area than the case where Pt simply deposits and grows the existing crystals. At potentials less than 0.3 V, secondary nucleation becomes inhibited by adsorbed hydrogen atoms on the Pt surface. The surface coverage of the hydrogen atoms increases with a decrease in deposition potential below 0.3 V. At 0.1 V, the deposition overpotential is high enough to activate a high density of primary nucleation sites on the glassy carbon surface. On the other hand, the deposition potential is not so low that hydrogen adsorption and evolution on the Pt surface severely

inhibit secondary nucleation. In the single potential step technique of this work, the glassy carbon electrode is stepped to 0.1 V in order to maximize the specific area of the Pt films.

The remaining features of the first cyclic voltammogram in Figure 5-5 is due to side reactions. Peak C is due to the reduction of hydrogen ions to adsorbed hydrogen atoms [52]. At more cathodic potentials, hydrogen evolution on the already deposited Pt particles becomes the dominant reaction. On the returning branch of the cyclic voltammogram, the dip in current at peak D is a result of the oxidation of H_2 suppressing the cathodic current of Pt deposition. The second dip at peak E is associated with the oxidation of hydrogen atoms to hydrogen ions.

The second cyclic voltammogram in Figure 5-5 shows one peak for Pt deposition. The Pt particles and nuclei that were formed in the first sweep catalyze Pt deposition during the second sweep. The reaction given by Equation (5.14) anodically shifts more than 0.3 V. The Pt(II) that forms quickly reduces to Pt in the presence of Pt nanoparticles. The second sweep shows that it is the formation of Pt nuclei on the low surface energy substrates that requires cathodic potentials where hydrogen adsorption and evolution is a side reaction. Once Pt nuclei form on the substrate, the cathodic potential needed for the diffusion limited deposition of Pt is about 0.45 V. This fact supports the use of the double potential step technique to deposit Pt on glassy carbon [42, 43]. In the double potential step method, the substrate potential is first stepped from the open circuit potential (OCP) to a high overpotential where the rate of primary nuclei formation is high. For the case of Pt deposition, the potential can be stepped from the OCP to a potential of -0.2 V for 1 sec. The potential is then stepped to potential where the metal nuclei

undergo diffusion controlled growth. For the case of Pt deposition, this is in the potential range of 0.45 to 0.25 V. Potentials less than 0.25 V are not desired since the surface concentration of hydrogen atoms increases and the atoms inhibit secondary nucleation on the Pt particles.

5.2.3 Rotating Disk Electrode (RDE)

The rotating disk electrode (RDE) and rotating ring disk electrode (RRDE) techniques are the most extensively used hydrodynamic techniques in electrochemistry. The techniques essentially involve the rotation of the working electrode at a constant angular velocity while the electrochemical reaction is occurring. In the RDE technique, a single circular disk is rotated. In the RRDE technique, a concentric ring electrode is included with the disk. Both the disk and the ring are usually made of the same material. In a typical RRDE application, the disk is the primary electrode where the reaction under study occurs. Its potential is scanned in the same way as the disk electrode is scanned in the RDE technique. The ring, on the other hand, is held at a potential that oxidizes or reduces, under diffusion control, a product from the disk reaction. Thus, the RRDE technique allows for the detection and measurement of reaction intermediates and/or products. In the specific case of the ORR, the rate of production of the peroxide intermediate can be measured.

There are several advantages to using the RDE and RRDE techniques. First, the RDE and RRDE are two of the few convective electrode systems for which the hydrodynamic and convective-diffusion equations have been solved rigorously [53]. Second, the working electrode can be reused after simple polishing and cleaning procedures. Finally, the rapid decay of transients and the stable mass transfer

characteristics result in highly reproducible experimental results. These techniques have proven to be invaluable in the study of the kinetics of the ORR. Recently, the RDE and RRDE techniques have been combined with Pt single-crystal electrodes or with Pt particles supported on carbon black (thin-film method) [5, 54]. These experiments have provided new insight into the kinetic pathway of the ORR as well as its complex dependence on the structure of the Pt catalyst. In this work, the RDE technique was used to obtain the kinetic parameters of Pt films electrodeposited on glassy carbon. The RRDE technique, which allows for the measurement of peroxide intermediates, was not used in this work.

Figure 5-6 is a schematic of a typical three-electrode cell used in RDE experiments.

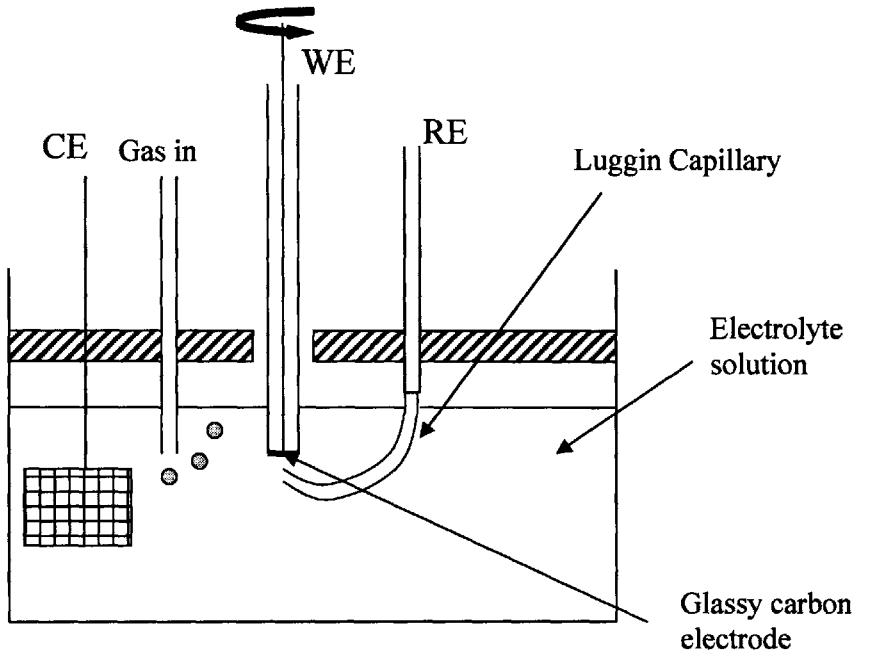

Figure 5-6: Schematic of a typical rotating disk electrode setup

The working electrode (WE) is in a cell with two other electrodes, the counter electrode and the reference electrode (RE). The counter electrode (CE) (or auxiliary electrode) is

the source or sink for electrons flowing to or from the working electrode. The counter electrode is often a Pt screen or wire. It is sometimes placed in its own fritted glass container in order to minimize the risk of contaminating the working electrode with the reaction products from the counter electrode.

The reference electrode measures the potential difference between itself and the working electrode. Its potential is set by the redox reaction that is occuring on its surface. The redox reaction is assumed to be at thermodynamic equilibrium since the reaction has a high exchange current density and a near zero current flows through the reference electrode. The reference electrode is incased in a glass tube filled with a solution which is often different from the solution of the cell. The reference electrode solution is ionically connected to the cell solution by a Vycor frit. Since the solutions are different, the electrochemical potential of each ion differs across the interface of the frit. This nonequilibrium condition leads to a liquid junction potential that contributes to the potential difference between the working and reference electrode. The liquid junction potential cannot be measured, but it can be estimated numerically using transport equations (refer to reference [55]). In all the experimental work of this dissertation, the liquid junction potentials are assumed to be negligible.

The reference electrode is often combined with a Luggin capillary, which is a glass tube with a Vycor frit at one of its ends. The Luggin capillary is filled with the solution of the cell. The tip of the Luggin capillary is placed sufficiently close to the working electrode in order to minimize the ionic resistance between the tip and the working electrode. However, it is not placed so close as to disturb the velocity and concentration profile of the RDE. The Luggin capillary is also used to reduce any

contamination of the working electrode with species found in the solution of the reference electrode.

The working electrode (WE) is a disk of the electrode material imbedded in a rod of an insulating material. Teflon is the most commonly used insulating material. The surface of the working electrode must be flush with the surface of the insulating material. It is also important that there is no leakage of the solution between the sides of the working electrode and the insulator. If these conditions are not satisfied, the RDE theory may not accurately describe the transport process at the working electrode.

The basic theory of RDE was derived by Levich [56].[7]. The current density of the working electrode, i, is given by

$$i = 0.62nFD^{2/3}\left(C_b - C_s\right)\nu^{-1/6}\omega^{1/2} \tag{5.17}$$

where C_b and C_s are the concentrations of the reacting species in the bulk of the solution and at the surface of the electrode respectively. ω is the angular velocity of the rotating disk, D is the binary diffusion coefficient of the reacting species with the solvent, ν is the kinematic viscosity of the solution, and n is the number of electrons transferred in the electrode reaction. When the electrode reaction is under mass transfer control, the surface of the reaction goes to zero. Thus, the limiting current, i_{lim}, for the rotating disk is given by

$$i_{\text{lim}} = 0.62nFD^{2/3}C_b\nu^{-1/6}\omega^{1/2} \tag{5.18}$$

[7] The Levich equation is derived assuming that the reacting species is transported to the rotating disk by diffusion and convection. The migration flux is assumed negligible. For a reacting species that is charged, this assumption is only valid when the species is accompanied with a sufficient concentration of a supporting electrolyte.

As expected, the limiting current is independent of potential. Combining Equations (5.17) and (5.18) yields an expression for the ratio of C_s *to* C_b,

$$\frac{C_s}{C_b} = 1 - \frac{i}{i_{\lim}} \tag{5.19}$$

According to Equation (5.18), a plot of limiting current versus the square root of the angular velocity should results in a straight line passing through the origin. The slope of this straight line is

$$b = 0.62nFD^{2/3}C_b\nu^{-1/6}, \tag{5.20}$$

The slope, b, is often used to calculate the diffusivity-solubility product, $D^{2/3}C_b$, when n of the reaction and ν of the solution are known. In the case of oxygen reduction reaction, oxygen can react to water, $n = 4$, or react to peroxide, $n = 2$ on the rotating disk. For this situation, the slope is used to calculate the net number of electrons transferred. The value of n gives some information on the reaction pathway of the ORR.

Consider a simple irreversible redox reaction,

$$O + ne^- \rightarrow R \tag{5.21}$$

that can be modeled with a single global kinetic expression. The Bulter-Volmer like kinetic equation for this reaction is

$$i = \left(\frac{C_s}{C_b}\right)^m i_k \tag{5.22}$$

where

$$i_k = i_o \exp\left[-\frac{\eta}{\left(\frac{RT}{\alpha_c F}\right)}\right] \tag{5.23}$$

m is the reaction order of the reactant. i_o *and* α_c are the exchange current density and cathodic transfer coefficient of the reaction respectively.[8] The value of both of these expressions is obtained experimentally. The expression in parenthesis is the Tafel slope for the reaction. η is the overpotential. i_k is the kinetic controlled current density. That is, it is the current density of the reaction in the absence of any transport losses. Combining Equations (5.19) with (5.22) gives

$$\frac{i}{i_k} = \left(1 - \frac{i}{i_{\text{lim}}}\right)^m \tag{5.24}$$

Chin points out that the reaction order of the reacting species can be obtained from the slope of $\ln(i)$ vs. $\ln\left(1 - \frac{i}{i_{\text{lim}}}\right)$. For a first order reaction, Equation (5.24) can be rewritten as

$$\frac{1}{i} = \frac{1}{i_k} + \frac{1}{b}\omega^{-1/2} \tag{5.25}$$

This equation shows a linear relationship between $1/i$ and $\omega^{1/2}$ in the mix kinetic and mass transfer regions. A graph of $1/i$ verses $\omega^{-1/2}$ at different overpotentials is known as the Koutecky-Levich plot. A straight line for this plot confirms a first order reaction for the reacting species at that overpotential. The intercept of the line is the inverse of the kinetic current at that overpotential. A plot of η verses $\ln(i_k)$ is known as the diffusion

[8] In the Bulter-Volmer equation (see Chapter 2), the symmetry factor β is in the place of the cathodic transfer coefficient of Equation (5.23). The difference between these two parameters should be made clear since they are often misinterpreted. As explained by Gileadi [86], the symmetry factor is defined for a single step reaction. It is related to the shape of the free-energy barrier and to the position of the activated complex along the reaction coordinate. Its value is between 0 and 1. To describe a multi-step reaction, β is replaced with the transfer coefficient. α_c and α_a are experimental parameters obtained from the current-potential relationship. The values can possibly be calculated by postulating a reaction mechanism for the multi-step reaction. Refer to Section 2.6.1 or reference [86] for further discussion.

corrected Tafel plot, and for a reaction with constant Tafel slope it yields a straight line with a slope of $-\frac{\alpha_c nF}{RT}$ and an intercept of $\ln(i_o)$.

5.2.4 Cyclic Voltammetry (CV) and Linear Sweep Voltammetry (LSV)

In order to investigate the kinetics of the electrode reaction, knowledge of the physical and chemical nature of the catalyst surface is needed. Cyclic voltammetry (CV) and linear sweep voltammetry (LSV) are common electrochemical techniques used to characterize the surface of an electrode. The techniques involve applying a linear potential sweep to the working electrode. The sweep rates typically range from 10 mV/s to about 1000 V/s with conventional electrodes and up to 10^6 V/s with ultra-microelectrodes (UME) [53]. In the case of CV, electrode starts at particular potential and is scanned anodically or cathodically to another potential. The potential is then scanned back, at the same scan rate, to its original potential. In the case of LSV, the electrode is first held at a particular potential for period of time and then the electrode is scanned anodically or cathodically to another potential.

In the experimental work of this dissertation, the CV and LSV techniques are used to measure and/or detect adsorbents on the electrodeposited Pt films surface. These adsorbents include reaction intermediates such as adsorbed hydrogen or hydroxyl atoms or impurities such as chloride ions. The techniques are not used in this work to obtain the kinetic parameters of the ORR. For complex reactions, such as the ORR, where the electrode also reacts with the species in the electrolyte, using CV and LSV are neither ideal nor simple techniques for the quantitative evaluation of kinetic parameters. These techniques are not ideal because it is often not possible to derive analytical expressions

describing current-potential relationship. The experimental behavior must be compared to the predictions from simulations. In the case of a multi-step reaction, these techniques are most useful in interpreting qualitative and semi-quantitative behavior [53].

Characteristics of Cyclic Voltammograms of Polycrystalline Pt:

A typical cyclic voltammogram of polycrystalline Pt in 0.5 M H_2SO_4 solution deairated with an inert gas is given in Figure 5-7 [57]. The anodic scan (increasing potential scan) results in the positive current and the cathodic scan (decreasing potential scan) results in the negative current. The voltammogram can be divided into three potential regions: (1) the hydrogen adsorption/desorption region (0.05 to 0.4 V vs. NHE), (2) double layer region (0.4 to 0.6 V vs. NHE) and (3) oxide formation/reduction region (0.6 to 1.2 V vs. NHE).

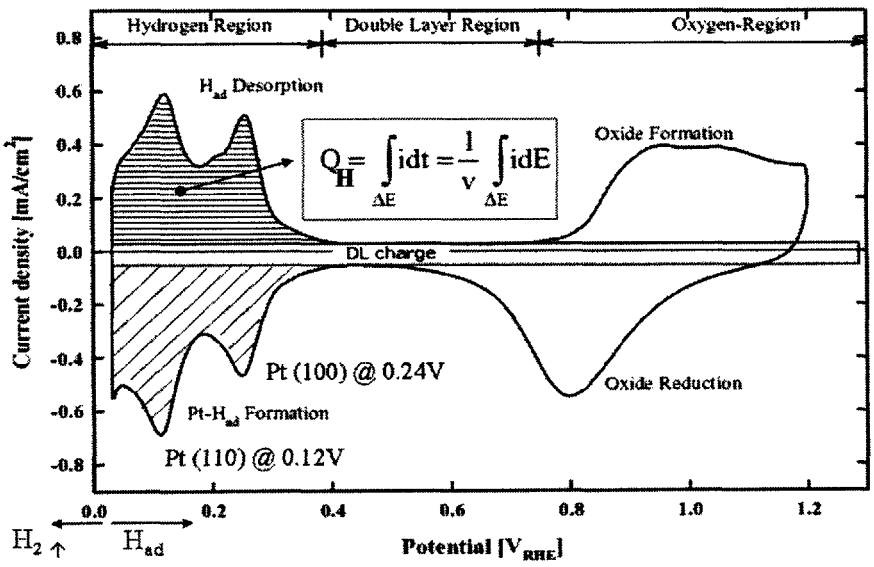

Figure 5-7: Cyclic voltammogram of polycrystalline Pt in 0.5 M H_2SO_4

The shaded portions of the voltammogram in the hydrogen adsorption/desorption region represents the total charge per geometric area associated with a monolayer coverage of the Pt with hydrogen atoms. Note that the integrated area does not include

the double layer charge of the region. Hydrogen atoms adsorb onto the surface Pt electrode by the following reaction:

$$H_3O^+ + e^- + Pt = PtH_{ad} + H_2O \tag{5.26}$$

At the typical scan rates of voltammetry, this reaction is assumed to be reversible. In the case of a reversible reaction, the fractional coverage, Θ, of the Pt surface with hydrogen atoms depends on the potential of the electrode and not on the scan rate. If one denotes the charge required to form a complete monolayer of hydrogen as Q_H, then the charge for a fractional coverage of the electrode is

$$Q_{H,\theta} = Q_H \Theta \tag{5.27}$$

Thus, the adsorption of hydrogen atoms yields a dependence of the charge on the potential. In electrochemistry, this is referred to as an adsorption pseudocapacitance, C_H:

$$C_H = Q_H \left(\frac{\partial \Theta}{\partial E} \right)_{T,P} \tag{5.28}$$

where E is the potential of the electrode. The current density measured in the hydrogen adsorption/desorption region, which is beyond the double layer charging current, is due to hydrogen adsorption pseudocapacitance. The current density is not constant because, unlike a pure capacitor, such as that associated with the double layer C_{dl}, C_H is strongly dependent on potential.

In this dissertation, the total charge for hydrogen desorption (refer to Figure 5-7) is used to determine the electrochemically active area of the Pt film. Using Q_H to determine the area of Pt is based on the assumption of one absorbed hydrogen atom per Pt surface atom. If one assumes that the atomic surface density of the Pt electrode is

roughly equal to the average atomic surface density of the low-index Pt single crystal planes (i.e. $2.04 \times 10^{-9} mol/cm^2$), then the reference charge for hydrogen atom monolayer on Pt is about 200 μC/cm^2_Pt [58]. In the literature 200, 210, and 220 μC/cm^2_Pt have been used as the reference charge. In this dissertation, 210 μC/cm^2_Pt will be used as the reference charge.[9] Thus, the specific area of a Pt film was calculated by applying the following equation:

$$SA = \frac{Q_H}{\left(210 \times 10^{-6}\right) Pt_L} \tag{5.29}$$

where Pt_L is the loading of the Pt film per geometric area.

In the hydrogen adsorption/desorption region, there are several peaks observed. The shape, number, and size of these peaks depend on the crystal faces of the exposed Pt, pretreatment of electrode, solution impurities, temperature, and supporting electrolyte [53]. The peaks at a potential of 0.12 V is a result of hydrogen adsorption/desorption on the Pt(110) low-index crystal face. The peak at a potential of 0.24 V is a result of hydrogen adsorption/desorption on the Pt(100) low-index crystal face.

In the double layer region illustrated in Figure 5-7, only the non-Faradaic current passes across the electrolyte-electrode interface. In the anodic sweep, this region extends from 0.4 V to about 0.8 V. For a constant scan rate, the current is constant in this region and the current is proportional to the scan rate. A current that changes in this region (adsorption pseudocapacitance) is usually an indication that impurities are present on the Pt electrode surface. This fact is discussed further below.

[9] The unit cm^2_Pt denotes real surface area of Pt.

In the oxide formation/reduction region, the state of the surface oxide has been extensively studied [59, 60, 61]. On the surface, the following reaction scheme was proposed by Conway *et al.* [62]:

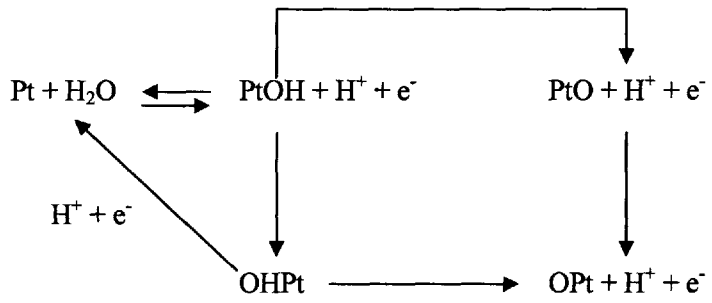

(5.30)

At potentials less than 1.0 V, OH atoms are reversibly adsorbed onto the Pt surface atoms. PtOH is known to suppress the kinetics of the ORR, but it does not affect the pathway of the reaction [5]. Some of the OH atoms can penetrate into the Pt lattice and become OHPt. OHPt is known as the place-exchange state of PtOH. The driving force for the place-exchange is an increase in the coordination of the OH ligands about the surface of Pt atoms [24]. During the cathodic scan, the reduction of OHPt is more difficult than PtOH because OH has passed through the Pt lattice. OHPt is the irreversible form of adsorbed hydroxyl atom. For this reason, its formation has historically been called "oxide" formation. Unlike PtOH, OHPt both suppresses the kinetics of the ORR and affects the pathway of the reaction. At potentials greater than 1.0 V, Pt surface atoms are irreversibly oxidized to PtO. This oxide both suppresses the kinetics of the ORR and alters the reaction pathway [5].

The Effects of Chloride Impurity on the Pt Cyclic Voltammogram:

In this work, cyclic voltammetry were used to test for impurities both in the electrolyte solution and on the surface of the electrode. Chloride ions are a possible

impurity in the solutions that were used. The saturated calomel reference electrode has KCl as the supporting electrolyte (see Section 5.3.2). Thus, the reference electrode is a possible source for this impurity. As explained in Section 5.2.3, a Luggin capillary is used to limit possible contamination of the working electrolyte solution. The Pt films are electrodeposited from $PtCl_6^{-2}$ anion. Thus, for every atom of Pt deposited, six chloride ions are released. Some of these chloride ions adsorb onto the surface deposited Pt film. If the electrode is not appropriately cleaned (see Section 5.3.1), the adsorbed chloride ions will remain on the surface of the Pt film. Chloride ions are known to irreversibly adsorb onto the surface of Pt. The chloride ions suppress the kinetics of the ORR and alter the cyclic voltammetry of the Pt [31]. For this reason, great care should be taken to eliminate chloride ions adsorbed on the surface of the Pt films and chloride ions in the electrolyte solutions used for voltammetry and the rotating disk electrode experiments.

Figure 5-8 shows the cyclic voltammograms of a Pt disk electrode (from Pine Instruments Company) in a solution 0.5 M H_2SO_4 and in a solution of 0.5 M H_2SO_4 + 10^{-5} M KCl. The former voltammogram is referred to as the pure voltammogram and the latter is referred to as the contaminated voltammogram in the figure. The potential was scanned at a rate of 50 mV/sec. The figure shows that this small concentration of chloride ions significantly alters the cyclic voltammogram of the Pt disk. The strong adsorption of the chloride ions causes the amount of oxide formation and reduction on the contaminated electrode to be less than that on the pure electrode. Also, the peak oxide reduction current of the contaminated voltammogram is slightly shifted to a lower potential compared to that of pure voltammogram. This observation indicates that the

chloride ions suppressed the PtOH reduction kinetics. The site blocking effect of the chloride ions also causes a reduction in the electrochemically active area.

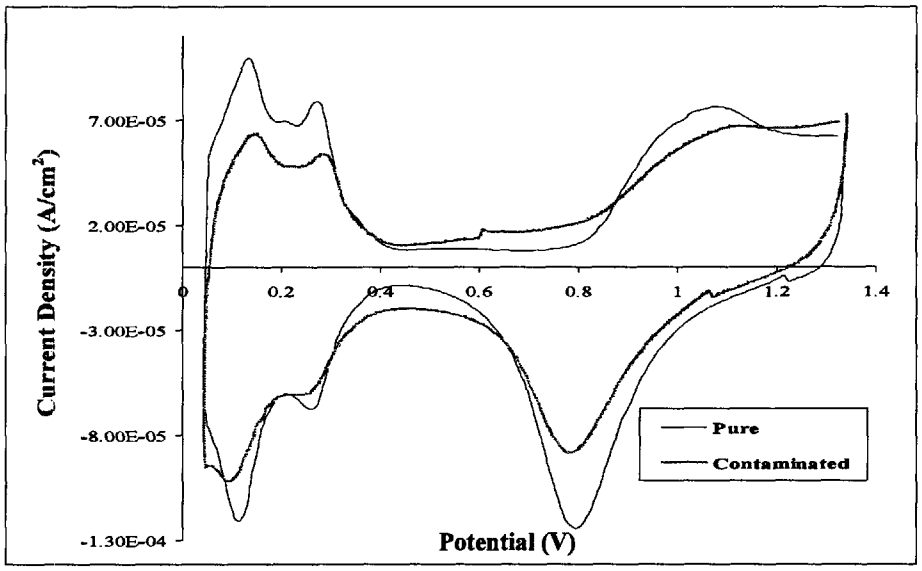

Figure 5-8: Cyclic voltammograms of polycrystalline Pt in pure 0.5 M H_2SO_4 and in 0.5 M H_2SO_4 + 10^{-5} M KCl, the CV in the KCL containing solution is referred to as the contaminated CV

The figure clearly shows that the hydrogen desorption charge is less for the contaminated voltammogram than for the pure voltammogram. This result indicates that a certain amount of the chloride atoms remain adsorbed on the Pt surface even at 0.05 V. Also, the hydrogen desorbtion peaks are shifted to more positive potential and the hydrogen adsorption peaks are shifted to a more negative potential. The shifting of these peaks is probably a result of the effects of chloride pseudocapacitance. The chloride atoms compete for adsorption sites with the hydrogen atoms. It may also indicate that the adsorbed chloride atoms suppressed the hydrogen atom adsorption and desorption reactions.

Another important feature of the contaminated voltammogram is the presence of an adsorption pseudocapacitance in the double layer region. This is clearly seen in the

double layer region of the anodic sweep. Stamenkovic *et al.* examined chloride adsorption on the Pt(111) crystal face and found that the ion continuously adsorbs on that surface for a potential region between 0.3 and 0.9 V [31]. Thus, the pseudocapacitance observed in the double layer region is believed to be a result of following reaction on the Pt(111) facets:

$$Pt + Cl^- \rightarrow Pt(Cl)_{ad} + e^- \tag{5.31}$$

It is believed that other impurities will produce similar adsorption effects on the Pt. Therefore, examining the cyclic voltammogram for pseudocapacitance in the double layer region is the most direct method for detecting impurities on the surface of the Pt electrode from voltammetry. Impurities in the bulk of the solution were detected by comparing the voltammograms of the electrode at 0 and 2000 rpm. The rotation of the electrode would increase the flux of impurities to the electrode and make them more detectible by voltammetry.

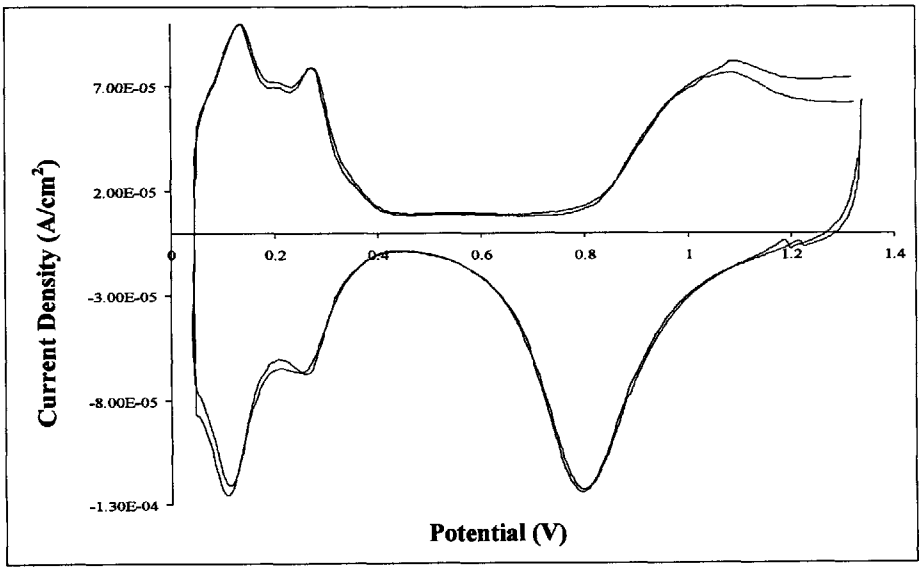

Figure 5-9: Cyclic voltammograms of polycrystalline Pt in pure 0.5 M H_2SO_4 at a rotation rate of 0 and 2000 rpm, the figure shows negligible difference between the two voltammograms

Figure 5-9 is a voltammogram of the Pt disk electrode at 0 and 2000 rpm in a pure 0.5 M H_2SO_4 solution. There are only slight differences in the voltammograms, which indicates a pure solution.

5.3 Experimental Procedure and Setup

5.3.1 Cleaning of Glassware and Electrode

Glassware:

The glassware was cleaned by first washing it with micro-90 and then rinsing it out with distilled water. The glassware was filled with a solution of 1:1 sulfuric and nitric acid. This solution remained within the glassware for at least 24 hours. Finally, the glassware was rinsed again with distilled water. The final rinsing was done with ultra-pure water from VWR.

Glassy Carbon Electrode with Pt Film After Electrodeposition:

After electrodeposition, chloride atoms are adsorbed on the deposited Pt films. Adsorbed chloride atoms are known to alter the voltammogram of Pt and suppress the ORR kinetics. In order to remove the chloride atoms from the Pt film, the working electrode was placed within a three electrode cell. The cell is a standard voltammetry cell from Pine Instrument Company. It was filled with a fresh supply of 0.5 M sulfuric acid. The sulfuric acid solution was prepared from ultra pure water and 98% H_2SO_4 ACS Reagent grade from VWR. A Pt wire was used as the counter electrode and a saturated calomel electrode with Luggin capillary was used as the reference electrode.

The sulfuric acid solution was deaerated with nitrogen (Grade-5 from BOC Gases) for 15 minutes. The electrode was then held at 0 V for 1 minute to desorb the chloride atoms from the Pt film. While at 0 V, the electrode was rotated at 3500 rpm to transport the desorb chloride atoms away from the working electrode. The electrode was quickly removed from the cell, rinsed with ultra pure water, and soaked in ultra pure water until it was used.

Glassy Carbon Electrode with Pt film After RDE Experiments:

After the RDE experiments with a working electrode consisting of a Pt film deposited on glassy carbon, the electrode was removed from the Teflon holder (see Section 5.3.2). The Pt film was removed from the glassy carbon electrode by polishing the electrode with a 600 grit sand paper (from Buehler) followed by 10 minutes of ultrasonication in ultra pure water. The glassy carbon electrode was then placed back in the Teflon holder. The glassy carbon electrode was polished to a mirror finish by polishing it with a 1 μm Al_2O_3 solution on a nylon polishing cloth (from Buehler), rinsing it in distilled water, and then ultrasonicating it for 10 minutes in ultra pure water. After the sonication, the electrode was rinsed with ultra pure water. This procedure was repeated with a 0.3 μm Al_2O_3 polishing solution and then with a 0.05 μm Al_2O_3 polishing solution. Before each deposition experiment, several voltammograms were recorded in a nitrogen purged 0.5 M H_2SO_4 solution both to ensure that the glassy carbon surface was free of Pt and to control the reproducibility of the surface area of the electrode.

5.3.2 Electrodes and Instruments

Working Electrode:

The working electrode was either a 5 mm glassy carbon electrode disk or a 0.5 mm Pt disk. Both electrodes were purchased from the Pine Instrument Company. The electrodes, when in use, were held in a Teflon holder. Figure 5-10 is a picture of the of the glassy carbon electrode imbedded in the E4 Series ChangDisk RDE tip with AFE3M stainless steel shaft (both from the Pine Instrument Company). The electrode disk was press fitted into the holder using the interchange toolkit provided by the Pine Instrument Company. The working electrode disks are removable. The same Teflon disk holder can be used repeatedly with different disk samples. In this work, three glassy carbon electrodes and one Pt disk electrode were used. When fitting or removing a disk, great care was taken not to deform the Teflon holder. Any leakage of the electrolyte solution between the electrode material and the insulator would prevent the electrode from obtaining accurate RDE data.

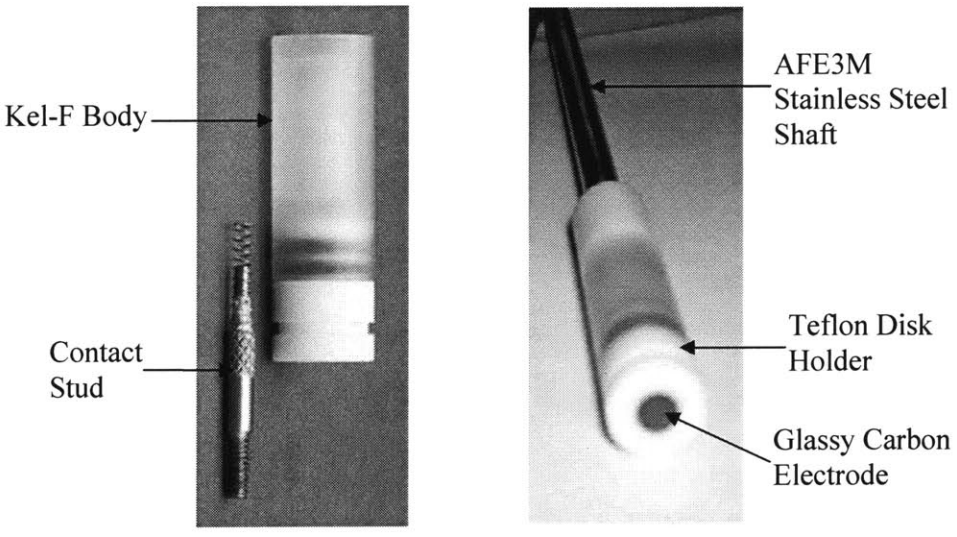

Figure 5-10: Glassy carbon working electrode in E4 Series ChangDisk RDE tip from the Pine Instrument Company

The Teflon holder is pressed into the Kel-F body shown in Figure 5-10. The Kel-F body screws onto the shaft. An electrical connection is made between the shaft and the electrode disk with a contact stud also shown in the picture. This electrode setup has a maximum operating temperature of 30°C. Temperatures in excess of 30°C can possibly deform the Teflon holder and lead to leakage of the electrolyte between the holder and disk.[10]

Reference Electrode:

A saturated calomel reference electrode (SCE) is used in all electrochemical experiments of this work. Two SCE were purchased from the Pine Instrument Company. The SCE consists of a mercury tip covered by a layer of mercury(II) chloride. A saturated solution of potassium chloride surrounds the electrode. A porous frit (salt bridge) is used for the junction between the reference electrode solution and the solution of the cell. The reversible redox reaction that occurs at the electrode is

$$Hg_2Cl_2 + 2e^- = 2Hg + 2Cl^- \qquad (5.32)$$

The standard potential difference between the SCE and the NHE is 0.241 V. This is slightly lower than the values of 0.263 and 0.271 V measured for the two SCE electrodes used in this work. The difference between the measured values and the theoretical value may partly be due to the junction potential of the reference electrode and the Luggin capillary. The Luggin capillaries used in this work were purchased from Princeton Applied Research.

[10] The temperature limit of 30C was recommended by a Pine Instrument technician. He stated that higher temperatures may deform the Teflon holder. This is the primary reason why temperatures above room temperature were not used in this work.

Instruments:

The 1287A Potentiostat from Solartron was used to control the potential or current of the working electrode in this work. The CorrWare program was used to control the potentiostat from a desktop computer. The CorrView program was used to visualize the data, perform the current integration of the voltammograms, and calculate Tafel slopes. The Modulated Speed Rotator (MSR) from the Pine Instrument Company was used to rotate the working electrode. All SEM images were taken with the Joel 6320FV field-emission high-resolution microscope found in the MIT Center for Materials Science and Engineering.

5.3.3 Electrodeposition of Pt films

A three electrode cell was used to electrodeposit Pt onto the glassy carbon electrode. The cell is a standard voltammetry cell from Pine Instrument Company. A Pt wire was used as the counter electrode, and a saturated calomel electrode with Luggin capillary was used as the reference electrode. The deposition solution consisted of 5 mM of K_2PtCl_6 (99.99+% from Sigma-Aldrich) and 1 M H_2SO_4 prepared from ultra pure water and 98% H_2SO_4 ACS Reagent grade from VWR. The sulfuric acid acted as the supporting electrolyte.[11] Before deposition, the solution was deaerated by bubbling nitrogen (Grade-5 BOC Gases) into it for 15 minutes using a purge tube (model G0094 from Princeton Applied Research). After 15 minutes, the purge tube was held above the

[11] A supporting electrolyte is added to the deposition solution in order to minimize the migration flux of the chloroplatinate ion in the bulk of the solution and in the diffusion layer. That is, the $PtCl_6^{2-}$ ion is transported to the electrode only by convection and diffusion. The supporting electrolyte is also used to minimize the potential drop within the diffusion layer. A supporting electrolyte can affect the deposition kinetics. In this case, sulfuric acid has been shown to slightly enhance the deposition kinetics by decreasing the thickness of outer Hemholtz plane (OHP) [48]. A thinner OHP leads to a higher electric field for a given potential drop across the OHP. It is the electric field that drives the reaction. Thus, the supporting electrolyte effectively increases the rate constant for the reduction reaction.

solution in order to maintain a positive pressure within the deposition cell. The solution was unstirred during deposition. All depositions were carried out at room temperature.

Two types of potential modulation were used to deposit Pt onto the glassy carbon electrode, the single potential step (SPS) technique and the double potential step (DPS) technique. In the SPS technique the working electrode was first held at a potential of 0.8 V for 30 seconds. This potential is only slightly lower than the OCP. The electrode potential was then stepped to 0.1 V and held at this potential until the desired amount of Pt was deposited on the glassy carbon. In the DPS technique, the working electrode was first held at 0.8 V for 30 seconds. The electrode was stepped from 0.8 V to -0.2 V for 1 second and then step to 0.3 V. The electrode potential was held at 0.3 V until the desired amount of Pt was deposited on the glassy carbon.

In both the SPS and the DPS techniques, all the Pt was assumed to deposit during the potential hold at 0.1 and 0.3 V respectively. The amount of Pt deposited, i.e. the loading Pt_L, was estimated from the integrated charge measured on the current versus time transient response, Q_{ED}, at these potentials. Thus, assuming 100% Faradaic efficiency, the Pt_L is given by

$$Pt_L = \left(\frac{Q_{ED}}{nF}\right) mw_{Pt} = 195.078\left(\frac{Q_{ED}}{385940}\right) \tag{5.33}$$

where mw_{Pt} is the molecular weight of Pt. After deposition, the electrode was removed from the deposition solution, thoroughly rinsed with ultra pure water, and then underwent the chloride cleaning procedure described in Section 5.3.1.

5.3.4 Voltammetry

The electrodeposited Pt films were characterized using cyclic and linear sweep voltammetry. All voltammetry was conducted using the same three electrode setup described above. The voltammetry solution was 0.5 M H_2SO_4 prepared from ultra pure water and 99.999% sulfuric acid from Sigma-Aldrich. Before the voltammetry, the solution was deaerated with nitrogen for 15 minutes. During the voltammetry the purge tube was placed above the solution.

In the case of cyclic voltammetry, the potential was scanned between 0.05 and 1.3 V five or six times. The scan rate was 50 mV/sec. The final potential scan was recorded as the voltammogram for the Pt film. In the case of linear sweep voltammetry, the electrode potential was held at 0.9 V for 1 minute. The potential was scanned from 0.9 to 0.4 V at scan rate of 50 mV/sec.

5.3.5 Rotating Disk Electrode (RDE)

A three electrode cell was used for the RDE experiments in this work. The cell is a RDE cell from Pine Instrument Company. A Pt wire was used as the counter electrode, and a saturated calomel electrode with Luggin capillary was used as the reference electrode. Contamination is a serious concern for RDE experiments. For this reason, the Pt wire, Luggin capillary, and purge tube used in the RDE setup were not used in other experiments. The RDE solution was 0.5 M H_2SO_4 prepared from ultra pure water and 99.999% sulfuric acid from Sigma-Aldrich. Before a RDE experiment, the solution was saturated with oxygen (Grade-5 from BOC gases) for 15 minutes. During the RDE experiment the purge tube was placed above the solution.

An RDE experiment involved measuring the potentiodynamic scan of the working at the following angular rates of rotation: 500, 750, 1000, 2000, 2500, 3500 rpm. To insure a clean and reproducible surface, electrodes were subjected to potential holds at 0.93, 0.05, and 0.22 V for 30 seconds each prior to polarization measurements. At each rotation speed, the potential was scanned anodically from 0.22 to 0.99 V at a scan rate of 10 mV/sec. After the RDE experiments, the electrode was removed from the solution, rinsed with ultra pure water, and soaked in ultra pure water until it was used again. The RDE experiments were conducted again on the same electrode at a later time. For each Pt loading, four or five RDE experiments were conducted over one or two day period.

5.4 Results and Discussion

5.4.1 Electrodeposition of Pt Films onto a Glassy Carbon Substrate

Single Potential Step (SPS) Deposition:

A typical current versus time transient response recorded for a single potential step from the 0.8 V to 0.1 V is shown in Figure 5-11. The transient response consists of three periods. At times less then 3.5 seconds, the current rapidly decreases from a peak current. In the succeeding part of the transient, the current density increases with time and goes through a maximum value i_m at the time t_m. After the maximum current, the current gradually decreases and then reaches a steady state value at times greater than 50 seconds.

The charge of electricity that passed through the working electrode during the initial portion of the transient is about 2,600 $\mu C/cm^2$. This charge is far in excess of the

charge associated with the charging/discharging of the double layer of the electrode. For this reason, it is believed that Pt nuclei formation and growth occurs during this very short period. The charge is roughly equivalent to that required for the deposition of 2 monolayers of Pt from Pt(IV) ions. Lin-Cai *et al.* observed a similar initial response when they applied a single potential step to deposit Pt on glassy carbon from a K_2PtCl_4 solution [52].

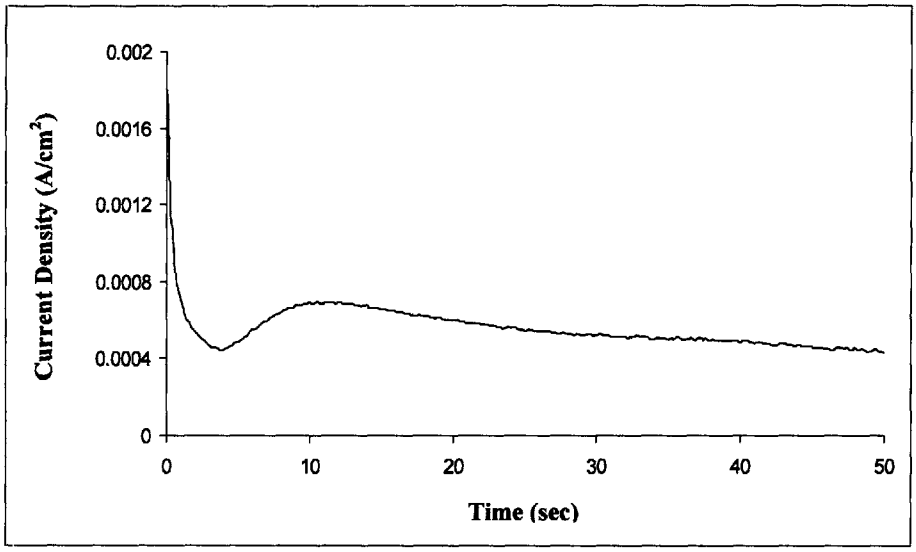

Figure 5-11: Current vs. time transient response for Pt film electrodeposited by a single potential step from the 0.8 V to 0.1 V

At times greater than 3.5 seconds, the transient response has a shape associated with hemispherical growth of metal nuclei under diffusion control. According the theory of Scharifker and Hills (S-H theory), the rise in current is due the increase in nucleus size and/or an increase in the number of nuclei [63]. The growth of each nucleus is limited by spherical diffusion around it. In the time period near the maximum current, the spherical diffusion zones overlap and mass transfer becomes linear in the case of a planar substrate. This change in diffusion regime leads to a decrease of the current with time according to the Cottrell equation (Equation (5.42)).

The S-H theory considers two limiting conditions involving the rate of nucleation of the metal nuclei: instantaneous nucleation or progressive nucleation. Instantaneous nucleation corresponds to the growth of nuclei on a number of sites that were all activated at the same time. Progressive nucleation corresponds to growth of nuclei on sites that are activated during the course of electrodeposition [63]. Assuming a fixed number of nucleation sites with similar activities, the density of the growing nuclei, N, should saturate exponentially with time according to

$$N(t) = N_o\left[1 - \exp(-At)\right] \tag{5.34}$$

where N_o is the density of available nucleation sites, and A is the nucleation rate constant. Both N_o and A increase with an increase in the electrodeposition overpotential. The nucleation rate constant is given by

$$A = K_1 \exp\left[\frac{-bs\varepsilon^2}{zek_BT\eta}\right] \tag{5.35}$$

where K_1 is the rate constant, b is the geometric factor that depends on the shape of the 2D cluster, s is the area occupied by one atom on the surface of the nucleus, ε is the edge energy, k_B is the Boltzmann constant, z is the electronic charge of the ion, and e is the charge of the electron [64]. Equation (5.35) shows that the rate of nucleation exponentially increases with an increase in the overpotential. In the case of instantaneous nucleation $(At >> 1)$, Equation (5.34) reduces to $N(t) = N_o$, while in the case of progressive nucleation $(At << 1)$, the equation reduces to $N(t) = AN_o t$.

The S-H theory models for instantaneous and progressive nucleation are given by Equations (5.36) and (5.37), respectively.

$$\frac{i^2}{i_m^2} = \frac{1.9542}{t/t_m}\left\{1-\exp\left[-1.2564\left(\frac{t}{t_m}\right)\right]\right\}^2 \tag{5.36}$$

$$\frac{i^2}{i_m^2} = \frac{1.2254}{t/t_m}\left\{1-\exp\left[-2.3367\left(\frac{t}{t_m}\right)^2\right]\right\}^2 \tag{5.37}$$

References [65] and [66] describe some of the controversies and approximations involved in the S-H theory. Despite the limitations of the model, it does provide a straightforward and widely used method for the analysis of the nucleation mode and nucleation density. It is used in this section to characterize the nucleation mode of the Pt deposit and to determine the diffusion coefficient of the chloroplatinate ion.

Figure 5-12 compares the plot, in terms of the normalized variables $(i/i_m)^2$ and t/t_m, of the experimental data given in Figure 5-11 to the theoretical transients given by Equations (5.36) and (5.37). At times less than t_m, the experimental transient response coincides with the theoretical response for progressive nucleation. This result is different from the result reported by Plyasova *et al.* [51]. They too electrodeposited Pt onto glassy carbon at 0.1 V using the single potential step technique. In their experiments, Pt was electrodeposited from a 10 mM H_2PtCl_6 + 10 mM HCL solution. They found that the Pt deposition followed the instantaneous nucleation mode. The difference in the results of Plyasova *et al.* work and that of this work may be due to the different deposition solution used. The concentration of the chloroplatinate ion is known to affect the nucleation mode [48]. Instantaneous nucleation is typically favored at higher concentrations of the chloroplatinate ion. For example, Gloaguen *et al.* observed for Pt electrodeposition in a dilute solution, i.e. 2 mM of H_2PtCl_6, the transient response showed a good correlation

with the theoretical curve for progressive nucleation [67]. However, for a more concentrated solution of 10 mM of H_2PtCl_6, the transient response coincided with the theoretical curve for instantaneous nucleation.

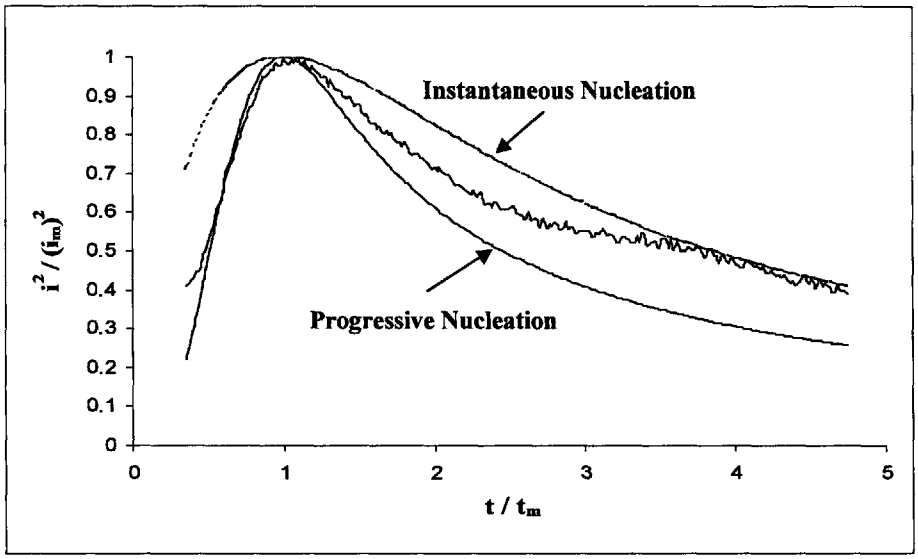

Figure 5-12: $(i/i_m)^2$ versus t/t_m analysis of transient response shown in Figure 5-11. $i_m = 6.96 \times 10^{-4}$ A/cm^2 and $t_m = 10.54$ sec

Another possible explanation for the observed difference in nucleation modes is that the surface properties of the glassy carbon used by Plyasova *et al.* were different from those of the glassy carbon disk used in this work. The condition of the glassy carbon can affect the Pt deposit. For example, Shimazu *et al.* heat treated their glassy carbon at 750 °C. They measured higher specific areas for Pt films deposited on the heat treated glassy carbon than those deposited on the untreated glassy carbon. They surmised that the increase in specific area was due to the heat treated glassy carbon's higher activity for Pt deposition. The difference in nucleation modes between Plyasova *et al.* deposits and those of this work may be due to our use of a less active glassy carbon substrate.

Regardless of the reason, the fact that progressive nucleation occurs at 0.1 V on the glassy carbon of this work, suggests 0.1 V may not be the potential that results in a SPS deposited film of maximum specific area. Generally, specific area increases when the nucleation mode shifts from progressive nucleation to instantaneous nucleation [67].

The SEM image given in Figure 5-13 shows Pt clusters that vary in size from 50 to 200 nm. This observation supports progressive nucleation as the nucleation mode for the deposition of Pt on the glassy carbon.

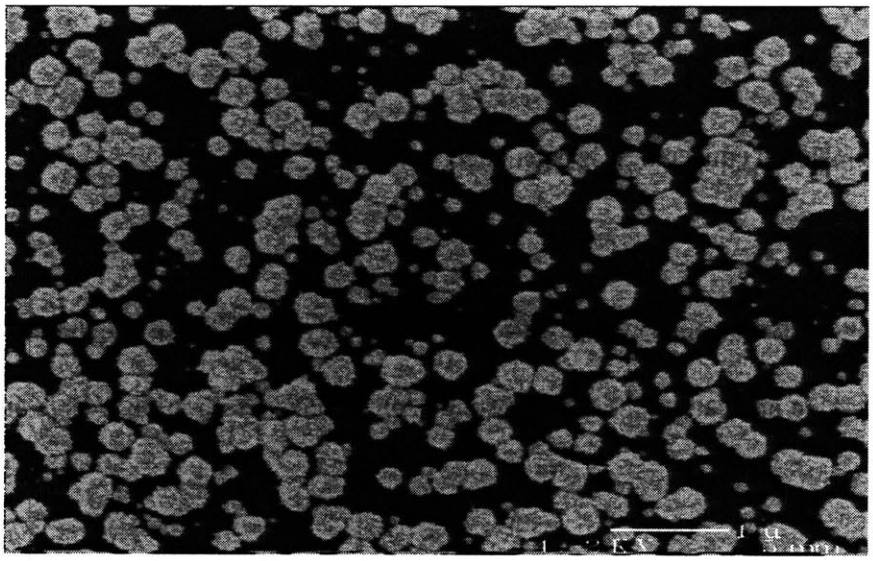

Figure 5-13: SEM image of Pt particles produced during the SPS deposition

When progressive nucleation occurs, the diffusion coefficient, D, of the reducing ion can be estimated according to the formula

$$i_m^2 t_m = 0.2598 D\left(nFC_o\right)^2 \tag{5.38}$$

where C_o is the bulk concentration of the reacting ion, and n is the number of electrons transferred during the electrodeposition reaction. For the experimental transient given in Figure 5-11, $i_m = 6.96\times10^{-4}\, A/cm^2$ and $t_m = 10.54\,\text{sec}$. The diffusion coefficient of the chloroplatinate ion calculated from Equation (5.38) is $D = 5.2\times10^{-6}\, cm^2/\text{s}$. This value

is close to the previously reported diffusion coefficient of $D = 4.5 \times 10^{-6}\, cm^2/\mathrm{s}$, which was obtained for the same deposition solution as the one used in this work [49]. The fairly accurate prediction of the diffusion coefficient by the S-H theory and the good fit of the progressive nucleation equation with the data for $t < t_m$ support the use of the S-H theory in modeling the deposition process. The model captures some aspects of chloroplatinate ion transport and Pt film growth.

The product AN_o is calculated from the formula

$$i_m = 0.4615 nFC_o D^{3/4} \left(\frac{4}{3} k_m A N_o \right)^{1/2} \tag{5.39}$$

k_m is the material constant. It is calculated from

$$k_m = \left(8\pi C_o mw / \rho \right)^{1/2} \tag{5.40}$$

where mw is the molecular weight and ρ is the density of the depositing metal. Finally, for progressive nucleation, the density of nucleation sites at saturation, N_s, is given by

$$N_s = \left(\frac{3AN_o}{8k_m D} \right)^{1/2} \tag{5.41}$$

For the transient response given in Figure 5-11, the density of nucleation sites at saturation is calculated to be $N_s = 5.5 \times 10^5\, cm^{-2}$. This value is four orders of magnitude lower than the $1.5 \times 10^9\, cm^{-2}$ particle density counted from the SEM image given in Figure 5-13. The counting was done by assuming each particle resulted from the growth of a single nucleus. Gloaguen *et al.* observed a similar discrepancy between the nucleation density calculated from S-H theory and the value they counted from a SEM image [67]. In their case, they electrodeposited Pt onto highly oriented pyrolytic graphite

at 0.1 V. The nucleation densities they calculated were of the order of 10^6 cm^{-2}, while the particles densities counted from the SEM images were of the order of 10^{10} cm^2. They attributed the discrepancy to the significant mobility of Pt particles on the substrate at room temperature. They surmised that during the initial time period of deposition, $t < 0.3\,\text{sec}$, large amounts of very small Pt particles $(\approx 1\,nm)$ are formed on the surface of the graphite. These small particles are very mobile and assemble into larger clusters by collision. At $t > 3\,\text{sec}$, the rapid growth of a small number of these clusters results in a transient response that can be adequately described by the S-H theory. Thus, at times less than t_m, the hemispherical diffusion zone surrounds the Pt clusters not individual Pt particles.

Similar to the observations made by Gloaguen *et al.*, Figure 5-13 shows small particles near agglomerations of large particles. These small particles are not connected to the agglomerates. Also, the particles appear to have a height much smaller than their diameter, which suggest a growth that is different from hemispherical. Based on these observations, it is believed that the phenomenon described by Gloaguen *et al.*, related to the mobility of Pt cluster on the substrate, is the reason for the discrepancy in the calculated and counted nucleation density for Pt films deposited by the SPS technique in this work.

Figure 5-12 shows that at later times the experimental current decreases more slowly than the theoretical model. At the deposition potential of 0.1 V, there is no side reaction that could produce the observed deviation from the progressive nucleation model. This behavior has been observed by Floate *et al.* during the electrodeposition of cobalt onto graphite [68] and by Plyasova *et al.* [51] during the electrodeposition of Pt onto

glassy carbon by the single potential step technique. Floate *et al.* attributed the higher current to enhanced diffusion and rapid replacement of the reducing ion through hemispherical diffusion to growth centers. Plyasova *et al.* attributed the transient response to the interplay between the primary nucleation on the support surface and the secondary nucleation on the surface of the electrodeposited Pt nanoparticles. Secondary nucleation causes the surface area of the Pt deposit to increase more rapidly than what would be expected for semi-hemispherical particle growth. This, in turn, leads to a higher current. They defined the onset of secondary nucleation as the moment in the normalized transient response when the experimental current exceeds the value predicted by the S-H theory.

Figure 5-14 is an SEM image of the same deposit shown in Figure 5-13 but at higher magnification.

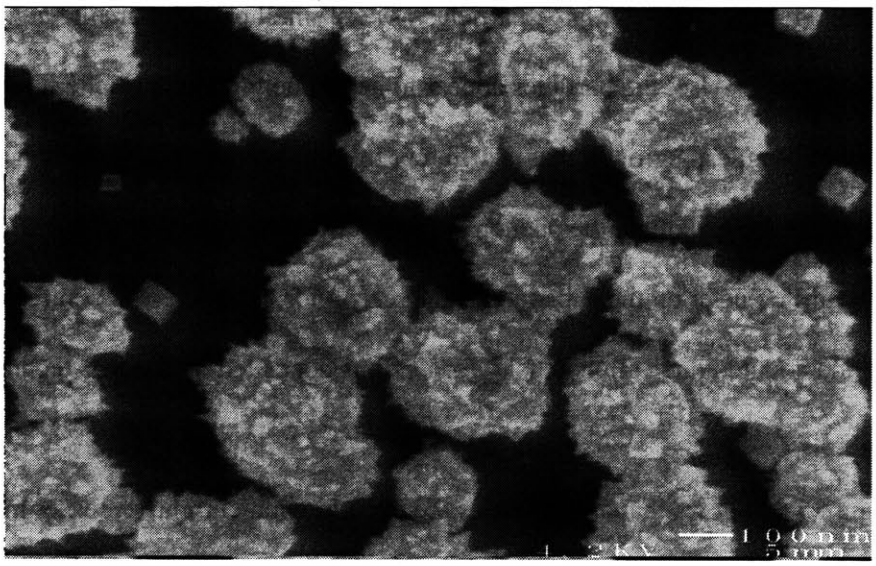

Figure 5-14: SEM image of Pt particles produced during the SPS deposition, higher magnification than Figure 5-13

The SEM image clearly shows the presence of small crystallites formed as a result of secondary nucleation. These crystallites are numerous and appear to be less than 20 nm

in size. Based on this observation, the large particles ($\approx 200\,\text{nm}$) are believed to be agglomerates of these Pt crystallites. This assertion is supported by the high specific area measured for the electrodeposited Pt films of this work (see below). Similar to the observation made by Plyasova *et al.*, the higher current at times greater than t_m compared to the current predicted by the S-H theory is due to the larger Pt area produced as a result of secondary nucleation.

The SEM image of Figure 5-14 shows that the individual crystallites grow as cubes. However, the crystallites that make up the agglomerates appear to grow as lamellas. Similar observations were made by Plyasova *et al.* for much thicker Pt films deposited on glassy carbon [51]. The reason for the preferential growth in the $\langle 200 \rangle$ direction is not fully understood. This fact should be studied further in light of the ORR sensitivity to surface crystallographic orientation.

Double Potential Step (DPS) Deposition:

A typical current versus time transient response recorded during the DPS deposition is shown in Figure 5-15. The transient response was recorded after the current was stepped from the potential of -0.2 V to a constant potential of 0.3 V. Unlike the SPS transient response, there is no observed maximum in current at times beyond the double layer charging period. This observation suggests that the DPS deposition produced a higher density of nucleation sites (or Pt clusters) than what was produced during the SPS deposition. According to the S-H theory, as the density of nucleation sites increases the time of the current maximum, t_m, decreases. At sufficiently large densities, t_m is expected to be on the scale of 100 ms or less. Thus, for the DPS deposition, t_m is within the time period of the double layer charging due to the high density of nucleation sites.

The current maximum associated with the transition from hemispherical diffusion to planar diffusion cannot be resolved from the transient response.

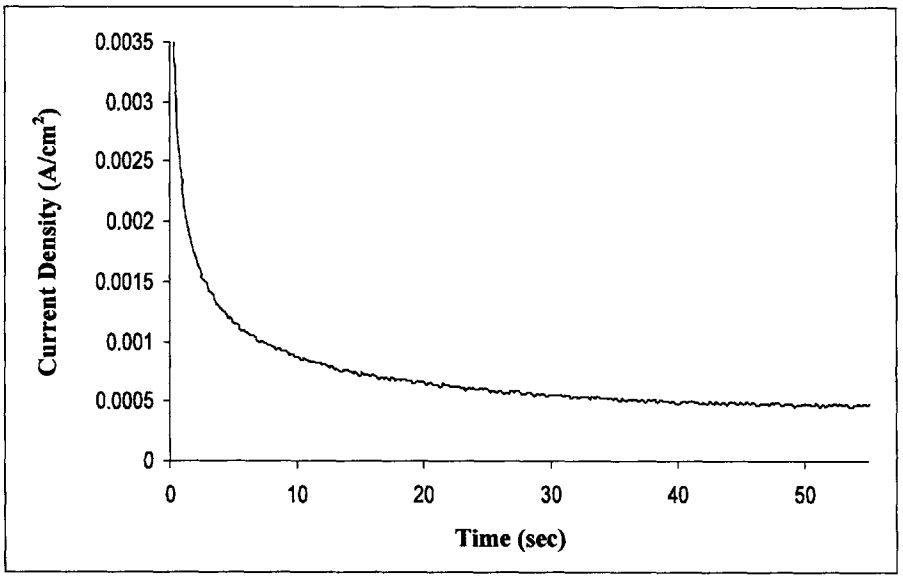

Figure 5-15: Current vs. time transient response recorded after the second step of the DPS deposition

Figure 5-16 is a plot a current versus time$^{-0.5}$ for the transient response given Figure 5-15.

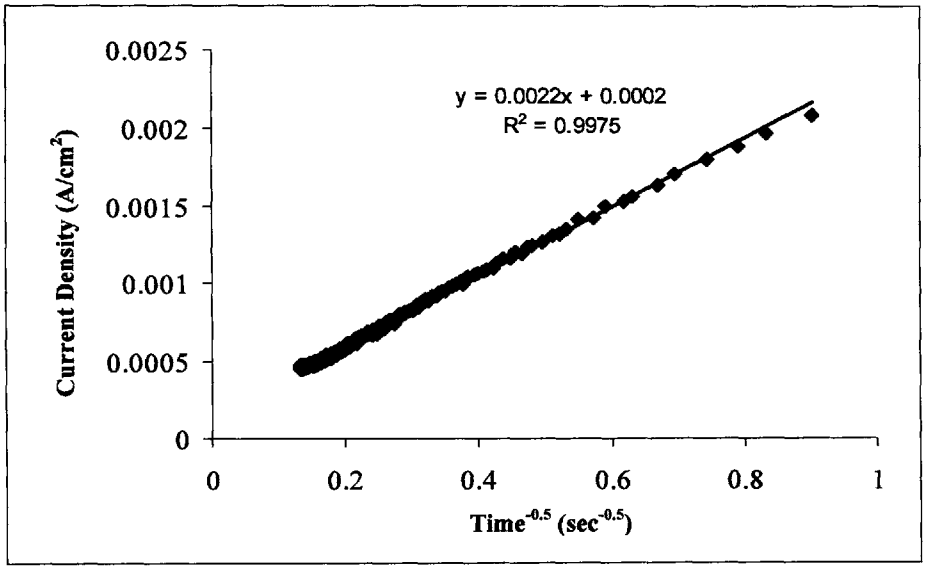

Figure 5-16: Plot of current vs. time$^{-0.5}$ for the transient response given in Figure 5-15.

The plot is linear which suggest that the current evolved under planar diffusion control. The Cottrell equation,

$$i = \left(\frac{nFD^{1/2}C_o}{\pi^{1/2}} \right) t^{-1/2} \tag{5.42}$$

models this diffusion phenomenon. A least square linear regression was applied to the data. The square of the correlation coefficient is close to unity which indicates that the data fits the Cottrell equation well. The slope of the linear regression can be used to calculate the diffusion coefficient of chloroplatinate ion. The calculated diffusion coefficient is $D = 4.1 \times 10^{-6} cm^2 / s$. This value is only 9 % lower than the value previously reported in literature for the same solution [49].

The Cottrell equation predicts that that deposition current should go to zero at long times. However, the intercept of the line in Figure 5-16 has a value of 0.2 mA/cm^2. For Pt films with deposition times longer than 75 seconds, the current reached a steady state value about 0.5 mA/cm^2 or in some cases it slightly increased with time. In this region of the transient response, $t_m > 75 \text{sec}$, the Cottrell equation is no longer valid. The transient response deviates from Cottrell behavior for two reasons. First, secondary nucleation creates Pt films with small crystallites. The higher specific area of the film and the enhanced hemispherical diffusion near growing crystallites can lead to a current density that is constant or even increases with time in the case of dendrite growth. Second, convective effects become important at long times because the buildup of density gradients and stray vibrations cause disruption of the diffusion layer. The diffusion layer can transform from that of semi-infinite diffusion to a diffusion layer resulting from natural convection [53].

Figure 5-17 is a SEM image of a Pt film produced by DPS deposition. The size of the Pt agglomerates is about the same, which suggests instantaneous nucleation and growth. Assuming that each agglomerate was produced from a single nucleus, the SEM image gives a nucleation density of about 10^{10} cm^{-2}. Shimazu *et al.* used the DPS technique to deposit Pt films onto glassy carbon substrate [42]. They counted a nucleation density of $4 \times 10^{10} cm^{-2}$. The nucleation density obtained in this work is similar to the values reported in the literature.

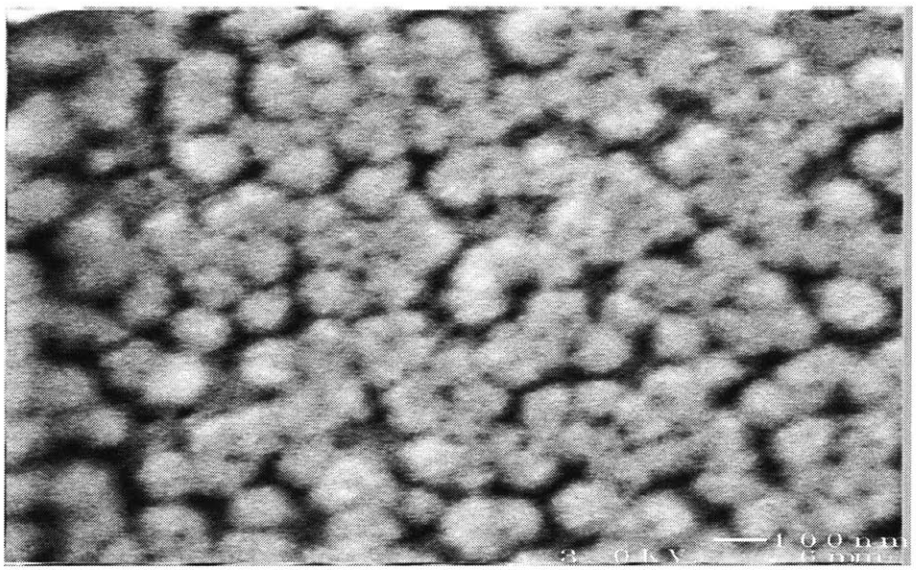

Figure 5-17: SEM image of Pt film produced from the DPS deposition

It is believed that all the nuclei were formed during the 1 second potential hold at -0.2 V. Duarte *et al.* [43] electrodeposited Pt on glassy carbon using the DPS technique. They varied the duration of the first potential step at $-0.259V$ from 0.2 to 5 seconds. They found that the specific area of the Pt films increased with an increase in the duration of the first step.[12] In this work, the duration was kept to 1 second in order to minimize

[12] The data of Duarte *et al.* should be viewed with some skepticism. For a potential hold at -0.259 V for more than 1 second, a significant amount of Pt is expected to be deposited. However, Daurte *et al.* make no mention of including this Pt mass in their calculations of the specific area of the Pt films.

the amount of Pt deposited during first step since this mass of Pt cannot be calculated from Equation (5.33). This equation is invalid since Pt electrodeposition was not the only reaction contributing to the current. When the potential was stepped from 0.8V to -0.2 V for 1 sec, both double layer charging and side reactions such as hydrogen evolution contributed significantly to the total charge passed during the step. In fact, when the duration of the first step was extended beyond 2 seconds, hydrogen gas bubbles were clearly visible on the surface of the electrode. Figure 5-18 contains the cyclic voltammograms of a glassy carbon electrode freshly polished with no Pt and a glassy carbon electrode after a potential step from 0.8 V to -0.2 V for 1 second in the deposition solution. The latter is referred to as the glassy carbon with a nucleation layer.

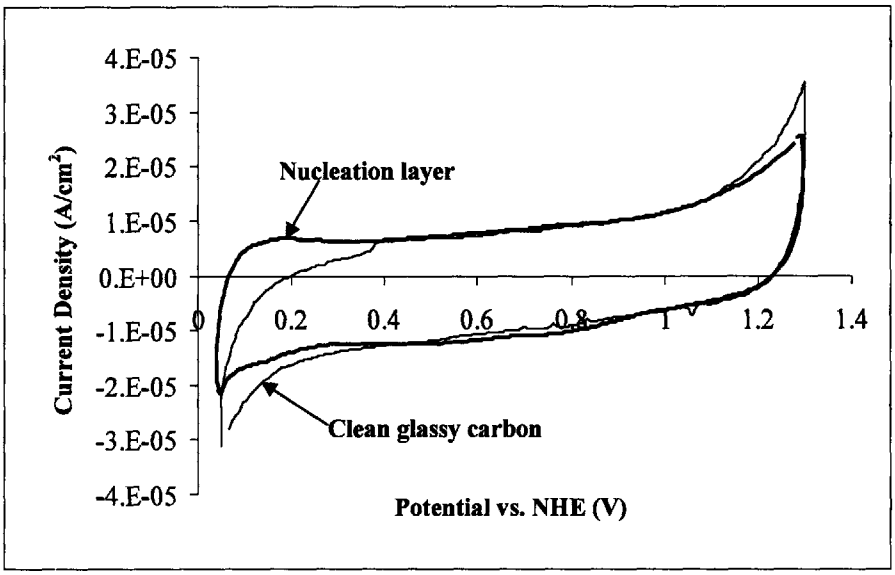

Figure 5-18: Cyclic voltammograms of glassy carbon surface freshly polished with no Pt (Titled: Clean glassy carbon) and the glassy carbon electrode after a potential hold at -0.2 V for 1 second in the deposition solution (Titled: Nucleation layer)

The characteristic peaks associated with polycrystalline Pt are not present in either of the cyclic voltammograms. The voltammograms deviate significantly from each other only in the hydrogen adsorption/desorption region (0.4 to 0.05 V). This difference is most

likely due to the presence of small Pt particles on the surface of the glassy carbon. These, Pt particles did not produce a hydrogen desorption charge that is resolvable from the cyclic voltammogram. In other words, the current magnitude in the hydrogen adsorption/desorption region is not greater than the current magnitude in the double layer region. Lin-Cai *et al.* electrodeposited Pt onto glassy carbon using the SPS technique [52]. They observed no hydrogen adsorption/desorption peaks on glassy carbon until a Pt loading of 0.5 $\mu g/cm^2$ or greater was deposited on the carbon surface. This result has been interpreted in terms of the interaction between Pt particles and the glassy carbon electrode. Since the nucleation layers of this work did not appear to produce any hydrogen desorption charge, the amount of Pt deposited during the first potential step of the DPS deposition is assumed to be less than 0.5 $\mu g/cm^2$. This small amount of Pt was not included in the total loading of the Pt films formed by DPS deposition.

5.4.2 Cyclic Voltammograms of DPS Deposited Pt Films

Before producing the cyclic voltammograms, the chloride atoms were desorbed from the Pt surface by conducting the electrode cleaning procedure described in Section 5.3.1. Figure 5-19 shows cyclic voltammograms of DPS deposited Pt films of different loadings. As expected, the adsorption, desorption, and double layer currents all increased with an increase in the Pt loading. The peaks associated with hydrogen atom adsorption/desorption on the Pt(110) and Pt(100) facets are not as prominent on the voltammograms of the electrodeposited Pt films as those peaks are observed to be on the Pt disk voltammogram (see Figure 5-8). This observation may be an indication that chloride atoms were not fully desorbed from the surface Pt films. The chloride contaminated voltammogram in Figure 5-8 shows that the peaks are suppressed in a

solution containing 10^{-5} M of KCl. This observation is consistent with the fact that chloride ions were found to adsorb on the surface of the Pt(100) single-crystal face at a higher coverage than they are on the Pt(111) single-crystal face in the hydrogen adsorption/desorption region [31].

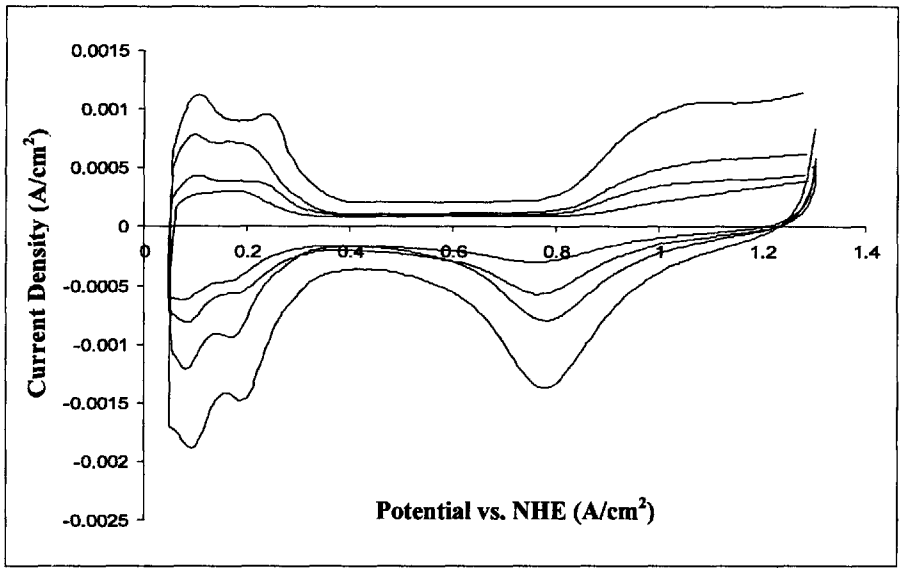

Figure 5-19: Cyclic voltammograms for different loadings of DPS electrodeposited Pt films. The loadings are 9.89, 19.2, 39.97, and 60.54 μg/cm². A larger loading produced larger hydrogen adsorption/desorption charge.

The chloride contaminated voltammogram in Figure 5-8 also shows a pseudocapacitance in the double layer region of the voltammogram. As previously mentioned, this pseudocapacitance is due the adsorption of chloride ions on the Pt(111) facets. The voltammograms in Figure 5-19 do not show a pseudocapacitance in the double layer potential region. The pseudocapacitance would indicate the adsorption of chloride ions that were desorbed during the cathodic sweep. Since this behavior is absent, chloride poisoning is not believed to be the reason for observed differences in the voltammograms of the electrodeposited Pt films compared to that of polycrystalline Pt.

The voltammograms in Figure 5-19 show that ratio of the charge associated with hydrogen adsorption/desorption on the Pt(110) and Pt(100) facets to the total hydrogen adsorption/desorption charge is less than that of polycrystalline Pt. The voltammograms also show that this ratio increases as the Pt loading increases. A likely explanation for the first observation is that the electrodeposited Pt films have a lower number density of the Pt(110) and Pt(100) facets than the number density on polycrystalline Pt. The second observation suggests that the number density of these facets increases as the Pt loading increases.

Differences in the crystallography of electrodeposited Pt films and polycrystalline Pt have been observed by several researchers using XRD patterns [8, 51, 69, 70]. The Pt(111) plane is the predominantly exposed crystal plane for polycrystalline Pt disk. It is also found to be the predominantly exposed crystal plane for electrodeposited Pt films [8, 51, 69]. Cui *et al.* electrodeposited Pt on carbon nanofibers and found that the Pt(111) plane was 44% of the total exposed crystal planes [70]. Electrodeposited Pt films are observed to have a higher number density of the high-Miller-index facets, such as (210), (211), (311) and (331), compared to the number density for polycrystalline Pt [69]. Voltammograms of high-Miller-index single-crystals have peaks in the range of 0.1 to 0.3 V. However, the areas under these peaks are smaller than the area under the hydrogen adsorption/desorption peaks of the Pt(110) and Pt(100) single-crystals [71, 72]. Also, a voltammogram of the Pt(111) single-crystal has only a small peak around 0.4 V [32, 71]. For these reasons, the voltammogram of a electrodeposited film, where the film has higher surface ratios of the Pt(111) facets and high-Miller-index facets compared to these surface ratios on polycrystalline Pt, will have less prominent hydrogen

adsorption/desorption peaks. On the other hand, the increase in the charge of the hydrogen desorption peaks with in increase in the Pt loading, observed in Figure 5-19, could indicate an increase in the surface ratio of Pt (110) and Pt(100) as the loading increasing.

Another major difference between the crystallography of electrodeposited Pt and that of polycrystalline Pt is the value of the lattice parameter. The lattice parameter of electrodeposited Pt films is smaller than that of bulk polycrystalline Pt [51]. The decrease in lattice parameters of electrodeposited metals as compared to bulk metals is probably the common feature of electrodeposited metals [73]. Plyasova *et al.* surmised that the lattice compression of electrodeposited Pt is not due to any equilibrium size effects. The crystallite size of the Pt deposits (10 to 20 nm) is beyond the size for which these effects are expected. The lattice compression is, instead, due the high density of intergrain boundaries. Intergrain boundaries are the planar defects that lie in between the Pt crystallites that originate from the recurring secondary nucleation events. When these crystallites grow in close proximity to each other, they exert a mutual strain. Lattice compression is known to affect both the adsorption and electrocatalytic properties of the Pt catalyst. The implications of smaller lattice parameters for the DPS deposited films are discussed further in Section 5.4.2.

Cyclic voltammetry, at best, gives some qualitative information concerning the crystallography of the electrodeposited film. Unfortunately, this information is ambiguous. In future work in this area, cyclic voltammetry should be combined with XRD to obtain better qualitative and quantitative information on the crystallography of the electrodeposited Pt films and how it changes with Pt loading.

5.4.3 Specific Area of Electrodeposited Pt Films

As previously discussed in Section 5.2.2, Pt electrodeposition is believed to result in films with specific areas much higher than films deposited by other techniques such as physical vapor deposition. The reason the electrodeposited Pt films have higher specific areas is because electrodeposition produces films that are made up of crystallites that are 20 nm or less in size. These small crystallites result from the dominance of secondary nucleation events over the simple growth of primary nucleation particles.

Figure 5-20 contains the plots of the specific area versus Pt loading for the DPS and SPS deposited films. It also contains a plot of the specific area versus Pt loading for the sputter deposited films of reference [1].

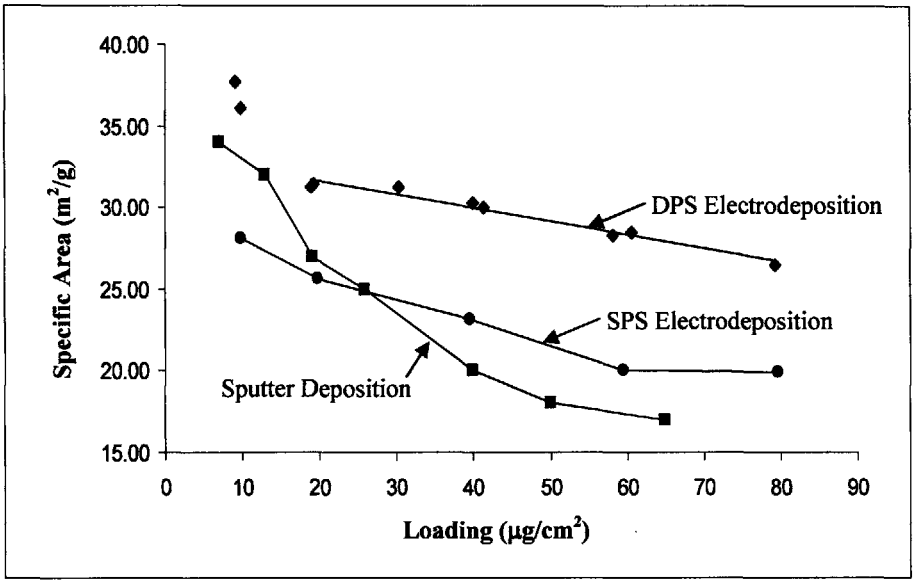

Figure 5-20: Plots of the specific area vs. Pt loading for films electrodeposited by the DPS and SPS deposition techniques. Included is the specific area vs. Pt loading plot for sputter deposited films of references [1].

The figure shows that DPS deposition produces films with specific areas that are greater than those of sputter deposited films for all Pt loadings. At the high Pt loading of 80

$\mu g/cm^2$, the specific area of the DPS deposited film is about 26.5 m^2/g. This value is about 66 % greater than the specific area of a sputtered film of the same loading.

The specific areas of SPS deposited films are less than those of the DPS deposited films. These results are not surprising. During DPS deposition, the number of Pt growth centers was 10 times the number during SPS deposition. A higher number of growth centers results in higher concentrations of the chloroplatinate ions in the depletion zones at a given current density. Higher chloroplatinate concentrations promote secondary nucleation events that produce a large number of small Pt crystallites. Comparing the SEM images of Figure 5-13 and Figure 5-17, one observes that both the agglomerates and the Pt crystallites are smaller for the DPS deposited film than the SPS deposited film. Plyasova *et al.* used XRD to measure the Pt(111) crystallites size for Pt films deposited on glassy carbon [51]. They found that the crystallite size was lower at higher potentials (or lower overpotentials). They attributed this result to the fact that lower potentials promote both hydrogen atom adsorption and lower concentrations of chloroplatinate ions in the depletion zones. Both these factors inhibit secondary nucleation. The DPS method allows for the majority of the Pt to be deposited at potentials where secondary nucleation is optimal (300 – 400 mV).

At low loading $\left(Pt_L < 30\mu g/cm^2\right)$, the sputter deposited films have specific areas that are higher than those of the SPS deposited films. This result is probably due to the higher density of primary nucleation sites for the sputter deposited film than that for films electrodeposited by the SPS technique. The higher the number of primary nucleation sites, the smaller the size and higher the specific area of the primary particles. At higher loadings, the specific areas of the sputter deposited films are now less than

those of the SPS deposited films. The SPS deposited films have higher specific areas at high loadings because these films grow by increasing both the number of crystallites and the size of the crystallites. In the case of the sputter deposited films, film growth occurs only by increasing the size of the primary crystallites. A simple model is developed below to explore this point further.

Deposited Pt Film Area Model:

The loading, Pt_L, and the surface area, A_{Pt}, of Pt per unit area of the glassy carbon substrate can be expressed by the following equations assuming a cubic structure with an average particle size of r:

$$Pt_L = \rho_{Pt} r^3 N_p \tag{5.43}$$

$$A_{Pt} = 5r^2 N_p \tag{5.44}$$

where N_p and ρ_{Pt} are the particle density and the density of Pt $\left(\rho_{Pt} = 21.4\, g/cm^3\right)$, respectively. Pt_L in Equation (5.43) can be nondimensionalized $\left(Pt_L^*\right)$ by dividing the equation by Pt_L^o. Pt_L^o is interpreted as the minimum Pt loading for which a hydrogen desorption charge can be resolved from the voltammogram. Based on the work by Lin-Cai *et al* (refer to the discussion above), Pt_L^o is assumed to have a value of $0.5\,\mu g/cm^2$. Equation (5.43) can be rewritten as

$$Pt_L^* - 1 = \frac{\rho_{Pt} r^3 N_p}{Pt_L^o} \tag{5.45}$$

In Equation (5.45) Pt_L^* is replaced with $Pt_L^* - 1$ because A_{Pt} is assumed to be equal to zero when $Pt_L^* = 1$. For the deposition condition when N_p is assumed to be constant and r is assumed to vary, Equations (5.44) and (5.45) can be combined to give

$$A_{Pt} = 5\rho_{Pt}^{-2/3}\left(N_p^o\right)^{1/3}\left(Pt_L^o\right)^{2/3}\left(Pt_L^* - 1\right)^{2/3} \tag{5.46}$$

where N_p^o is the initial particle density of the Pt loading. For the deposition condition when N_p is variable and r is constant, Equations (5.44) and (5.45) can be combined to give

$$A_{Pt} = 5\rho_{Pt}^{-2/3}\left(N_p^o\right)^{1/3}\left(Pt_L^o\right)^{2/3}\left(Pt_L^* - 1\right) \tag{5.47}$$

Based on this simple model for the Pt deposition, the surface area of Pt is related to the Pt loading by the general expression

$$A_{Pt} = \alpha\left(Pt_L^* - 1\right)^{\kappa} \tag{5.48}$$

where α is proportional to $\left(N_p^o\right)^{1/3}$ and κ is a value that indicates how the Pt film is growing. κ is related to the rate of growth of crystallite size and particle density by

$$\kappa = \frac{2\dfrac{d\ln r^*}{dPt_L^*} + \dfrac{d\ln N_P^*}{dPt_L^*}}{3\dfrac{d\ln r^*}{dPt_L^*} + \dfrac{d\ln N_P^*}{dPt_L^*}} \tag{5.49}$$

where $N_p^* = N_p / N_p^o$ and $r^* = r/r^o$. r^o is the initial crystallite size, and its value is related to N_p^o and Pt_L^o by

$$r^o = \left(\frac{Pt_L^o}{\rho_{Pt} N_p^o}\right)^{1/3} \tag{5.50}$$

$\kappa = 1$ if the Pt film is growing only by increasing the number particle of constant size, and $\kappa = 2/3$ when the Pt film is growing only by increasing the size of the crystallites. Generally, these values represent the maximum and minimum value for κ. Since a high A_{Pt} is desired, a κ value of 1 is desired. As Equation (5.49) shows, $\kappa = 3/4$ if

$$\frac{d\ln r^*}{dPt_L^*} = \frac{d\ln N_P^*}{dPt_L^*} \tag{5.51}$$

Thus, for $\kappa < 3/4$, the growth of the deposit occurs predominantly by growing existing crystallites. For $\kappa > 3/4$, the growth of the deposit occurs predominantly by increasing the number of crystallites.

The data in Figure 5-20 can be plotted in the form A_{Pt} versus $Pt_L^* - 1$ as shown in Figure 5-21.

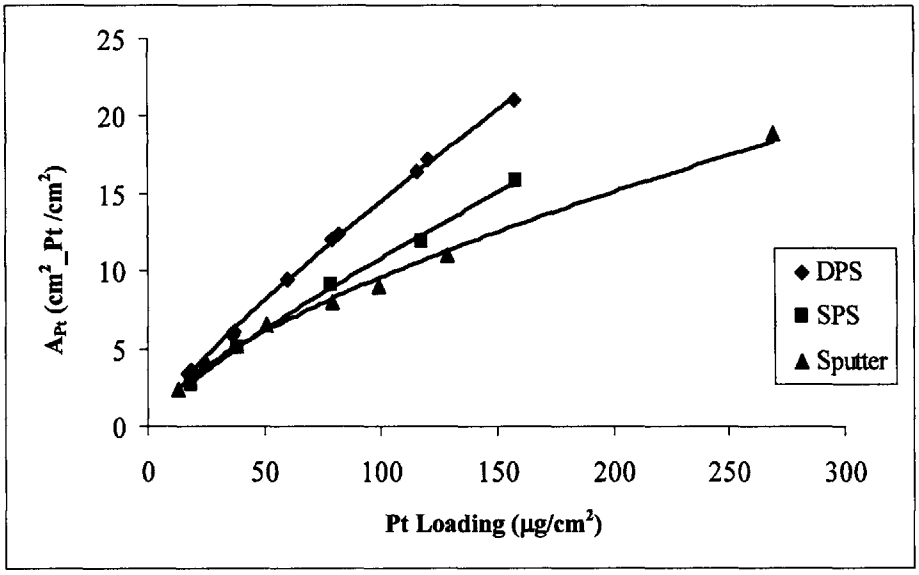

Figure 5-21: Plots of A_{Pt} vs. $Pt_L^* - 1$ for Pt films deposited by the DPS and SPS deposition techniques of this work and the sputter deposited films of reference [1].

Type of Pt Deposition	κ	α	R^2
DPS	0.8431	0.2988	0.9978
SPS	0.8071	0.2635	0.9985
Sputter	0.654	0.4725	0.9938

Table 5-2: Parameters of the deposition model

With κ and α as the fitting parameters, the data in Figure 5-21 are fitted to the model. The square of the correlation coefficients listed in Table 5-2 indicate that the data for all three types of deposition techniques fit the model quite well.[13]

As expected, the value of κ is highest for DPS deposited Pt films and is lowest for the sputter deposited Pt films. The κ values for films deposited by both the DPS and SPS techniques are greater than 0.75. These results indicate that, for both types of electrodeposition techniques, Pt film growth occurs principally by increasing the number of crystallites. These crystallites originate from secondary nucleation events on existing particles. Shimazu *et al.* electrodeposited Pt films using the DPS technique [42]. Their films had a value of $\kappa \approx 1$. Similar to Shimazu *et al.* deposits, the growth of the electrodeposited Pt films of this work is dominated by secondary nucleation events.

The α value for the DPS deposited films is only 13% greater than the value for the SPS deposited films. This result is not consistent with fact that DPS deposited films were counted, from the SEM images, to have a nucleation density 10 times greater than that of the SPS deposited films. Based on the previously stated proportionality, $\alpha \propto \left(N_p^o\right)^{1/3}$, the α value for the DPS films should be about 2.15 times greater than that of the SPS films. This discrepancy between the predicted values and the values that fit the data may be due to the limitations of this very simple model. It may also be related to the somewhat arbitrary value given for Pt_L^o. There is no reason to assume that the Pt_L^o for the DPS deposited films should be equal to the Pt_L^o for the SPS deposited films.

---

[13] Replacing Pt_L^* with $Pt_L^* - 1$ in Equation (5.45) improved the ability of the data to fit the model.

The κ value for sputter deposited film is approximately equal to the value expected for films that grow only by increasing crystallite size. Secondary nucleation does not occur during sputter deposition. The α value for sputter deposited Pt films is significantly larger than that of the electrodeposited films. Since $\alpha \propto \left(N_p^o\right)^{1/3}$, this result suggests that sputter deposition results in a higher density of primary nucleation sites than the DPS technique. At low loadings, a high primary nucleation density results in films with high specific areas. At higher loadings, it is the frequency of secondary nucleation events that mostly affects the specific area of the films. Based on these observations, a proposed deposition technique may involve first sputter depositing Pt as a thin film $\left(Pt_{L,sputter} < 20\mu g/cm^2\right)$ on the carbon surface. The sputter deposition is followed by electrodeposition of Pt to the desired loading. This deposition procedure, which uses a physical vapor deposited Pt seed layer, may produce Pt films with higher specific areas than films deposited by the DPS technique. This conjecture is explored in the work discussed in Chapter 6.

5.4.4 Oxygen Reduction Reaction on the DPS Deposited Pt Films

Figure 5-22 shows the potentiodynamic profiles for oxygen reduction at different rotation rates on the 39.97 μg/cm^2 Pt film electrodeposited by the DPS technique. All Pt loadings produced similar potentiodynamic profiles. The curves in Figure 5-22 show the characteristic behaviors that have been reported previously for polycrystalline Pt.

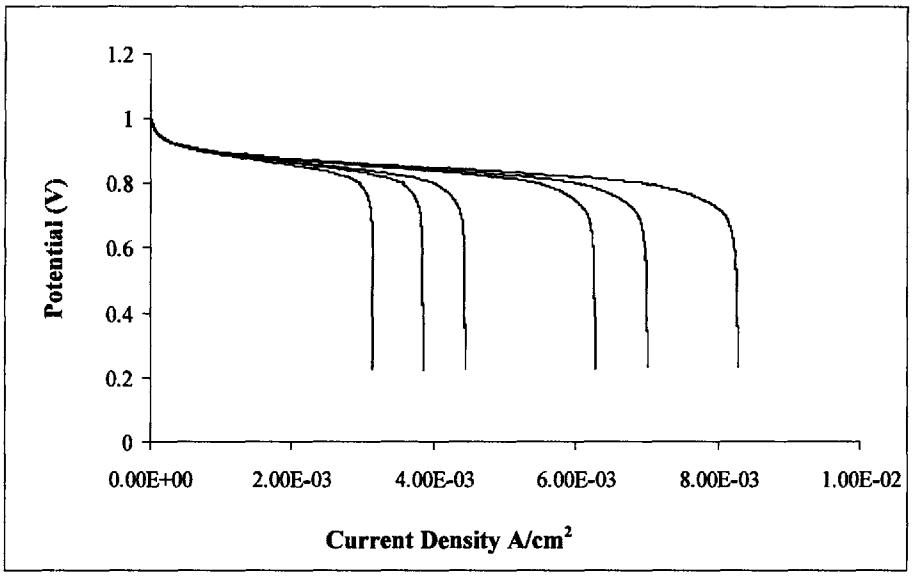

Figure 5-22: Potentiodynamic curves for the 39.97 μg/cm² Pt film deposited by the DPS deposition technique. The potentiodynamic scans were taken during electrode rotation at 500, 750, 1000, 2000, 2500, and 3500 rpm. The limiting current increases with an increase in the rpm.

Each curve has a well define limiting current below 0.5 V. The limiting currents remain constant even within the hydrogen adsorption/desorption potential region.

In similar potentiodynamic profiles of the Pt(111) and Pt(100) single-crystals, the limiting current, at a given rotation, decreased in value at potentials less than 0.3 V. RRDE experiments indicated that this drop in limiting current is related to the formation of hydrogen peroxide [5, 24, 32]. The presence of adsorbed hydrogen atoms on the electrode surface prevents the breaking of the O-O bond. Consequently, only two electrons are exchanged in the reduction of the oxygen molecules to peroxide. As the reduction reaction shifts from a predominately 4 electron transfer reaction to a 2 electron transfer reaction, the limiting current value decreases. In the case of the Pt(111) single-crystal, at 0 V the limiting current is half the current value expected for the four electron reaction, which indicates that all the reacting oxygen is reduced to peroxide [32].

Potentiodynamic profiles of polycrystalline Pt and dispersed Pt particles do not show this reduction in the limiting current even though the Pt(111) facets account for a major portion of the active surface of these catalyst. The lack of significant peroxide formation on these catalysts is attributed to the presence of the Pt(110) facets, higher-Miller index facets, and surface defects, all of which are highly active towards peroxide reduction [32]. Thus, in both these types of catalyst, any peroxide that is produced on one site of the catalyst quickly diffuses to a peroxide active sight where it is reduced to water. This process occurs at a much faster rate than the diffusion of peroxide to the bulk of the solution. The electrodeposited Pt films have both a high density of defects and crystal facets that are capable of readily reducing any peroxide formed on the Pt(111) facets. Therefore, the ORR remains mostly a 4 electron transfer reaction even at potentials well within the hydrogen adsorption/desorption region.

As expected, Figure 5-22 shows that the limiting current increases with an increase in rotation rate. Figure 5-23 is a Levich plot of the potentiodynamic scans shown in Figure 5-22. The Levich plot shows that the limiting current is proportional to the square root of the rotation and that the limiting current goes to zero, within experimental error, when the rotation goes to zero. These results are consistent with the Levich equation's predictions for reactant transport to a rotating disk (see Equation (5.18)). Using the value for the slope of the curve in Figure 5-23, $b = 4.317 \times 10^{-4}$ A/cm^{2}sec$^{0.5}$, and taking the oxygen diffusion coefficient to be $D = 1.8 \times 10^{-5}\, cm^2/\text{sec}$, the oxygen concentration to be $C_b = 1.15 \times 10^{-6}\, mol/cm^3$ and the electrolyte kinematic viscosity to be $\nu = 0.01\, cm^2/\text{sec}$. Equation (5.20) gives an electron transfer number of $n = 4.24$. Values for $n > 4$ have been reported previously when the

rotating disk had a rough surface [74]. It was believed that the rough surface of the disk led to a slight reduction of the hydrodynamic boundary layer below the value predicted by the Levich model. At the rotation rates used in this work, the boundary layer thickness is predicted to be on the scale of 10 μm [54]. The thickness of the Pt films is no greater than 100 nm. Since the deposited films are about two orders of magnitude smaller than the boundary layer, it is unlikely that they affected the boundary layer.

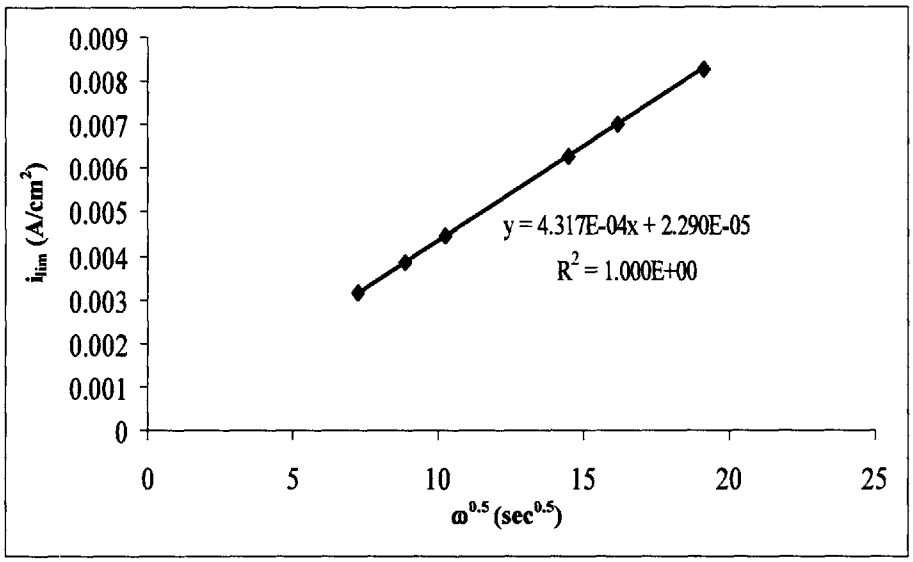

Figure 5-23: Levich plot of the potentiodynamic scans shown in Figure 5-22

The SEM image of Figure 5-17 shows that the Pt films consist of hemispherical agglomerates. Hemispherical diffusion around these agglomerates may explain the slightly enhance transport of oxygen beyond what is predicted by planer diffusion across a boundary layer.

All deposited films tested had a $n > 4$ (see Table 5-3). In contrast, the polished Pt disk tested in this work had a $n = 3.87$. Since the same procedure was used to calculate n for the Pt disk and the deposited films, the Pt disk result suggests that the high values

of n calculated for the deposited films were not due to experimental error or the use of incorrect values for the diffusion-solubility product and electrolyte viscosity.

Some of the data given in Figure 5-23 were plotted in the Koutechy-Levich plot shown in Figure 5-24.

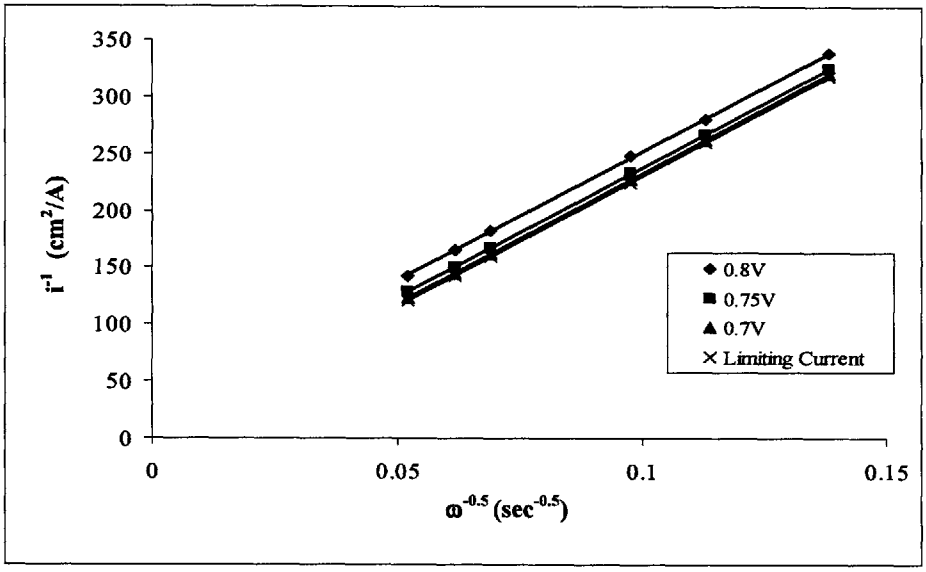

Figure 5-24: Koutechy-Levich plots of some of the data from the potentiodynamic scans shown in Figure 5-22

All potential values produced linear plots that are parallel to each other. These results indicate that the reaction is first order with respect to the concentration of molecular oxygen. In most electrolytes, the ORR on Pt is observed to be first order with respect to the concentration of oxygen regardless of the Pt crystallography [5].[14] There are examples when the Koutechy-Levich plots have been reported to deviate from a line even though the ORR is first order with respect to oxygen [75, 76, 77]. In those cases, the non-linearity of the curves was a result of the reaction occurring on a partially active rotating disk. The transport phenomenon was complicated by the fact that reactants near

[14] Trifluoromethane sulfonic acid was measured to have a reaction order with respect to oxygen of about 0.5 [84, 85]. Chang postulated that this reaction order is due to the oxygen bond disassociation reaction being the rate determining step [84].

the inactive parts of the electrode were transported to the active parts either by convection, bulk diffusion, or surface diffusion. Under these conditions, the Levich model is no longer valid.

In typical Koutecky-Levich plots, the intercept of the limiting current line is zero [53]. This occurs because the kinetic current has increased to a value where its inverse is essentially zero compared to the inverse of the limiting current (see Equation (5.25)). However, the intercept is equal to 0.8 cm^2/A for the limiting current line in Figure 5-24. This result is consistent with the previously mentioned fact that the kinetic current for the ORR does not increase indefinitely with an increase in overpotential. In fact, a limiting kinetic current, $i_{k,\lim}$, is measurable from the RDE data. For the electrodeposited films of this work, the limiting kinetic current multiplied by the Pt film's roughness factor, A_{Pt}, is of the order of 1 A/cm^2. Schmidt *et al.*, using the thin-film RDE technique, measured this parameter to be 0.040 A/cm^2 for a Pt loading of 28 $\mu g/cm^2$ of Pt/C [54]. Table 5-3 lists the electron transfer number and the parameter $\left(i_{k,\lim} \cdot A_{Pt}\right)$ for the Pt disk and electrodeposited Pt films. Note that the Pt loading 0 $\mu g/cm^2$ is used to denote Pt disk in Table 5-3 and in all other tables and figures in this chapter.

The intercepts of the Koutecky-Levich plots were used to produce the diffusion-corrected Tafel plots shown in Figure 5-25. The figure consists of a Tafel plot for the ORR on the clean 39.97 $\mu g/cm^2$ Pt film and that for the ORR on the same film before it underwent the chloride cleaning procedure. The Tafel plot of the clean film has two Tafel regions. At potentials greater than 0.80 V, the Tafel slope is about 58 mV/decade. At potentials between 0.8 and 0.65 V, the Tafel slope is about 120 mV/decade.

Pt Loading ($\mu g/cm^2$)	n	$i_{k,lim} \cdot A_{Pt} \approx$ (A/cm^2)
0	3.87	—
9.89	4.18	—
19.2	4.22	0.81
30.36	4.06	1.42
39.97	4.24	1.25
60.54	4.27	0.998

Table 5-3: Electron transfer number, n, and $i_{k,lim} \cdot A_{Pt}$ for the Pt disk (0 $\mu g/cm^2$) and electrodeposited Pt films

These results are comparable to previously reported Tafel slopes for polycrystalline Pt in dilute sulfuric acid [3].

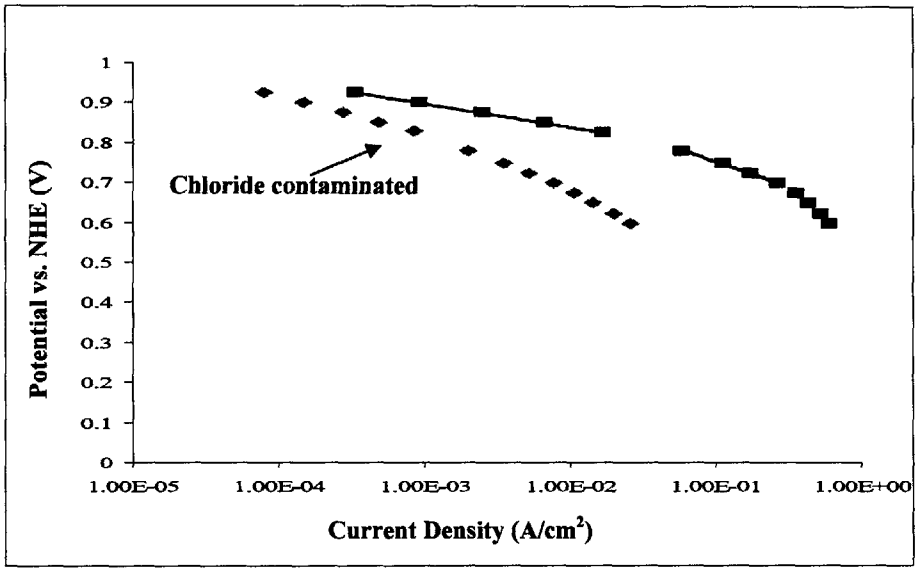

Figure 5-25: Diffusion-corrected Tafel slope of 39.97 $\mu g/cm^2$ Pt film with and without adsorbed chloride atoms

A Tafel slope of 120 mV/decade typically indicates that the first electron transfer reaction is the rate determining step. The halving of the Tafel slope at low overpotentials has been observed repeatedly for both polycrystalline Pt and Pt/C. As was discussed in detail

in Section 5.2.1, this change in the Tafel slope is due to the transition of the oxygen adsorption isotherm from a Langmuir isotherm to a Temkin isotherm.

Table 5-4 list the Tafel slopes of the remaining Pt films tested. For both the low overpotential and high overpotential Tafel slopes, there appears to be no correlation between their values and the Pt loading. The Tafel slopes are essentially constant regardless of loading.

Pt Loading ($\mu g/cm^2$)	Tafel Slope 0.95 to 0.8 V (mV/decade)	Tafel Slope 0.8 to 0.65 V (mV/decade)
0	58	120
9.89	59	120
19.2	59	120
30.36	60	121
39.97	57	120
60.54	60	120

Table 5-4: List of Tafel slopes for Pt films deposited by the DPS technique

The Effects of Adsorbed Chloride Atoms on the ORR:

Figure 5-25 shows that the kinetic currents of chloride contaminated film are significantly lower than those of the electrochemically cleaned film. For example, the clean film's kinetic current at 0.9 V is 6.3 times greater than that of the contaminated film. This result is consistent with the fact that adsorbed chloride atoms are known to suppress the ORR on the Pt catalyst [5, 31].

Stamenkovic *et al.* studied the ORR on the Pt(111) and Pt(100) single-crystals in sulfuric acid and perchloric acid. Both acids were combined with 10^{-3} M of KCl [31]. They found that the adsorbed chloride atoms dramatically reduced the ORR kinetics on

the Pt(100) in both acids. The adsorbed chloride atoms also altered the ORR reaction pathway on the Pt(100). In the pure electrolyte, the production of peroxide at potentials greater than 0.25 V was negligible. However, with adsorbed chloride atoms on the Pt(100) surface, hydrogen peroxide accounted for 25% of the reaction product in a potential range of 0.6 to 0.25 V. In the case of the Pt(111) surface, the adsorbed chloride atoms also dramatically reduced the ORR kinetics in perchloric acid. The ORR activity in a solution containing Cl^- was several orders of magnitude lower than in the pure perchloric acid. In sulfuric acid containing Cl^- anions, the kinetics of the ORR on the Pt(111) single-crystal is only negligibly reduced relative to pure sulfuric acid. This result is due to the fact that bisulfate atoms are already poisoning the Pt(111) surface in pure sulfuric acid. Since the chloride atoms are more strongly bonded to the Pt(111) surface, they simply replace the bisulfate atoms as the site blocking species on the Pt(111) surface. The chloride atoms do not significantly block any additional sites. Similar to the adsorbed bisulfate atoms, the adsorbed chloride atoms on the Pt(111) single-crystal did not alter the ORR reaction pathway.

The results of Stamenkovic *et al.* suggest that the ORR activity of the Pt(100), Pt(110), and high-Miller index facets of the electrodeposited crystallites will be significantly reduced due to adsorbed chloride atoms. Chloride atoms adsorb strongly on all these surfaces. The ORR activity on the Pt(111) facets of the electrodeposited films is probably negligibly altered in the presence of adsorbed chloride atoms since these surface are already poisoned by the bisulfate atoms. The observed reduction in the ORR activity of the electrodeposited Pt films that were not cleaned to remove the adsorbed chloride

atoms is primarily due to chloride atoms blocking active sites on crystal planes other than the Pt(111) plane.

Figure 5-25 shows that the adsorbed chloride atoms affected the value of the Tafel slope above 0.85 V, but they did not appear to significantly affect the value of Tafel slope below 0.85 V. The Tafel slope of the contaminated film is around 90 mV/decade. Recall that the reduction of the Tafel slope by half as the potential increases above 0.8 V is due to the increase in hydroxyl atom coverage, which causes a shift of adsorption isotherm from a Langmuir isotherm to a Temkin isotherm. The presence of chloride atoms is known to suppress the adsorption of hydroxyl atoms [31]. If we assume that the hydroxyl atom coverage is half the value predicted by Equation (5.7), the Tafel slope at low overpotentials would increase to 90 mV/decade.

Oxygen Reduction Activity:

Figure 5-26 and Figure 5-27 show the specific activity and mass activity at 0.9 V of the electrodeposited Pt films, respectively. The kinetic current density of the catalyst at 0.9 V is often used to compare the activity of different catalyst. This is done because, in most electrode configurations, the current density at 0.9 V is not as susceptible to the influences of mass transport. In some articles, the exchange current density is reported instead of the kinetic current at 0.9 V. This is not done here since its value depends strongly on the calculated Tafel slope. For example, a kinetic current density of 0.04 mA/cm^2 at 0.9 V has an exchange current density of $6.5\times10^{-11}\,A/cm^2$ and $1.3\times10^{-10}\,A/cm^2$ for a measured Tafel slope of 57 mV/decade or 60 mV/decade, respectively. For a given diffusion-corrected Tafel plot, the value of the Tafel slope can

vary 3 mV/decade or more depending on the potential range used to calculate its value. This problem is exacerbated if the linear region of the Tafel plot is limited.

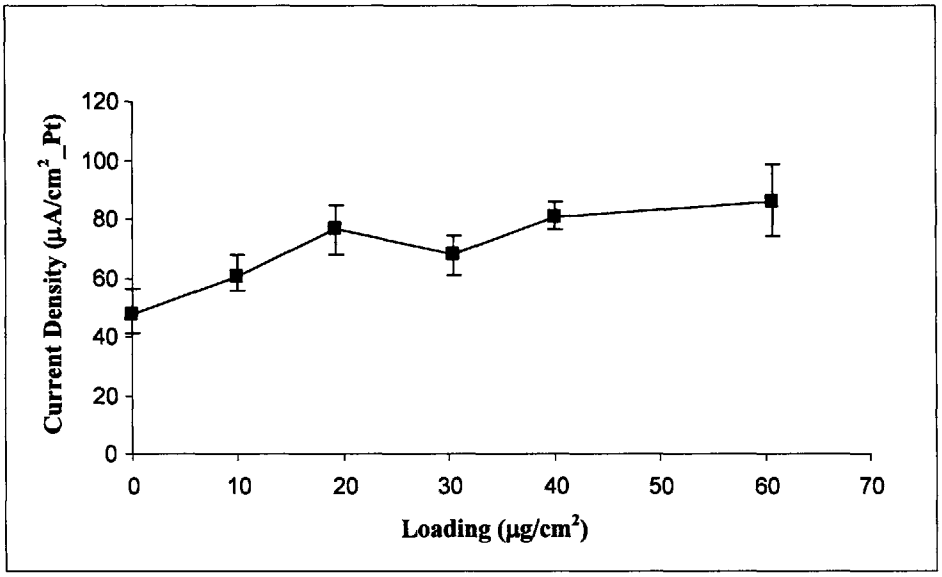

Figure 5-26: Plot of kinetic current density at 0.9 V versus Pt loading for DPS electrodeposited Pt films[15]

The measured specific activity of the polycrystalline Pt disk is approximately equal to the values reported by Paulus *et al.*, who used the RRDE technique to obtain its value [3]. The consistency of the ORR kinetic data for polycrystalline Pt obtained in this work with values reported in the literature indicates that the RDE technique was properly applied in this work. The activity of the electrodeposited Pt films is similar to the values reported by Poirier *et al.* for sputter deposited Pt films [1]. The highest specific activity they measured was about 70 $\mu A/cm^2$.

Figure 5-26 shows that the specific activity of the electrodeposited Pt films of this work generally increases in an increase in Pt loading. This trend is opposite the trend

[15] The error bars indicate variation in specific activity for 4 or 5 different experimental runs over a period of a day or two days. No trend in the change in activity was observed over the measuring period.

reported by Poirier *et al.* [1]. They sputter deposited Pt onto glassy carbon and used the RDE technique to measure the Pt films activity. They found that the specific activity of the deposited films decreased with an increase in Pt loading in the loading range of 6.6 to 200 $\mu g/cm^2$. For these sputter deposited films, the average grain size of the film increased from 2 to 10 nm as the loading increased. Poirier *et al.* also found that the specific activity of the sputter deposited films correlated with the average lattice parameter of the film. The specific activity increased with an increase in lattice compression.

It is well known that lattice compression can lead to enhanced catalytic activity. For example, alloying dispersed Pt with transition metal is believed to enhance the activity of the ORR by decreasing the nearest neighbor distance for the alloy catalysts [78]. Jalan showed that high activity resulted as the Pt alloy nearest neighbor distance approached 2.72 $\mathring{A}$ [79]. Poirier et al. surmised that the lattice compression of their sputter deposited films is enhancing the ORR activity in much the same way.

Recently, Singer sputter deposited Pt on electrospun nanofiber membranes [80]. He found that the specific activity of the deposited films increased slightly with Pt loading in 0.5 M sulfuric acid at room temperature. The activity increased from 59 to 75 $\mu A/cm^2$ for Pt loading between 21 and 112 $\mu g/cm^2$. These activity values and the increase in activity with loading are similar to the results reported here.

In this work, the increase in specific activity with an increase in loading compensated for the decrease in specific area with an increase in loading. Figure 5-27 shows that mass activities of the electrodeposited Pt films are essentially constant with respect to Pt loading in the loading range of 10 to 60 $\mu g/cm^2$.

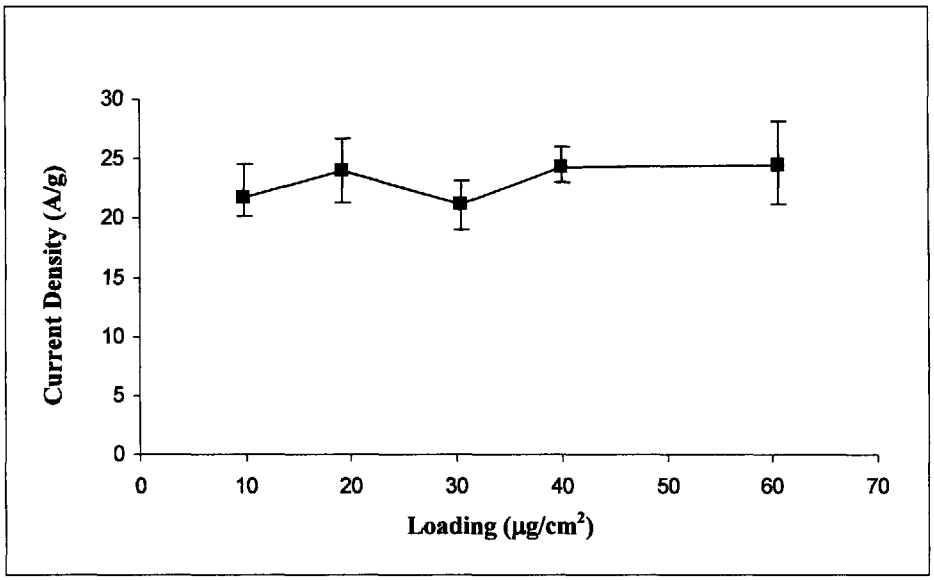

Figure 5-27: Mass activity at 0.9 V versus Pt loading for DPS electrodeposited Pt films

In the case of sputter deposited Pt films, both Poirier *et al.* and Singer showed a significant drop in mass activity of their films with increasing loading. In Singer's work the increase in specific activity was unable to compensate for the dramatic reduction in specific area with an increase in loading. In Poirier *et al.* work, the mass activity experienced a more precipitous decline with an increase loading since both the specific activity and the specific area decreased with an increase in loading. It is unclear why Poirer *et al.* and Singer observed different trends for specific activity versus Pt loading. Differences in the physical vapor deposition parameters or deposition substrate are possible explanations. Regardless, these results strongly support the proposition that electrodeposition should be used to deposit Pt films in the cylindrical pores of the microfabricated catalyst layer.

Open Circuit Potential (OCP):

Figure 5-28 contains a plot of the OCP of the Pt film versus the loading. As was discussed in Section 2.6.1, the OCP of a Pt electrode exposed to an oxygen saturated

electrolyte is typically measured to be around 1.0 V and not the reversible potential of 1.23 V.

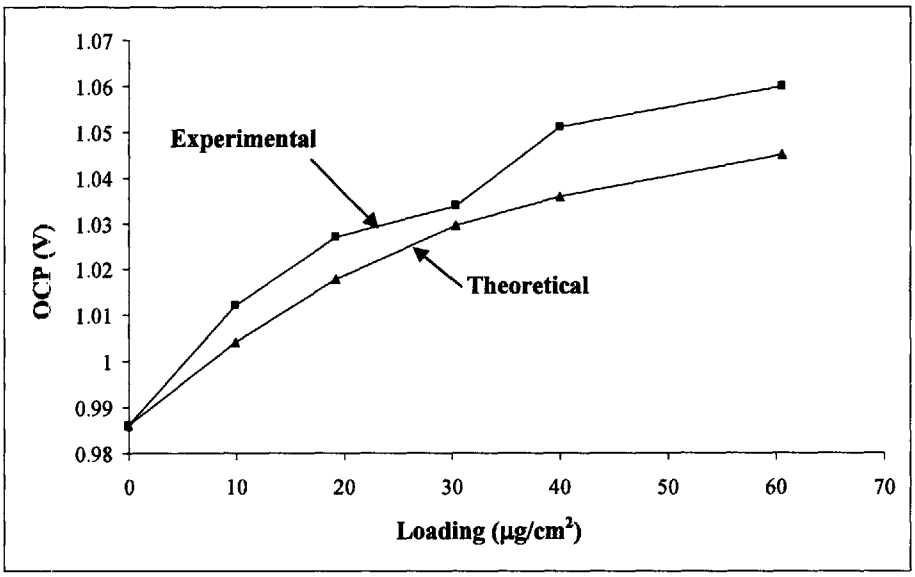

Figure 5-28: The OCP versus Pt loading for DPS electrodeposited Pt films

The OCP is a consequence of the balance between the reduction and oxidation reactions occurring on the electrode when no outside current is flowing to or from the electrode. This is why the OCP is also referred to as a mixed potential. In the configuration of this experiment, it is believed that the OCP is due oxygen reduction to water for the reduction current and the oxidation current results from a combination of Pt dissolution and oxide formation reactions. At potential near 1.0 V the oxidation of water to oxygen is negligible.

A simple expression for the OCP can be obtained by assuming that the rate of oxygen reduction in the potential region near the OCP is given by the Tafel equation,

$$i_{ORR} = i_o A_{Pt} \exp\left(\frac{2.3\left(E_{REV} - E\right)}{0.060}\right) \tag{5.52}$$

where E_{REV} is the reversible potential. The above Tafel equation assumes that the 60 mV/decade Tafel slope is valid at potentials greater than 0.95 V. At these high potentials, the Tafel slope is not expected to be this value since oxide formation is expected to affect the Tafel slope. However, 60 mV/decade is used since the actual Tafel slope is not known. At the OCP, the oxygen reduction current is equal to the oxidation current, i_{mix}. Therefore, the OCP, E_{OCP}, is given by

$$E_{OCP} = E_{REV} - (0.06)\log\left(\frac{i_{mix}}{i_o \cdot A_{Pt}}\right) \tag{5.53}$$

This equation and the measured E_{OCP} for the Pt disk can be used to calculate the ratio i_{mix}/i_o for the polycrystalline Pt disk. The curve labeled theoretical is a plot of Equation (5.53) with i_{mix}/i_o assumed to be constant and equal to the value calculated for polycrystalline Pt. In Figure 5-28, the theoretical OCP is seen to increase with an increase in loading since the Pt roughness factor, A_{Pt}, increases with an increase in loading. i_{mix} is expected to increase with an increase in the OCP. For this reason, the theoretical curve provides the upper limit for OCP if one assumes that the exchange current density remains constant irrespective of Pt loading. Figure 5-28 shows that the measured OCP for the electrodeposited Pt films is greater than the value predicted by the theoretical curve. These results strongly suggest that the ORR activity of the electrodeposited Pt films is greater than that of the polycrystalline Pt disk. This conclusion is consistent with the activity measurements made at 0.9 V.

Activity of Deposited Pt Film Compared to Supported Pt Nanoparticles (Pt/C):

Paulus *et al.* measured the ORR specific activity of supported Pt nanoparticles (Pt/C) using the thin-film RDE technique [3].[16] They measured an activity of 11.6 $\mu A/cm^2$ for the ORR on Pt/C in 0.5 M sulfuric acid at 20°C. Figure 5-26 shows that the specific activity of polycrystalline Pt disk is more than 4 times that of Pt/C. The figure also shows that the specific activities of the electrodeposited Pt films are 5 to 7.4 times greater than that of Pt/C. It is believed that the observed differences in the ORR activity between the electrodes tested in this work and that of Pt/C are primarily due to the difference in coverage of bisulfate atoms on the surfaces of these catalysts.

The activity of the Pt(111) single-crystal is two orders of magnitude less than that of the other low-index planes because of the formation of bidimensionally ordered bisulfate adlayers on the Pt(111) surface. The ordering of the bisulfate adlayer increases the bisulfate coverage and the adlayer's stability compared to the disordered adlayer [72]. Both these factors act to reduce the ORR activity on the Pt(111) surface by an order of magnitude from the value expected if the adlayer remained disordered on this surface [71, 72]. The ordered structure of the bisulfate is very sensitive to long-range order. For example, the spike at 0.45 V on the Pt(111) cyclic voltammogram, which is associated with the disordered-order transition, is observed only for terraces wider than 20 atoms [71]. Increasing the step density on the Pt(111) terraces was found to make the adlayer more disordered and consequently its blocking effect towards oxygen adsorption decreased [72]. Thus, the presence high step density facets lead to an increase the

[16] 20 wt% Pt supported on Vulcan XC72 (E-TEK)

electrocatalytic activity of Pt. The Pt(110) single-crystal is a "fully-stepped" surface and it has the highest activity among the low-index crystal planes in sulfuric acid.

Recently, Macia *et al.* [71] and Kuzume *et al.* [72] explored the ORR activity of stepped Pt surfaces belonging to the crystallographic $[01\bar{1}]$ zone and surfaces belonging to the $[1\bar{1}0]$ zone, respectively.[17] An important graph from each of these papers is shown in Figure 5-29. The graphs plot the activity versus the Miller indices for the Pt stepped surfaces. In Kuzume *et al.* paper, the activity of the stepped surfaces was characterized by using the potentials at a current density of half the diffusion limiting current density at a rotation speed of 1600 rpm (half-height potential, $E_{1/2}$). This was done since the Tafel plot of surfaces in the $[1\bar{1}0]$ zone did not show a significant linear region that can be used to accurately extrapolate to the exchange current density, i_o, values. The $E_{1/2}$ and $\ln(i_o)$ values should have the same qualitative behavior.

Both the graphs of Figure 5-29 show that for the surfaces with Pt(111) terraces (these are data points on the left side of the graphs), the ORR activity significantly increases with an increase in step density. It should be noted that for graph (a) the surface with the highest step density is the Pt (311) surface, but the activity of the Pt(311) surface is less than that of the Pt(211). Therefore, the electrocatalytic activity is not completely associated with the step. The Pt(211) surface has the highest catalytic activity for the $[01\bar{1}]$ zone.

---

[17] Surfaces in the $[01\bar{1}]$ zone are high-Miller index planes located in the stereographic triangle between (111) and (100) poles. These surfaces can be classified in two different series, surfaces with terraces with (111) symmetry and (100) steps and surfaces with (100) terraces and (111) steps. Surface in the $[1\bar{1}0]$ zone is also classified in two different series, surface with (111) terraces separated by monatomic (110) steps and surfaces with (110) terraces and (111) steps.

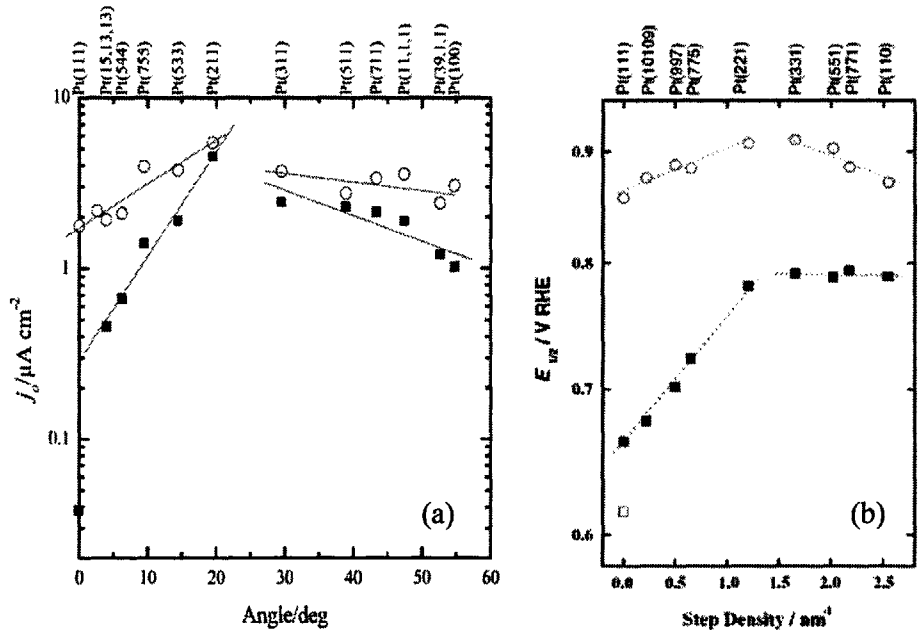

Figure 5-29: (a) Plot of exchange current density vs. the angle of the surface with respect to the Pt(111) surface in (shaded squares) 0.5 M H_2SO_4 and (open circles) 0.1 M $HClO_4$ [71]. (b) Plot of $E_{1/2}$ for oxygen reduction vs. step density at rotation rates of 1600rpm in (shaded squares) 0.5 M H_2SO_4 and (open circles) 0.1 M $HClO_4$ [72]

Figure 5-29's graph (a) also shows that the extrapolated value for Pt(111) surface (step density = 0 and angle = 0) is one order of magnitude higher than the measured value for Pt(111) single crystal. As previously mentioned, this is due to long-range ordering of absorbed bisulfate anions on the Pt(111) surface. These long-range effects are not observed on step surfaces. On graph (b) the activity of the surface from Pt (331) to Pt(110) showed no structure dependence. This is a result of the fact that these surfaces are a series of mono- and bi-atomic (111) terraces separated by (111) monatomic steps. Therefore, there is no room on the terraces to form bidimensionally ordered adlayers.

Most carbon-supported Pt nanoparticles are cubo-octahedral crystallites. The cubo-octahedral structure is the most thermodynamically stable form of the Pt particles. For an average Pt particle diameter of 3.7 nm, the fraction of the crystallites surface atoms found among the Pt(100) facets is only 13%. The remaining surface fractions are

65% for Pt(111) facets and 22% for corner and edge sites [58]. The Pt(100) facets are believed to be more active for the ORR than the other facets and sites by one or two orders of magnitudes in sulfuric acid. Thus, only about 13% of the surface atoms are essentially active during the ORR on Pt/C.

XRD data of polycrystalline Pt and electrodeposited Pt films reveal that Pt(111) plane accounts for about 50 to 40% of the total crystal planes. The remaining crystal planes include Pt(200), Pt(220), Pt(400), Pt(311), and other high-Miller index planes [70]. These crystal planes have activity similar to and greater than Pt(100) plane. Thus, in the case of polycrystalline Pt and electrodeposited Pt films, 50% or more of the surface atoms are active in the ORR. This value is significantly greater than the 13% active surface for Pt/C. It is also sufficient to explain the higher activity of the ORR on polycrystalline Pt and electrodeposited Pt compared to the ORR activity on Pt/C.

The activity of polycrystalline Pt is also observed to be greater in perchloric acid. Figure 5-30 is a plot of the specific activity of Pt at 0.9 V vs. Pt specific area from reference [4]. The 0 m^2/g denotes polycrystalline Pt disk. The figure shows that the specific activity of polycrystalline Pt is about 10 times greater than that of the Pt/C Since the anion of perchloric acid is known *not* to adsorb on any of the crystallographic surfaces of Pt, its adsorption is not responsible for the observed differences in activity among Pt crystal planes [29].

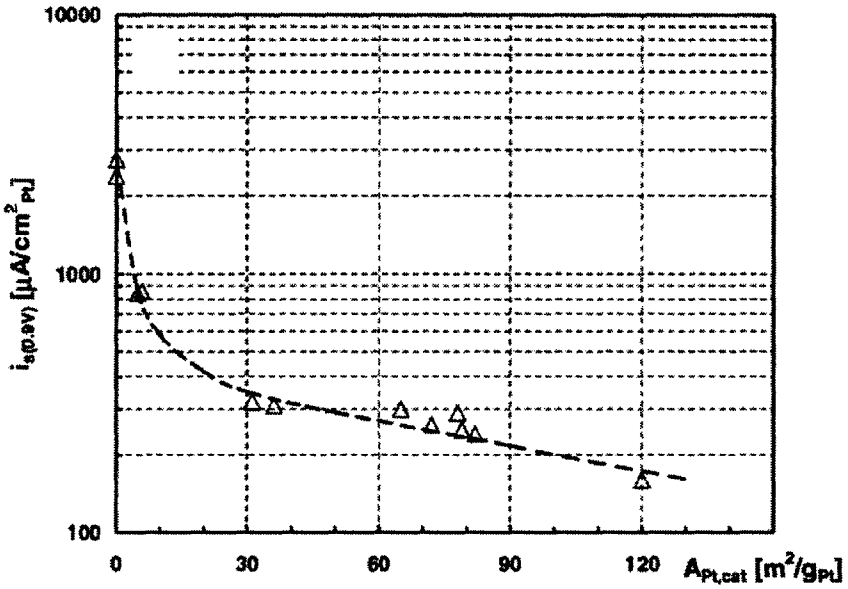

Figure 5-30: The ORR specific activities of polycrystalline Pt (shown at "0 m^2/g_{Pt}"), Pt-black (data at ca. 5 m^2/g_{Pt}), and Pt/C catalysts at 0.9 V and 60 °C. Activities determined via RDE measurements in O_2 saturated 0.1 M $HClO_4$. The potentiodynamic curves were obtained from positive-going sweeps at 20 mV/s, going from 0 to 1.0 V (RHE) [4]

Single-crystal RRDE studies show that the variation of the ORR activity in perchloric acid is relatively small between the three low index surfaces. The Pt(110) and Pt(111) surfaces are more active than the Pt(100) surface by about a factor of 4 to 5. These levels of structural sensitivity are much smaller than what were observed for these same crystal surfaces in KOH or H_2SO_4. In these electrolytes, the activities varied from one to two orders of magnitude. The Pt(100) surface activity is less than the other two planes as a result of stronger adsorption of OH_{ad} atoms on this surface. [29]. This fact suggests that the ORR activity on the Pt/C should slightly increase with a decrease in their size since the ratio of Pt(100) to Pt(111) facets decreases with a decrease in size of the cubo-octahedral crystallite. It also suggests that the ORR activity on Pt/C should be greater than or about the same as the ORR activity on polycrystalline Pt since the fraction of the Pt(111) facets is higher for the nanoparticles than polycrystalline Pt. Both of these

suggestions are contradicted by the experimental results reported in Figure 5-30. The reasons for the contradictions are not fully understood. However, the observed behavior may still be related to the structure sensitive adsorption of OH_{ad} atoms. Takasu *et al.* reported an increase in specific activity of Pt nanoparticles with an increase in particles size in 5 mM of $HClO_4$. They also reported a significantly higher activity for polycrystalline Pt compared to the Pt nanoparticles. Takasu *et al.* attributed the observed particle size effect to the interaction between the adsorbed oxygen containing molecule, OH_{ad}, and the surface Pt atoms [81]. They pointed out that the energy separation between the highest occupied energy level for oxygen and the valence band of Pt decreases with a decrease in Pt particle size. For this reason, they argued that the adsorption strength between OH_{ad} and Pt would be much stronger with a decrease in particle size. The stronger adsorption of OH_{ad} atom with a decrease in particle size is supported by the measured 80 mV cathodic shift of the oxide reduction peak of supported Pt/C from the value of polycrystalline Pt.

Similar to polycrystalline Pt, the activity of electrodeposited Pt is expected to be higher than that of Pt/C in perchloric acid. This hypothesis should be verified in future works. The RDE experiments for the electrodeposited Pt films should be repeated in perchloric acid and KOH to further our understanding of the ORR on electrodeposited thin Pt films.

Activity of Deposited Pt film Compared to Bulk Polycrystalline Pt:

Both the activity measurements (see Figure 5-26 and Figure 5-27) and OCP measurements (see Figure 5-28) indicate that the specific activities of the electrodeposited Pt films are greater than that of polycrystalline Pt. Furthermore, the

specific activities of the Pt films increase with an increase in Pt loading. The higher ORR activity on electrodeposited Pt may be related to an increase in the number of high step density facets over the number density on the polycrystalline Pt surface. As was mentioned earlier, researchers have observed a higher number density of high-Miller index facets for films deposited under certain electrodeposition conditions [69]. Figure 5-29 shows that the ORR activity of high-Miller index facets can be greater than the activity on the Pt(111) and Pt(100) facets. The increase in activity with an increase in Pt loading may indicate that the number density of the high-Miller index facets as well as Pt(100) and Pt (110) facets increase with an increase in Pt loading. The cyclic voltammograms in Figure 5-19 supports this hypothesis. Furthermore, SEM image of the large crystallites produced by the SPS technique (see Figure 5-14) suggests that crystallites preferentially grow in the $\langle 200 \rangle$ direction. A growth in this direction may be beneficial to the Pt film's ORR activity. Further study is needed in this area.

The deposition of Pt occurs rapidly. For this reason, the Pt film is expected to have a high density of point and line defects [51]. These defects my not fully relax during potential cycling of the electrodeposited films. As a result, the Pt films that were tested may have a higher density of defects than polycrystalline Pt. Defects on Pt(111) terraces are known to increase the activity of the ORR in sulfuric acid [72, 75]. Defects do not enhance the ORR activity in perchloric acid [75]. For this reason, it is believe that the defects on Pt(111) terraces disrupt the ordered bisulfate and, as a result, increase activity of the Pt(111) terraces compared to defect free terraces.

Another explanation for the measured higher ORR activity on the electrodeposited Pt films compared to that on polycrystalline Pt is a possible lattice

compression of the electrodeposited crystallites. An increase in the ORR specific activity on a thin Pt films is known to be associated with an increase in lattice compression [1]. This result is a corollary to the known effect that alloying dispersed Pt with transition metals results in higher activity due to a decrease in nearest neighbor distance, which produces a favorable configuration for oxygen adsorption and reaction [1, 78, 79]. As was previously discussed, electrodeposited films do show a decrease in the size of the lattice parameter compared to polycrystalline Pt [8, 51]. This lattice compression is a result of a high density of intergrain boundaries. For example, during electrodeposition, secondary Pt crystals growing in the neighborhood of each other exert mutual strain. This strain can increase as the two crystallites grow in size [51]. Therefore, the increase in specific activity with an increase in loading observed for the DPS deposited Pt films of this work may be a result of the increase in lattice compression as the crystals grow in size. In future work, XRD study should be combined with RDE study in order to explore this hypothesis.

5.4.5 Hydroxyl Atom Desorption Characteristic

Figure 5-31 contains the plots of the linear sweep voltammograms of the DPS electrodeposited Pt films. The figure shows that the peak current increases with an increase in Pt loading. The figure also shows that the potential at the oxide reduction peak current increases with an increase in Pt loading. The positive shift between the 9.89 and 60.54 $\mu g/cm^2$ film is about 20 mV. This shift in the potential at peak current may indicate a reduction in the adsorption strength of the hydroxyl atoms [4].

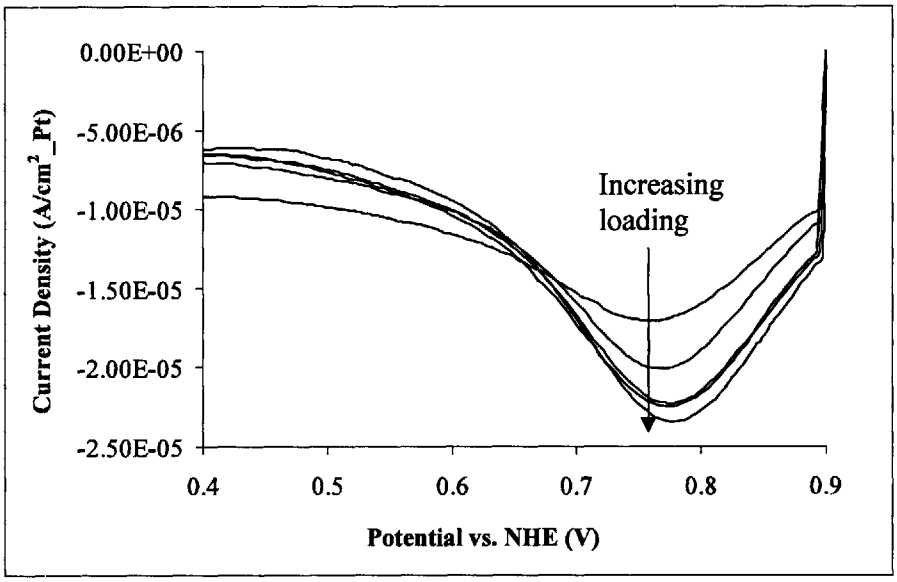

Figure 5-31: Linear sweep voltammograms of the DPS electrodeposited Pt films. Pt loading: 9.89, 19.2, 30.36, 39.97, and 60.54 μg/cm^2, peak increases with increase in loading

The hydroxyl atom coverage was estimated by calculating the charge passed during the linear sweep. This charge was subtracted from the charge associated with the double layer current to obtain the hydroxyl atom desorption charge, Q_{OH}. For each electrodeposited film, the double layer current value was obtained from its cyclic voltammogram. The hydroxyl atom coverage is calculated by applying the equation

$$\Theta_{OH} = \frac{Q_{OH}}{\left(210\times10^{-6}\right)\left(A_{Pt}\right)} \tag{5.54}$$

Figure 5-32 is a plot of the hydroxyl atom coverage versus the Pt loading. The figure shows that the coverage increases with loading. This trend may be a result of the reduction in the coverage of bisulfate atoms on the Pt surfaces. A Pt surface with a lower coverage of bisulfate atoms is capable of adsorbing a greater amount of hydroxyl atoms. As was previously mentioned, the increase in Pt film activity with an increase in loading may be related to an increase in the number density of high-Miller index facets and an

increase in the number density of point and line defects. An increase in both these factors has been shown to decrease bisulfate atom coverage and lead to an increase the coverage of hydroxyl atoms on Pt [71, 72, 75]. Furthermore, the positive shift in the potential at peak current suggests that the added hydroxyl atoms are not strongly adsorbed on the surface of Pt. As the Pt loading increased, the strongly adsorbed bisulfate atom may have been replaced with reversibly adsorbed hydroxyl atoms. Thus, the results in Figure 5-32 are consistent with the observed increase in Pt film activity with increase Pt loading.

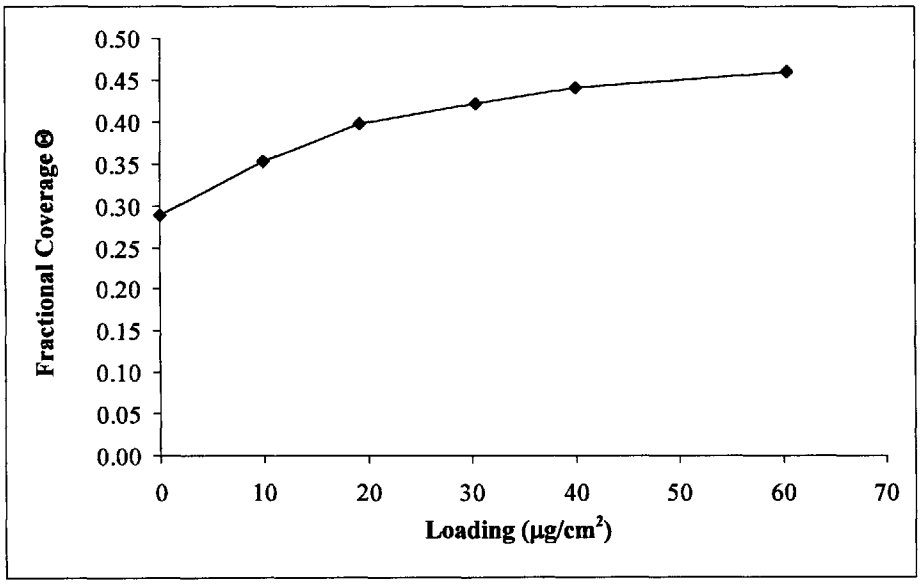

Figure 5-32: Hydroxyl atom coverage versus the Pt loading for DPS electrodeposited films

5.5 Conclusion

Thin Pt films were electrodeposited on a polished glassy carbon substrate by the single potential step (SPS) and the double potential step (DPS) techniques. The DPS technique produced Pt films with specific areas greater than 25 m^2/g for Pt loadings as high as 80 $\mu g/cm^2$. The SPS technique produced Pt films with lower specific areas than

the DPS deposited films. However, both electrodeposition techniques, at high Pt loadings, produced Pt films with higher specific areas than films sputter deposited on glassy carbon. Electrodeposition produces higher area films because secondary nucleation on existing Pt crystallites allows the films to grow principally by increasing the number of crystallites rather than increasing the size of the crystallites. In the case of sputter deposition, secondary nucleation is absent and the Pt film grows by increasing the size of the crystallites and a layer-by-layer growth.

Sputter deposition has the advantage of depositing Pt films that are essentially free of adsorbed contaminants. In the case of Pt electrodeposition from the $PtCl_6^{2-}$ anion, six chloride ions are produced for every Pt atom deposited. Unfortunately, a certain amount of these chloride atoms adsorb onto the surface of the deposited Pt crystallites and severely reduce their ORR activity. In this work, it was shown that the chloride atoms can be successfully desorbed from the Pt surface by treating the film at a reducing potential of 0.V vs. NHE for 30 to 60 seconds.

The ORR reaction pathway on the chloride-free Pt films was determined to be essentially the same as that of polycrystalline Pt and Pt/C. For all Pt films, the Tafel slope was measured to be around 60 mV/decade at low overpotentials. At potentials between 0.8 and 0.65 V vs. NHE, the Tafel slope doubled to a value of about 120 mV/decade. At potentials below 0.4 V, the electron transfer number for the ORR remained about 4 electrons. Therefore, the ORR did not shift to predominately peroxide formation at potentials in the hydrogen adsorption/desorption region. The kinetic current also approached a limiting value at high overpotentials.

The specific activities of the Pt films at 0.9 V in 0.5 M sulfuric acid were higher than the activity of a Pt disk electrode. Also, the activity of the Pt films increased with an increase in Pt loading. Compared to the specific activity of Pt/C, the specific activities of the electrodeposited Pt films were 5 to 7.4 times greater. The enhanced activity of the electrodeposited Pt films may be due to a number of contributory factors. The currently recognized factors are:

(a) A higher surface ratio of Pt crystallographic orientations advantages to the ORR, for example, an increase in the number density of crystal facets with high step densities.

(b) An increase in the number density of point and line defects on the surfaces of the crystallites.

(c) Increase in lattice compression resulting from the mutual strain that Pt crystallites, growing in close proximity, exert on each other.

The increase in specific activity due to factors (a) and (b) is believed to be related to the reduction in bisulfate atom coverage on the surface of the crystallites. Strongly adsorbed bisulfate atoms inactivate the ORR sites by blocking oxygen adsorption. Therefore, a reduction in its coverage increases the number of active sites on the Pt surface. In the case of factor (c), lattice compression is believed to produce a favorable configuration for dioxygen adsorption and dissociation. Therefore, the increase in specific activity of the Pt is related to a fundamental gain in the turn-over frequency of the active sites.

The maximum mass activity for Pt/C occurs at a specific area value of around 75 m^2/g [4, 35, 36]. Therefore, the mass activity of the electrodeposited Pt films is surprisingly about 2.5 times greater than that of Pt/C. Sputter deposited films and the

electrodeposited films have similar specific activity. However, the electrodeposited films have an enhanced mass activity due to its higher specific area.

The characterization of thin films and the study of the ORR kinetics on them are exciting areas of research, especially considering the enhanced reactivity these types of films show. With regards to catalyst layer preparation for air electrodes, the bulk of the research has focused on producing and maintaining high catalyst dispersion. However, the thin Pt film technology provides a new direction that might alleviate the problems associated with dispersed catalyst. For example, Pt films have been shown to be much more resilient to Pt area loss due to particle growth and dissolution [82]. In the past, thin Pt films were not favored for fuel cell applications since high Pt loadings are required. The advantages of these films are lost once the loading is increased to values greater than 100 $\mu g/cm^2$. The microfabricated electrode design solves this problem by increasing the surface area for Pt deposition by a factor of 10 or more over the geometric area of the cell. Thus, the actual loading of the Pt film remains low while still maintaining the required loading on the geometric area basis. The thin film technology concept is also being successfully applied in the research work of Debe *et al.* of 3M [82, 83] . For a brief review of this work see Section 3.3.4.

References

[1] J.A. Poirier and G.E. Stoner, "Microstructual effects on electrocatalytic oxygen reduction activity of nano-grained thin-film platinum in acid media", *J. Electrochem. Soc.* Vol. 141, p.425, 1994.

[2] L.J. Bregoli, "The influence of platinum crystallite size on electrochemical reduction of oxygen in phosphoric acid", *J. Electrochimica Acta* Vol. 23, p. 489, 1978.

[3] U.A. Paulus, T.J. Schmidt, H.A. Gasteiger, and R.J. Behm, "Oxygen reduction on a high-surface area Pt/Vulcan carbon catalyst: a thin-film rotating ring-disk electrode study", *J. Electroanal. Chem.*, Vol. 495, p. 134, 2001.

[4] H.A. Gasteiger, S.S. Kocha, B. Sompalli, and F.T. Wagner, "Activity benchmarks and requirements for Pt, Pt-alloy, and non-Pt oxygen reduction catalysts for PEMFCs", *Applied Catalysis B: Environmental*, Vol. 56, p. 9, 2005.

[5] N.M. Markovic, T.J. Schmidt, V. Stamenkovic, and P.N. Ross, "Oxygen Reduction Reaction on Pt and Pt Bimetallic Surfaces: A Selective Review", *Fuel Cells*, Vol. 1, p. 105, 2001.

[6] M. Peuckert, T. Yoneda, R.A. Dalla Betta, and M. Boudart, "Oxygen Reduction on Small Supported Platinum Particles", *J. Electrochem. Soc.* Vol. 133, p. 944, 1986.

[7] A. Kucernak and J. Jiang, "Mesoporous Platinum as a Catalyst for Oxygen Electroreduction and Methanol Electrooxidation", *Chemical Engineering J.*, Vol. 93, p. 81, 2003.

[8] L.M. Plyasova, I. Yu Molina, S.V. Cherepanova, N.A. Rudina, O.V. Sherstyuk, E.R. Savinova, S.N. Pron'kin, and G.A. Tsirlina, "Disperse Electrolytic Platinum and Palladium Deposits of Submicron Thickness on Polycrystalline Supports: An X-ray Diffractometry and Microscopy Study", *Russ. J. Electrochem.*, Vol. 38, p. 1116, 2002.

[9] K. Tammeveski, T. Tenno, J. Claret, and C. Ferrater, "Electrochemical Reduction of Oxygen on Thin-Film Pt Electrodes in 0.1 M KOH", *Electrochimica Acta*, Vol. 42, p. 893, 1997.

[10] M.V. Brussel, G. Kokkinidis, I. Vandendael, and C. Buess-Herman, "High Performance Gold-Supported Platinum Electrocatalyst for Oxygen Reduction", *Electrochemistry Communications*, Vol. 4, p. 808, 2002.

[11] J. Zhang, Y. Mo, M.B. Vukmirovic, R. Klie, K. Sasaki, and R.R. Adzic, "Platinum Monolayer Electrocatalysts for O_2 Reduction: Pt Monolayer on Pd (111) and on Carbon-Supported Pd Nanoparticles", *J. Phys. Chem B.*, Vol. 108, p. 10955, 2004

[12] M. Huang, Y. Jin, H. Jiang, X. Sun, H. Chen, B. Liu, E. Wang, and S. Dong, "Designed Nanostructured Pt Film for Electrocatalytic Activities by Underpotential Deposition Combined Chemical Replacement Techniques", *J. Phys. Chem. B*, Vol. 109, p. 15264, 2005.

[13] J.D.E. McIntyre, S. Srinivasan, and F.G. Will, Editors, Proceedings of the Symposium on Electrode Materials and Processes for Energy Conversion and Storage", Vol.77-6, Princton NJ: The Electrochem. Soc. Inc, 1977

[14] D. Scherson, D. Tryk, M. Daroux, and X.Xing, Editors, *Structural Effects in Electrocatalysis and Oxygen Electrochemistry*, Proc. Vol. 92-11, Pennington NJ: The Electrochem. Soc. Inc, 1992

[15] A.J Appleby, *Catalysis Reviews*, Vol. 4, p 221, 1970

[16] R.R. Adzic, "Recent Advances in the Kenetics of Oxygen Reduction" in *Electrocatalysis,* J. Lipkowski and P.N. Ross, Editors, p 197

[17] K. Kinoshita, *Electrochemical Oxygen Technology*, John Wiley & Sons, New York, 1992.

[18] W. Wroblowa, Y.C. Pan, and J. Razumney, " Electroreduction of Oxygen – New Mechanistic Criterion", *J. Electroanal. Chem.*, Vol. 69, p. 195, 1976.

[19] M.R. Tarasevich, A. Sadkowski, and E. Yeager, i*n Comprehensive Treatise in Electrochemistry*, J.O.M. Bokris, B.E. Conway, E. Yeager, S.U.M Khan, R.E. White, Editors, p 301, Plenum Press, New York 1983

[20] N.M Markovic, H.A. Gasteiger, B.N. Grgur, and P.N. Ross, "Oxygen Reduction Reaction on Pt(111): Effects of Bromide", J. Electroanal. Chem., Vol. 467, p. 157, 1999.

[21] E. Yeager, M. Razaq, D. Gervasio, A. Razaq, and D. Tryk, "The Electrolyte Factor in O_2 Reduction Electrocatalysis", in *Structural Effects in Electrocatalysis and Oxygen Electrochemistry*, D. Scherson, D. Tryk, M. Daroux, and X.Xing, Editors, Proc. Vol. 92-11, Pennington NJ: The Electrochem. Soc. Inc, p. 440, 1992

[22] M.R. Tarasevich and V.S. Vilinskaya, Electrokhimiya, Vol. 9, p. 96, 1973

[23] D.B. Sepa, M.V. Vojnovic, and A. Damjanovic, "Reaction Intermediates as a Controlling Factor in the Kinetics and Mechanism of Oxygen Reduction at Platinum Electrodes", *J. Electrochimica Acta* Vol. 26, p. 781, 1978.

[24] N.M. Markovic, H.A. Gasteiger, and P.N. Ross, "Oxygen Reduction on Platinum Low-Index Single-Crystal Surfaces in Alkaline Solution: Rotating $Ring_{Pt(hkl)}$ Disk Studies", *J. Physical. Chem.*, Vol. 100, p. 6715, 1996.

[25] D.R. de Sena, E.R. Gonzalez, and E.A. Ticianelli, "Effect of Phosphoric Acid Concentration on the Oxygen Reduction and Hydrogen Oxidation Reactions at a Gas Diffusion Electrode", *J. Electrochimica Acta* Vol. 37, p. 1855, 1992.

[26] K.L. Hsueh, E.R. Gonzalez, and S.S. Srinivasan, "Effects of Phosphoric Acid Concentration on Oxygen Reduction Kinetics at Platinum", *J. Electrochem. Soc.* Vol. 131, p. 823, 1984.

[27] J.C. Huang, R.K. Sen, and E. Yeager, "Oxygen Reduction on Platinum in 85% Orthophosphoric Acid", *J. Electrochem. Soc.* Vol. 126, p.786, 1979.

[28] S. Clouser, Ph.D. Thesis, Chemistry Department, Case Western Reserve University, Cleveland, Ohio, 1982.

[29] N.M Markovic, H. Gasteiger, and P.N. Ross, "Kinetics of Oxygen Reduction on Pt(hkl) Electrodes: Implications for the Crystallite Size Effects with Supported Pt Electrocatalysts', *J. Electrochem. Soc.*, Vol. 144, p.1591, 1997.

[30] F.EL Kadiri, R. Faure, R. Durand, "Electrochemical Reduction of Molecular-Oxygen on Platinum Single-Crystals", *J. Electroanal. Chem.*, Vol. 301, p. 177, 1991.

[31] V. Stamenkovic, N.M. Markovic, and P.N. Ross, "Structure-Relationships in Electrocatalysis: Oxygen Reduction and Hydrogen Oxidation Reactions on Pt(111) and Pt(100) in Solutions Containing Chloride Ions", *J. Electroanal. Chem.*, Vol. 500, p. 44, 2001.

[32] N.M. Markovic, H.A. Gasteiger, and P.N. Ross, "Oxygen Reduction on Platinum Low-Index Single-Crystal Surfaces in Sulfuric Acid Solution: Rotating Ring-Pt(hkl) Disk Studies", *J. Physical Chem.*, Vol. 99, p. 3411, 1995.

[33] M.L. Sattler and P.N. Ross, "The Surface Structure of Pt Crystallites sup.orted on Carbon Black", *Ultramicroscopy*, Vol. 20, p.21, 1986

[34] P.N. Ross, "Structure-Property Relations in Noble metal Electrocatalysis", LBL-21733, Lawrence Berkeley Laboratory, Berkeley, CA (June 1986); presented at the Gordon Conference on Chemistry at Interfaces, Meriden, NH, July 21-25, 1986.

[35] P.N. Ross, "Oxygen Reduction on Supported Pt Alloys and Intermetallic Compounds in Phosphoric Acid", EPRI-1533, Contract RP 1200-5, Final Report prepared for the Electric Power Research Institute, Palo Alto, CA (September 1980).

[36] K. Kinoshita, "Particle Size Effects for Oxygen Reduction on Highly Dispersed Platinum in Acid Electrolytes", *J. Electrochem. Soc.*, Vol. 137, p. 845, 1990.

[37] S Hirano, J Kim, and S Srinivasan, "High Performance Proton Exchange Membrane Fuel Cells with Sputter-Deposited Pt Layer Electrodes", *Electrochimica Acta*, Vol. 42, p. 1587, 1997.

[38] P. Brault, A. Caillard, A.L. Thomann, J. Mathias, C. Charles, R.W. Boswell, S. Escribano, J. Durand, and T.Sauvage, "Plasma Sputtering Deposition of Platinum into Porous Fuel Cell Electrodes", *J. Physics D: Applied Physics*, Vol. 37, p. 3419, 2004.

[39] S.Y. Cha and W.M. Lee, "Performance of Proton Exchange Membrane Fuel Cell Electrodes Prepared by Direct Deposition of Ultrathin Platinum on the Membrane Surface", *J. Electrochem. Soc.*, Vol. 146, p. 4055, 1999

[40] R. O'Hayre, S. Lee, S, Cha, and F.B. Prinz, "A Sharp Peak in the Performance of Sputtered Platinum Fuel Cells at Ultra-Low Platinum Loading", *J. Power Sources*, Vol. 109, p. 483, 2002

[41] M.A. Phillips, V. Ramaswamy, B.M. Clemens, W.D. Nix, "Stress and Microstructure Evolution During Initial Growth of Pt on Amorphous Substrates", *J. Meter. Res.*, Vol. 15, p. 2540, 2000.

[42] K. Shimazu, K. Uosaki, and H. Kita, "Structure of Pt Microparticles Dispersed Electrochemically onto Glassy Carbon Electrodes", *J. Electroanal. Chem.*, Vol. 256, p. 481, 1988.

[43] M.M.E Duarte, A.S. Pilla, J.M. Sieben, and C.E. Mayer, "Platinum Particles Electrodeposited on Carbon Substrates", *Electrochemistry Communications*, Vol. 8, p. 159, 2006.

[44] B. Gollas, J.M. Elliot, and P.N. Barlett, "Electrodeposition and Properties of Nanostructured Platinum Films Studied by Quartz Crystal Impedance Measurements at 10 MHz", *Electrochimica Acta,* Vol. 45, p. 3711, 2000

[45] S.D. Thompsan, L.R. Jordan, A.K. Shukla, and M. Forsyth, "Platinum Electrodeposition from $H_3Pt(SO_3)_2OH$ solutions", *J. Electroanal. Chem.*, Vol. 515, p. 61, 2001

[46] A.M. Feltham and M. Spiro, *Chemical Review*, Vol. 71, p. 177, 1971.

[47] A.J. Bard, R. Parsons, and J. Jordan, *Standard Potentials in Aqueous Solutions*, Marcel Dekker Inc., New York, 1985

[48] G. Lu and G. Zangari, "Electrodeposition of Platinum on Highly Oriented Pyrolytic Graphite. Part I: Electrochemical Characterization", *J. Phys. Chem. B*, Vol. 109, p. 7998, 2005

[49] K. Shimazu, D. Weisshaar, and T. Kuwana, "Electrochemical Dispersion of Pt Microparticles on Glassy Carbon Electrodes", *J. Electroanal. Chem.*, Vol. 223, p. 223, 1987.

[50] A.L.Y Lau and A.T. Hubbard, "Study of the Kinetics of Electrochemical Reactions by Thin-Layer Voltammetry: III. Electroreduction of the Chloride Complexes of Platinum(II) and (IV)". *J. Electroanal. Chem.*, Vol. Vol. 24, p. 237, 1970.

[51] L.M. Plyasova, I.Y. Molina, A.N. Gavrilov, S.V. Cherepanova, O.V. Cherstiouk, N.A. Rudina, E.R. Savinova, and G.A. Tsirlina "Electrodeposited Platinum Revisited: Tuning Nanostructure via the Deposition Potential", *Electrochimica Acta*, Vol. 51, p. 4477, 2006.

[52] J. Lin-Cai and D. Pletcher, "A Substrate Effects on the Catalytic Activity of Electrodeposited Platinum Layers", J. Electroanal. Chem., Vol. 149, p. 237, 1983.

[53] A.J. Bard and L.R. Faulkner, Electrochemical Methods: *Fundamentals and Applications*, John Wiley & Sons, Inc., New York, New York, 2001.

[54] T.J Schmidt and H.A. Gasteiger, "Rotating Thin-Film Method for Supported Catalysts", in *Handbook of Fuel Cells – Fundamentals, Technology, Applications*, W. Vielstich, H.A. Gasteiger, and A. Lamm, Editors, Wiley, John & Sons, 2003.

[55] J. Newman and K.E. Thomas, *Electrochemical Systems*, Third Edition, John Wiley & Sons, Inc., Hoboken, New Jersey, 2004.

[56] V.G. Levich, *Physicochemical Hydrodynamics*, Prentice-Hall, New Jersey, 1962

[57] C.R. Lee, Power Point Presentation at 2006 KIMM-MIT Workshop.

[58] T.J. Schmidt, H.A. Gasteiger, G.D. Stab, P.M. Urban, D.M. Kolb, and R.J. Behm, "Characterization of High-Surface-Area Electrocatalysts Using a Rotating Disk Electrode Configuration", *J. Electrochem. Soc.*, Vol. 145, 1998.

[59] H. Angerstein-Kozlowska, B.E. Conway, and W.B.A. Sharp, "The Real Condition of Electrochemically Oxidized Platinum Surfaces, Part I, Resolution of Component Processes", *J. Electroanal. Chem.*, Vol. 43, p. 9, 1973

[60] B.E. Conway and S. Gottesfeld, "Real Condition of Oxidized Platinum Electrodes, Part II, Resolution of Reversible and Irreversible Processes by Optical and Impedance Studies", *Chem. Soc., Faraday Trans.*, Vol. 69, p. 1090, 1973.

[61] B.V. Tilak, B.E. Conway, and H. Angerstein-Kozlowska, "The Real Condition of Oxidized Pt Electrodes, Part III, Kinetic Theory of Formation and Reduction of Surface Oxides", *J. Electroanal. Chem.*, Vol. 48, p. 23, 1973.

[62] B.E. Conway and D.M. Novack, "Hysteresis in Formation and Reduction of Submonolayer Quantities of Surface Oxide at Pt in an Almost Anhydrous Solvent", *J. Electrochem. Soc.*, Vol. 128, p. 956, 1981.

[63] B. Scharifker and G.Hills, "Theoretical and Experimental Studies of Multiple Nucleation", Electrochimica Acta, Vol. 28, p. 879, 1983.

[64] J. Puippe, and F. Leaman, *Theory and Practice of Pulse Plating*, American Electroplaters and Surface Finishers Society, 1986.

[65] M.E. Hyde and R.G. Compton, "A Review of the Analysis of Multiple Nucleation with Diffusion Controlled Growth", *J. Electroanal. Chem.*, Vol. 549, p. 1, 2003.

[66] M.Y. Abyaneh, "Modeling Diffusion Controlled Electrocrystallization Processes", *J. Electroanal. Chem.*, Vol. 586, p. 196, 2006.

[67] F. Gloaguen, J.M. Leger, C. Lamy, A. Marmann, U. Stimming, and R. Vogel, "Platinum Electrodeposition on Graphite: Electrochemical Study and STM Imaging" *Electrochimica Acta,* Vol. 44, p. 1805, 1999.

[68] S. Floate, M. Hyde, and R.G. Compton, "Electrochemical and AFM Studies of the Electrodeposition of Cobalt on Glassy Carbon: an Analysis of the Effect of Utrasound", *J. Electroanal. Chem.*, Vol. 523, p. 49, 2002.

[69] F.J. Rodriguez Nieto, M.A. Pasquale, C.R. Cabrera, and A.J. Arvia, "Morphology of Platinum Electrodeposits in the Three-Dimensional Sublayer to Full Layer Range Produced Under Different Potential Modulations on Highly Oriented Pyrolytic Graphite", *Langmuir*, Vol. 22, p. 10472, 2006.

[70] H. Cui, J. Ye, W. Zhang, J. Wang, and F. Sheu, "Electrocatalytic Reduction of Oxygen by a Platinum Nanoparticle/Carbon Nanotube Composite Electrode", *J. Electroanal. Chem.,* Vol. 577, p. 295, 2005.

[71] M.D. Macia, J.M. Campina, E. Herrero, and J.M. Feliu, "On the Kinetics of Oxygen Reduction on Platinum Stepped Surfaces in Acidic Media", *J. Electroanal. Chem.*, Vol. 564, p. 141, 2004.

[72] A. Kuzume, E. Herrero, and J.M. Feliu, "Oxygen Reduction on Stepped Platinum Surfaces in Acidic Media", *J. Electroanal. Chem.*, Vol. 599, p. 333, 2007.

[73] Y.D. Gamburg, "Grain size of Electrochemically Deposited Metal as a Function of Overpotential", *Russ. J. Electrochem.*, Vol. 35 p. 1020, 1999.

[74] E. Ahlberg, F. Falkenberg, J.A. Manzanare, and D.J. Schiffrin, "Convective Mass Transfer to Partially Recessed and Porous Electrodes", *J. Electroanal. Chem.*, Vol. 548, p. 85, 2003.

[75] V. Komanicky, A. Menzel, K. Chang, and H. You, "Investigation of Oxygen Reduction Reaction Kinetics at (111)-(100) Nanofaceted Platinum Surfaces in Acidic Media", *J. Phys. Chem. B*, Vol. 109, p. 23550, 2005.

[76] R. Landsber and R. Thiele, "Über den einfluss inaktiver oberflächenbereiche auf den diffusionsgrenzstrom an rotierenden scheibenelektroden und die transitionszeit bei galvanostatischen messungen", *Electrochimica Acta*, Vol. 11, p. 1243, 1966

[77] D.E. Rosner, "Reaction Rates on Partially Blocked Rotating Disks-Effect of Chemical Kinetic Limitations", *J. Electrochem. Soc.*, Vol. 113, p. 624, 1966

[78] C.F. Kroen, G.E. Stoner, and S.R. Taylor, in *Proceedings of the Intersociety Energy Conversion Engineering Conference*, W.D. Jackson and D.A. Hull, Editors, Vol. 3, p. 1569, IEEE Publishing Services, New York, 1989.

[79] V. Jalan and E.J. Taylor, "Importance of Interatomic Spacing in Catalytic Reduction of Oxygen in Phosphoric Acid", *J. Electrochem. Soc.*, Vol. 130, p. 2299, 1983.

[80] S. Singer, M.S. Thesis, Mechanical Engineering Department, Massachusetts Institute of Technology, Cambridge, MA, 2006.

[81] Y. Takasu, N. Ohashi, X.G. Zhang, Y. Murakami, H. Minagawa, S. Sato, and K. Yahikozawa, "Size Effects of Platinum Particles on the Electroreduction of Oxygen", *Electrochimica Acta*, Vol. 41, p. 2595, 1996.

[82] M.K. Debe, A.K. Schmoeckel, G.D. Vernstrom, and R. Atanasoski, "High Voltage Stability of Nanostructured Thin Films Catalysts for PEM Fuel Cells", *Journal of Power Sources*, Vol. 161, p. 1002, 2006.

[83] M.K. Debe, "Novel Catalyst, Catalyst Support and Catalysts Coated Membrane Methods," *Handbook of Fuel Cells – Fundamentals, Technology and Applications*, W. Vielstich, H.A. Gasteigher, A. Lamn, Editors, Vol. 3, John Wiley & Sons, 2003.

[84] H.H. Chang, M.S. Thesis, Chemical Engineering Department, Clarkson University, Potsdam, NY, 1984.

[85] K. Hsueh, PhD Thesis, Chemical Engineering Department, Clarkson University, Postdam, NY, 1982.

[86] E. Gileadi, *Electrode Kinetics for Chemists, Chemical Engineers, and Material Scientist*, Wiley-VCH, New York, NY, 1993.

Chapter 6

Oxygen Gain Measurements on Thin Platinum Films Electrodeposited on PTFE-Bonded Microporous Membranes

6.1 Introduction

In the electrode design concept, Pt is deposited within the catalyst layer as thin films on the surface of the microfabricated cylindrical holes rather than dispersed nanoparticles uniformly distributed within the micropores of the catalyst layer matrix. The thin film technology is used in order to minimize the required diffusion length of oxygen in the electrolyte phase. According to Weber *et al.*, fuel cells with Pt deposited thin films were first investigated by Cahan and Bockris in the late 1960s [1]. In his PhD dissertation work, Cahan prepared electrodes by sputtering Pt films on polished Vycor plates [2]. The Vycor material had a porosity of 25%, nearly all in 5 nm pores. Since Vycor glass is not electronically conductive, a gold collecting grid was sputtered over the Pt film to collect the current. For this electrode, Cahan found that currents for the oxygen reduction reaction (ORR) could be measured up to 100 mA/cm^2 at reported Pt loadings of 5 to 20 μg/cm^2 without any oxygen diffusion losses. The elimination of diffusion losses is a result of the thinness (< 10 nm) of the Pt film. Asher and Batzold, motivated by the implications of Cahan's work, sputter deposited much thicker Pt films (loadings up to 260 μg/cm^2) onto Vycor glass and porous nickel substrates [3]. Porous nickel is a more practical substrate than Vycor glass since it is both electronically conductive and cheaper

than Vycor glass. In the case of Pt films deposited on Vycor glass, their half-cell studies indicted that the films showed no oxygen diffusion losses. These results were consistent with the results of Cahan. However, electrodes with Pt films on porous nickel showed significant oxygen transport losses. Asher and Batzold's electrodes proved to be inadequate for two reasons. First, thick Pt films employed in their study had too low a specific area. Second, the sintered nickel surface was laden with hemispherical depressions that were 6 microns or more in diameter. The roughness of the substrate resulted in wells where thick electrolyte films covered the Pt surface. These films hindered oxygen transport to the Pt surface. The performance of their electrode increased as the size of these hemispherical depressions was reduced.

The results of Asher and Batzold's work demonstrate the importance of the substrate that the Pt film is deposited on. The substrate's surface must be as smooth as possible and have pores less than 1 μm. Substrates with a rough surface have regions on their surface were a thick electrolyte film can cover the Pt film and essentially block oxygen transport to the film. The Pt film must also be deposited only on the surface of the substrate and not within the substrates pores. Pt particles that are deposited within the pores of the substrate can be starved of oxygen during the operation of the electrode. Thus, in order to minimize oxygen transport losses, the Pt film needs to be of uniform thickness, smooth, and extremely thin.

In the work presented in this chapter, thin Pt films were electrodeposited on the 15 wt% PTFE-bonded membranes described in Chapter 4. Three electrodeposition techniques were used to deposit the Pt films: 1) single potential step deposition, 2) double potential step deposition, and 3) single potential step deposition on a sputter deposited Pt

seed layer. These Pt films were characterized using cyclic voltammetry and scanning electron microscopy. The oxygen transport within the deposited films was studied by using a half-cell apparatus to conduct oxygen gain experiments. A simple one dimensional model was developed to help in the interpretation of the oxygen gain results.

6.2 Theory of Oxygen Gain

Oxygen transport within an electrode is not directly measured. Instead, theoretical models for the electrode are postulated and fitted to the voltage/current plot of the electrode. The model that best fits the data is then used to determine the effectiveness of oxygen transport. In general, kinetic, ion transport, electron transport, and reactant gas transport limitations affect the voltage/current behavior of the electrode. Thus, an effective model must accurately describe all these coupled phenomena.

To reduce the model complexity, fuel cell researchers often use the oxygen gain of an electrode to characterize the efficiency of oxygen transport processes occurring in an electrode [4]. The oxygen gain is defined as the difference in electrode potential at a given current density when the cathode is operated successively on a low and then a high partial pressure of oxygen. The oxygen gain experiment is useful because, under certain conditions, the measured oxygen gain is independent of the ionic and electronic transport limitations of the electrode. Thus, models used to simulate oxygen gain behavior need not consider ion and electron transport.

Theory:

Consider a porous electrode of arbitrary shape with a thin Pt film deposited on a portion of the electrode surface (see Figure 6-1). The porous electrode is fully saturated

with an electrolyte. The fraction of the electrode surface where the Pt film was deposited on is the only region of the electrode that is electrochemically active. The Pt film is sufficiently thin that the liquid (electrolyte) and solid potential of the film depends only on its position on the electrode surface.

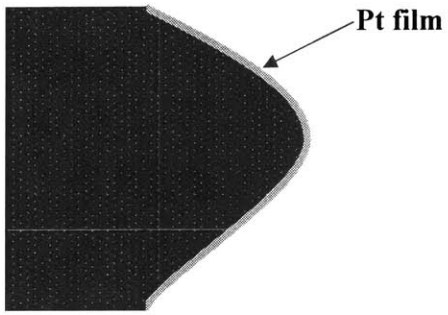

Figure 6-1: Porous electrode of arbitrary shape with a thin Pt film deposited on a portion of the electrode surface

For this electrolyte saturated electrode, the transport equations for current in the liquid, i_l, and solid, i_s, phases are

$$\vec{i}_l = -\sigma_{eff}\vec{\nabla}\Phi_l \tag{6.1}$$

$$\vec{i}_s = -\kappa\vec{\nabla}\Phi_s \tag{6.2}$$

where σ_{eff} and κ are the effective ionic conductivity of the electrolyte and the electronic conductivity of the electrode, respectively. Φ_s is the potential of the solid phase of the electrode. Φ_l is defined as the potential of a hydrogen reference electrode in equilibrium with the electrolyte at the point considered. The reference electrode potential is assumed to be independent of the activity of the gaseous reactants. Equation (6.1) is valid under the assumption of no concentration gradients in the electrolyte [5].

Since there are no electrochemical reactions occurring within the electrode, the charge conservation equations for the liquid and solid phases are

$$\vec{\nabla} \cdot \vec{i}_l = 0 \tag{6.3}$$

$$\vec{\nabla} \cdot \vec{i}_s = 0 \tag{6.4}$$

Equation (6.3) is combined with Equation (6.1) to give

$$\nabla^2 \Phi_l = 0 \tag{6.5}$$

Equation (6.4) is combined with Equation (6.2) to give

$$\nabla^2 \Phi_s = 0 \tag{6.6}$$

Equations (6.5) and (6.6) are the Laplace's equation for the potential distribution in the liquid electrolyte phase and solid phase, respectively. The solutions to these equations only depend on the geometry and boundary conditions.

In the oxygen gain experiment of the electrode illustrated in Figure 6-1, the only boundary condition that changes is the condition on the Pt film. For the oxygen reduction reaction that is first order with respect to the partial pressure of oxygen, it can be shown that the current density of the Pt film is related to the pressure of oxygen, P_{O_2}, and the potentials of the electrolyte and solid phases at the electrode surface by the following general expression:

$$i = P_{O_2} \frac{\exp\left[\dfrac{U^{ref} - \left(\Phi_s^b - \Phi_l^b\right)}{b}\right]}{f\left(\Phi_s^b - \Phi_l^b\right)} \tag{6.7}$$

where f is a general function that depends on the difference the solid phase and liquid phase potentials. The form of the function depends on the nature of oxygen transport to and within the active region. The thin liquid film [6], agglomerate [7, 8], and wedge-meniscus [9, 10] models give analytical expressions for this function. It is important to

note that the function f does not depend on the partial pressure of oxygen. The superscript b denotes that the potential is measured at the boundary of the electrode.

Taking the gradient of both sides of Equation (6.7) and combining the result with Equations (6.1), (6.2), and (6.7) gives

$$\vec{\nabla} \ln i = -\left(\frac{\vec{\nabla}\Phi_s^b - \vec{\nabla}\Phi_l^b}{b} \right) - \left(\frac{\vec{\nabla} f\left(\Phi_s^b - \Phi_l^b\right)}{f\left(\Phi_s^b - \Phi_l^b\right)} \right) \tag{6.8}$$

The boundary condition given by Equation (6.8) combined with Equations (6.1) through (6.4) constitutes the equations needed to determine the current and potential fields in the solid and electrolyte phases. The key point made here is that these equations are independent of the pressure of oxygen. For the given boundary condition, the current and potential distributions in the two phases are the same for all values of the uniform pressure of oxygen. Thus, the oxygen gain at a given current is independent of the ionic and electronic transport losses of the system.

Oxygen Gain with no O_2 Transport Losses:

Let us now consider the specific case where the Pt film experiences no oxygen transport losses and the oxygen reduction reaction (ORR) is described by a Tafel equation. Under these conditions, Equation (6.7) reduces to

$$i = i_o \left(\frac{P_{O_2}}{P_{O_2}^{ref}} \right) \exp\left[\frac{U^{ref} - \left(\Phi_s^b - \Phi_l^b\right)}{b} \right] \tag{6.9}$$

where i_o is the exchange current density and b is the Tafel slope. U^{ref} is the reversible potential of the ORR at the reference conditions. Its value does not change with a change in the partial pressure of oxygen, P_{O_2}.

The measured potential, E_m, is given by

$$E_m = \left(\Phi_{WE} - \Phi_{RE}\right) = \left(\Phi_{WE} - \Phi_s^b\right) + \left(\Phi_s^b - \Phi_l^b\right) + \left(\Phi_l^b - \Phi_{RE}\right) \tag{6.10}$$

where Φ_{WE} and Φ_{RE} are the potential of the working electrode leads and reference electrode leads, respectively. Based on the arguments made previously, the first and last terms in parenthesis on the right hand side of Equation (6.10) are independent of the partial pressure of oxygen. Thus, the difference in measured potential, ΔE_{Gain}, at a given current when the electrode is operated successively in air and oxygen is given by

$$\Delta E_{Gain} = E_m\left(O_2\right) - E_m\left(air\right) = \left(\Phi_s^b - \Phi_l^b\right)_{O_2} - \left(\Phi_s^b - \Phi_l^b\right)_{air} \tag{6.11}$$

Combining Equations (6.11) and (6.9) gives

$$\Delta E_{Gain} = b' \log\left(\frac{P_{O_2,(O_2)}}{P_{O_2,(air)}}\right) \tag{6.12}$$

where b' is the Tafel slope in Volts per decade. For a Tafel slope of 120 mV/decade, the numerical value for Equation (6.12) is

$$\Delta E_{Gain} \approx 83.9\,\text{mV/decade} \tag{6.13}$$

Therefore, if the Pt film kinetics obey a Tafel-like current-potential relation and the electrode experiences no transport losses for oxygen in the gas or electrolyte phase, then oxygen gain is predicted to be independent of applied current.

6.3 Experimental

6.3.1 Experimental Setup

Figure 6-2 is a picture of the experimental setup used for all experiments presented in this chapter.

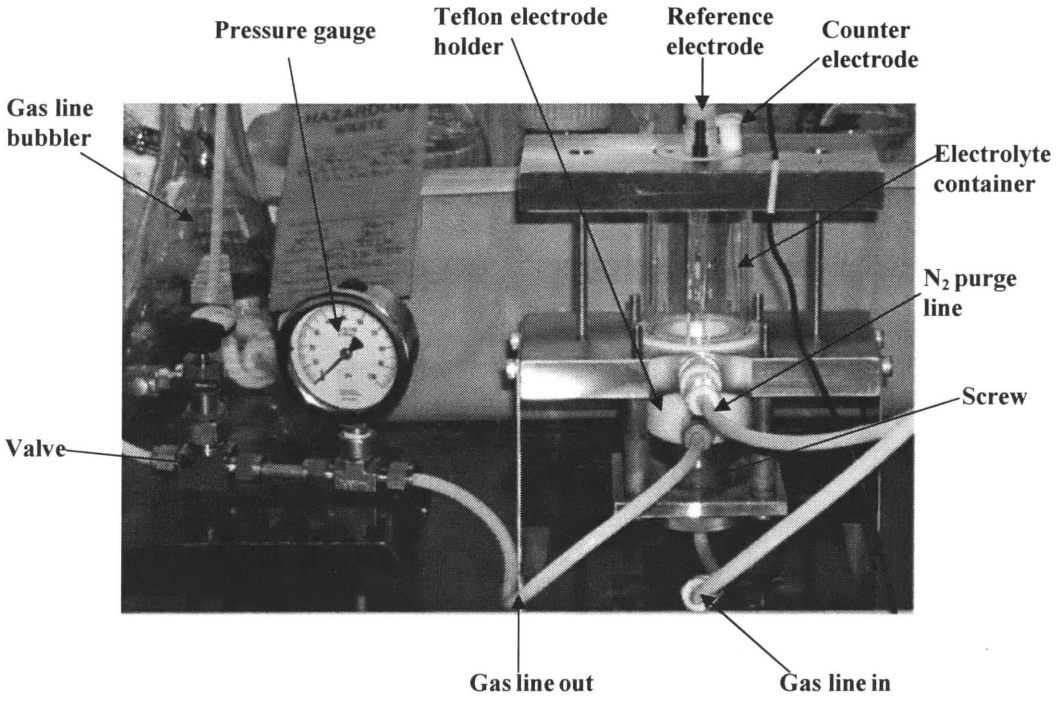

Figure 6-2: Picture of half-cell experimental setup

A saturated calomel reference electrode (SCE) was used as the reference electrode. However, all potentials mentioned in this chapter are referred to the normal hydrogen electrode (NHE). One or two Pt wires (0.5 mm OD) were used as the counter electrode. Both the reference electrode and counter electrode were purchased from the Pine Instrument Company. During the experiments, the Pyrex electrolyte container was filled to about 3/4 its height with the electrolyte solution. This level of filling ensured that enough of the counter electrode was wetted with the electrolyte. During each experiment, the electrolyte solution in the container was purged with nitrogen gas (Grade-5 BOC Gases). The nitrogen gas was allowed to flow at a rate of 2 to 4 bubbles per second. This rate of bubbling ensured the electrolyte solution remained free of oxygen from the atmosphere.

As Figure 6-2 shows, the all-Teflon electrode holder was held in place by sandwiching it between a large screw and the body of the half-cell apparatus. A more detailed schematic of the electrode holder is illustrated in Figure 6-3. The holder consists of two parts: the main body that houses the electrode and the cap.

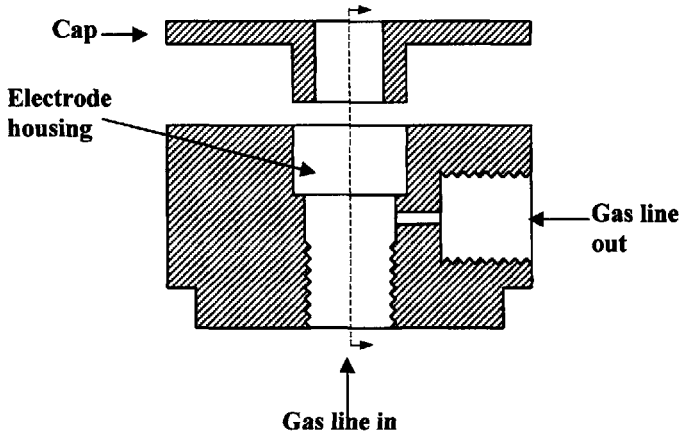

Figure 6-3: Schematic of half-cell electrode holder

Depending of the experiment, the membrane was placed in the electrode housing along with Kalrez® washers, a Pt washer, and a Pt foil or mesh. A Pt wire was welded to the Pt washer in order to provide a means of electrically connecting the membrane to the potentiostat. The details of what accompanied the electrode when it was placed in the housing are provided below for each experiment.

The gas line that is attached to the Teflon holder was used to transport nitrogen, oxygen, or air depending on the experiment. The gas blankets the bottom side of the membrane, while the top side of the membrane is exposed to the electrolyte solution. The downstream valve was fully opened so that the back pressure of the gas was maintained at gauge pressure of 0 bar unless specified otherwise. The gas regulator's valve was used to control the flow rate of the gas. During the experiments, the gas was allowed to flow at a rate of 1 to 2 bubbles per second. This flow rate is much higher than

the stoichiometric flow of oxygen or air needed in the oxygen gain experiments (see below).

A 1287A Potentiostat from Solartron was used to control the potential or current of the working electrode. The CorrWare program was used to control the potentiostat from a desktop computer. The CorrView program was used to visualize the data and to perform the current integration to calculate the charge of a voltammogram or a current vs. time transient response.

6.3.2 Experimental Procedure

Electrodeposition on Membranes:

In the electrodeposition experiments, Pt was deposited on 15 wt% PTFE-bonded membranes. This type of membrane was determined to have the right balance of hydrophobicity when dry and high breakthrough pressure when it is saturated with an electrolyte. Refer to Section 4.4.2 for more details. The membranes were 5/8 inch in diameter. Each membrane was dried in an air oven at 120°C for 30 min before Pt was deposited on one of its surface.

The half-cell experimental setup shown in Figure 6-2 was used to electrodeposit Pt onto the membrane's surface. The deposition solution consisted of 5 mM of K_2PtCl_6 (99.99+% from Sigma-Adlrich) and 1 M H_2SO_4 made from 98% ACS reagent grade H_2SO_4 from VWR and ultra pure water. The sulfuric acid acted as the supporting electrolyte.

The membrane was placed in the electrode housing in the manner shown in Figure 6-4.

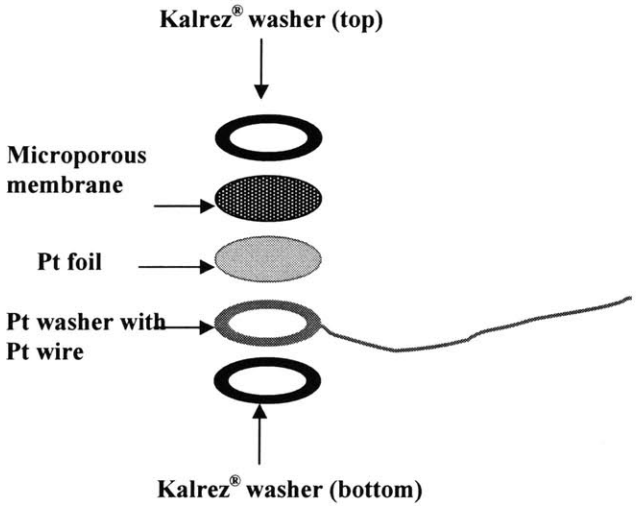

Figure 6-4: Schematic of how the membrane is placed in electrode housing for the electrodeposition and cyclic voltammetry experiment

The membrane was sandwiched between two Kalrez® washers that helped prevent liquid water from leaking out of the electrode housing. The inner area of the washers was 1 cm^2. Thus, Pt was only able to deposit on the exposed area of the membrane's surface. Only the top surface of the membrane was in contact with the deposition solution. Since the pores of the membrane do not spontaneously absorb water, the deposition solution remained on the top surface of the membrane during deposition. Cyclic voltammograms were used to confirm that the electrolyte did not leak into the membrane's pores.

A Pt foil and Pt washer with Pt wire were placed on the bottom side of the membrane. The Pt foil (2 mils thick) was used to ensure a uniform distribution of potential along the membrane. The foil is also used to detect leaking since a wetted Pt foil would produce characteristic Pt peaks during voltammetry. The Pt wire was welded to the Pt washer by a technician from the Scientific Instruments Company.

Before deposition, the deposition solution was deaerated by bubbling nitrogen through the N_2 purge line for 20 minutes. Nitrogen also flowed through the gas line for

20 minutes to remove all oxygen in the gas line and in the gas compartment of the electrode holder. During deposition, nitrogen continued to flow through the purge line and the gas line to minimize the diffusion of oxygen to the membrane/solution interface. The purging of oxygen from the half-cell apparatus was crucial. Any oxygen that was present would diffuse and quickly react at the membrane/solution interface, and consequently, lower the Faradaic efficiency of Pt electrodeposition.

Three types of electrodeposition techniques were used to deposit Pt on the 15 wt% PTFE-bonded membranes. In the single potential step (SPS) technique, the membrane was first held at a potential of 0.7 V for 30 seconds. This potential was slightly lower than the open circuit potential (OCP) of the membrane. The membrane potential was then stepped to 0.1 V and held at this potential until the desired amount of Pt was deposited on the membrane. In the double potential step (DPS) technique, the membrane was first held at 0.7 V for 30 seconds. The membrane potential was stepped from 0.7 V to -0.2 V for 1 second and then stepped to 0.3 V. The membrane potential was held at 0.3 V until the desired amount of Pt was deposited on the membrane.

In the single potential step with seed layer (SPS-S) technique, Pt was electrodeposited on a membrane that had a sputter deposited Pt layer on its surface. The Pt sputtering was performed in the Microsystems Technology Lab (MTL) at MIT. The MRC RF sputtering machine with MTL's Pt target was used. The sputter machine was set to an Argon flow of 60 sccm and at a power of 100 W. Based on previous users' estimates, the RF sputtering chamber typically deposits 23 nm of Pt in 4 minutes. This was estimated to be equivalent to ~0.05 mg Pt/cm^2 (or ~0.0125 mg Pt/cm^2 per minute) by using the density of Pt and assuming a continuous flat layer. A Control experiment

performed by Singer indicated that the Pt deposition rate was 0.014 mg Pt/cm^2 per minute [11]. Pt was sputtered on a 1 cm^2 area of the membrane for 90 seconds. The amount of Pt deposited was about 21 μg/cm^2. Pt was electrodeposited on the sputtered membrane by stepping the membrane potential from the open circuit potential to 0.45 V. The membrane potential was held at 0.45 V until the desired amount of Pt was deposited on the membrane.

The distance between the tip of the reference electrode and the membrane surface was about 1.5 cm. For this reason, the current interrupt capability of the 1287 Potentiostat was used when the membrane potential was held at the potential of Pt deposition.[1] For example, in the DPS technique, the current interrupt capability was only active when the potential was held at 0.3 V and not during the 1 second potential hold at -0.2 V.

In the SPS, the DPS, and the SPS-S deposition techniques, all of the Pt was assumed to deposit during the potential hold at 0.1, 0.3, and 0.45 V, respectively. The amount of Pt deposited, i.e. the Pt loading , Pt_L, was estimated from the integrated charge, Q_{ED}, calculated from the current versus time transient response at the deposition potentials. Thus, assuming 100% Faradaic efficiency, the Pt_L is given by

$$Pt_L = \left(\frac{Q_{ED}}{nF}\right) MW_{Pt} = 195.078\left(\frac{Q_{ED}}{385940}\right) \tag{6.14}$$

where MW_{Pt} is the molecular weight of Pt.

[1] The current interrupt technique can sometimes be used effectively to correct for the uncompensated ohmic resistance in the solution or solid phases. Most modern potentiostat have the current interrupt capability. It is important to note that the current interrupt technique does not compensate for ohmic resistances that are in parallel with capacitive elements. In electrochemistry, both concentration gradients and the double layer produce capacitive elements. Refer to reference [23] for a review of this technique.

Cleaning of Electrode:

After electrodeposition, chloride atoms are adsorbed on the deposited Pt film. Adsorbed chloride atoms are known to alter the voltammogram of Pt and to suppress the oxygen reduction reaction (ORR) kinetics. After deposition, the membrane was removed from the electrode holder and washed thoroughly with ultra pure water. The membrane was then dried in an air oven at 120°C for 30 minutes. The membrane was placed back in the thoroughly cleaned half-cell apparatus (see Figure 6-2). All components were cleaned with ultra pure water. The membrane was placed in the electrode holder in the same manner as it was for the Pt electrodeposition experiments (see Figure 6-4).

The electrolyte container was filled with a fresh supply of 0.5 M sulfuric acid. The sulfuric acid solution was prepared from ultra pure water and 98% H_2SO_4 ACS Reagent grade from VWR. Before the electrochemical cleaning, the sulfuric acid solution was deaerated with nitrogen for 20 minutes. Nitrogen also flowed through the gas line for 20 minutes to remove all oxygen in the gas compartment of the electrode holder. The membrane was held at 0 V for 4 minutes to desorb the chloride atoms from the Pt film. During this potential hold, nitrogen continued to flow through the purge line and the gas line to minimize the diffusion of oxygen to the membrane/solution interface. After 4 minutes, the sulfuric acid solution was quickly emptied from the electrolyte container. The electrolyte container was then filled with a fresh supply of ultra pure water 4 or 5 times to thoroughly rinse out the contaminated sulfuric acid. The membrane was kept in the half-cell apparatus during the rinsing process.

Cyclic Voltammetry:

The electrodeposited Pt films were characterized using cyclic voltammetry. For each membrane, the voltammetry was conducted right after the membrane cleaning procedure described above without removing the membrane from the half-cell apparatus. The voltammetry solution was 0.5 M sulfuric acid prepared from ultra pure water and 99.999% sulfuric acid from Sigma-Aldrich. Before voltammetry, the sulfuric acid solution was deaerated with nitrogen for 20 minutes. Nitrogen also flowed through the gas line for 20 minutes to remove all oxygen in gas compartment of the electrode holder. During voltammetry, nitrogen continued to flow through the purge line and the gas line.

During cyclic voltammetry, the potential was scanned between 0.05 and 1.3 V five or six times. The scan rate was 50 mV/sec. The final potential scan was recorded as the voltammogram for the Pt film. After voltammetry, the membrane was removed from the electrode holder and rinsed out thoroughly with ultra pure water. The membrane was then dried in an air oven at 120°C for 30 minutes.

Oxygen Gain:

The oxygen gain experiments were conducted on the 15 wt% PTFE-bonded membranes with Pt films deposited by the DPS technique. The membranes were first saturated with water using the saturation procedure described in Section 4.3.1. The water-saturated membrane was then saturated with 3.7 M H_2SO_4 by soaking it in the electrolyte for more than 24 hours. The sulfuric acid solution was prepared from ultra pure water and 99.999% sulfuric acid from Sigma-Aldrich.

The half-cell setup shown in Figure 6-2 was used to conduct the oxygen gain experiments. The acid-saturated membrane was placed in the electrode holder in the manner shown by Figure 6-5.

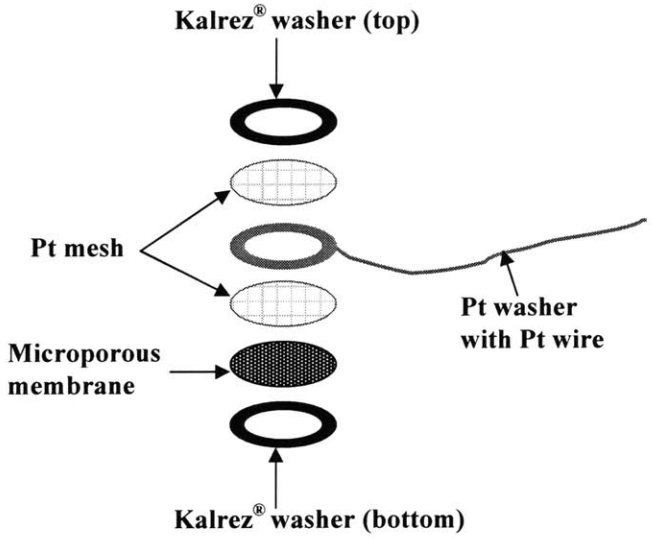

Figure 6-5: Schematic of how the membrane is placed in electrode housing for the oxygen gain experiments

The Pt film side of the membrane faced downward so that it was exposed to the gas compartment of the electrode holder. On the electrolyte side of the membrane (top side), the Pt washer with Pt wire was sandwiched between two Pt screens. The Pt screens were 5/8 inch diameter circles punched from a Pt (99.9%) gauze 100 mesh stock purchased from Sigma-Aldrich. The Pt screens were used to ensure a uniform distribution of potential along the membrane. The screens did not significantly increase the ionic resistance between the membrane and the reference electrode.

The electrolyte container was filled to about 3/4 its height by the 3.7 M sulfuric acid solution. Before the oxygen gain experiment, the sulfuric acid solution was deaerated with nitrogen for 20 minutes. Oxygen (Grade-5 BOC gases) or air (20% O_2 and 80% N_2 from BOC gases) flowed through the gas line for 20 minutes before the

experiment. The back pressure of the gas line was set to approximately 0.07, 0.5, or 1 bar. These pressures kept the electrolyte from leaking into the electrode holder's gas compartment. The pressures were also greater than the hydrostatic pressure of the electrolyte on the membrane's top surface. During the experiment, the nitrogen gas continued to flow through the purge line while oxygen or air flowed through the gas line. Oxygen or air flowed through the gas line at a rate of 1 to 2 bubbles per second. This flow rate is much higher than the stoichiometric flow for the current densities used in the oxygen gain experiments.

Two sets of oxygen gain experiments were conducted on each membrane. The first set of experiments involved flowing air, at a back pressure of 0.07 bar, through the gas line and measuring the electrode potential at different current densities. The air was then replaced with oxygen, at back pressure of 0.07 bar, and the potential of the electrode was measured at the same current densities but under the new O_2 partial pressure condition. When the gas line was changed from air to oxygen, oxygen gas was allowed to flow through the gas line for 20 minutes before starting the experiment. The difference in measured potential during oxygen flow and that during air flow, at a given current density, is the oxygen gain.

The second set of experiments involved flowing oxygen through the gas line with a back pressure of 0.5 bar and then a back pressure of 1 bar. For each current density value, the potential measurement made previously for oxygen flow with a back pressure 0.07 bar is subtracted from the potential measurement made at back pressures of 0.5 and 1 bar. These oxygen gain measurements were conducted to examine if the higher gas pressures altered the gas-electrolyte interface.

6.4 Results and Discussions

6.4.1 Electrodeposition of Pt Films onto Porous Carbon Membrane

Figure 6-6 shows the typical current versus time transient responses recorded for the three different types of electrodeposition techniques.

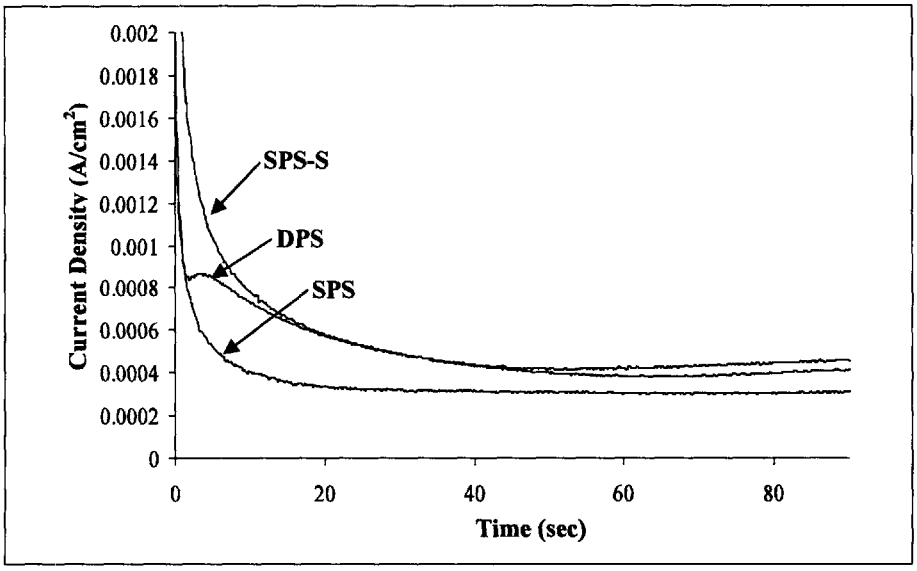

Figure 6-6: Representative current vs. time transient responses recorded for the three different types of deposition techniques

The double layer charging/discharging current for the DPS and SPS deposition techniques are about the same. This observation suggests that, for both of these deposition techniques, an equal amount of the membrane's surface area is wetted by the electrolyte during the initial time of Pt deposition. The double layer charging/discharging current for the SPS-S technique, however, is significantly higher than that of the other techniques. This result indicates that more surface area is wetted by the electrolyte during deposition by the SPS-S technique than during deposition by the other techniques. This result is not surprising because the sputtered Pt seed layer was not only deposited on the surface of the membranes. Due to the membrane's porosity, a certain fraction of the

sputtered particles were deposited as far as 1 μm deep into the membrane [12]. The contact angle between the aqueous electrolyte and Pt is about 0° [2]. For this reason, the presence of Pt particles within the membrane improved the ability of the electrolyte to wet the internal pores of the membrane that have Pt particles deposited within them. Thus, the higher double layer charging/discharging current of the SPS-S transient response was due to the additional capacitance that both the wetted Pt seed layer and flooded membrane pores provided. The cyclic voltammograms of the SPS-S deposited Pt films support this conclusion.

Figure 6-6 shows that at times greater than 15 seconds the current transient for the SPS-S deposition is approximately equal to that for the DPS deposition. This observation suggests that the ion transport and Pt film growth mechanism for both these techniques are about the same at times greater than 15 seconds. This observation is consistent with the expectation that the growth of the Pt films were under diffusion control for both SPS-S and DPS deposition techniques. Under diffusion control, the difference in deposition potential between the two techniques would not affect the current behavior in the planar diffusion region of the transient response.

At times greater than 50 seconds, the SPS-S and DPS currents began to slightly increase with time. These results are due to both concentration gradient driven free convection and the growth of the Pt film within the boundary layer. Similar observations were made for Pt deposition on glassy carbon (see Section 5.4.1).

The current versus time transient responses for the SPS-S technique did not show the current maximum associated with the transition form hemispherical diffusion to planner diffusion. Similarly, the DPS deposition on glassy carbon did not produce this

current maximum. In the case of glassy carbon, the absence of a current maximum was attributed to the high density of growth centers, which caused the current maximum to fall within the time region of the double layer charging/discharging current. As a result, the current maximum was not resolvable from the transient response. A similar effect was probably preventing the observation of a current peak for the SPS-S deposition. In this case, the masking of the current peak by the double layer current was partially due to the high density of growth centers resulting from the deposited seed layer. Figure 6-7 (a) shows the Pt particles sputter deposited on the membrane surface.

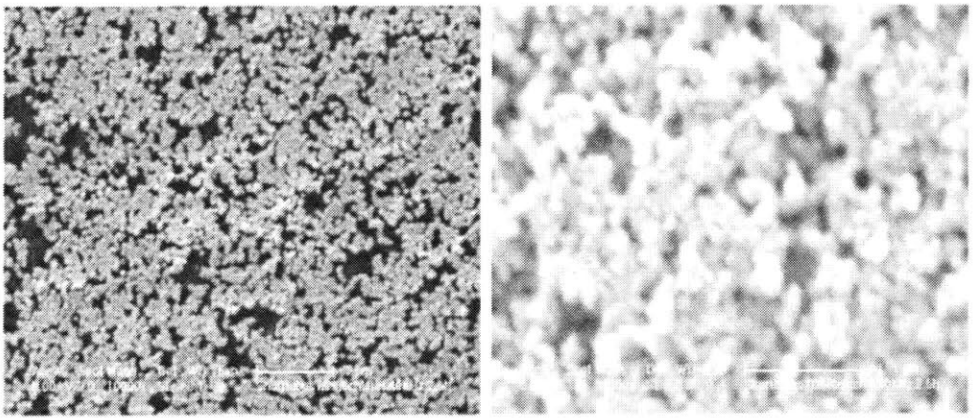

(a) (b)

Figure 6-7: Image (a): surface image of Pt seed layer. Pt was sputtered for 90 seconds producing a Pt loading of 21.2 μg/cm^2. Image (b) surface image of Pt film deposited by the SPS-S deposition technique. Pt loading of 61.25 μg/cm^2

The particles almost blanket the entire surface of the membrane. Thus, there is very little space for prolonged hemispherical diffusion without interaction with other growth centers. Another factor which may have partially contributed to the masking of the current maximum was the higher charging/discharging current and time of the SPS-S deposition. As Figure 6-6 shows, the double layer charging/discharging period extends beyond that of the DPS deposition. Without the additional capacitance of the SPS-S deposition, the current maximum may have been resolvable from the transient response.

The SPS deposition technique also yielded current vs. time transient responses that monotonically decreased with time. However, for this technique, the currents at all times were significantly lower than the currents produced from the SPS-S deposition technique. Figure 6-8 contains the plots of the current versus the inverse of the square root of time for all three transient responses given in Figure 6-6. The data point at short times, $t < 5$ seconds, and at long times, $t > 45$ seconds, are omitted from the plots given in Figure 6-8.

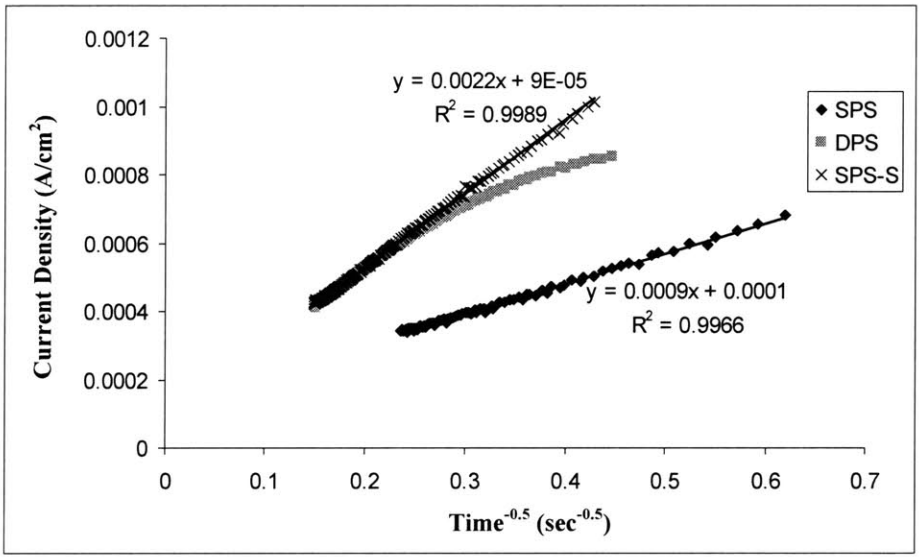

Figure 6-8: Plots of the current versus time$^{-0.5}$ (Cottrell plots) for all three transient responses given in Figure 6-6. The data point at short times, $t < 5$ seconds, and at long times, $t > 45$ seconds, are omitted from the plots. A least square linear regression was applied to the SPS and SPS-S data

The SPS and SPS-S data yielded linear plots which suggest that the surface reactions occurred under planar diffusion control for most of the deposition period. Figure 6-8 more clearly shows that the SPS-S and DPS transient responses are essentially the same at long times. Recall from Section 5.4.1 that the Cottrell equation,

$$i = \left(\frac{nFD^{1/2}C_o}{\pi^{1/2}} \right) t^{-1/2} \tag{6.15}$$

effectively describes the transient response for deposition under planar diffusion control. The slope of the SPS plot is approximately half that of the SPS-S plot.[2] This halving of the slope indicates that the dominant reaction occurring during the SPS deposition on the porous membrane is

$$PtCl_6^{2-} + 2e^- \rightarrow PtCl_4^{2-} + 2Cl^- \qquad (6.16)$$

For this reaction n in the Cottrell equation is equal to 2 in stead of 4, which explains the halving of SPS slope compared to the SPS-S slope.

The fact that no current maximum was observed on the current versus time transient responses during SPS deposition is consistent with the conclusion that reaction (6.16) was the dominant reaction. Based on the Scharifker and Hills theory, the initial increase in current is due to the increase in Pt area and Pt nuclei while spherical diffusion dominates [13]. Since no Pt was being deposited, the current simply decreased with time. The behavior of SPS deposition on the membrane is different from what was observed for the SPS deposition on glassy carbon at 0.1 V (see Section 5.4.1). On glassy carbon, the SPS deposition yielded a transient response that was consistent with the 4 electron reduction of chloroplatinate ion to Pt atoms,

$$PtCl_6^{2-} + 4e^- \rightarrow Pt + 6Cl^- \qquad (6.17)$$

Previous studies have found that, for Pt deposition on glassy carbon or graphite electrodes in contact with a chloroplatinate ion containing solution, Pt deposition at potentials less than 0.2 V provide a sufficient overpotential for Pt nucleation and growth [14, 15, 16]. However, this appears not to be the case for SPS deposition on the PTFE-

[2] The slope of the SPS-S Cottrell plot is equal to slope obtained for the Cottrell plot of the DPS deposition on glassy carbon (refer to Section 5.4.1). The diffusion coefficient calculated from this slope is $D = 4.1 \times 10^{-6}\, cm^2/s$, which is only 9 % lower than the value previously reported in the literature for the same deposition solution [15].

bonded membranes used in this work. The reasons for this behavior are not fully understood. One possible explanation is that the carbon black particles that formed the PTFE-bonded membranes were contaminated with adsorbed organic functional groups. Surface functionalities, either from organic impurities or carbon corrosion, can be detrimental to Pt deposition [14].

The carbon black particles were not pretreated before they were used to make the membranes. After forming the PTFE-bonded membranes, they were heat treated in an air oven at 280°C for 30 minutes to decompose the surfactant. The temperature and time of this procedure may not have been sufficient to completely remove the organic residue from the surfactant. The PTFE-bonded membranes were observed to have a lower open circuit potential (OCP) than glassy carbon electrodes. Since organic contaminates are known to reduce the OCP of an electrode, the OCP measurements support the idea of a contaminated membrane. Also, the double layer charging/discharging current (from the cyclic voltammogram) of the PTFE-bonded membranes were observed to be higher than that of glassy carbon. A pseudocapacitance resulting from the absorbed organic molecules may have contributed to the higher current (see below for further discussion). In future work, the membranes should be more rigorously cleaned to reduce the presence of surface contaminants. Additionally, Fourier transform infrared (FTIR) spectroscopy and other techniques should be used to investigate the surface groups on the carbon. A determination should be made on how these surface groups affect Pt deposition.

The SPS deposited films were visually inspected after deposition. Regardless of deposition time, most of the surface remained black, which indicated that Pt was not deposited in that region. For deposition times greater than 30 seconds, small randomly

distributed sections of the membrane appeared gray in color. This color change indicated that Pt particles were deposited on these regions of the membrane. In these cases, Pt nuclei were most likely formed by the disproportionation reaction,

$$2PtCl_4^{2-} \rightarrow Pt+PtCl_6^{2-}+2Cl^- \tag{6.18}$$

The growth the Pt nuclei then proceeded by the reaction given by Equation (6.17). The gradual transition from the 2 electron reaction to a 4 electron reaction probably explains the increase in current at times greater than 30 seconds for the SPS transient response.

The DPS technique yielded transient responses that produced a current peak that fell outside the double layer charging/discharging current. As Figure 6-6 and Figure 6-8 show, the DPS transient response approaches that of the SPS-S at long times. The current maximum, i_m, at the time t_m of the DPS plot shown in Figure 6-6 can be used to plot the instantaneous nucleation and progressive nucleation curves predicted by the theory of Scharifker and Hills [13]. Recall from Section 5.4.1 that the instantaneous nucleation equation is

$$\frac{i^2}{i_m^2} = \frac{1.9542}{t/t_m}\left\{1-\exp\left[-1.2564\left(\frac{t}{t_m}\right)\right]\right\}^2 \tag{6.19}$$

and the progressive nucleation equation is

$$\frac{i^2}{i_m^2} = \frac{1.2254}{t/t_m}\left\{1-\exp\left[-2.3367\left(\frac{t}{t_m}\right)^2\right]\right\}^2 \tag{6.20}$$

Figure 6-9 compares the plot, in terms of the reduced variables i/i_m and t/t_m, of the DPS transient response data to the theoretical transients given by Equations (6.19) and (6.20). In the time range near the current maximum, the DPS experimental data follows the theoretical response for instantaneous nucleation. The SEM images given in Figure 6-10

show that the deposited Pt clusters are about equal in size. This observation supports instantaneous nucleation as the deposition mode for DPS deposition on the PTFE-bonded membranes. When instantaneous nucleation occurs, the diffusion coefficient, D, of the reducing ion can be estimated form the formula

$$i_m^2 t_m = 0.1629 D(nFC_o)^2 \tag{6.21}$$

where C_o is the bulk concentration of the reacting ion, and n is the number of electrons transferred during the electrodeposition reaction.

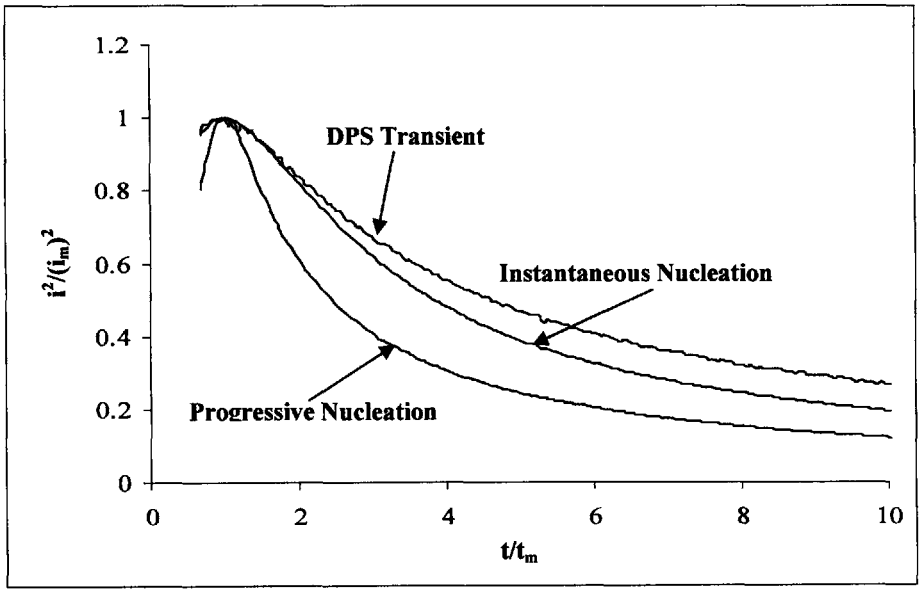

Figure 6-9: $(i/i_m)^2$ versus t/t_m analysis of the DPS experimental data, $i_m = 8.7\times10^{-4}\,A/cm^2$ and $t_m = 3.62\,\text{sec}$

For the DPS transient given Figure 6-6, $i_m = 8.7\times10^{-4}\,A/cm^2$ and $t_m = 3.62\,\text{sec}$. The diffusion coefficient of the chloroplatinate ion calculated from Equation (6.21) is $D = 4.52\times10^{-6}\,cm^2/\text{sec}$. This value is essentially equal to the previously reported

diffusion coefficient of $D = 4.5 \times 10^{-6}\, cm^2 / \sec$, which was obtained for the same deposition solution as the one used in this work [15]

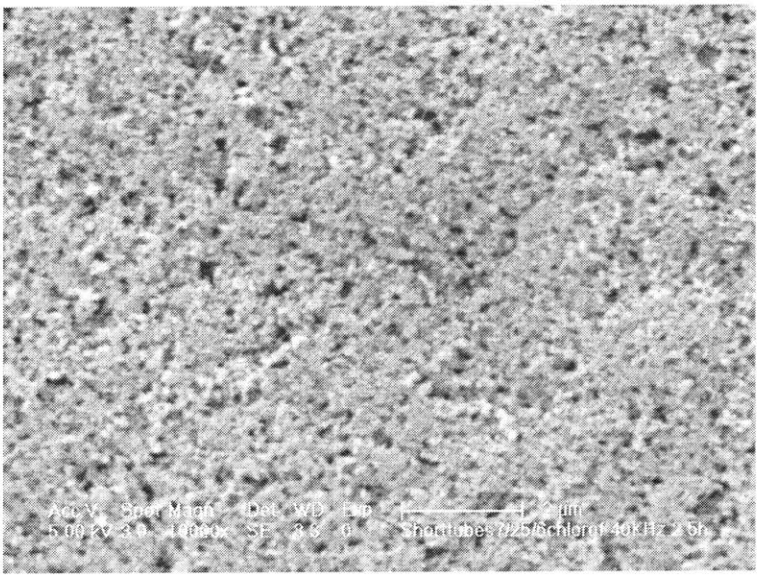

Figure 6-10: Surface image of Pt film deposited by the DPS deposition technique. Pt loading of 79.2 μg/cm^2

The transient responses during DPS deposition on glassy carbon did not produce a current peak (see Section 5.4.1). There was no resolvable peak because the DPS technique saturated the glassy carbon surface with Pt nuclei, which caused the t_m value to decrease to a time where the current peak was masked by the charging/discharging current. However, in the case of DPS deposition on the PTFE-bonded membrane, the porosity of the membrane prevents surface saturation by Pt nuclei.

The t_m values obtained for SPS deposition on glassy carbon were around 10.54 sec. This value is about 3 times greater than the t_m values observed for DPS deposition on the membrane. The smaller t_m value for DPS deposition on the membrane indicates that this technique produces a higher density of nucleation centers than the SPS deposition technique on glassy carbon. Based on the Scharifker and Hills theory, the

nucleation density for the DPS deposition on the membrane is 3 times greater than that for SPS deposition on glassy carbon. Additionally, the DPS deposition on the membrane operated under instantaneous nucleation mode while SPS deposition on glassy carbon operated under a progressive nucleation mode.

Figure 6-9 shows that shortly after the peak current the experimental current is greater than the current of the theoretical instantaneous nucleation curve. A similar observation was made for SPS deposition on glassy carbon. In that case, the experimental current exceeded the current predicted by the progressive nucleation equation. In both of these situations, the currents are higher than the theoretical currents because secondary nucleation causes the surface area of the Pt deposits to increase at a faster rate than what is expected for semi-hemispherical growth of particles. The high specific area measurements for these films support this conclusion.

6.4.2 Cyclic Voltammograms of Membranes

Figure 6-11 contains the cyclic voltammograms of a polished glassy carbon and oven dried 15wt% PTFE-bonded membrane. The current density of the membrane was greater than that of the glassy carbon. This result may indicate a higher double layer specific capacitance value and/or a higher wetted surface area of the membrane compared to that of the glassy carbon. Carbon surfaces exhibit a double layer capacitance of 10 to 20 $\mu F/cm^2$ in aqueous electrolytes [17]. The natural difference in specific capacitance among different carbon types, may contribute to the observed difference in the voltammograms given in Figure 6-11. The membrane may also have a higher specific capacitance as a result of a pseudocapacitance caused by adsorbed organic functional

groups on the carbon black surface. The glassy carbon surface most likely has a lower amount of these functional groups.

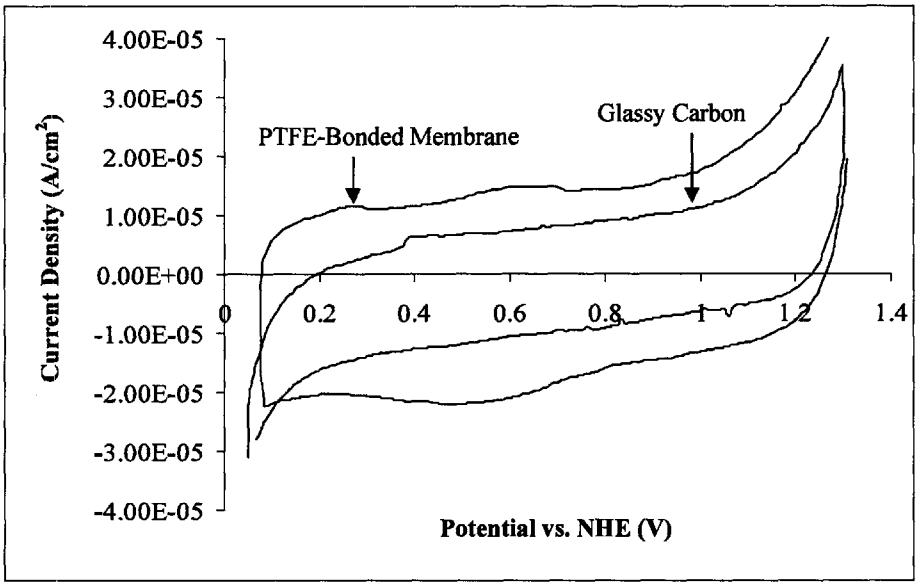

Figure 6-11: Voltammograms of glassy carbon electrode and 15 wt% PTFE-bonded membrane in 0.5 M H_2SO_4 solution

It is believed that the major reason for the differences in the voltammograms given in Figure 6-11 is the higher wetted area of the membrane compared to that of polished glassy carbon. Although the membrane is porous and electrolyte does not imbibe into the membrane, the wetted area of the membrane can still be greater than the polished glassy carbon due to the surface roughness of the membrane. For example, Vulcan XC72 carbon black has a specific area of 254 m^2/g. The average size of the particles is about 30 nm in diameter. The measured specific area of the Vulcan XC72 is greater than the 100 m^2/g expected for smooth carbon spheres with a diameter of 30 nm. The higher specific area is due to small cavities on the carbon black particles. The wetted area of the membrane is increased as a result of these cavities.

Figure 6-12 is a voltammogram of a PTFE-bonded membrane saturated with 0.5 M sulfuric acid. The average anodic current density in the double layer region (0.4 to 0.6 V) of the voltammogram is about 0.23 A/cm^2. This value for the unsaturated membrane of Figure 6-11 is about 1.3×10^{-5} A/cm^2. These results suggest that the wetted area of the saturated membrane is about 18,000 times that of the dry membrane and about 35,000 times that of the polished glassy carbon. If one assumes that the glassy carbon was atomically smooth and the specific capacitance of the glassy carbon is equal to that of the carbon black, then the wetted surface area of membrane per geometric area is 35,000 cm^2_C/cm^2.[3] The solid mass of the 15 wt% PTFE-bonded membranes used in this work is about 15 mg.

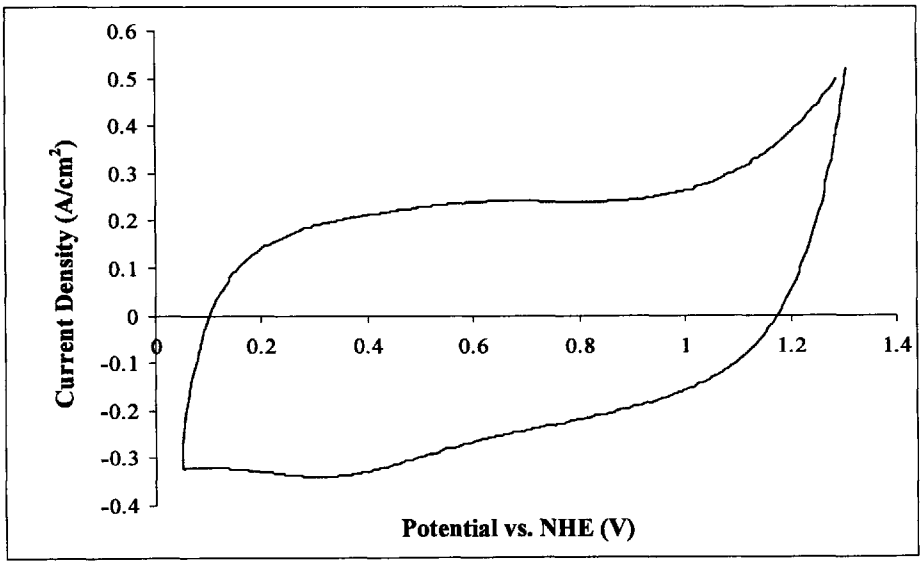

Figure 6-12: Voltammogram of 15 wt% PTFE-bonded membrane fully saturated with 0.5 M H_2SO_4

A 15 wt% PTFE-bonded membrane with this mass has a carbon surface area of about 32,000 cm^2_C/cm^2. This value is approximately equal to the wetted area ratio between

[3] The unit cm^2_C denote the surface are of carbon black.

the saturated membrane and glassy carbon. These results provide strong evidence that the membranes were fully saturated with the electrolyte. The porosity measurements of the PTFE-bonded membranes also supported this conclusion (see Section 4.4.1).

Figure 6-13 contains the cyclic voltammograms of a 15 wt% PTFE-bonded membrane with no Pt and a 15 wt% PTFE-bonded membrane with a nucleation layer. The nucleation layer was deposited on the membrane via a potential hold at -0.2 V for 1 second while the membrane was exposed to the electrodeposition solution.

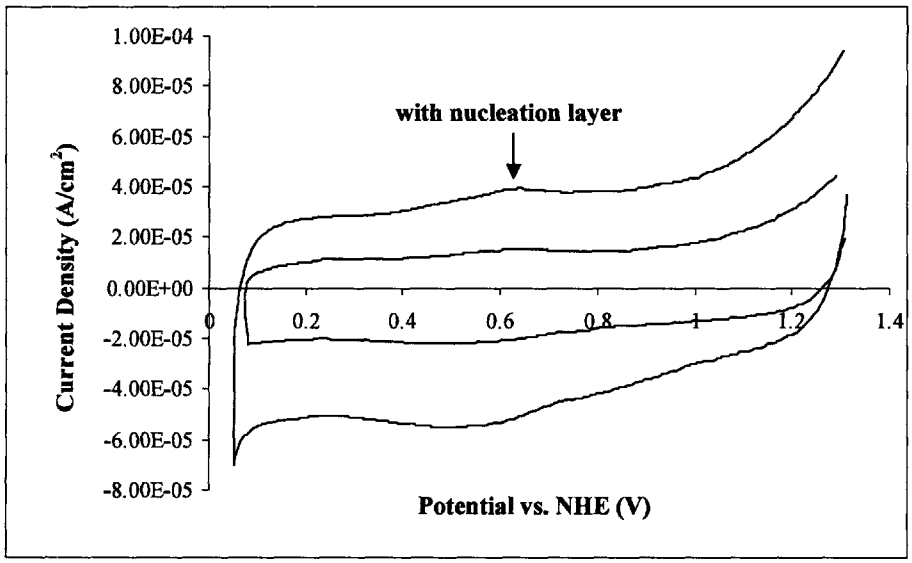

Figure 6-13: Voltammograms of 15 wt% PTFE-bonded membrane with no Pt and with Pt nucleation layer

Figure 6-13 shows that the anodic current density in the double layer region more than doubles in the presence of a nucleation layer. This increase in double layer charging current is not due to the deposited Pt nuclei.[4] Rather, the presence of Pt nuclei improves the wettability of the membrane surface. This conclusion is supported by the fact that water was attached to the surface of membranes with a nucleation layer after the dry

[4] A comparison of the voltammograms of a glassy carbon electrode with and without a nucleation layer showed negligible differences in the current density in the double layer region. Refer to Figure 5-18.

membranes were submerged in water. The membranes without a nucleation layer remained completely dry after being submerged in water.

For Pt films electrodeposited by the DPS technique, the membrane's capacitance per geometric area did note increase beyond what was expected for an increase in Pt area. This observation suggests that Pt only deposited on the nuclei that were formed during the potential step at -0.2 V. The additional Pt deposits, unlike the nucleation layer, did not increase the ability of the deposition solution to wet the internal pores of membrane. Thus, the DPS technique deposits Pt strictly on the surface of the membrane just like it would if the membrane was not porous. Consequently, the resulting Pt film is flat and very thin. Such a film is preferred since a thin active region maximizes the density of triple phase boundaries. A high density of triple phase boundaries allows the entire Pt film to operate under no oxygen transport losses at high current densities (see Section 6.4.2).

6.4.3 Cyclic Voltammograms of Pt Films:

Figure 6-14 contains representative cyclic voltammograms for Pt films deposited by the three deposition techniques. The Pt loadings are 58.9, 59.8, and 61.3 $\mu g/cm^2$ corresponding to the Pt film deposited by the SPS, DPS, and SPS-S techniques, respectively. The peaks for the hydrogen atom adsorption/desorption on the Pt(110) and Pt(100) facets are not as prominent on these voltammograms as those peaks are observed to be on voltammograms for polycrystalline Pt. A similar observation was made for Pt films deposited on glassy carbon (see Section 5.4.1). In the case of the Pt films electrodeposited on glassy carbon, the differences in hydrogen peaks between the films and polycrystalline Pt were attributed to differences in the Pt crystallography.

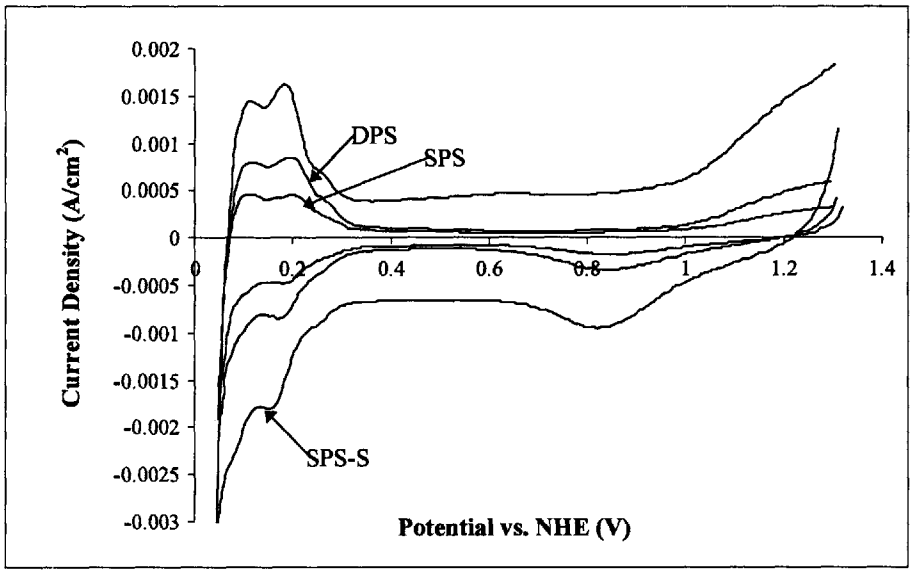

Figure 6-14: Cyclic voltammograms for Pt films deposited by the three deposition techniques. The Pt loadings are 58.9, 59.8, and 61.3 μg/cm² corresponding to the Pt film deposited by the SPS, DPS, and SPS-S techniques, respectively

The electrodeposited Pt films are believed to have a lower number density of Pt (110) and Pt(100) facets compared to the number density of these facets found on the surface of polycrystalline Pt. These facets are replaced with high-Miller index facets and Pt(111) facets [18]. The hydrogen peaks on the cyclic voltammograms of the electrodeposited Pt are observed to be less prominent because the areas under the peaks of the high-Miller-index single-crystals are less than that of the Pt (110) and Pt(100) single-crystals [19, 20]. The crystallography of the electrodeposited Pt film is found to be less dependent on deposition substrate than deposition potential [21]. For this reason, it is believed the Pt crystallography for electrodeposited Pt on the PTFE-bonded membrane is similar to that of Pt electrodeposited on glassy carbon.

The cyclic voltammograms of Pt films deposited on glassy carbon (Figure 5-19) and on PTFE-bonded membrane (Figure 6-14), show that the potential range for the hydrogen adsorption/desorption region is smaller for Pt films deposited on a membrane

than Pt films deposited on glassy carbon. This difference in the hydrogen adsorption/desorption region is a result of the non-uniform potential distribution along the membrane during voltammetry. Another manifestation of this non-uniformity is the absence of the second hydrogen adsorption peak. Figure 6-14 shows, for all three types of deposited Pt films, the current decreases continuously after the first adsorption peak. The second peak is masked by the beginning of hydrogen evolution on certain locations on the Pt film. The presence of a Pt foil on the backside of the membrane (see Figure 6-4) mitigates this problem. Figure 6-15 show a cyclic voltammogram measured without the Pt foil on the backside of the membrane.

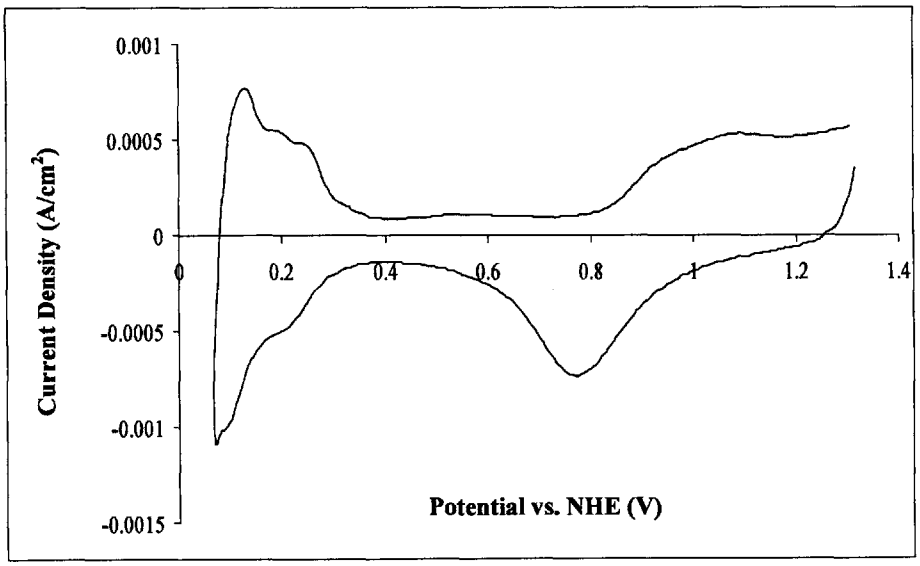

Figure 6-15: Cyclic voltammogram of Pt film taken without the Pt foil on the backside of the membrane. The Pt film was deposited by the DPS technique and the Pt loading is 29.7 μg/cm²

The voltammogram produced three peaks during the anodic scan in the hydrogen adsorption/desorption region. The first and most prominent peak was due to the oxidation of H_2 produced during the cathodic scan. The presence of this peak makes it difficult to accurately measure the hydrogen atom desorption charge needed to calculate

the Pt film area. For this reason, any condition that caused this peak to appear was avoided.

Figure 6-14 shows that double layer charging current of Pt film deposited by the SPS-S deposition technique is much greater than that of the other films. The higher charging current is not only due to a higher specific area of Pt deposited by the SPS-S technique. As was previously discussed, the sputtered Pt film allows the electrolyte to wet pores as far as 1 μm deep into the membrane. This additional wetted area results in a higher double layer charging/discharging current. Unlike the DPS technique, SPS-S deposition allows Pt to deposit within the pores that are near the surface of the membrane.

Figure 6-16 is a voltammogram of Pt film deposited by the DPS technique on the surface of a 10 wt% PTFE-bonded membrane.

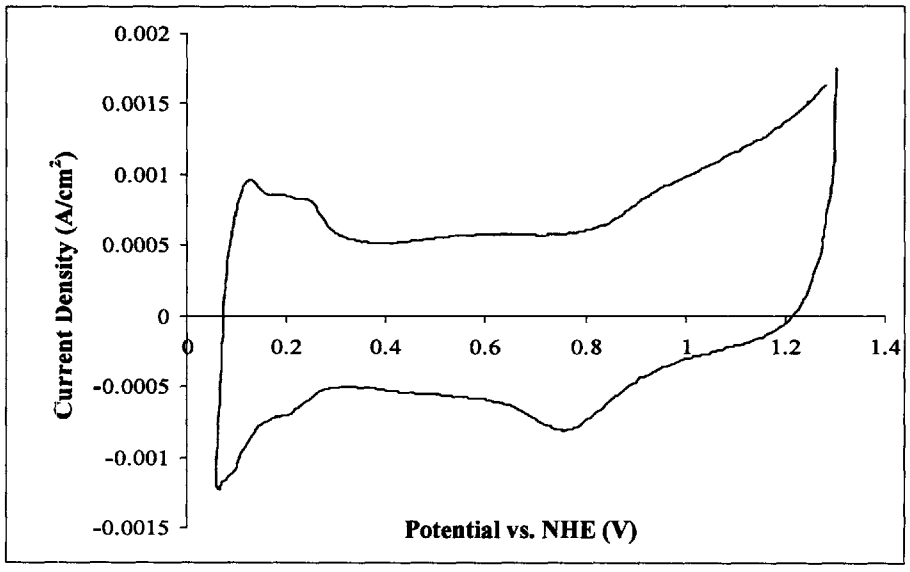

Figure 6-16: Cyclic voltammogram of Pt film deposited on 10 wt% PTFE-bonded membranes. The Pt loading is 20.1 μg/cm².

The double layer charging current for this Pt film/membrane is much greater than that of Pt films deposited by the DPS technique on 15 wt% PTFE-bonded membranes. This

result indicates that the lower PTFE content allowed the electrolyte to wet some the pores near the surface of the membrane. Furthermore, the double layer charging current of the 10 wt% PTFE-bonded membrane was observed to increase over time. This observation indicates that the electrolyte was slowly leaking into the membrane. An increase in double layer charging current was not observed for membranes with a PTFE content of 15 wt% or higher.

During electrodeposition, the deposition solution should not leak into the pores of the membrane. This ensures that Pt deposits only on the surface of the membrane and an ultra thin Pt film results. Since a thin film is desired, Pt should not be deposited on membranes with PTFE content of 10 wt% or less.

6.4.4 Specific Area of Electrodeposited Pt Films

Figure 6-17 contains the plots of the specific area versus Pt loading for films deposited by all three deposition techniques.

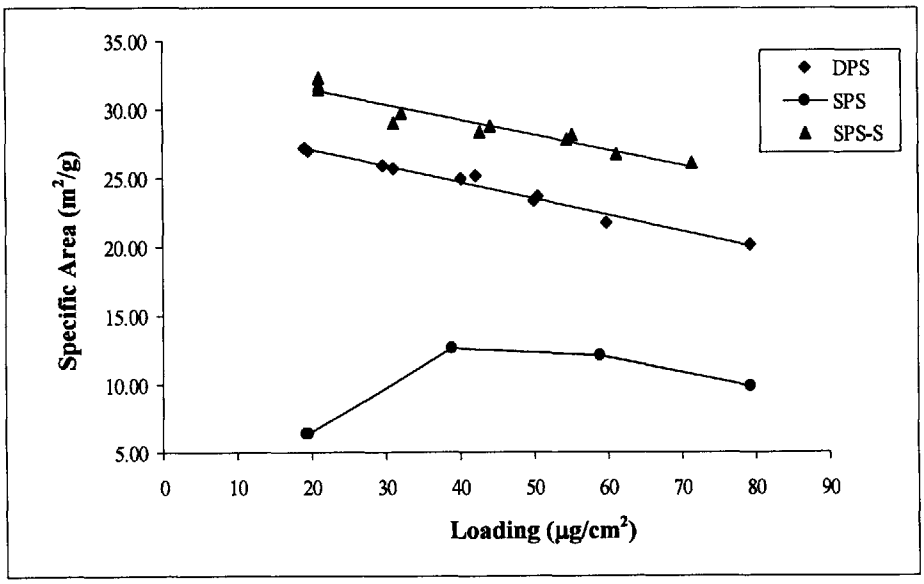

Figure 6-17: Plots of the specific area vs. Pt loading for films electrodeposited by the DPS, SPS, and SPS-S deposition techniques

As expected, the specific areas of SPS deposited Pt films are much lower than those of films deposited by other two techniques. Recall that the Pt loading for all films was calculated assuming 100% Faradaic efficiency for the deposition of Pt (see Equation (6.14)). In the case SPS deposition, Pt deposition is not the dominant reaction. Therefore, the calculated loading of the SPS films is much higher than the actual Pt loading on the membrane. Consequently, the calculated specific area is much smaller than the actual value. For the SPS films, the specific area is first observed to increase with loading. This occurs because as the deposition time increased, more Pt nuclei and small Pt particles were formed on the surface of the membrane by the disproportionation reaction. The presence of the Pt particles increased the Faradaic efficiency for Pt deposition. At longer deposition times, the growth of these particles outpaced the benefits of a higher Faradaic efficiency. As a result of this, the specific area is observed to decrease.

The SPS-S deposited Pt films have a specific area that is about 4 m^2/g higher than the DPS deposited films at a given Pt loading. The sputtered Pt film was deposited both on the surface of the membrane and within a small region inside the membrane. This additional Pt growth area promotes secondary nucleation, which is essential to producing high specific area films. Thus, the higher specific areas of the SPS-S deposited films compared to those of the DPS deposited films are due to the additional area that Pt deposited in the pores provide to the SPS-S deposited films.

In Section 5.4.1 it was shown that that the Pt surface area per unit area of substrate (or roughness factor), A_{Pt}, can fit the empirical equation

$$A_{Pt} = \alpha\left(Pt_L^* - 1\right)^{\kappa} \tag{6.22}$$

where $Pt_L^* = Pt_L / Pt_L^o$. Pt_L^o is interpreted as the minimum Pt loading for which hydrogen desorption charge can be resolved from the voltammogram. It is assumed to have a value of 0.5 μg/cm^2. α and κ are the fitting parameters. The simple model developed in Section 5.4.1 suggests the parameter κ indicates how the Pt film is growing. $\kappa = 1$ if Pt film is growing only by increasing the number of particles of constant size, and $\kappa = 2/3$ if the Pt film is growing only by increasing the size of the crystallites.

Figure 6-18 shows the plots of A_{Pt} vs. $Pt_L^* - 1$ for the Pt films deposited by the SPS-S and DPS techniques. The figure shows that the data for both techniques fits Equation (6.22) very well.

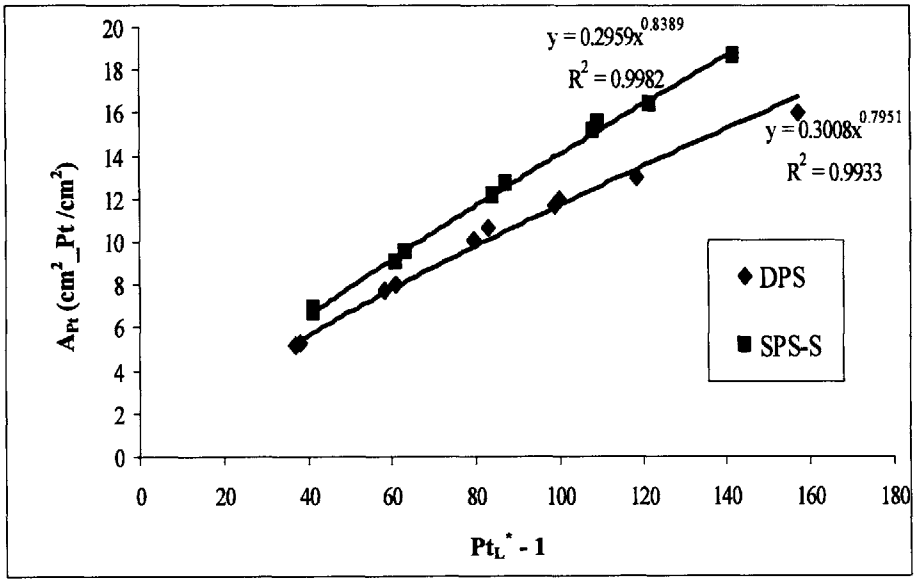

Figure 6-18: Plots of A_{Pt} vs. $Pt_L^* - 1$ for Pt films deposited by the DPS and SPS-S deposition techniques

The values for the fitting parameters as well as the square of the correlation coefficients are listed in Table 6-1. The κ value for both of the SPS-S and DPS techniques are greater than 0.75. These results suggest that for both types of electrodeposition

techniques the Pt film growth is dominated by secondary nucleation, which causes the increase in particle density over the increase in crystallite size.

Type of Pt Deposition	κ	α	R^2
SPS-S	0.8389	0.2959	0.9982
DPS	0.7951	0.3008	0.9933

Table 6-1 Parameters of deposition model

Although SPS-S technique produces films with a higher specific area than films deposited by the DPS technique, the latter is favored since Pt is only deposited on the surface of the membrane. An ultra thin film is desired in order to minimize the potential of oxygen transport losses within the electrolyte. The DPS films were the only films tested for their oxygen gain behavior in this work.

6.4.5 Oxygen Gain of Pt Films

Figure 6-19 contains the typical potential vs. time transient responses at different current values. At current values less than 100 mA/cm^2, the potential of the membranes tested reached a well defined steady state value. At higher current values, the potential transients grew unstable. Figure 6-19 shows that the potential transient for the 40.2 $\mu g/cm^2$ Pt film in pure oxygen became unstable around 140 mA/cm^2. The reason for the potential instability is not known. One possibility is the electrolyte-gas interface was disrupted due to excessive heating of the liquid electrolyte within the active regions of the electrode.

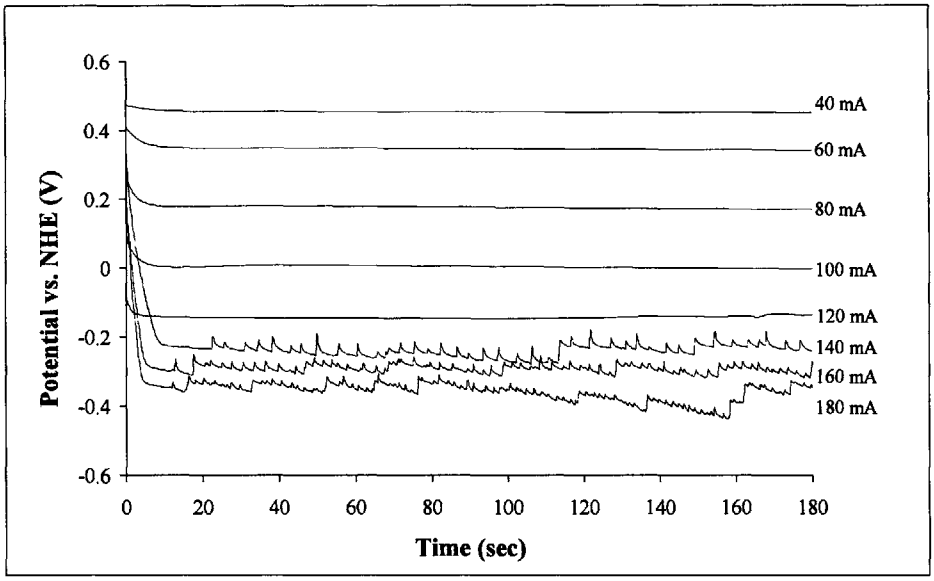

Figure 6-19: Potential vs. time curves for 40.2 μg/cm^2 Pt film deposited by the DPS deposition technique. Electrode was in 100% oxygen at 0.07 bar gauge pressure

Unlike conventional electrodes, the active region of the Pt film electrode of this work is extremely thin. For this reason, the volumetric heat generation resulting from the electrochemical reaction within the deposited film is much greater than the volumetric heat generation in the catalyst layer of conventional electrodes. Cahan, in 1968, used dark field microscopy to study the effect of heat generation on an electrolyte meniscus in contact with a Pt foil [2]. The electrolyte was 0.5 M sulfuric acid. The meniscus was formed in between a Pt foil and a SiO_2 window. The distance between them was 1 mm. Cahan observed that in the presence of hydrogen or oxygen and with the Pt foil at a high overpotential the edges of the meniscus became jagged and irregular. The jagged edges were observed to move erratically around the same mean position as occupied by the resting meniscus. Liquid droplets were also observed to form 25 to 125 μm from the main meniscus tip. Through modeling, Cahan determined the active region of the meniscus was no more than 100 nm from tip. Thus, the volumetric heat generation was

extremely high. For this reason, Cahan surmised that the observations he made were due to the effects that heat generation from the electrochemical reaction had on the meniscus, which he coined "meniscus heat effect". For the Pt films of this work, a similar excessive heating and moving of the liquid-gas interface may be responsible for the unstable potential measurements. In future work, a half-cell experiment should be designed which allows *in situ* observation of the Pt film surface.

In the Pt film electrode of this work, another phenomenon, slightly different than what as observed by Cahan, may have disrupted the electrolyte gas interface. A significant fraction of the heat generated at the liquid gas interface may be removed by evaporation of water from the sulfuric acid solution. The water that is evaporated from the interface is replenished by liquid water permeating through the membrane. Recall from Section 4.4.3 that the average liquid permeability of a PTFE-bonded membrane is about $1.42 \times 10^{-15}\,\mathrm{cm}^2$. This extremely low permeability indicates that a high pressure gradient is needed to move the electrolyte mass towards the Pt film. At a high enough evaporation rate, the liquid pressure in the pores can drop below a value that results in liquid boiling. This hypothesis was tested by developing a simple model for heat generation at the Pt film and water transport for the electrodes of this work. The MATLAB scripts for the model are given in Appendix C. The description of the model is given below.

Water Transport and Oxygen Gain Model:

Consider a system where the Pt film supported on a PTFE-bonded membrane is placed in the half cell apparatus in the manner described in Section 6.3.2. The membrane is saturated with 3.7 M sulfuric acid. The Pt film side of the membrane is exposed to

either oxygen or air. The top side of the membrane is exposed to 3.7 M sulfuric acid in the electrolyte container. The pressure of gas is slightly above atmospheric pressure in order to overcome the hydrostatic head of the electrolyte column. Gas flows at a modest rate of 1 to 2 bubbles per second. The assumptions and essential equations of the model are provided below.

The potential and mass fraction (or concentration) of the electrolyte within the membrane are assumed to be uniform. The potential is set equal to 0, and the mass fraction is assumed to be 0.30. The mass fraction of sulfuric acid in 3.7 M H_2SO_4 solution is about 0.30 [22]. A detailed model using the concentrated solution theory, where the potential and mass fraction were not assumed to be uniform, was developed. The solutions to this model indicated that the uniform potential and mass fraction assumptions are valid for the current densities applied in this work. Within the membrane's pores, the temperature of the electrolyte is constant and equal to 25°C.

The Pt film active region is assumed to be infinitely thin. The Tafel equation is used to describe oxygen reduction on the Pt film. The Tafel slope is assumed to be independent of temperature and equal to 120 mV/decade. The exchange current density, i_o, is dependent on temperature and the ORR activation energy, E_A, is assumed to be 25 kJ/mol. The Tafel equation is

$$i = i_o(T) A_{Pt} P_{O_2} \exp\left(\frac{\eta}{0.120}\right)$$

where (6.23)

$$i_o(T) = i_o(T=298)\exp\left[\left(\frac{E_A}{R}\right)\left(\frac{1}{T}-\frac{1}{298}\right)\right]$$

i is the applied current density and P_{o_2} is the oxygen partial pressure, in bars, at the Pt film interface. T is the temperature of the Pt film. The heat flux of the Pt film, $\dot{q}_k$, is only due to the kinetic irreversibilities. It is given by

$$\dot{q}_k = 0.120 i \log\left(\frac{i}{i_o(T) A_{Pt} P_{o_2}}\right) \tag{6.24}$$

Equation (6.24) assumes no oxygen transport losses within the Pt films. At a steady state, all the heat generated is assumed to transfer out of the film by evaporation of water.

The temperature of the liquid electrolyte in contact with Pt film is T. The water vapor at Pt film interface is in thermodynamic equilibrium with the electrolyte, 3.7 M H_2SO_4. The water vapor pressure in bars is given by the correlation [22]

$$P_{H_2O,@Pt} = \exp\left[-0.0001808T^2 + 0.16803T + 37.773\right] \tag{6.25}$$

The difference in partial molar enthalpy of water leaving the electrolyte phase and entering the gas phase is assumed to be equal to the heat of vaporization of pure water. This assumption is valid since the heat of solution for H_2SO_4 and liquid water is small in comparison to the heat of vaporization of water. The heat flux removed by evaporation, $\dot{q}_{evap}$, is given by

$$\dot{q}_{evap} = N_{H_2O} \Delta H(T) = N_{H_2O}\left(-0.03T^2 - 24.2T + 53{,}880\right) \tag{6.26}$$

where N_{H_2O} is the molar flux of water in the gas phase. At steady state $\dot{q}_k = \dot{q}_{evap}$.

Gas transport from the Pt film to a distance 4 mm away from the film is modeled using the Stefan-Maxwell diffusion equations,

$$\vec{\nabla} P_i = \sum_{j \neq i}^{n} \frac{RT_G}{P_G D_{i,j}} \left(P_i \vec{N}_j - P_j \vec{N}_i\right) \tag{6.27}$$

where P_i is the partial pressure of species i, N is the molar flux of species i or j, $D_{i,j}$ is the binary diffusion coefficient of species i and j, P_G is the total pressure of the gas which is assumed to be constant and equal to 10^5 Pa, T_G is the temperature of the gas, and n is the total number of species in the gas phase. The Stefan-Maxwell equation has $n-1$ independent equations. The above differential equations are solved numerically for an oxygen and water system or oxygen, water, and nitrogen system. The Pt film is at a position of $x = 0.4\,cm$. Note that the molar fluxes are constant since there are no homogeneous reactions within the gas compartment of the electrode holder. The molar flux for oxygen is given by

$$N_{O_2} = \frac{i}{4F} \tag{6.28}$$

An iterative scheme is used to obtain the molar flux of water and the temperature of the Pt film. An illustration of the iterative scheme is given in Figure 6-20.

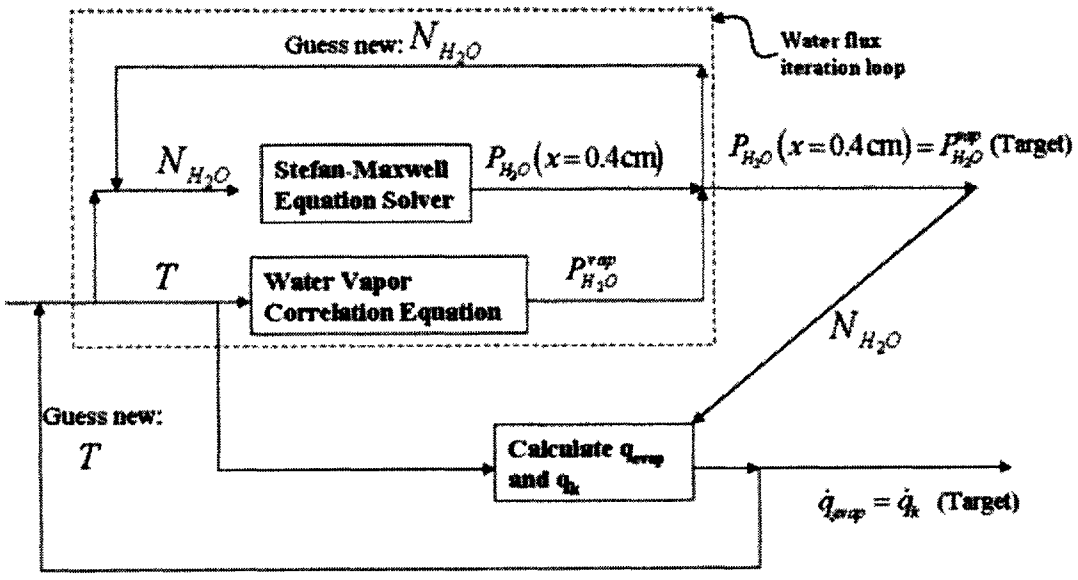

Figure 6-20: Illustration of the iterative scheme for oxygen gain model

For a guessed temperature of the film, the flux of water is guessed and Equation (6.27) is solved. The flux is increased or decreased until the partial pressure of water at $x = 0.4\,cm$ is equal to the partial pressure given by Equation (6.25). The water flux that satisfied this condition is then used to calculate $\dot{q}_{evap}$ from Equation (6.26). These series of calculations are repeated until the guessed temperature of the film leads to $\dot{q}_k = \dot{q}_{evap}$ to within 0.1%. It should be noted that the water flux is negative.

The membrane is assumed to remain saturated with electrolyte regardless of liquid pressure between 1 and 0 bar. For a gas pressure of 1 bar and an electrolyte pressure of 0 bar, the capillary pressure is still below the values that lead to gas bubbling for the PTFE-bonded membranes (see Section 4.4.2). The flow of the electrolyte in the membrane pores is governed by Darcy's Law. The electrolyte pressure at the Pt film interface, $P_{L,@Pt}$, is given by

$$P_{L,@Pt} = 1 - \left(\frac{\mu_e L}{k}\right)\frac{\dot{m}}{\rho_e} \tag{6.29}$$

where μ_e and ρ_e are the dynamic viscosity and density of the electrolyte, respectively. k and L are the permeability and thickness of the membrane, respectively. $\dot{m}$ is the mass flux of the electrolyte towards the Pt film interface. Its value is given by

$$\dot{m} = N_{H_2O} mw_{H_2O} - N_{O_2} mw_{O_2} \tag{6.30}$$

where mw_i is the molecular weight of species i. The pressure of the electrolyte at the top surface of the membrane is assumed to be 1 bar.

The above model was applied to the 40.2 μg/cm^2 Pt deposit. The parameters of the model are given in Appendix C. Figure 6-21 contains the theoretical plots of the Pt

film temperature and electrolyte pressure at the Pt film versus the applied current when Pt film is exposed to oxygen. The model predicts that the liquid pressure drops below 0 bar around 80 mA/cm^2. In reality the liquid would begin to boil in the pores before the pressure drops below 0 bar. Therefore, the model does suggest that liquid boiling due to an excessive drop in the liquid pressure can disrupt the liquid-gas interface which, in turn, causes an unstable potential. The experimental data has the current going unstable around 140 mA/cm^2 and not the predicted 80 mA/cm^2. This discrepancy may be related to the assumption that all the heat from the electrochemical reaction is removed by water evaporation. The elevated temperature of Pt interface indicates that other modes of heat transfer, such as natural convection in the gas phase and conduction through the membrane, are operative in the system. An exclusion of these heat transfer modes may explain the above mentioned discrepancy.

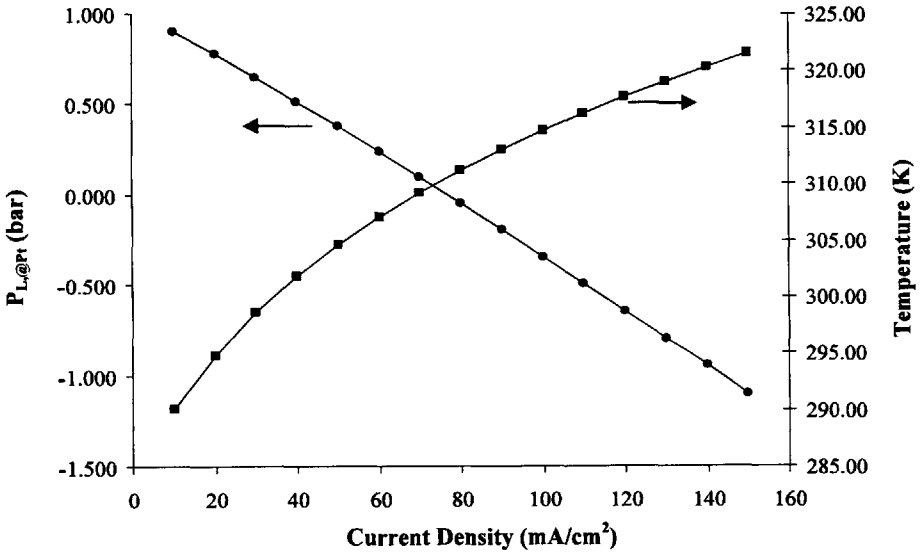

Figure 6-21: Model predictions for liquid electrolyte pressure at the Pt film vs. current density and temperature at the Pt film vs. current density

Although this present model is limited, it does provide qualitative support for the hypothesis that boiling of the electrolyte at the Pt film interface is the cause of the

potential instability. In future work, the model should be extended to include other heat transfer modes.

Oxygen Gain Data:

Figure 6-22 and Figure 6-23 contain the data for the oxygen gain experiments conducted in this work. Figure 6-22 contains the curves for an oxygen gain from air at 0.07 gauge pressure to oxygen at 0.07 gauge pressure. For all the Pt loadings, the curves are essentially constant up to a current density of about 130 mA/cm^2.

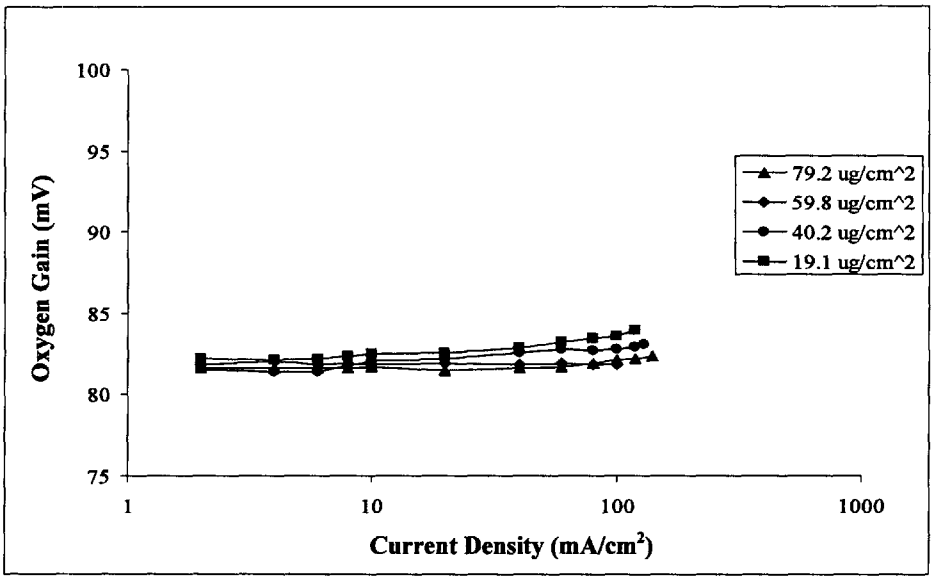

Figure 6-22: Oxygen gain vs. current density for DPS deposited films. Low pressure: 20% oxygen and 80% nitrogen at 0.07 bar gauge pressure and high pressure: 100% oxygen at 0.07 bar gauge pressure

The oxygen gain values are also approximately equal to the theoretical value for no oxygen transport losses (see Section 6.2). These results indicate that the Pt films, regardless of Pt loading, show no significant oxygen transport losses. As previously mentioned, a similar conclusion was reached by Cahan and Asher *et al.*, who sputter deposited thick Pt films onto Vycor glass. However, the results of this work have greater implications than the work done by Cahan and Asher *et al.* First, the PTFE-bonded

membrane is a much more practical material to deposit a Pt film than Vycor glass. Thus, practical electrodes that take advantage of the thin film catalyst deposits can be fabricated. Second, Cahan and Asher *et al.* did their experiments in oxygen at 1 bar. The results of this work indicate that even in air, at 20% the level of oxygen, the Pt films show no oxygen transport losses up to a current density of 130 mA/cm^2.

Figure 6-23 contains the oxygen gain results for two sets of experiments.

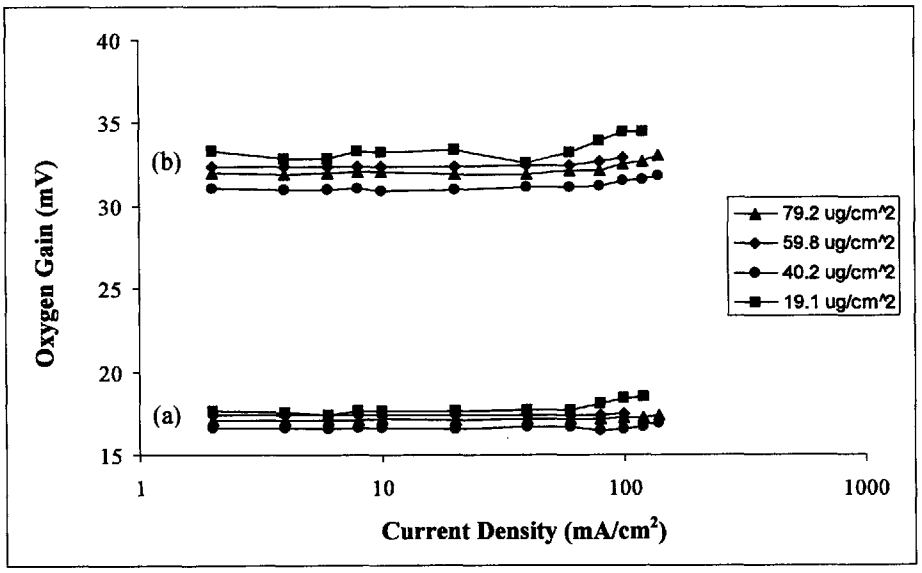

Figure 6-23: Oxygen gain vs. current density for DPS deposited films. The two sets of data are: (a) oxygen gain from a low pressure of 100% oxygen at 0.07 bar gauge to a high pressure of 100% oxygen at 0.5 bar gauge, and (b) oxygen gain from a low pressure of 100% oxygen at 0.07 bar gauge to a high pressure of 100% oxygen at 1 bar gauge

The first set involves the oxygen gain for increasing gauge pressure of oxygen from about 0.07 to 0.5 bar. The second set involves the oxygen gain for increasing the gauge pressure of oxygen from 0.07 to 1 bar. Both of these sets of experiments were done to see if higher capillary pressures would alter the liquid-gas interface and consequently affect the oxygen gain in different manner than increasing the partial pressure of oxygen at constant total pressure. The results of both sets of experiments indicate that the higher capillary pressures did not affect the oxygen gain results. The oxygen gain values are

essentially constant and the values are approximately equal to the theoretical value for no oxygen transport effects.

Figure 6-24 compares the oxygen gain curve for the 40.2 μg/cm^2 Pt film to the oxygen gain curve predicted by the theoretical model.

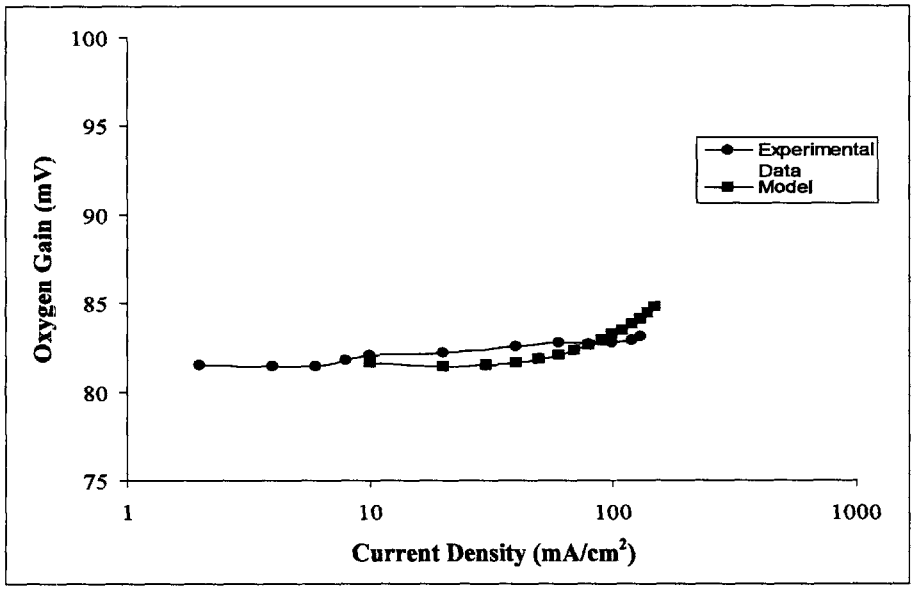

Figure 6-24: Experimental data and model predictions for oxygen gain on 40.2 μg/cm^2 Pt film deposited by the DPS deposition technique. Low pressure: 20% oxygen and 80% nitrogen at 0.07 bar gauge pressure and high pressure: 100% oxygen at 0.07 bar gauge pressure

The oxygen gain values of the model are approximately equal to the experimental data. At low current density, the model slightly under predicts the oxygen gain. This may have occurred because the actual Tafel slope of the Pt film is slightly greater than the 120 mV/decade assumed in model. Both the oxygen gain values of the model and experimental data slightly increase with an increase in the current density. However, the oxygen gain values of the model increases faster than the experimental data. The increase in oxygen gain of model is due to the higher partial pressure of water at the Pt film interface as the temperature of the film increases with an increase in current density.

A higher partial pressure of water results in a lower partial pressure of oxygen. It is also a result of the higher flux of water vapor at higher current densities, which has an adverse effect on the diffusion of oxygen gas to the Pt film. Both of these effects are greater when the film is exposed to air than when it is exposed to oxygen. This is due to the fact that more heat is generated when the film is exposed to air than when it is exposed to oxygen (see Equation (6.24)). The fact that the oxygen gain values of the model increase faster with an increase in current density than the measured oxygen gain values provides additional evidence that the model may be over predicting the temperature of the Pt film. A model that incorporates other modes of heat transfer will result in a lower partial pressure of water and lower flux of water at a given current density. This, in turn, will decrease the rate by which the oxygen gain increases with an increase in current density.

6.5 Conclusion

Electrodeposited Pt Films:

Thin Pt films were electrodeposited onto the 15 wt% PTFE-bonded membranes by the single potential step (SPS), the single potential step with Pt seed layer (SPS-S), and the double potential step (DPS) techniques. Since a dry polymer-bonded membrane did not imbibe the deposition solution, Pt was easily electrodeposited only on the surface of the porous membranes without the use of any pore-blocking material. The DPS technique produced Pt films with specific areas that ranged from 27 to 20 m^2/g for Pt loadings of 20 to 80 $\mu g/cm^2$. These specific areas are lower, at an equivalent loading, than the specific areas for Pt films deposited by the DPS technique on glassy carbon (see Section 5.4.3). The porosity of the membrane may explain the lower specific areas.

Another possibility is the lower activity for chloroplatinate reduction to Pt on the PTFE-bonded membranes compared to this activity on glassy carbon. This difference in activity was most apparent when the SPS deposition at 0.1 V did not lead to a dominant 4 electron reduction of chloroplatinate ion to Pt as it did on glassy carbon. Instead, the transient responses of SPS deposition on the membranes indicated that the 2 electron reduction reaction was dominant.

The SPS-S technique did produce Pt films with specific areas that were about 4 m^2/g greater than Pt films deposited by the DPS technique. These higher specific areas of the SPS-S films are believed to be due to the additional deposition of Pt within a 1 μm region from the surface of the membrane. Since Pt deposit within the membrane can be starved of oxygen during the operation of the cell, the benefits of higher specific areas for the SPS-S films may not be fully realized.

Oxygen Gain:

Oxygen gain experiments were conducted on DPS deposited Pt films. The results of the oxygen gain experiments indicate the electrodeposited Pt films experienced no oxygen transport losses in pure oxygen or in air up to a current density of 130 mA/cm^2. Previously, such enhanced oxygen transport behavior was only observed for Pt films deposited on Vycor glass. The polymer-bonded membranes presented in this dissertation represent a much more practical substrate for Pt deposition than Vycor glass. The results presented in this chapter strongly support the use of thin catalyst films in the proposed microfabricated electrode design. The microfabricated catalyst layer is predicted to operate essentially free of any oxygen transport losses (see Chapter 7).

The thin catalyst film technology can reduce oxygen transport losses. However, it may also introduce new challenges associated with localized heat generation. In the oxygen gain experiments, the potential transients were unstable at current densities greater than 130 mA/cm^2. This instability is believed to be the result of high volumetric heat generation within the platinum film. The excessive heating of the film disrupts the liquid-gas interface which, in turn, causes the potential instability. This phenomenon may be a problem for the microfabricated catalyst layer. For example, it may limit the operating current density of the electrode and/or limit the Pt loading within the cylindrical holes. The volumetric heat generation, at a given operating current density of the electrode, increases as the Pt loading increases. The high volumetric heat generation at the Pt film may also lead to excessive lost of electrolyte over the operating life of the cell. The model developed in Chapter 7 does not consider the thermal effects of the MFE. However, the results presented in this chapter suggest that these effects may be important.

References

[1] M.F. Weber, S. Mamiche-Afare, M.J. Dignam, L. Pataki, and R.D. Venter, "Sputtered fuel cell electrodes," *J Electrochem. Soc.*, Vol. 134, p. 1416, 1987.

[2] B. Cahan, PhD Thesis, Chemical Engineering Department, University of Pennsylvania, Philadelphia, PA, 1968.

[3] A.J. Asher and J.S. Batzold, in From Electrocatalysis to Fuel Cells, G. Sandstede, Editor, pp. 223-230, 1972.

[4] P. Bjornbom, "Influence of Diffusion Resistances on Gas Diffusion Electrodes", J. Electrochem. Soc., Vol. 133, p. 1874, 1986.

[5] J. Newman and K.E. Thomas, *Electrochemical Systems*, Third Edition, John Wiley & Sons, Inc., Hoboken, New Jersey, 2004.

[6] S. Srinivasan and H.D. Hurwitz, "Theory of a thin film model of porous gas-diffusion electrodes", *Electrochim. Acta*, Vol. 12, p. 495, 1967.

[7] J. Giner and C. Hunter, "The Mechanism of Operation of the Teflon-Bonded Gas Diffusion Electrode: A Mathematical Model", *J. Electrochem. Soc.*, Vol. 116, p. 1124, 1969.

[8] R.P. Iczkowski and M.B. Cutlip, "Voltage Losses in Fuel Cell Cathodes", *J. Electrochem. Soc.*, Vol. 127, p. 1433, 1980.

[9] J. O'M. Bockris and B.D. Cahan, "Effect of a Finite-Contact-Angle Meniscus on Kinetics in Porous Electrode Systems", *J. Chem. Phys.*, Vol. 50, p. 1307, 1969.

[10] K. Chan, G.S. Efthymiou, and J.F. Cocchetto, "A Wedge-Meniscus Model of Gas-Diffusion Electrodes", *Electrochim. Acta.*, Vol. 32, p. 1227, 1987.

[11] S. Singer, M.S. Thesis, Mechanical Engineering Department, Massachusetts Institute of Technology, Cambridge, MA, 2006.

[12] S Hirano, J Kim, and S Srinivasan, "High Performance Proton Exchange Membrane Fuel Cells with Sputter-Deposited Pt Layer Electrodes", *Electrochimica Acta*, Vol. 42, p. 1587, 1997.

[13] B. Scharifker and G.Hills, "Theoretical and Experimental Studies of Multiple Nucleation", Electrochimica Acta, Vol. 28, p. 879, 1983.

[14] J. Lin-Cai and D. Pletcher, "A Substrate Effects on the Catalytic Activity of Electrodeposited Platinum Layers", J. Electroanal. Chem., Vol. 149, p. 237, 1983.

[15] K. Shimazu, D. Weisshaar, and T. Kuwana, "Electrochemical Dispersion of Pt Microparticles on Glassy Carbon Electrodes", *J. Electroanal. Chem.*, Vol. 223, p. 223, 1987.

[16] M.M.E Duarte, A.S. Pilla, J.M. Sieben, and C.E. Mayer, "Platinum Particles Electrodeposited on Carbon Substrates", *Electrochemistry Communications*, Vol. 8, p. 159, 2006.

[17] K. Konoshita, *Carbon*, Wiley, New York, 1988.

[18] F.J. Rodriguez Nieto, M.A. Pasquale, C.R. Cabrera, and A.J. Arvia, "Morphology of Platinum Electrodeposits in the Three-Dimensional Sublayer to Full Layer Range Produced Under Different Potential Modulations on Highly Oriented Pyrolytic Graphite", *Langmuir*, Vol. 22, p. 10472, 2006.

[19] M.D. Macia, J.M. Campina, E. Herrero, and J.M. Feliu, "On the Kinetics of Oxygen Reduction on Platinum Stepped Surfaces in Acidic Media", *J. Electroanal. Chem.*, Vol. 564, p. 141, 2004.

[20] A. Kuzume, E. Herrero, and J.M. Feliu, "Oxygen Reduction on Stepped Platinum Surfaces in Acidic Media", *J. Electroanal. Chem.*, Vol. 599, p. 333, 2007.

[21] L.M. Plyasova, I.Y. Molina, A.N. Gavrilov, S.V. Cherepanova, O.V. Cherstiouk, N.A. Rudina, E.R. Savinova, and G.A. Tsirlina "Electrodeposited Platinum Revisited: Tuning Nanostructure via the Deposition Potential", *Electrochimica Acta*, Vol. 51, p. 4477, 2006.

[22] D.D. Wagman, *The NBS Tables of Chemical Thermodynamic Properties: Selected Values for Inorganic and C1 and C2 Organic Substances in SI Units*, American Chemical Society and the American Institute of Physics for the National Bureau of Standards, New York, 1982.

[23] E. Gileadi, *Electrode Kinetics for Chemists, Chemical Engineers, and Material Scientist*, Wiley-VCH, New York, NY, 1993.

Chapter 7

1-D Model of the Microfabricated Electrode (MFE)

7.1 Introduction

In this chapter, a 1-D half-cell model of the microfabricated electrode (MFE) is developed and the results of the model are presented. The MFE is in concentrated phosphoric acid and it is under the typical operating conditions of modern phosphoric acid fuel cells (PAFC). The model uses the experimental results from chapters 4, 5, and 6 in order to properly simulate the performance of the various components of the MFE. The results of the model are used to optimize the geometry of the microfabricated catalyst layer and to predict the potential performance of the MFE.

7.2 Description of System

The half-cell model consists of four layers: 1) the backing layer, 2) the diffusion layer, 3) the catalyst layer (patterned), and 4) the catalyst layer (un-patterned). The portion of the microfabricated catalyst layer that has the cylindrical holes will be referred to as simply the catalyst layer. The portion of the microfabricated catalyst layer that is not patterned will be referred to as the matrix layer. The functions of all four layers were described in detail in Chapter 3. The anode is not included in this model since the main purpose of the model is to predict the performance of the MFE electrode in a half-cell

experiment. Half-cell experiments are often used to measure the performance of electrodes in liquid electrolytes.

An illustration of the system is given in Figure 7-1. Recall, from the description given Section 3.4.1, that the catalyst layer consists of an array of uniform cylindrical holes spaced evenly apart. The radius of the cylindrical holes is represented by the symbol r and the hole-to-hole spacing is given by $2s$. s is half distance between the hole-to-hole spacing. It is referred to as "the spacing" in this chapter. The thickness of the catalyst layer is represented by the symbol L_{CL}.

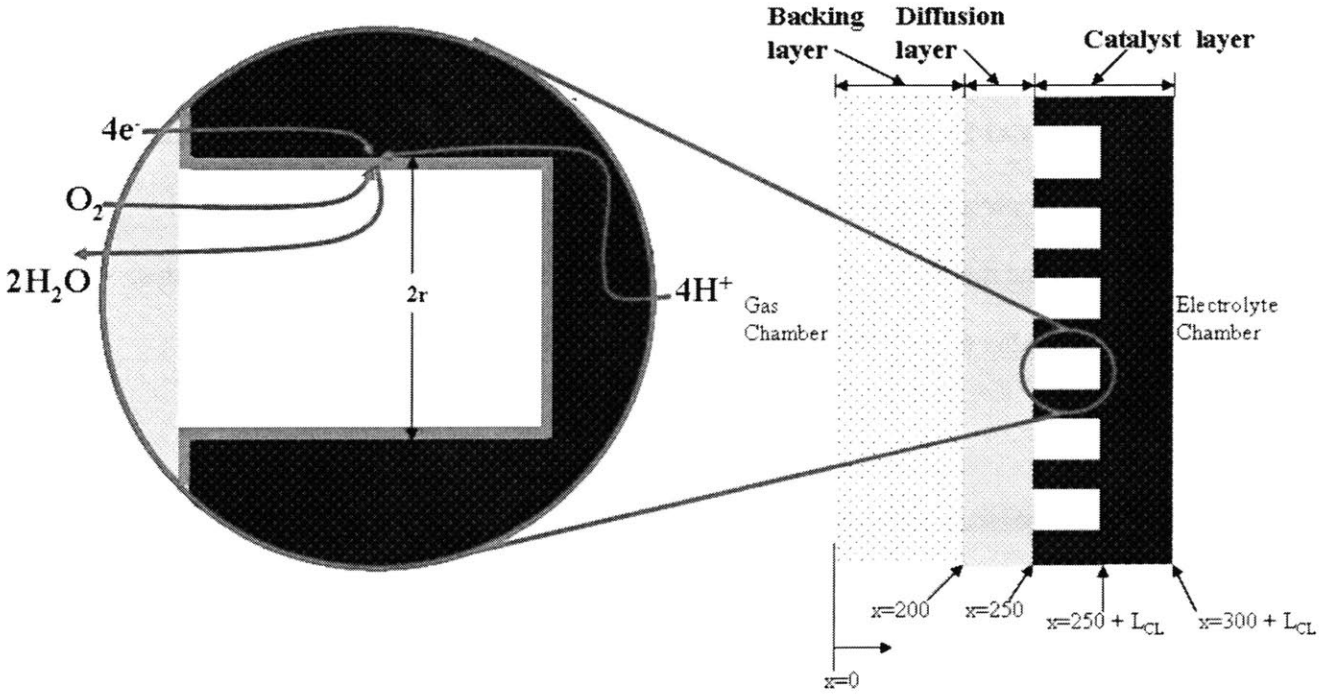

Figure 7-1: Schematic of half-cell system. Dimensions are in microns

The backing layer is made from wet-proof Toray carbon paper and the diffusion layer is made from carbon black bonded by sintered PTFE. Both layers are completely free of the electrolyte. The relevant properties of each layer are found in the literature. The catalyst layer is assumed to be made from the PTFE-bonded membranes described in

Chapter 4. The catalyst layer membrane has been embossed to form the three-dimensionally patterned macro-texture illustrated in Figure 3.9 and Figure 7-1. The matrix layer is simply the portion of the membrane which was not patterned. The properties of the PTFE-bonded membranes presented in Chapter 4 are the properties of the microporous region of the catalyst layer and the matrix layer.

It is assumed that uniform Pt films were loaded onto the microporous surfaces of the cylindrical holes by the double potential step technique described in Chapter 5 and 6. The Pt loading, Pt_L, is used to specify the amount of Pt that is loaded in these cylindrical holes. Pt_L is the mass of Pt per the total substrate area on which the Pt film is deposited. Thus, it has the same meaning as that given in Chapters 5 and 6. The experimental results from Chapter 6 are used to characterize the behavior of the Pt films in the model.

In PAFCs, the total Pt loading of the cathode catalyst layer per planar area of the electrode, $Pt_{L,total}$, ranges from 0.5 to 2 mg/cm^2. State-of-the-art cathodes for PAFCs commonly use 0.5 mg/cm^2 for the total loading. The thickness of the MFE catalyst layer is related to r, s, Pt_L, and $Pt_{L,total}$ by the following relationship:

$$L_{CL} = \left(\frac{Pt_{L,total}}{Pt_L} - 1 \right) \left(\frac{(2r+2s)^2}{2\pi r} \right) \tag{7.1}$$

The cylindrical holes of the catalyst layer are free of electrolyte. The microporous region of the catalyst layer and the entire matrix layer are saturated with electrolyte. These layers are assumed to remain saturated with the electrolyte regardless of the liquid pressure. The high breakthrough pressures of the PTFE-bonded membranes (See Section 4.4.2) support this assumption. The concentration of the electrolyte is assumed to be

uniform throughout the cell. The temperature of the electrode is also assumed to be uniform.

7.3 Mathematical Model

7.3.1 Backing Layer and Diffusion Layer

The backing and diffusion layers are used to transport electrons, reactant gases, and product gases to or from the catalyst layer. The transport equation for electrons in these layers is given by Ohm's law,

$$\vec{i}_s = -\kappa \vec{\nabla} \Phi_s \tag{7.2}$$

where $\vec{i}_s$ is the current flux due to electron flow in the solid regions of the layers and Φ_s is the electrical potential of the solid phase. The subscript s in these terms denotes solid phase. κ is the electric conductivity of the solid phase. The backing layer is made from Toray carbon paper. It has a through plane electric conductivity of 12.5 S/cm. The diffusion layer is assumed to have an electric conductivity value of 1 S/cm. Since no electrochemical reactions occur in the backing and diffusion layers, the electron conservation equation in both layers is

$$\vec{\nabla} \cdot \vec{i}_s = 0 \tag{7.3}$$

For a 1-D system this conservation equation reduces to

$$i_s = \text{constant} \tag{7.4}$$

The current flux is not known *a priori*. For this reason, its value is guessed and an iterative technique is used to determine the actual current flux. The details of this iterative technique are discussed in Section 7.3.4.

Both the backing and diffusion layers are assumed to be free of the electrolyte. Thus, the total porosity of these electrodes is used to transport gases to or from the catalyst layer. The gas transport in these layers is modeled using the Stefan-Maxwell equations modified with the Knudsen diffusion term,

$$\vec{\nabla} P_i = \sum_{j \neq i}^{n} \frac{RT}{P_G D_{i,j}^{eff}} \left(P_i \vec{N}_j - P_j \vec{N}_i \right) - \frac{RT}{D_{K,i}^{eff}} \vec{N}_i \tag{7.5}$$

$P_{i \text{ or } j}$ and $N_{i \text{ or } j}$ are the partial pressure and molar flux of species i or j, respectively. P_G is the total pressure of the gas. Recall that Equation (7.5) is valid only when the total gas pressure is assumed to be constant (see Section 2.6.3). R and T are the ideal gas constant and the temperature, respectively. n is the number of gases that makes up the mixture. $D_{i,j}^{eff}$ is the effective binary diffusion coefficient between species i and j. By the Onsager reciprocal relationship, $D_{i,j}^{eff} = D_{j,i}^{eff}$. The superscript eff denotes that the diffusion coefficients are corrected for the porosity, ε, and tortuosity, τ, for gas transport in the porous medium,

$$D_{i,j}^{eff} = \frac{\varepsilon}{\tau} D_{i,j} \tag{7.6}$$

The Bruggeman expression is used to calculate the tortuosity [1],

$$\tau = \varepsilon^{-0.5} \tag{7.7}$$

$D_{K,i}^{'}$ is the effective Knudsen diffusion coefficient of species i. Using the kinetic theory of gases to express the mean free path of the molecule, the Knudsen diffusion coefficient is given by

$$D_{K,i} = \frac{2 r_K}{3} \left(\frac{8RT}{\pi m w_i} \right)^{\frac{1}{2}} \tag{7.8}$$

where r_K is the average pore radius of the porous medium and mw_i is the molecular weight of species i. Equation (7.5) is written shorthand for $n-1$ independent equations. For the oxygen, nitrogen, and water vapor mixture of this model, Equation (7.5) produces two independent equations. The constraint of constant total pressure is used to remove the nitrogen partial pressure term in these equations.

Since it assumed that there are no reactions in the backing or diffusion layers, the conservation equations for each gas species in these layers is given by

$$\vec{\nabla} \cdot \vec{N}_i = 0 \tag{7.9}$$

For a 1-D system this conservation equation reduces to

$$\vec{N}_i = \text{constant} \tag{7.10}$$

The flux of oxygen is assumed to be stoichiometrically related to the current flux. Thus, the oxygen flux is given by

$$\vec{N}_{O_2} = -\frac{\vec{i}_s}{4F} \tag{7.11}$$

where F is the Faraday's constant. Note that the above expression has a negative sign. This is because the direction of the oxygen flux is opposite to that of the current flux in the backing and diffusion layers. Equation (7.11) assumes that all oxygen that diffuses to the catalyst layer reacts. This is a very good assumption since the matrix layer effectively prevents any diffusion of oxygen to the anode. The flux of water vapor, $\vec{N}_{H_2O}$ is also assumed to be stoichiometrically related to the current flux,

$$\vec{N}_{H_2O} = \frac{\vec{i}_s}{2F} \tag{7.12}$$

Although water can be transported by the electrolyte in the catalyst and matrix layers, the condition given by Equation (7.12) is often used in the model of phosphoric acid cells [2, 3, 4]. Since nitrogen is an inert gas in the cell, its flux throughout the system is given by

$$\vec{N}_{N_2} = 0 \tag{7.13}$$

Boundary Conditions:

The solid phase potential at $x = 0$ is referenced to a normal hydrogen electrode placed within the electrolyte at position $x = 250\,\mu m$ (the interface of the diffusion and catalyst layers).[1] This solid phase potential is a specified value in the model. This potential is not the electrode potential. The electrode potential is defined as the difference between the solid phase potential at $x = 0$ and the electrolyte potential at position $300 + L_{CL}$. The potential of the electrolyte at any position is always defined using a normal hydrogen electrode located at the position of interest. The electrode potential is always lower than the specified solid phase potential indicated above. When plotting the performance curve of the electrode, the electrode potential is used.

The partial pressures of the gas at position $x = 0$ are also specified in the model. The partial pressures used by Fuller *et al.* in their model are used in this model [3]. The values for the inlet gas partial pressures are $P_{O_2} = 0.1918$ and $P_{H_2O} = 0.0866$.

In this model, the contact resistances between each interface are assumed to be negligible. This simplification does not affect the results of the model significantly since conductivity value of the diffusion layer is chosen to compensate for the lack of contact resistances in the model. Since there are no contact resistances, the solid phase potential

[1] The liquid phase potential at $x = 250\,\mu m$ is arbitrarily set to a zero value

throughout the system is continuous. The gas partial pressures are also assumed to be continuous throughout the system.

7.3.2 Catalyst Layer

Electron flow in the catalyst layer is also governed by Ohm's law. However, Equation (7.2) is modified since the catalyst layer porous matrix is patterned with an array of holes,

$$\vec{i}_s = -\kappa\varphi\vec{\nabla}\Phi_s \tag{7.14}$$

where φ is the volume fraction of the catalyst layer that is the microporous matrix region. Based on the geometric parameters of the catalyst layer, φ has a value of

$$\varphi = 1 - \frac{\pi r^2}{(2r+2s)^2} \tag{7.15}$$

It should be noted that Equation (7.14) is only valid for a 1-D model. Equation (7.5) is also used to model gas phase transport in the catalyst layer. The effective diffusion coefficients in the catalyst layer is given by

$$D_{i,j}^{eff} = (1-\varphi)D_{i,j} \tag{7.16}$$

Ion Transport in Concentrated Phosphoric Acid:

As was discussed in Section 2.6.2 the governing equation for ion transport in an electrolyte is generally more complex than Ohm's law. Concentrated phosphoric acid partially dissociates (about 10%), according to reference [5], to

$$5H_3PO_4 \rightleftarrows 2H_4PO_4^+ + H_2PO_4^- + H_3O^+ + H_2P_2O_7^{2-} \tag{7.17}$$

The thermodynamics and transport parameters of concentrated phosphoric acid at the operating conditions of a PAFCs are not that well known. For this reason, concentrated

solution theory has not been used to model the transport of ions in concentrated phosphoric acid. Fortunately, Ohm's law has been proven to be an adequate expression for modeling current flow in phosphoric acid with the fuel cells operating at a current density of $1\,A/cm^2$ or less [2, 3, 4, 6]. Ohm's law is also used in this model:

$$i_l = -\sigma^{eff}\vec{\nabla}\Phi_l \tag{7.18}$$

where i_l is the current flux in the electrolyte and Φ_l is the potential of a normal hydrogen electrode in equilibrium with the electrolyte at the point considered. The effective ionic conductivity, σ^{eff}, is given by

$$\sigma^{eff} = (\sigma_b \varepsilon_{CL})\varphi \tag{7.19}$$

where σ_b is the bulk conductivity of phosphoric acid and ε_{CL} is the porosity of the catalyst layer matrix. The justification for using Equation (7.19) for the effective ionic conductivity was discussed in Section 4.4.4.

In concentrated phosphoric acid, the flow of current is principally due to the motion of protons. For example, the transference number of protons in orthophosphoric acid at 313 K is $t_{H^+} \approx 0.975$ In the presence of an electrochemical potential field, protons migrate by a proton switching mechanism (Grotthus mechanism). In concentrated phosphoric acid, the phosphoric acid molecules and phosphate anions are associated by hydrogen bonds as shown in Figure 7-2. According to Gileadi, the switching of protons can be accomplished by the rearrangement of the internal bonds as shown in the Figure 7-2. Thus, in the proton switching mechanism, current flows by the motion of protons and not by the motion of the massive ions given in Equation (7.17).

The fact that most current is due to this proton switching mechanism is the reason why Ohm's law can effectively describe current flow in phosphoric acid.

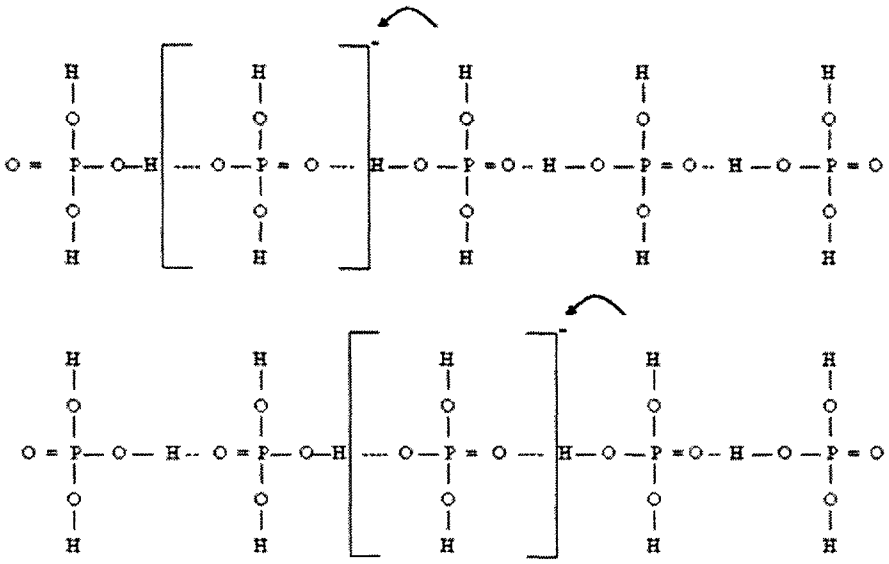

Figure 7-2: Schematic of proton-switching mechanism (Grotthus mechanism) for proton transport in concentrated phosphoric acid. The phosphoric acid molecules and phosphate anions are associated by hydrogen bonds.

Although the proton switching mechanism contributes to most of the current, electrolyte motion is observable at high current densities. Since motion of the phosphoric acid leads to flooding of the anode, the migration of phosphate anions is assumed to result in the volume flux of electrolyte towards the anode. The phosphate ion flux is given by

$$\vec{N}_{H_2PO_4^-} = -\left(\frac{t_-}{F}\right) i_l \tag{7.20}$$

where t_- is the transference number with respect to the mass average velocity of the phosphate ion. The value of this parameter in concentrated phosphoric acid is not known. For the purposes of this model, t_- is assumed to be 0.025, which is obtained

$$t_- = 1 - t_{H^+} \tag{7.21}$$

where t_{H^+} is assumed to have a value of 0.975 in concentrated phosphoric acid at a temperature of 200 °C. Equation (7.20) assumes that current flows purely by migration and the concentration of phosphoric acid is uniform. The volume flux towards the anode due to the flux of the phosphate anions, v_-, is therefore given by

$$\vec{v}_- = -\left(\frac{\bar{V}_- t_-}{F}\right)\vec{i}_l \tag{7.22}$$

where $\bar{V}_-$ is the partial molar volume of the phosphate anion.

At steady state the electrolyte volume content of the pores remain constant and the volume average velocity is zero. For this reason, the volume flux associated with the migration of the phosphate anion must be equal in magnitude and opposite in direction to the volume flux associated with the pressure driven flow of the electrolyte. Therefore, it is proposed that the gradient in electrolyte pressure is given by the following equation:

$$\vec{\nabla} P_l = -\left(\frac{\mu}{k}\right)\left(\frac{\bar{V}_- t_-}{F}\right)\left(\frac{1}{\varphi}\right)i_l \tag{7.23}$$

where P_l is the pressure of the electrolyte, k is the liquid permeability of the microporous matrix of the catalyst layer and μ is the viscosity of the electrolyte. The term $(1/\varphi)$ is included in the equation since the electrolyte saturated matrix is only a fraction of the catalyst layer. Equation (7.23) assumes that the microporous regions are fully saturated with the electrolyte and that the pressure driven flow of the electrolyte is governed by Darcy's law. Recall that this equation was first introduced in Section 4.4.3.

Electrochemical Reaction and Conservation Equations:

The catalyst layer is treated using the macrohomogeneous models [7]. In this approach, the porous electrode theory is used. At each discretization point, an

effectiveness factor is used to capture the effects of oxygen transport within the active region of the catalyst layer. In this model, the active region is the thin Pt film deposited on the surface of the cylindrical holes. Since the model is 1-D, each discretization point is actually a plane perpendicular to the x-axis. Using this approach, the conservation of current yields

$$\vec{\nabla} \cdot i_s = -\vec{\nabla} \cdot i_l = a_{Pt} i_{ORR} E \tag{7.24}$$

Using Faraday's law, the oxygen gas and water vapor conservations equations are respectively

$$\vec{\nabla} \cdot \vec{N}_{O_2} = -\frac{1}{4F} a_{Pt} i_{ORR} E \tag{7.25}$$

and

$$\vec{\nabla} \cdot \vec{N}_{H_2O} = \frac{1}{2F} a_{Pt} i_{ORR} E \tag{7.26}$$

i_{ORR} is the current density resulting the oxygen reduction reaction (ORR) on the Pt surface. This current density is based on the real surface area of Pt. E is the effectiveness factor that accounts for oxygen mass transfer and reaction within the Pt film. a_{Pt} is the total surface area of Pt per unit volume of the catalyst layer. Its value is calculated from

$$a_{Pt} = A_{Pt} \left(\frac{2\pi r}{(2r + 2s)^2} \right) \tag{7.27}$$

Recall from Section 6.6.4 that A_{Pt} is the roughness factor for Pt film deposited on a microporous substrate. In Chapter 5 and 6 it was shown that A_{Pt} is related to the Pt loading, Pt_L,[2] by the following empirical equation:

$$A_{Pt} = \alpha\left(\frac{Pt_L}{Pt_L^o} - 1\right)^{\kappa} \tag{7.28}$$

Pt_L^o is interpreted as the minimum Pt loading for which hydrogen desorption charge can be resolved from the voltammogram. It is assumed to have a value of 0.5 μg/cm^2. α and κ are fitting parameters. In this model, the cylindrical holes are assumed to be loaded with a uniform film of Pt deposited by the double potential step (DPS) technique described in Chapter 6. For such films, $\alpha = 0.3008$ and $\kappa = 0.7951$.

The current density, i_{ORR}, is calculated by using the Tafel equation to model the ORR. The Tafel equation for the ORR in phosphoric acid at 473 K is

$$i_{ORR} = i_o\left(\frac{P_{O_2}}{P_{O_2}^{ref}}\right)\exp\left[\frac{1}{b}\left(U^{ref} - \Phi_l + \Phi_s\right)\right]$$
$$\text{where} \tag{7.29}$$
$$b = 0.09/2.3$$

The above equation assumes that the Tafel slope for the ORR is constant and equal to 90 mV/decade. This is the Tafel slope measured for the ORR in phosphoric acid [8]. In the experiments presented in Chapter 5, it was determined that the specific activity of the ORR in 0.5 M sulfuric acid is greater than polycrystalline Pt and that the activity increased with an increase in the Pt loading. Possible reasons for these observations were discussed in Section 5.4.4. The possible reasons for the enhanced activity are not

[2] The Pt loading is defined as the mass of Pt per area that the Pt film is deposited on. This term should not be confused with the total Pt loading, which is the mass of Pt per planar area of the electrode.

believed to be exclusive to 0.5 M sulfuric acid. Thus, the same effects may occur in concentrated phosphoric acid. However, in this model it is assumed that the exchange current density of the Pt films is independent of Pt loading and its value is equal to that of polycrystalline Pt.

The oxygen gain experiments presented in Chapter 6 suggest that Pt films deposited on the microporous membrane will show no oxygen transport losses up to a current density of 130 mA/cm^2. These experiments were conducted in 3.7 M sulfuric acid at room temperature. The permeability of oxygen in this electrolyte is on the order of $10^{-12}\, mol/(\sec \cdot cm)$. The permeability of oxygen in concentrated phosphoric acid at 400 K is slightly higher than this value. For this reason, it is believed that oxygen will also show no transport losses for a thin Pt film in concentrated phosphoric acid. Thus, in this model, the effectiveness factor is assumed to have a value of one $(E = 1)$ at all operating conditions of the electrode.

Boundary Conditions:

The ORR occurs on both boundaries of the catalyst layer due to the presence of Pt films as illustrated in Figure 7-1. Since the boundaries and Pt films are assumed to be infinitely thin, the reactions results in discontinuities in the current and molar fluxes at both these boundaries. The electron current flux on the catalyst layer side at position $x = 250$ is given by

$$i_{s,CL} = i_s + A_{Pt}\varphi i_{ORR} E \tag{7.30}$$

The subscript CL is used to indicate that current flux on the catalyst layer side of the boundary is different from the current flux on the diffusion layer side, i_s. The ionic current flux on catalyst layer side of the boundary is given by

$$i_l = -A_{Pt}\varphi i_{ORR}E \tag{7.31}$$

The ionic current flux on the diffusion layer side is zero. The oxygen flux on the catalyst layer side of the boundary is

$$N_{O_2,CL} = -\left(i_s + A_{Pt}\varphi i_{ORR}E\right)/\left(4F\right) \tag{7.32}$$

The P_{O_2}, P_{H_2O}, and Φ_m are continuous across the boundary at $x = 250$. P_l at this boundary is not known *a priori*. For this reason, the value of this liquid pressure is guessed and an iterative technique is used to determine its actual value. As previously mentioned, the potential of a NHE at $x = 250$ is arbitrarily set equal to zero,

$$\Phi_l = 0 \tag{7.33}$$

Thus, all potentials are referenced to the NHE at $x = 250$.

7.3.3 Matrix Layer

In the matrix layer the current due the migration of ions is governed by Equation (7.18). In this case, the effective conductivity is given by

$$\sigma^{eff} = \sigma_b \varepsilon_{CL} \tag{7.34}$$

The current conservation gives

$$\vec{i}_l = \text{constant} \tag{7.35}$$

This current flux must be equal to the current flux given by Equation (7.4). In the matrix layer, the momentum equation, Equation (7.23), reduces to

$$\vec{\nabla} P_l = -\left(\frac{\mu}{k}\right)\left(\frac{\bar{V}t_-}{F}\right) i_l \tag{7.36}$$

Boundary Conditions:

P_l and Φ_l are continuous across the boundary at position $x = 250 + L_{CL}$. Due to the reaction occurring on this boundary, the fluxes are not continuous. On the matrix layer side of this boundary, both i_s and N_{O_2} are equal to zero. The ionic current flux is equal to

$$i_{l,ML} = i_l - A_{Pt}(1-\varphi) i_{ORR} E \tag{7.37}$$

The subscript ML is used to indicate that ionic current flux on the matrix layer side of the boundary is different from this current flux on the catalyst layer side, i_l. The electrolyte pressure at position $x = 300 + L_{CL}$ is equal to 1 bar.

7.3.4 Method of Solution

The model described above contains 8 independent variables and 8 independent first order ordinary differential equations. The system of differential equations was solved using MATLAB and its ODE solvers. The methodology for solving the differential equations of this model is illustrated in Figure 7-3. As previously mentioned, the potential difference between the solid phase potential at $x = 0$ and a NHE electrode in the electrolyte at $x = 250$ is given. The current density, however, is not known so a guessed value for it is used to initiate the iteration process. The system of equations for the backing and diffusion layers are then solved.

The output of the diffusion layer solver, $P_{O_2}, P_{H_2O}, \Phi_s$, are three of the eight initial conditions needed for the for the catalyst layer solver. As indicated in Figure 7-3 and Section 7.3.2, these parameters are used to calculate the $i_s, i_l, and\ N_{O_2}$ initial conditions for the catalyst layer solver. The potential of the NHE at the diffusion/catalyst layer

interface is arbitrarily set to zero. All potentials in the system are referenced to this reference electrode. The electrolyte pressure at the diffusion/catalyst layer interface is not known *a priori*. For this reason its value is initially set at 1 bar, which is the pressure at position $x = 300 + L$. The actual pressure at position $x = 250$ will be lower than 1 bar.

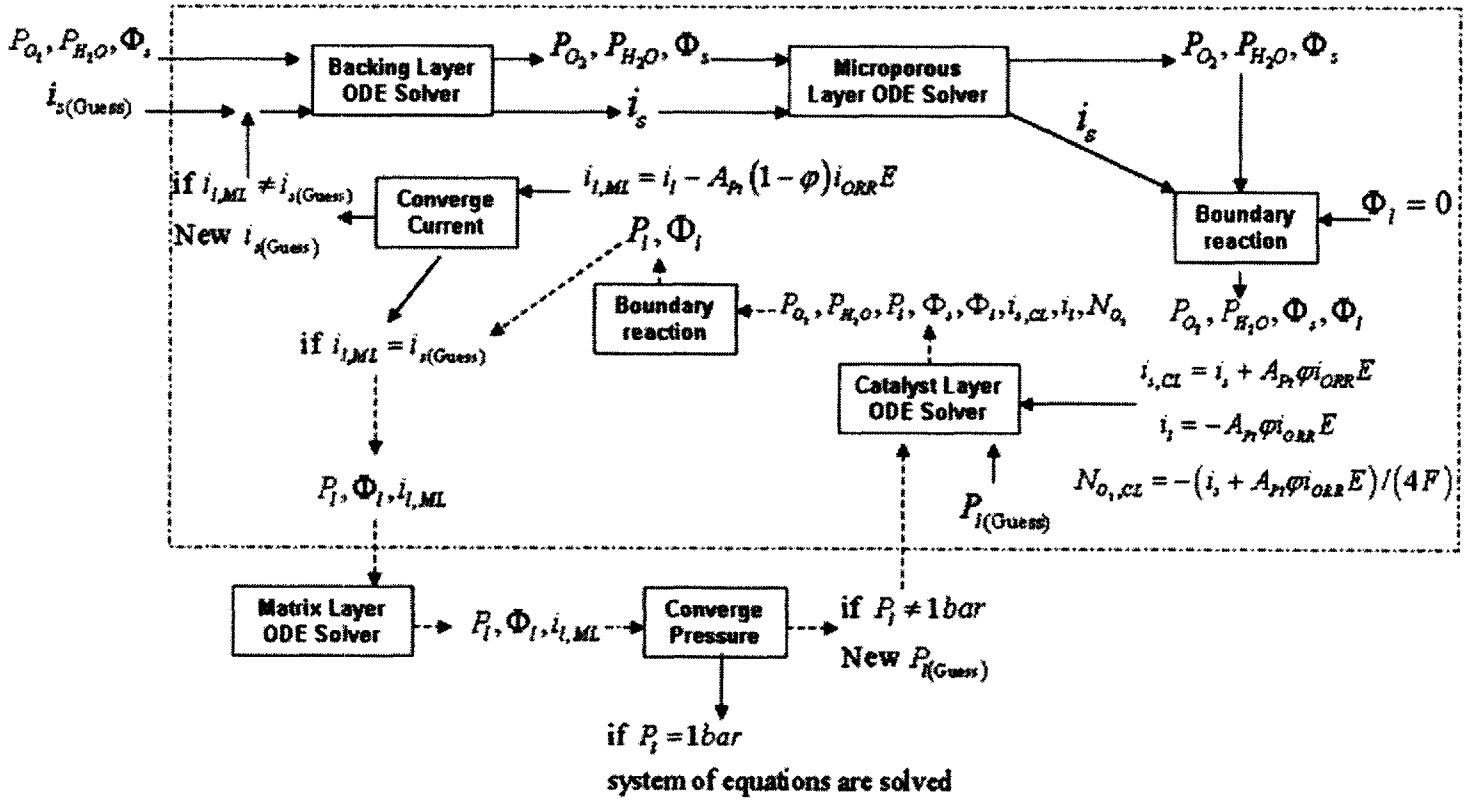

Figure 7-3: Illustration of the methodology for solving the differential equations of this model

The ODEs are solved in the order shown in Figure 7-3. The system of ODE solvers enclosed in the dotted box represents an iterative loop that ends when the ionic current that enters the matrix layer is equal to the guess electronic current that enters the backing layer. The "converge current" box drawn in the Figure 7-3 represents the technique used incrementally increase or decrease the new $i_{s(Guess)}$ from its previous value

in the iteration loop. The details of this convergence technique can be understood by reading the current_converge.m MATLAB script reproduced in Appendix D.

Once the current has converged, a second iterative loop is initiated to properly identify the pressure of the electrolyte at $x = 250$. The "converge pressure" box drawn in the Figure 7-3 represents the technique used incrementally decrease the new $P_{l(Guess)}$ from its previous value in the iteration loop. The details of this convergence technique can be understood by reading the pressure_converge.m MATLAB script reproduced in Appendix D. This iteration loop, indicated by the dash arrows, ends when the electrolyte pressure at the end of the matrix layer is equal to 1 bar. It is important to note that the guessed value of the electrolyte pressure does not affect the results of the other parameters. This fact is a result of the assumption that the micropores of both the catalyst and matrix layers will remain saturated regardless of the electrolyte pressure.

7.4 Results and Discussion

7.4.1 Catalyst Layer Optimization

$r, s,$ and Pt_L are the design parameters of the catalyst layer. As indicated by Equation (7.1), these parameters determine the thickness of the catalyst layer for a given total Pt loading. A parameter closely related to the thickness of the catalyst layer is the aspect ratio between the length of the cylindrical holes and its diameter, L_{CL}^{*}. Dividing Equation (7.1) by r gives

$$L_{CL}^{*} = \frac{1}{\pi}\left(\frac{Pt_{L,total}}{Pt_{L}} - 1\right)\left(1 + (s/r)^2\right)$$

where (7.38)

$$L_{CL}^{*} = \frac{L_{CL}}{2r}$$

The L_{CL}^{*} parameter is critical to the fabrication of the catalyst layer. A small aspect ratio simplifies the fabrication of the catalyst layer die and the process of making the catalyst layer from die. A small aspect ratio also greatly simplifies the process by which the catalyst is deposited within the cylindrical holes. These fabrication processes are not discussed in detail in this dissertation. However, since a small L_{CL}^{*} will greatly increase the feasibility of fabricating the catalyst layer, its value is considered in the catalyst layer optimization process presented in this section. For example, Equation (7.38) indicates that s should be less than r in order to keep the aspect ratio small.

The values of r and s are limited by the catalyst layer materials, the MFE fabrication process, and the capillary pressure requirements needed to keep the electrolyte from flooding the cylindrical holes. Considering that the flooded regions of the cell will have pore sizes of 1 μm or less, it is believed that the radius of the of the cylindrical holes needs to be 5 μm or greater. This order of magnitude difference in pore size between the desired dry and wet pores ensures that the cylindrical holes will not flood under normal operating conditions of the electrode. The hole-to-hole spacing is limited by the ability of the catalyst layer materials to penetrate the microfabricated die in either the proposed casting or embossing processes. For the polymer-bonded membranes presented in chapter 4, the minimum possible spacing appears to be about 0.5 μm. In the case of the Pt loading within the cylindrical holes of the catalyst layer, the loading should be high

$\left(> 50\mu g/cm^2\right)$ in order to have a thin catalyst layer. On the other hand, both the reduction in specific area and the increase in local heat generation associated with a high Pt loading limit the loading amount. In this section, the half-cell model is used to determine the optimal values for $r, s,$ and Pt_L.

Optimal Spacing (s)*:*

For a given r and Pt_L there is a value for s that maximizes that performance of the catalyst layer. As the spacing decreases, the thickness of the catalyst layer decreases. This has a beneficial effect on the catalyst layer performance. On the other hand, this also leads to a reduction in the value of φ (see Equation (7.15)), which reduces the effective ionic conductivity of the catalyst layer. The ionic conductivity is the parameter that most affects the performance of the electrode. Figure 7-4 shows the current density of the half-cell vs. the ratio s/r for several r values.

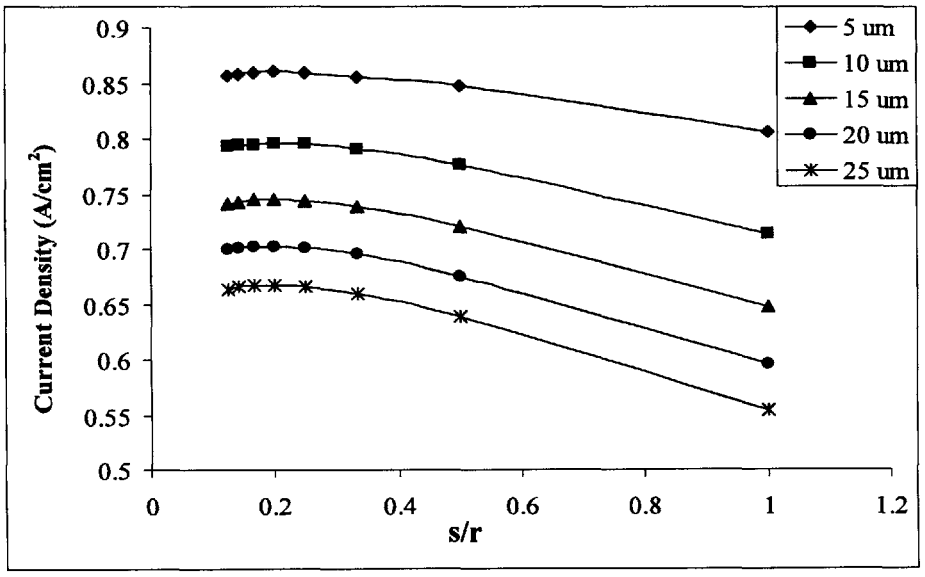

Figure 7-4: Current density of the half-cell vs. the ratio s/r for several r values. The electrode potential is 0.675 V.

The model appears to predict a optimal spacing between $(1/5)r$ and $(1/6)r$ regardless of the value of r. Additional simulations at different cell potentials and Pt_L values yielded the same result.

The main overpotentials in half-cell model are due to low exchange current density of the ORR and the low ionic conductivity of the electrolyte. All other losses are secondary. Based on this observation, a reduced order model of just the catalyst layer can be considered. It can be shown that such a model has one governing equation for a 1-D model. Combining Equations (7.18) and (7.24) gives

$$\sigma^{eff}\frac{d^2\Phi_l}{dx^2} = a_{pt} i_{ORR} \tag{7.39}$$

For this simplified model, P_{O_2} and Φ_s are uniform. Thus, i_{ORR} only varies with Φ_l. Equation (7.39) can be non-dimensionalized with respect to position and written in terms of the design parameters to give a Poisson-Boltzmann-like differential equation

$$\frac{d^2\eta}{d\left(x^*\right)^2} = A_{\text{Parameter}} i_o \left(\frac{P_{O_2}}{P_{O_2}^{ref}}\right)\exp\left[\frac{\eta}{b}\right]$$

where

$$\eta = U^{ref} - \Phi_l + \Phi_s \tag{7.40}$$

$$A_{\text{Parameter}} = \left(\frac{1}{\sigma_b \varepsilon_{CL}}\right)\left(\alpha\left(\frac{Pt_L}{Pt_L^o}-1\right)^{\kappa}\right)\left(\frac{Pt_{L,total}}{Pt_L}-1\right)^2\left(\frac{(2r+2s)^2}{2\pi r(2r+2s)^2 - 2\pi^2 r^3}\right)$$

$$x^* = x/L_{CL}$$

The total area of Pt in the catalyst layer is not dependent parameters r and s. For this reason, the r and s values that minimizes the $A_{\text{Parameter}}$ will maximizes the total current produced by the catalyst layer For example, the s that minimizes the $A_{\text{Parameter}}$ and therefore maximizes the total current is

$$s = 0.253r \tag{7.41}$$

This value only depends on the radius and it is close to the value obtained from the higher order model. The slight difference between in the values is probably due to the fact that the higher order model considers oxygen transport losses in the gas phase. Based on the results of the 1-D model and the reduced order mode, the spacing in the design of the catalyst layer of the MFE is set to be $s = (1/5)r$ regardless of Pt loading or operating conditions. This value for the spacing has the added benefit of helping keep the aspect ratio between length of the cylindrical holes and its diameter small.

Optimal Pt Loading (Pt_L)*:*

Unlike r and s, the Pt loading, Pt_L, affects both the potential distribution within the catalyst layer (i.e. the $A_{\text{Parameter}}$ for the case of the reduced order model) and the total area of Pt catalyst layer. Increasing Pt_L decreases the thickness of the catalyst layer, which reduces the Ohmic and gas transport losses within the catalyst layer. However, increasing the loading reduces the total Pt area, which increases the kinetic overpotential within the catalyst layer. As a result of these two competing effects, there is an optimal Pt loading for the electrode. Unfortunately, this optimal loading is dependent on the geometry of the catalyst layer and the operating condition of the electrode. Even in the case of the reduced order model given by Equation (7.40), an analytical expression for the Pt loading that maximizes the current is not attainable.

Figure 7-5 is a plot of the total current of the half-cell vs. Pt_L for several r values. The plots show that as the radius of the cylindrical holes increase, the optimal Pt_L increases. This result is consistent with the fact that with a larger radius size, a higher Pt

loading is needed to keep the catalyst layer sufficiently thin to in order to minimize Ohmic losses from the flow of ions.

Figure 7-6 is a plot of the Pt loading that maximizes current $\left(Pt_{L,\max}\right)$ vs. r for several electrode potentials. The curves show that as the as polarization of the electrode increases, a higher Pt loading is needed in order to maximize the current.

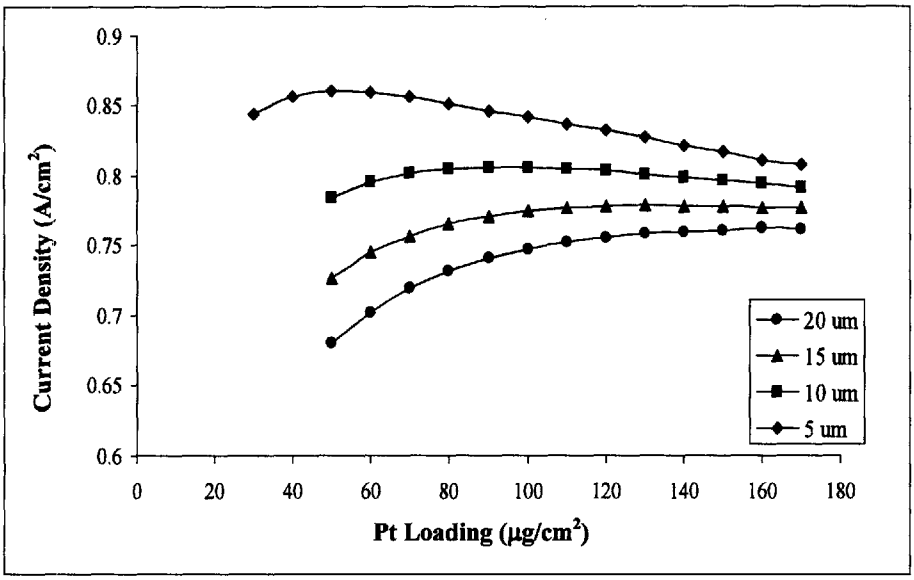

Figure 7-5: Plot of current density vs. Pt loading for several cylindrical hole radii. The Electrode potential is 0.675 V.

The plot also shows that the slope of the curves increase as the polarization of the half-cell increases. These results are not surprising. As the potential of the electrode decreases below 0.725 V, transport losses contribute more to the electrode's additional polarization than kinetic losses. Therefore, more emphasis is placed on reducing these losses by increasing the Pt loading than the kinetic losses associated with the Pt area loss.

Both Figure 7-5 and Figure 7-6 show that for certain combinations of cylindrical radii and electrode potential, the optimal Pt loading is greater than $100\mu g/cm^2$. These results were obtained under the assumption that the Pt film roughness factor as a function

of Pt loading remains the same at loading greater than $100\mu g/cm^2$ and that these Pt films experience no oxygen transport losses. The specific areas and oxygen transport characteristics were not measured for films with a Pt loading greater than $80\mu g/cm^2$ (see Chapter 6). Thus, it is uncertain that these assumption apply to Pt films greater than $80\mu g/cm^2$.

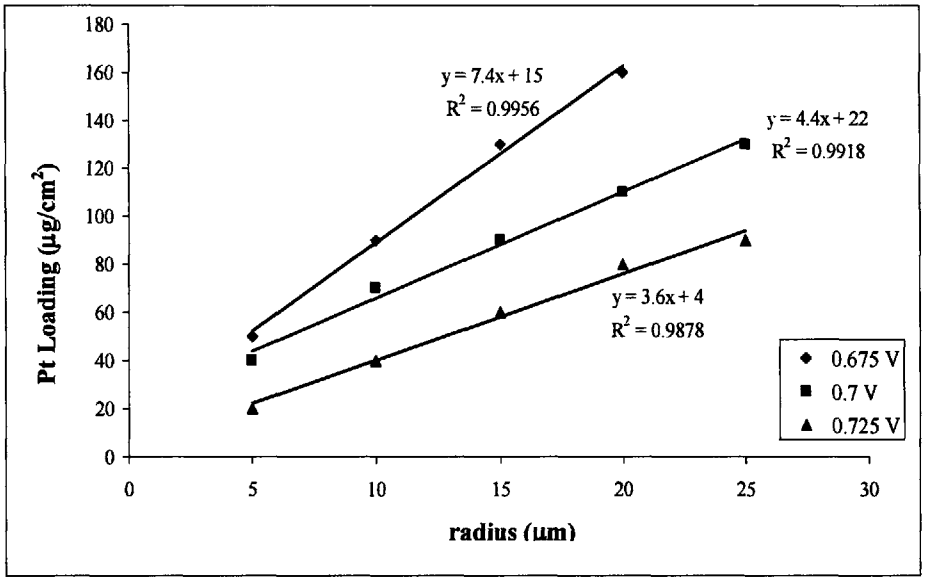

Figure 7-6: Plot of the Pt loading that maximizes current $\left(Pt_{L,\max}\right)$ vs. r for several electrode potentials.

There is evidence in the literature that indicates that electrodeposited Pt films with a loading grater than $100\,\mu g/cm^2$ have specific areas that are consistent with what is predicted by Equation (7.28). For example, Plyasova *et al.* used the single potential step technique to deposit Pt at a loading of approximately $200\mu g/cm^2$ on glassy carbon [9]. These thick Pt films had a specific area of around $20\,m^2/g$. This specific area is only 14 % higher than the value predicted by Equation (7.28).

The assumption that Pt films greater than $100\,\mu g/cm^2$ experience no oxygen transport losses is problematic. At high Pt loadings the films thickness can grow to the point where the film is no longer 100% effective with respect to oxygen transport. Asher and Batzold electrodeposited films up to a loading of $260\,\mu g/cm^2$ onto Vycor glass. They found that these films in 3.7 M sulfuric at room temperature experienced no oxygen transport loss up to a current density of $100\,mA/cm^2$. Their experiments, however, were conducted only in pure oxygen enviroment and not in both oxygen and air, like the experiments presented in Chapter 6. Such films can be 100% effective in oxygen but still experience oxygen transport losses in air at the maximum current density of $100\,mA/cm^2$.

The required current density of the Pt films within the catalyst layer of the MFE increases as the Pt loading increase. This current density is defined as the current per area the Pt film is deposited on. The required current density of the Pt films is given by

$$i_{Pt} = \left(\frac{Pt_L}{Pt_{L,total}} \right) i_s \tag{7.42}$$

Thus, a catalyst layer with a Pt loading of $120\,\mu g/cm^2$ producing a total current density of $800\,mA/cm^2$, the amount of current produced per area the Pt film is deposited on is $192\,mA/cm^2$. The results from Chapter 6 suggest that Pt films cannot support current density requirements over $140\,mA/cm^2$ due to excessive volumetric heat generation. A thick film in the MFE catalyst layer may not be able to support current densities greater than this amount without suffering from oxygen transport losses or excessive volumetric heat generation.

7.4.2 Electrode Performance

The results from the 1-D model indicate that the optimal design of the microfabricated catalyst layer is a cylindrical hole radius of $10\mu m$ with a spacing of $2\mu m$. Since the typical operating potential of 0.7 to 0.675 V, the Pt loading within the cylindrical holes should be approximately $50\mu g/cm^2$. Based on these parameters the thickness of the catalyst layer is $41\mu m$. The aspect ratio between the length of the cylindrical holes and its diameter is approximately four. It is believed that this aspect ratio is manageable from a standpoint of fabricating the catalyst layer and depositing the catalyst in the cylindrical holes.

Figure 7-7 contains the simulated performance curves of the MFE with the parameters given above and the performance curve of the conventional porous carbon electrode (PCE).

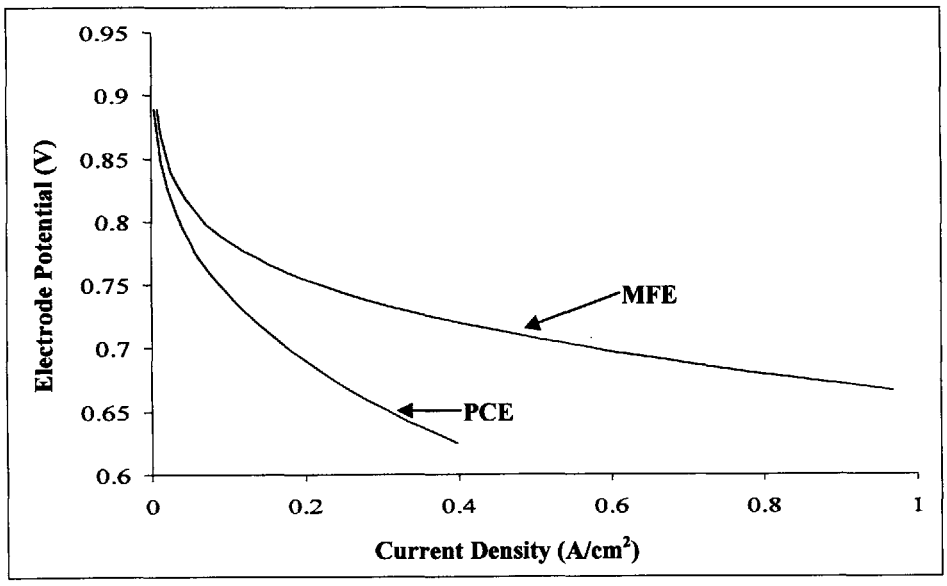

Figure 7-7: Performance curve of MFE with a catalyst parameters of $r = 5\mu m, s = 1\mu m, L_{CL} = 41\mu m$, and $Pt_L = 50\mu g/cm^2$. Performance curve of PCE using the parameters from Fuller et al [3].

The performance curve for PCE is a reproduction of the curve given in Section 3.2.2. The figure shows that even at high electrode potentials, in the kinetic overpotential region of the performance curve, the MFE performs better than the PCE. This result is due to the assumption that the specific activity of the Pt film is equal to that polycrystalline Pt and is also due to the fact that Pt utilization value for PCE is 60%. The specific activity of polycrystalline Pt has been shown to be three times greater than that of supported Pt nanoparticles in concentrated phosphoric acid [10]. This higher specific activity of the Pt film is able to compensate for it lower specific area.

At potentials less than 0.725 V, the MFE outperforms the PCE for two major reasons. First, the MFE is predicted not to experience any oxygen transport losses in the active regions of the catalyst layer. In contrast, oxygen transport losses contribute about 8.4 mV to the PCE polarization in air at a current density of $200\,mA/cm^2$ [2]. The other major reason is that the MFE has an effective ionic conductivity that is five times greater than that of PCE. In the PCE, Ohmic polarization due to ion flow contributes about 11.8 mV to the cell polarization at a current density of $200\,mA/cm^2$ [2].

The higher current densities of the MFE introduce new concerns regarding electrolyte motion and localized heat generation. These are two effects that increase with an increase in current density. The potential effects of localized heat generation were discussed with respected to the oxygen gain experiments presented in Chapter 5. In PAFCs, localized heat generation may have an important impact on electrolyte management since excessive heat generation can increase the evaporation of electrolyte. In future work, a non-isothermal model of the MFE should be developed to assess this potential problem.

In the case of electrolyte motion, this issue was considered by including Equation (7.23) in the model. To our knowledge this is the first time than an attempt has been made to model electrolyte motion in a PAFC electrode. Figure 7-8 shows the predicted electrolyte pressure at position $x = 250$ vs. the current density of the electrode. The electrolyte pressure is at its lowest value at this position. As the figure shows, the pressure is less than 1 bar at this position. For a current densities less than $1 A/cm^2$ the pressure drop is not greater than approximately $0.5 bar$. This potential drop is not expected to lead to a significant reduction in the saturation of the electrolyte or lead to the boiling of the electrolyte. In fact, this pressure distribution may help to ensure that the cylindrical holes of the catalyst layer do not flood with the electrolyte.

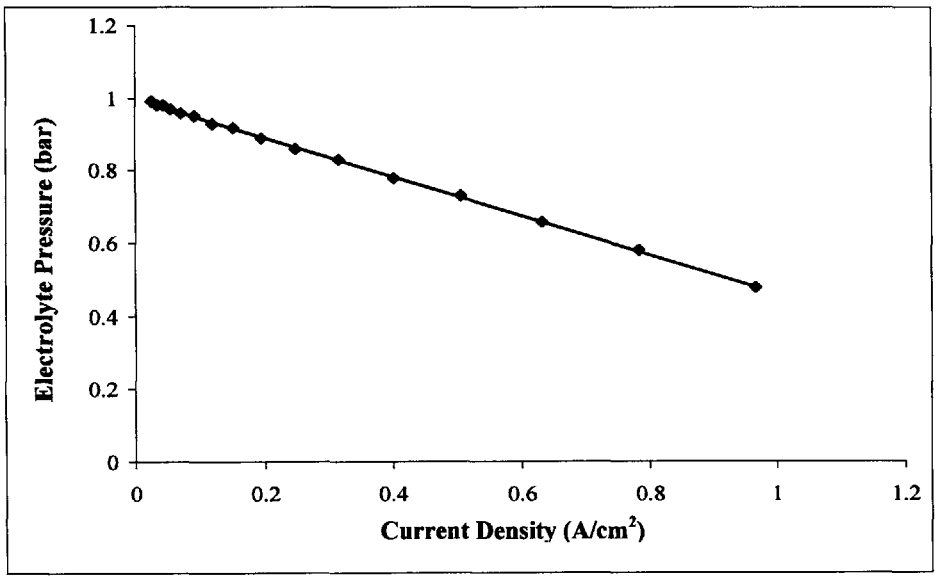

Figure 7-8: Electrolyte pressure at position $x = 250$ vs. the current density of the electrode

7.5 Conclusions

The 1-D model presented in this chapter indicates that the required geometry of the microfabricated catalyst layer is within the range of what are feasible using existing

microfabrication techniques. At the typical operating potentials of 0.7 or 0.675 V, the MFE current density is predicted to be 3.4 or 3.6 times greater than that of the PCE. At lower electrode potentials the difference in performance between MFE and PCE is even greater. It is believed that such possible improvements in the performance of the cathode of PAFCs warrant continued work to fabricate and test the MFE design concept presented in this dissertation.

References

[1] M. Kaviany, *Principles of Heat Transfer in Porous Media*, Springer, New York, 1999.

[2] R.P. Iczkowski and M.B. Cutlip, "Voltage Losses in Fuel Cell Cathodes", *J. Electrochem. Soc.*, Vol. 127, p. 1433, 1980.

[3] T.F. Fuller, F.J. Luczak, and D.J. Wheeler, "Electrocatalyst Utilization in Phosphoric Acid Fuel Cells", *J. Electrochem. Soc.*, Vol. 142, p. 1752, 1995.

[4] S.R. Choudhury, M.B. Deshmukh, and R.Renaswamy, "A two-demensional stead-state model for phosphoric acid fuel cells (PAFC)", *J. of Power Sources*, Vol. 112, p. 137, 2002.

[5] Th. Dippel, K.D. Kreuer, J.C. Lassegues, and D. Rodriguez, "Proton conductivity in fused phosphoric acid; A $^{1}H/^{31}P$ PFG-NMR and QNS study", *Solid State Ionics*, Vol. 61, p. 41, 1993.

[6] D.S. Chan and C.C. Wan, "Effect of Structure on Porous Gas-Diffusion Electrodes for Phosphoric Acid Fuel Cells", *J. Power Sources*, Vol. 50, p. 261, 1994.

[7] A.Z. Weber and J. Newman, "Modeling Transport in Polymer-Electrolyte Fuel Cells", *Chemical Review*, Vol. 104, p. 4679, 2004.

[8] H.R. Kunz and G.A. Gruver, "The Catalytic Activity of Platinum Supported on Carbon for Electrochemical Oxygen Reduction in Phosphoric Acid", *J. Electrochem. Soc.*, Vol. 122, p. 11279, 1975.

[9] L.M. Plyasova, I.Y. Molina, A.N. Gavrilov, S.V. Cherepanova, O.V. Cherstiouk, N.A. Rudina, E.R. Savinova, and G.A. Tsirlina "Electrodeposited Platinum Revisited: Tuning Nanostructure via the Deposition Potential", *Electrochimica Acta*, Vol. 51, p. 4477, 2006.

[10] P.N. Ross, "Structure-Property Relations in Noble metal Electrocatalysis", LBL-21733, Lawrence Berkeley Laboratory, Berkeley, CA (June 1986); presented at the Gordon Conference on Chemistry at Interfaces, Meriden, NH, July 21-25, 1986.

Chapter 8

Summary and Recommendations for Future Work

The objectives of the research presented in this dissertation were: 1) to propose a design for an air electrode that can be fabricated using existing microfabrication technologies and 2) to evaluate if such an electrode has the potential to improve the performance of liquid electrolyte fuel cells.

An air electrode consisting of a microfabricated catalyst layer was proposed. The catalyst layer is fabricated by using a microfabricated die to shape a porous carbon matrix into the reverse pattern of the die. The resulting dual-porosity layer consists of an array of cylindrical holes 10 μm in diameter with a hole-to-hole spacing of 2 μm and the micropores (pore size < 1 μm) of the carbon matrix. The cylindrical holes have a depth of 40 μm. The cylindrical holes are used for gas transport while the micropores are saturated with a liquid electrolyte for ion transport. The backing and microporous layers of MFE are similar to that of the conventional porous carbon electrode (PCE). The backing layer of the MFE is made from wet proof Toray carbon paper and the microporous layer is made from carbon black bonded with sintered PTFE. Unlike the PCE, the matrix layer is principally made from the additional thickness of the carbon matrix that is not patterned by the die. A thin insulating layer is placed between the matrix and anode to prevent shorting. The catalyst (Pt or Pt alloy) is loaded into the microfabricated structure by electrodepositing thin catalyst films (loading < $100\,\mu g/cm^2$) within the cylindrical holes. The film is deposited only on the surface of the microporous

carbon matrix and not within its micropores in order to maximize the density of triple-phase boundaries.

There are multiple issues that must be addressed in order to evaluate the feasibility of this microfabricated electrode (MFE) design concept. In this dissertation, three issues were investigated: 1) identification of the best material to use for the porous carbon matrix of the catalyst layer, 2) the study of electrokinetic parameters of electrodeposited Pt films, and 3) the study of oxygen transport behavior within a Pt film supported on the surface of a microporous carbon membrane. Some of the important conclusions from these investigations are given below.

8.1 Identification of the Best Material to use for the Porous Carbon Matrix of the Catalyst Layer

8.1.1 Summary

Two types of polymer-bonded carbon materials were identified as materials that may be suitable for the catalyst layer matrix, the polytetrafluoroethylyne (PTFE) bonded membrane and the polyethersulfone (PES) bonded membrane. These materials were formed into thin membranes in order to characterize them. They were formed with varying polymer content in order to determined how the relevant properties of the membranes changed with polymer content.

Both types of membranes were found to have high porosities $(> 50\%)$, which helps to increase the effective ionic conductivity of the electrolyte saturated membrane. The PTFE-bonded and the PES-bonded membranes did not imbibe liquid water or

electrolyte when they were oven dried. In order to saturate these membranes with liquid water or electrolyte, isopropanol was used as an intermediary fluid. Once saturated with water, the membranes had high breakthrough capillary pressures. Excluding the 25 wt% PTFE-bonded membrane, the measured breakthrough capillary pressures of all other membranes tested were greater than 0.7 bar. The dual wetting behavior of the polymer-bonded membranes is a favorable property. It allowed for Pt to be electrodeposited as a thin film only on the surface of the membrane and not within the pores. Thus, this property will allow for the electrodepositing Pt as a thin film within the cylindrical holes of the catalyst layer without having to physically block the micropores.

For most the polymer-bonded membranes tested, the effective ionic conductivity was found to be approximately equal to the bulk conductivity of the electrolyte times the porosity of the membrane. Thus, the tortuosity is approximately one for most of the membranes tested. The effective ionic conductivity of the MFE catalyst layer is expected to be 4 to 5 times greater than that of the PCE. Simulations of the MFE and PCE in concentrated phosphoric acid indicate that this property of the polymer-bonded membranes is one of the major reasons why the MFE is expected to significantly outperform the PCE.

The average permeability of PTFE-bonded and PES-bonded membranes are $1.42 \times 10^{-15}\ \text{cm}^2$ and $1.17 \times 10^{-15}\ \text{cm}^2$, respectively. These values are much lower than the permeability values predicted by the commonly used Carmen-Kozeny equation. The low permeability of the membranes raises issues concerning electrolyte management in the electrode. However, preliminary modeling of electrolyte motion in the electrode suggests that it will not pose a problem for the MFE. Additional work is needed in this area.

8.1.2 Future Work

Future work with these membranes should involve attempts to form them into the proposed catalyst layer geometry. Two techniques are proposed: 1) The casting of a PES and carbon black slurry onto a sacrificial die and 2) the embossing of a PTFE-bonded membrane using a sacrificial die. The casting technique has been proven possible by Dr. Chang Rae Lee (see Appendix A). He used a silicon die with a Nafion and carbon black slurry to fabricate the catalyst layer. This technique needs to be investigated with PES instead of Nafion, PES is a more practical polymer binder than Nafion.

The use of silicon as a sacrificial die is not practical. The use of potentially cheaper dies is essential to the economic feasibility of the proposed MFE design. The hot embossing of polymers such as PMMA is believed to be a very promising area to explore. The polymer embossing technique, on the scale of what is required for the MFE, is currently being investigated in such fields as macroelectronics and microreplication.

8.2 The Study of the Electrokinetic Behavior of Electrodeposited Pt Films

8.2.1 Summary

In the microfabricated electrode design, the catalyst is electrodeposited as thin films in the catalyst layer rather than highly dispersed support catalyst particles found in PCEs. The use of thin catalyst films in the catalyst layer is an essential characteristic of

the microfabricated electrode design. Experiments were conducted to further our knowledge of Pt electrodeposition and the oxygen reduction reaction (ORR) on electrodeposited Pt films.

Thin Pt films were electrodeposited on a polished glassy carbon substrate by the single potential step (SPS) and the double potential step (DPS) techniques. The DPS technique produced Pt films with specific areas greater than 25 m^2/g for Pt loadings as high as 80 $\mu g/cm^2$. The SPS technique produced Pt films with lower specific areas than the DPS deposited films. However, both electrodeposition techniques, at high Pt loadings, produced Pt films with higher specific areas than films sputter deposited on glassy carbon. Electrodeposition produces higher area films because secondary nucleation on existing Pt crystallites allows the films to grow principally by increasing the number of crystallites rather than increasing the size of the crystallites.

The ORR on the electrodeposited films was studied in 0.5 M sulfuric acid at room temperature. This electrolyte was chosen for the initial study the ORR on the Pt films since there are numerous data available for the ORR on supported Pt nanoparticles and polycrystalline Pt in this electrolyte. The data obtained in the ORR experiments were compared with data available in the literature. 0.5 M sulfuric acid was also chosen because it is a much simpler electrolyte to work with than concentrated phosphoric acid.

The ORR reaction pathway on the chloride-free Pt films was determined to be essentially the same as that of polycrystalline Pt and Pt/C. For all Pt films, the Tafel slope was measured to be around 60 mV/decade at low overpotentials. At potentials between 0.8 and 0.65 V vs. NHE, the Tafel slope doubled to a value of about 120 mV/decade. At potentials below 0.4 V, the electron transfer number for the ORR

remained about 4 electrons. Therefore, the ORR did not shift to predominately peroxide formation at potentials in the hydrogen adsorption/desorption region. The kinetic current also approached a limiting value at high overpotentials.

The specific activities of the Pt films at 0.9 V in 0.5 M sulfuric acid were higher than the activity of a Pt disk electrode. Also, the activity of the Pt films increased with an increase in Pt loading. Compared to the specific activity of Pt/C, the specific activities of the electrodeposited Pt films were 5 to 7.4 times greater. The enhanced activity of the electrodeposited Pt films may be due to a number of contributory factors. The currently recognized factors are:

(a) A higher surface ratio of Pt crystallographic orientations advantages to the ORR, for example, an increase in the number density of crystal facets with high step densities.

(b) An increase in the number density of point and line defects on the surfaces of the crystallites.

(c) Increase in lattice compression resulting from the mutual strain that Pt crystallites, growing in close proximity, exert on each other.

The maximum mass activity for Pt/C occurs at a specific area value of around 75 m^2/g. Therefore, the mass activity of the electrodeposited Pt films is surprisingly about 2.5 times greater than that of Pt/C in 0.5 M sulfuric acid. Sputter deposited films and the electrodeposited films have similar specific activity. However, the electrodeposited films have an enhanced mass activity due to its higher specific area.

8.2.2 Future Work

The characterization of thin films and the study of the ORR kinetics on them are exciting areas of research, especially considering the enhanced reactivity these types of films show. The ORR on these films should be studied at elevated temperatures and in other electrolytes such as perchloric acid and potassium hydroxide. The ORR on supported Pt nanoparticles has been well studied in these other electrolytes.

In order to better determine the reasons for the enhanced activity of the electrodeposited or sputter deposited Pt films, the rotating disk electrode (RDE) (or rotating ring disk electrode) study should be combined with X-ray diffractometry (XRD) measurements of the electrodeposited Pt films. XRD allows detail structural characterization of the electrode material. To our knowledge, no other group has yet reported experimental results that combine these two powerful techniques to study the ORR on electrodeposited Pt films.

The optimal current or potential modulation used to deposit Pt within the cylindrical holes maybe very different from the DPS technique studied in this dissertation. For this reason, future studies should involve conducting RDE and XRD experiments on thin films deposited using different potential and/or current modulations in order to determine if the deposition condition significantly alters the ORR activity and crystallography of the films.

8.3 The Study of Oxygen Transport Behavior within a Pt Film Supported on a Microporous Membrane

8.3.1 Summary

Thin Pt films were electrodeposited onto the 15 wt% PTFE-bonded membranes by the single potential step (SPS), the single potential step with Pt seed layer (SPS-S), and the double potential step (DPS) techniques. Since a dry polymer-bonded membrane did not imbibe the deposition solution, Pt was easily electrodeposited only on the surface of the porous membranes without the use of any pore-blocking material. The DPS technique produced Pt films with specific areas that ranged from 27 to 20 m^2/g for Pt loadings of 20 to 80 $\mu g/cm^2$. These specific areas are lower, at an equivalent loading, than the specific areas for Pt films deposited by the DPS technique on glassy carbon. The porosity of the membrane may explain the lower specific areas. Another possibility is the lower activity for chloroplatinate reduction to Pt on the PTFE-bonded membranes compared to this activity on glassy carbon. This difference in activity was most apparent when the SPS deposition at 0.1 V did not lead to a dominant 4 electron reduction of chloroplatinate ion to Pt as it did on glassy carbon. Instead, the transient responses of SPS deposition on the membranes indicated that the 2 electron reduction reaction was dominant.

Oxygen gain experiments were conducted on DPS deposited Pt films. The results of the oxygen gain experiments indicate the electrodeposited Pt films experienced no oxygen transport losses in pure oxygen or in air up to a current density of 130 mA/cm^2. Previously, such enhanced oxygen transport behavior was only observed for Pt films

deposited on Vycor glass. The polymer-bonded membranes presented in this dissertation represent a much more practical substrate for Pt deposition than Vycor glass. The results from the oxygen gain experiments strongly support the use of thin catalyst films in the proposed microfabricated electrode design. The microfabricated catalyst layer is predicted to operate essentially free of any oxygen transport losses within the active regions of the catalyst layer.

8.3.2 Future Work

Once the catalyst layer is formed, the catalyst (Pt or a Pt alloy) must be deposited within the cylindrical holes. Depositing metal uniformly within high aspect ratio holes can be challenging. Thus, work is needed to determine if this can be done in a cost effective fashion. Electrodeposition is the recommended method for depositing the Pt within the holes. Both modeling of the electrodeposition process and experimental studies need to be conducted to determine the optimal technique to uniformly deposit the catalyst within the holes.

The thin catalyst film technology can reduce oxygen transport losses. However, it may also introduce new challenges associated with localized heat generation. In phosphoric acid the localized heating effect may cause excess electrolyte evaporation and lead to an electrolyte management problems. The oxygen gain experiments presented in Chapter 6, should be conducted in concentrated phosphoric acid at temperature between 150 to 200 °C. These experiments along with a non-isothermal model of the MFE in phosphoric acid will shed light on the effects that localized heating has on electrolyte management.

Appendix A

Dr. Chang Rae Lee effectively prepared microfabricated catalyst layer using Nafion as the binder of the carbon black particles. His preparation procedure and some images of the resulting catalyst layer are presented here.

Preparation:

0.1 g of Vulcan XC72 was mixed with 1.0 g of 5% Nafioin solution. The resulting catalyst layer prepared with this mixture has Nafion content between 30-35 wt%. The mixture was sonicated and stirred several times over a 1 to 2 hour period. The sonication intervals were about 30 minutes long. After this mixing process, the slurry was spread unto the surface of the die using a blade. Figure A-1 shows images of the silicon die used by Lee.

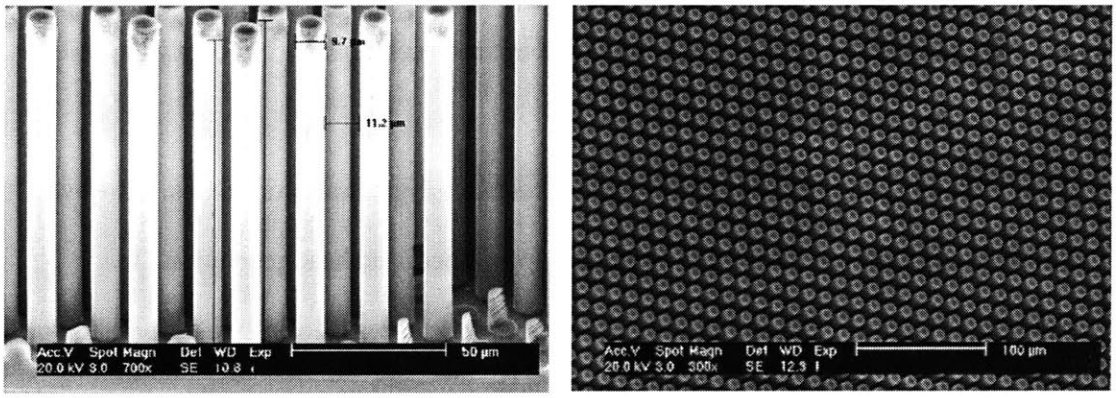

(a) (b)

Figure A-1: Images of silicon die microfabricated by deep reactive ion etching

The die was then placed in a vacuum oven at room temperature for 30 minutes to help in the infiltration of the slurry into the die. A Nafion membrane was then placed on top of the die. The Nafion membrane was needed to provide structural integrity. The Nafion-

bonded catalyst layer was not a free-standing membrane on its own. The silicon die, slurry, and Nafion membrane was placed back in the vacuum oven and dried at room temperature for 24 hours. The drying process was very important to the formation of the catalyst layer. If the membrane was not dried slowly, cracks easily formed on the catalyst layer. After the drying process, the silicon die was removed chemically. The silicon die etching solution was 50 wt% KOH at 70°C.

Nafion-Bonded Catalyst Layer Images:

Figure A-2 and Figure A-3 are SEM images of the catalyst layer after the silicon die has been etched away. The images show some defects in the catalyst layer structure. For the most part, however, the fabrication process was successful. Thus, Lee has shown that the microfabricated catalyst layer can be formed by casting a polymer and carbon black slurry on a microfabricated die.

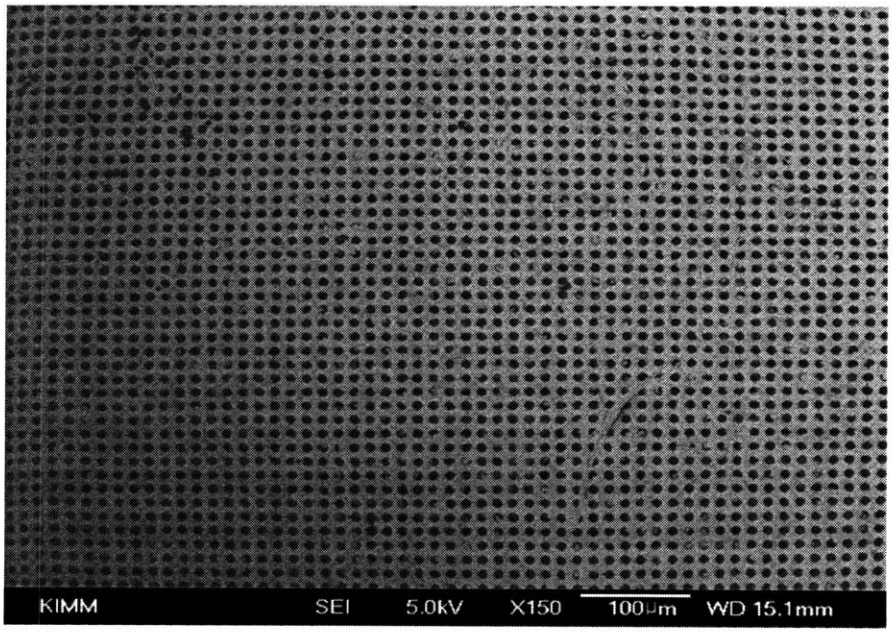

Figure A-2: Nafion-bonded microfabricated catalyst layer (top view)

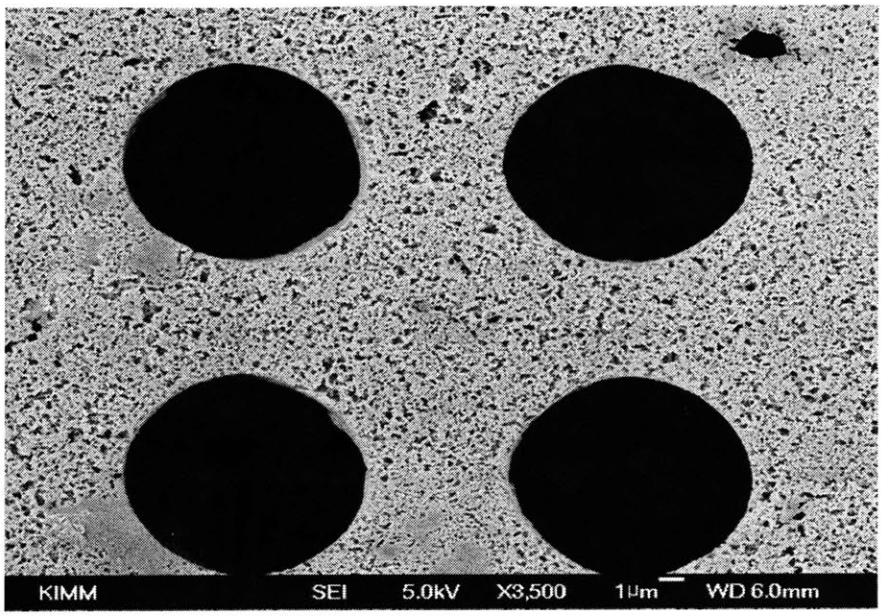

Figure A-3: Nafion-bonded microfabricated catalyst layer (top view) at higher magnification

Figure A-4 and Figure A-5 are SEM images of the side view of the catalyst layer.

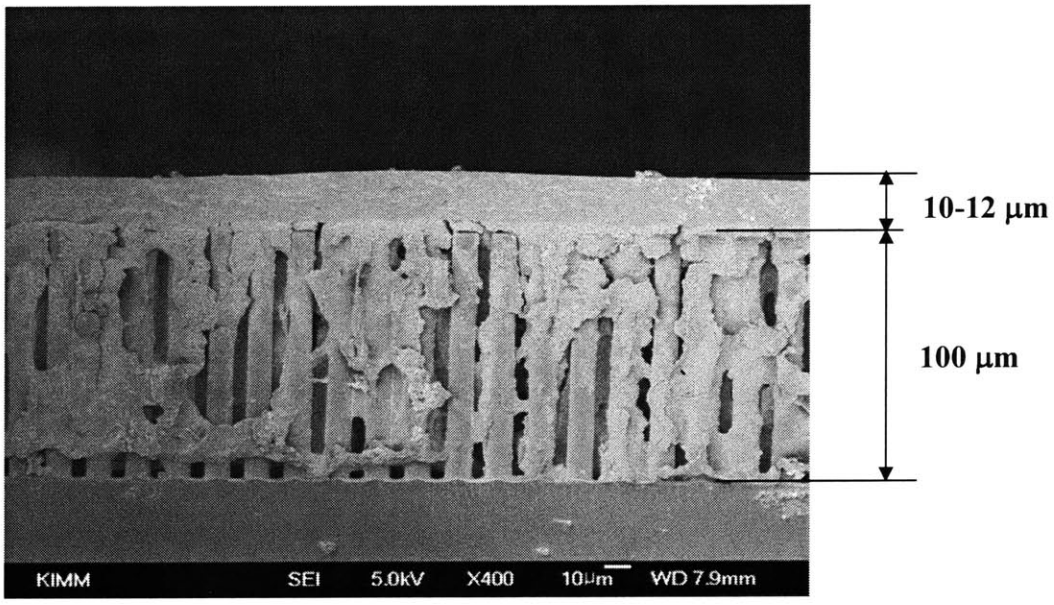

Figure A-4: Nafion-bonded microfabricated catalyst layer (side view)

The images show that the slurry effectively penetrates the entire silicon die. Some of the die's channels showed no carbon particles because they were removed when the die was broken.

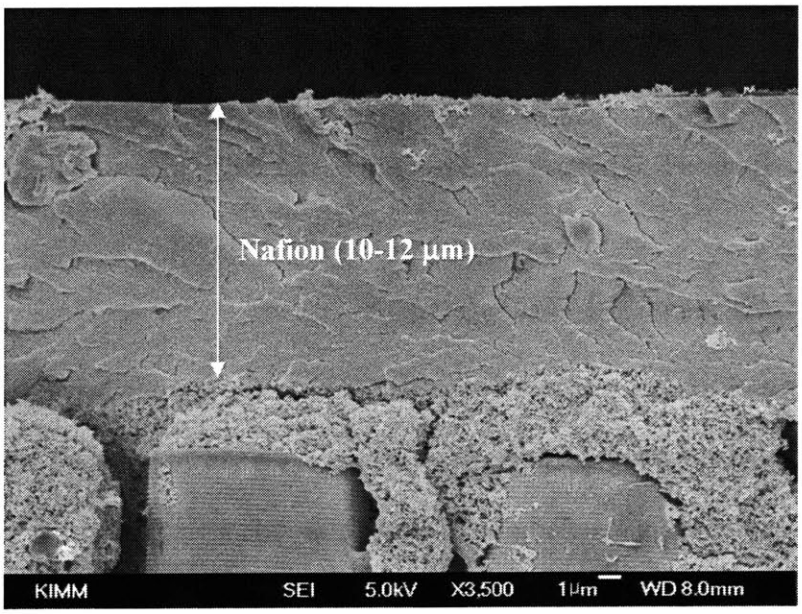

Figure A-5: Nafion-bonded microfabricated catalyst layer (side view) at higher magnification

Appendix B

The Preparation and Characterization of Carbon Aerogel Membranes and the Preparation of Carbon Aerogel Catalyst Layers

By:
Ronald S. Tharp, Fritz Pierre, Jr., and Dr. Chang Rae Lee

B.1 Carbon Aerogel Background

Carbon aerogels are most commonly created by the reaction between resorcinol (1, 3 dihydroxy benzene) and formaldehyde. The process is shown in Figure B-1. The two components are mixed in a molar ratio of 2 formaldehyde molecules to 1 resorcinol in a solvent such as water or alcohol. Sodium carbonate is added to serve as a catalyst. The solution pH can be adjusted by the addition of dilute nitric acid. The presence of the catalyst results in the creation of ionized resorcinol by hydrogen abstraction from one of the OH group to form an O^+. The formaldehyde molecules then attach themselves to the carbon ring at either two of the 2, 4, or 6 sites to form a hydroxymethyl derivative of resorcinol containing two CH_2OH functional groups. The level of catalyst is important because it is the creation of the ionized resorcinol by the catalyst that dramatically increases the chances of formaldehyde bonding, which creates the resorcinol derivative that undergoes condensation [1].

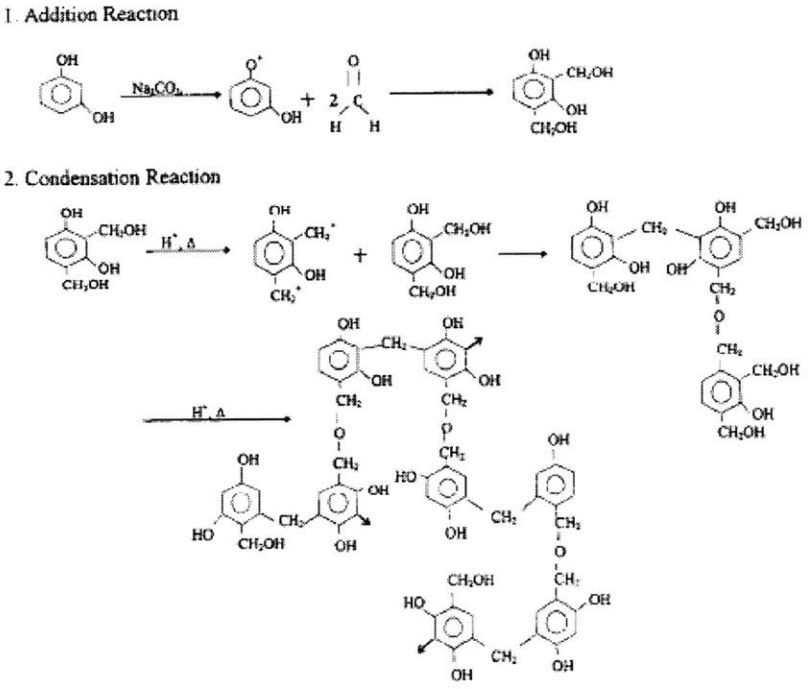

Figure B-1: The addition and condensation reactions involved in the forming of an organic aerogel [1]

During condensation, H^+ ions within the solution react to remove an OH^- group from one of the CH_2OH groups, thus creating a CH_2^+ group. The CH_2^+ from one resorcinol derivative usually joins itself to the benzene ring of another resorcinol derivative to create a methylene ($-CH_2-$) bridge. Sometimes the CH_2^+ may instead react with the CH_2OH group of another resorcinol derivative to create a methylene ether ($-CH_2OCH_2-$) bridge with an H+ ion as the byproduct [1]. Over time, the methylene ether bridges will disproportionate to form methylene bridges, forming formaldehyde as a byproduct. Depending on several factors, the curing time can vary from hours to days. During this time, monomers undergo further cross-linking to form nanometer-size clusters. Once a cluster is created, additional monomer groups attach themselves to the cluster. The result is that the cluster increases in size. The clusters continue to grow until all resorcinol is consumed. The size and appearance of the clusters within the gel

structure vary heavily with the ratio of resorcinol molecules to catalysts. With ratios between 50 and 300, a clear, red gel is formed. If the R/C ratio is set below 50, then the gel becomes opaque and contains precipitates [2].

After gelling is complete the gel has a complex structure of interconnected pores created by the intricate geometry of the joined particles. The next step is to evacuate the liquid solvent contained within the pores. The method used depends upon the solvent and several other elements of fabrication that will be discussed in a later section. In the most common case the solvent is water. Unfortunately, water has a very high surface tension of approximately 72.80 dynes/cm. Due to the low density of the aerogel and the small size of the pores, if the water were simply allowed to evaporate, its surface tension would render the aerogel useless by crushing all of the pores within the aerogel. In fact, almost any phase change process results in significant collapse of the pores.

The common solution is replacing the water with liquid CO_2. However, this is a long and complex process. Liquid CO_2 cannot directly replace the water. An organic solvent such as acetone must be used. The aerogel is soaked in acetone to allow the acetone to replace the water. Once the water has been replaced with acetone, the aerogel is placed within a high pressure chamber which is then filled with liquid carbon dioxide. Over the course of several days the liquid carbon-dioxide replaces the acetone within the pores. The temperature is slowly raised above the critical point of CO_2 at constant volume. Although the pressure is over 74 atmospheres, the degradation to the polymers is minimal. The super-critical carbon dioxide is vented until all carbon dioxide is removed. The pressure and temperature are returned to normal and the aerogel pores are left evacuated of liquid [2].

The organic aerogel is then pyrolyzed to create a carbon aerogel. During pyrolysis, the sample is placed within a nitrogen gas chamber. The temperature is then raised to between 800° and 1050° C. The bonds holding the hydrogen and oxygen atoms to the carbon skeleton break and the hydrogen and oxygen are removed. Eventually, all that remains is the porous carbon skeleton of the aerogel, which is referred to as a carbon aerogel. Pyrolysis is accompanied with a decrease in volume of approximately 50%. The final density, surface area, and pore size depend upon variables in gel composition, gel drying, and pyrolysis.

Effect of R/C Ratio:

The ratio of the amount of resorcinol to the amount of catalyst, also the called the R/C ratio, is an important element in determining the structure of the aerogel. The catalyst assists in the formation of the aerogel by ionizing the resorcinol molecules. The ionization of the resorcinol increases its propensity to react with formaldehyde to create functional monomer groups. The functional monomer groups cross-link to create nanometer-size clusters. Once a cluster is created, additional monomer groups will attach to the cluster. As the clusters grow in size, the surface area of the cluster and thus the number of reaction sites increase. The result is exponential growth in cluster size. Some of the methylene ether bridges break down to methylene bridges and release formaldehyde. Consequently, excess formaldehyde is always present and the particle growth continues until all the resorcinol is consumed [3].

The ratio of the resorcinol to the catalyst determines the likelihood of a cluster being formed. When the ratio has a small value, such as 50, the amount of catalyst is very large. The initial result is a significant number of clusters. With a large number of

clusters each attracting resorcinol monomers, the rate of particle growth is slowed. The end effect is that more clusters exist and each cluster has a small diameter of between 3-5 nm. When joined, the particles have large necks, creating the fibrous appearance shown in Figure B-2.

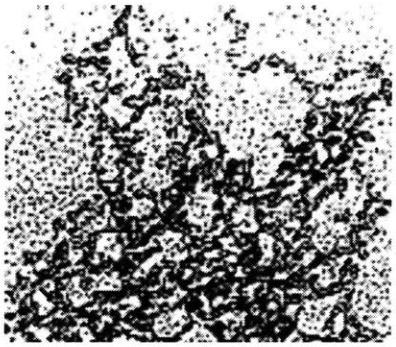

Figure B-2: Image of carbon aerogel (RC = 50). Note the fibrous appearance [3].

When the ratio is large, the amount of catalyst is fairly small. Fewer clusters are initially created, which results in less competition over resorcinol monomers. The clusters that do appear can easily grow in size. Due to how the number of reaction sites increases with volume, these clusters grow exponentially. The result is a small number of particles with large diameters between 11 and 14 nm. When joined, the particles have a "string of pearls"-like appearance as seen in Figure B-3 [3].

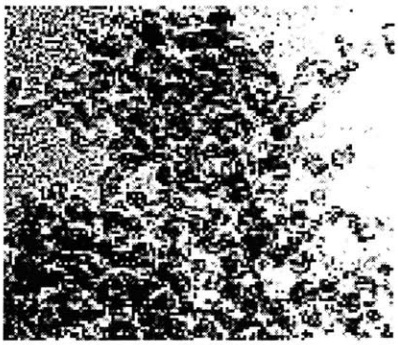

Figure B-3: Image of Carbon Aerogel (R/C = 200). Note the "string of pearls" appearance and larger particle size [3]

Other factors such as initial pH of the solution, the initial solid-to-solution ratio, and the pyrolysis temperature affect the structure of the resulting carbon aerogel. Tharp provides a review of how these facts affect the carbon aerogel [4].

B.2 Surfactant in Aerogel Fabrication

The greatest contribution to the collapse of pore structures is the surface tension of the solvent, which is present inside the mesopores of the aerogel. The most common solvent has been water. However, due to water's high surface tension, other solvents and solvent exchange methods have also been explored. Since the most complicated, time consuming, and expensive step in carbon aerogel fabrication is the supercritical CO_2 drying, work has been done to see if that step could be removed. A revolutionary idea was to use surfactants within the solvent.

Surfactants are compounds which have both a hydrophobic and hydrophilic end. The hydrophilic end tends to orient itself towards polar molecules when it is in a solution. The hydrophobic end tries to orient itself toward non-polar molecules and away from polar molecules as much as possible.

In a recent patent application, Bell *et al.* explored the possibility of using a water and surfactant solution during organic aerogel fabrication to remove the need for supercritical CO_2 drying [5]. The key to the use of surfactants is that water is very polar. The surfactant in the resorcinol-formaldehyde solution aligned themselves with their hydrophobic heads facing the solution and their hydrophobic tails facing each other. The resorcinol-formaldehyde polymer forms around these surfactant micelles as seen in Figure 14. The size of the micelles is related to the initial concentration of surfactant in

solution. Generally, a solution with higher surfactant concentration will have larger micelles and result in aerogels with larger pores. Bell found by adjusting the initial formulation of the solution, carbon aerogels can be formed with a narrow pore size distribution and with average pore sizes in the rage of 4nm to microns.

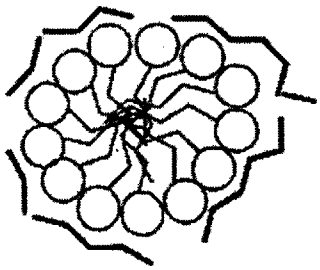

Figure B-4: Depiction of the micelle created by the surfactant within the pore. The micelle braces the pore and reduces the effect of the water surface tension [5].

The creation of the micelle has three primary advantages. The first advantage is that the usual diameter of the liquid crystal is such that it encourages the creation of mesopores rather than micropores. Since mesopores have the optimal properties for an electrode, the presence of the micelle should improve the performance of the electrodes manufactured using this method. The second advantage is that the contact between the water and the pore walls is reduced, thus decreasing the effective surface tension of the water. As a result, during the process of drying, the amount of stress placed on the walls is lower than if the surfactant were not used. The third advantage is that the micelle remains during the drying process. As such, the crystal acts like a series of struts bracing the pore walls against each other.

The combination of these three effects greatly reduces the likelihood of collapse. In fact, the effect is so significant that aerogels can be dried without having to replace the

water solvent; while still possessing a structure comparable to aerogels created by super-critical CO_2 drying. After air drying, the micelle are consumed by the pyrolysis process, leaving little trace. Thus, the use of surfactants allows for air drying without solvent exchange, while preserving the geometry of the aerogel and leaving no residue [5].

B.3 Carbon Aerogel Membrane Preparation

Four different aerogel types were prepared and tested. The preparation procedure for each of these aerogels is given below.

Organic aerogels via air drying with a low surface tension fluid:

The procedure for preparing this type of carbon aerogel was taken from the patent by Mayer *et al.* [6]. In this case, two types of aerogel membranes were made with different R/C ratios. One type of aerogel membrane was made with an R/C ratio of 50 which represented the highest level of catalyst that could be added without precipitate formation. The other type was made with an R/C ratio of 200, which corresponds to a low level of catalyst. Water was used as the solvent in the resorcinol-formaldehyde solutions. The 50 R/C ratio mixture consisted of 12.35 g of resorcinol, 19.91 g of 37% formaldehyde solution (water is the solvent), and 22.4 g of 0.1 M sodium carbonate. The 200 R/C ratio mixture consisted of the same amount of resorcinol and formaldehyde solution as the 50 R/C ratio mixture. For this type of membrane, the amount of the sodium carbonate solution added to the mixture was 5.6 g. For both mixtures, no additional water, other than that from the formaldehyde and sodium carbonate solutions, was added to the mixture. Each mixture was sealed in an airtight container and cured for 24 hours at room temperature, then 24 hours at 50°C, and finally an additional 24 hours

at 90°C. The container was sized so that aerogel membranes 3" by 6" were formed. The container could be adjusted to produce membranes with a thickness between 1mm to 100 um. Next, the water was exchanged with acetone and then with cyclohexane. The two samples were then allowed to air dry at room temperature to remove the cyclohexane.

Organic aerogels air dried with the aid of a surfactant:

Two types of aerogel membranes were made using the surfactant method described by Bell [5]. Both membranes were formed with an R/C ratio of 200. In one aerogel precursor mixture, the molar ratio of surfactant cetyltrimethylammonium (CTAC) to resorcinol was 0.06. For the other mixture, the ratio was set at 0.1. The 0.06 CTAC ratio mixture consisted of 6.175 g of resorcinol, 9.04 g of 37% formaldehyde solution, 0.714 g of 0.4 M sodium carbonate, and 4.307 g of a 25% CTAC solution (water is the solvent). The 0.1 CTAC ratio mixture consisted of the same amount of resorcinol, formaldehyde solution, and 0.4 M sodium carbonate solution as the 06 CTAC ratio mixture. For the type of membrane, the amount of the 25% CTAC solution added to the mixture was 7.18g. For both mixtures, no additional water, other than that from the formaldehyde, sodium carbonate, and CTAC solutions, was added to the mixture. These samples were then cured for 24 hours at 70° C in the same airtight container described above. Finally, the samples were air dried for 24 hours at room temperature followed by 3 hours within a 100° C convection oven.

All four aerogel membrane types were placed within an inert N_2 atmosphere oven. The temperature was increased by $1^{\circ}C/\text{min}$ until the temperature reached 1050° C. The samples were then kept at this temperature for 4 hours, during which the sample underwent pyrolysis, leaving a carbon skeleton.

The structure of the samples was explored by using a scanning electron microscope (SEM) to take pictures of the surface of each sample type. The density and average poor size of the samples was also measured. The aerogel membranes electronic and ionic conductivities were measured using the techniques described in Chapter 4.

B.4 Carbon Aerogel Membrane Properties

The aerogels prepared using a low surface tension fluid experienced noticeable shrinkage during the air drying process. The 200 R/C ratio aerogel shrunk by 10% when it was air dried. The 50 R/C ratio shrunk by 30% when it was air dried. The higher shrinkage of the 50 R/C ratio aerogel compared to the 200 R/C ratio aerogel is consistent with what is observed for aerogels dried by supercritical CO_2 [2].

Figure B-5 contains the SEM images of carbon aerogels dried using low surface tension fluid.

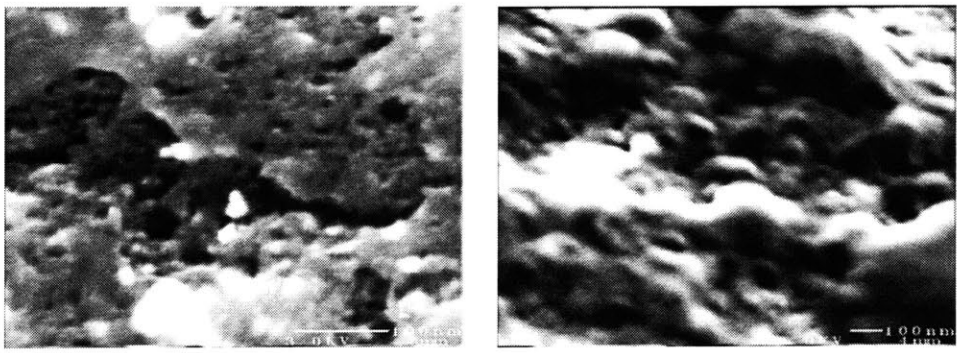

(a) (b)

Figure B-5: Image of carbon aerogels prepared using cyclohexane during the air drying process. Image (a) is the cleaved surface of the aerogel prepared with 200 R/C ratio. Image (b) is the cleaved surface of the aerogel prepared with 50 R/C ratio.

The 200 R/C ratio aerogel did have pores that were visible under SEM. The porosity did not appear to be continuous. From the SEM image, the average size of the pores was

determined to be less than 30 nm. The image of the 50 R/C ratio aerogel did not show any pores. It appears that these pores completely collapsed during air drying.

Figure B-6 contains the SEM images of the carbon aerogels prepared with the CTAC surfactant.

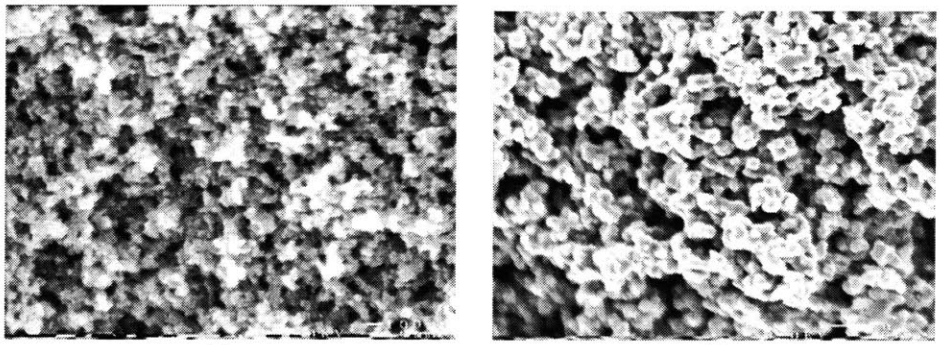

(a) (b)

Figure B-6: Image of carbon aerogels prepared by air drying with the aid of the CTAC surfactant. Both Images are of aerogels prepared with 200 R/C ratio. Image (a) is the cleaved surface of the aerogel prepared with 0.06 CTAC/R ratio. Image (b) is the cleaved surface of the aerogel prepared with 0.10 CTAC/R ratio.

In dramatic contrast to the membranes prepared with no surfactant, the SEM images show the aerogels prepared with surfactant were highly porous. The porosity was clearly continuous. The SEM images also show that the aerogels prepared with 0.1 CTAC/R ratio have larger particles and larger pores than aerogels prepared with 0.06 CTAC/R ratio.

Figure B-7 contains the SEM images of the surface of carbon aerogel membranes prepared with a 200 R/C ratio and 0.1 CTAC/R ratio. Image (a) is the surface of a membrane that was cast in a Lexan container. Image (b) is the surface of a membrane that was cast in a Teflon container. The skin of the membrane prepared on Lexan was not porous. It did have some surface scratches that allowed one to image, by SEM, what was below the skin.

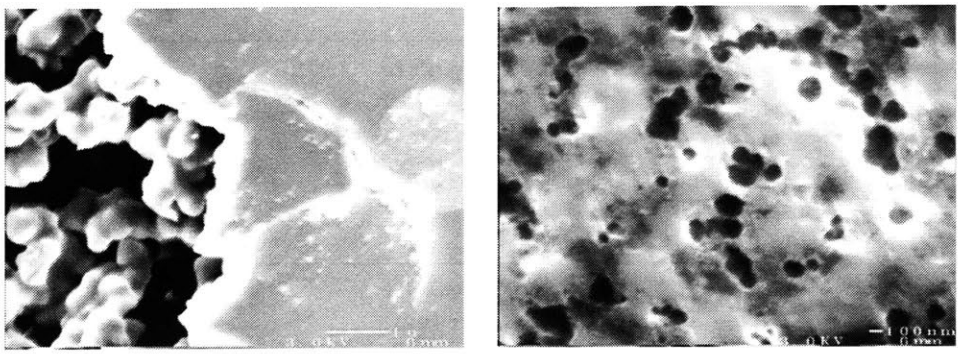

(a) (b)

Figure B-7: Image of carbon aerogels prepared by air drying with the aid of the CTAC surfactant. Both images are of aerogels prepared with 200 R/C ratio and 0.10 CTAC/R. Image (a) is the membrane skin of aerogel membrane prepared by casting on Lexan surface. Image (b) is the membrane skin of aerogel membrane prepared by casting on Teflon surface.

Image (a) shows the membrane skin and the porous structure that is underneath the skin. The skin of the membrane prepared on Teflon was porous as seen by Image (b). The Images of Figure B-7 indicate that the porosity of the aerogel membrane skin depends of the surface the aerogel is cast on. This observation suggests the surface properties of the aerogel can be adjusted by using different casting surfaces.

Porosity:

The porosity of the carbon aerogels were determined by measuring the apparent density of the aerogel and applying the following equation:

$$\varepsilon = \frac{1.42 - \text{density}}{1.42} \tag{1}$$

where 1.42 is the assumed density, in g/cm^3, of the amorphous carbon with no pores. The density and porosity of the aerogels are listed in Table B-1

No Surfactant

R/C	Density (g/cm^3)	Avg. Pore Size (nm)	Porosity
50	1.2	N/A	0.155
200	1.0	< 30	0.30

Surfactant (R/C = 200)

CTAC/R	Density (g/cm^3)	Avg. Pore Size (nm)	Porosity
0.06	0.65	100	0.54
0.10	0.55	500	0.61

Table B-1: Material properties for carbon aerogel samples for different R/C ratios and CTAC/R ratios. The surfactant samples have a lower density, continuous porosity, and larger mesopores

Electronic and Ionic Conductivity:

The electronic conductivity of the carbon aerogel membranes were measured using the four-point probe method described in Section 4.3.5. The conductivity of the aerogel membranes made from 200 R/C ratio and no surfactant was measured to be 86.4 S/cm. The electronic conductivity values of the aerogel membranes made with 200R/C ratio and surfactant were measured to be 34.2 and 40.7 S/cm for the CTAC/R ratios of 0.06 and 0.10, respectively.

Figure B-8 is a graph containing the measured ionic conductivity carbon aerogel membranes saturated with 3.7 M sulfuric acid. The ionic conductivity of the 50 R/C ratio with no surfactant membrane was not measured since all the pores of this membrane collapsed during air drying. The graph also contains data for the PES-bonded membranes and a theoretical value for the ionic conductivity of conventional porous carbon electrode impregnated with 3.7 M sulfuric acid. The solid line in the figure is a plot of the equation

$$\sigma_{eff} = \sigma_b \varepsilon \tag{2}$$

where σ_b is the bulk conductivity of the 3.7 M sulfuric acid solution. It value was measured to be $\sigma_b = 0.735\ S/cm$.

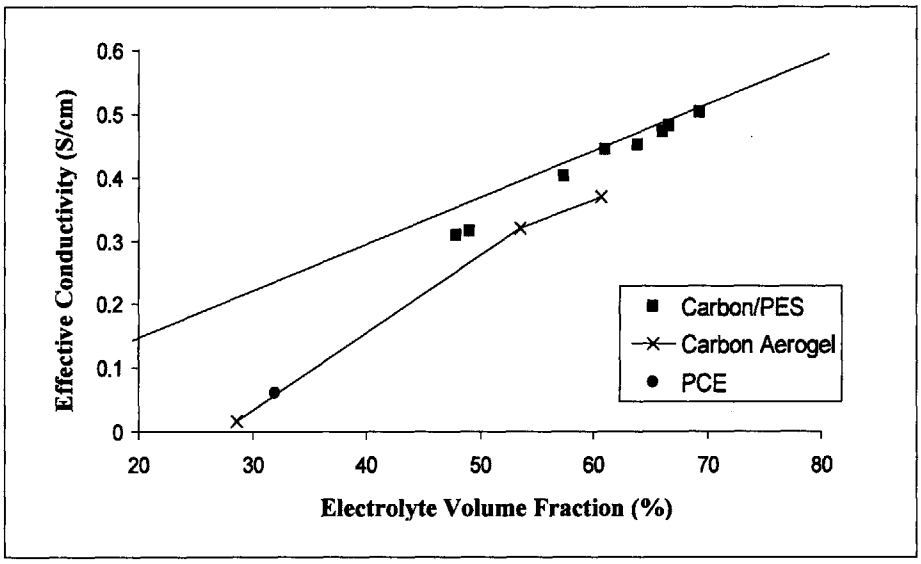

Figure B-8: Plot of ionic conductivity of membranes saturated with 3.7 M H_2SO_4. The carbon aerogel data points are for the both the 0.06 and 0.10 CTAC/R ratio prepared membranes and the 200 R/C ratio membrane prepared with no surfactant. The plot also includes the measured conductivity of the PES-bonded membranes and the theoretical conductivity of the porous carbon electrode (PCE).

General Observations of Carbon Aerogel Membranes:

The prepared carbon aerogel membranes were not flexible. For thicknesses less than 300 μm, the membranes were too brittle to work with. They easily cracked when they were placed in the property measuring instruments. All carbon aerogel membranes had a membrane skin that had a mirror-like polish to it. This membrane skin was not removed or scratched when a Q-tip was lightly brushed over it. Unlike the PTFE-bonded and PTFE-bonded membranes, liquid water spontaneously saturated the aerogel membranes.

B.5 Microfabricated Carbon Aerogel Catalyst Layer

Attempts were made to fabricate the carbon aerogel catalyst layers. A silicon die microfabricated by deep reactive ion etching was used. The aerogel precursor mixture was the 200 R/C ratio and 0.10 CTAC/R ratio type. Ultimately it was determined that the catalyst layer could not be formed by casting the aerogel in this die. The slight shrinking of the aerogel during air drying was detrimental to the formation of the catalyst layer. The preliminary results of the work done by Lee at KIMM are briefly presented below.

Die Fabrication and Filling:

Initially, holes were drilled in the surface of the sample through the use of a UV laser. For preliminary work this method worked fairly well. Unfortunately, a functional electrode would need an order of magnitude more holes of a smaller diameter than the laser method could provide. Thus, it was determined that future samples would need to made through the use of a microfabricated die, which the gel could be poured into.

The first step was the fabrication of the silicone die. Based upon the high ratio of depth to diameter needed for the die and the small hole sizes, it was determined that the silicon die would need to made by deep reactive ion etching (DRIE). Since the die was to be a negative image of the electrode, the die would need to have a series of poles corresponding to the hole locations in the electrode. The poles were designed to have a diameter of 10 micrometers with 5 micrometer spacing between poles. A mask corresponding to the pole locations was placed over a silicon wafer. DRIE was then used to remove the silicone around the poles to a depth of 100 micrometers, as seen in Figure B-9.

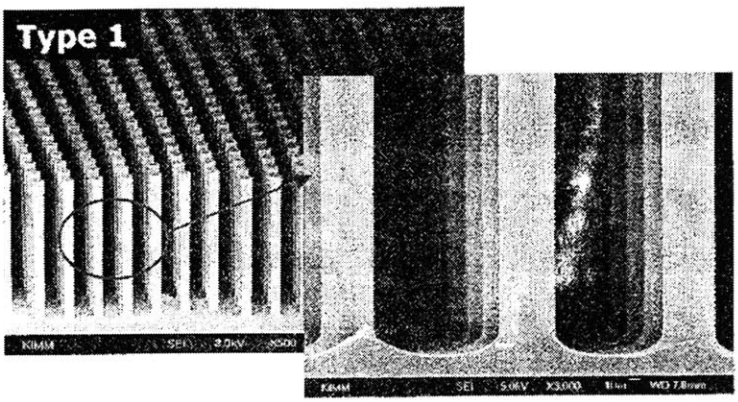

Figure B-9: Image of the Silicone Die created using DRIE

After the die was fabricated, a liquid RF solution was poured over the die. The die and RF solution were then processed and allowed to dry until the solution gelled. The resulting gel was then carbonized in an inert N_2 atmosphere to create a carbon aerogel.

Several problems were discovered during initial fabrication. During DRIE, the sides of the surface features which were not etched were coated with a thin passivating layer to protect them from the plasma used in etching. However, the protective coating was non-wetting. Since the solvent of the RF solution was water, the solution would not wet the sides of the poles. As a result, the die was not completely filled.

The solution to this problem was to treat the surface of the silicone die with O_2 plasma. The plasma eroded the protective coating from the surface of the die without significant erosion of the surface topography. As a result, the surface was much better at wetting the solution and filling of the die improved.

Another method used to improve filling was to place the samples in a vacuum chamber during the filling process. The low pressures differential caused the air within the silicone die to pass through the RF solution. The removal of the air allowed the RF

solution to better fill the die and avoided air pockets which would create flaws in the final carbon aerogel electrode.

The final and most pressing problem was the cracking of the die. The high surface tension of the water within the RF solution resulted in a high level of shrinkage occurring. Due to the thinness of the poles and the high ratio of pole height to diameter, the poles could not resist the shrinkage and were bent and broken during the process. Figure B-10 shows an image of a die taken after the drying process. Clear signs of the cracking and breaking of the poles can be seen. The top surface of the aerogel shows multiple cracks.

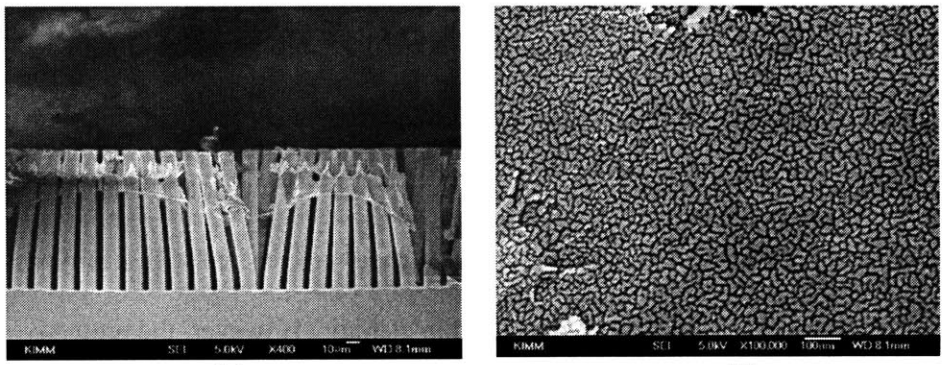

(a) (b)

Figure B-10: SEM images of aerogel cast on silicon die after air drying. The casting mixture contained a 200 R/C ratio and 0.10 CTAC ratio. Image (a) shows the breaking of the die caused by aerogel shrinking when air dried. Image (b) shows the cracking of the aerogel surface.

Conclusion:

The shrinking of the aerogel could not be avoided. For this reason, carbon aerogel is no longer considered to be a suitable material for the microfabricated catalyst layer.

References

[1] J.A. Ritter, "Effects of synthesis pH on the structure of carbon xerogels", *Carbon*; Vol. 35, p. 1271, 1997.

[2] R.W. Pekala; C.T. Alviso; F.M. Kong; and S.S. Hulsey, "Aerogels derived from multifunctional organic polymers", *Journal of Non-Crystalline Solids*; **1992**; 145; pp. 90-98.

[3] R.W. Pekala; C.T. Alviso; J.D. LeMay, "Organic aerogels: microstructural dependence of mechanical properties in compression", *Journal of Non-Crystalline Solids*; Vol.125; p. 67, 1990.

[4] R.S. Tharp, *Fabrication of Carbon-Aerogel Electrodes for Use in Phosphoric Acid Fuel Cells*, B.S Thesis, Mechanical Engineering Department, Massachusetts Institute of Technology, 2005.

[5] W. Bell and D. Steven, *Mesoporous Carbons and Polymers*, U.S. Pat. No. 6,737,445 (2004).

[6] S.T. Mayer, J.L. Kaschmitter, and R.W. Pekala, Method of Low Pressure and/or Evaporative Drying of Aerogel, U.S. Pat. No. 5,420,168 (1995).

Appendix C

Oxygen Gain Model's MATLAB Scripts

gain.m

```
%Written by Fritz Pierre
%This matlab script is used to simulate the oxygen gain, temperature, and liquid pressure
%during oxygen gain experiments
close all
clear all
%begin time
tic
%Global variables - these variables are used in several of the electrode
%model '.m' files.
global T_gas Pt Itot L N2_guess N1
%Define Parameter
%Universal Constants
R = 8.3;
F = 96485;
%Length for diffusion of gas (cm)
L = 0.4;
%Initial Guess forTemperature of film
T = 293;
%Total Pressure of Gas Phase
Pt = 1;
%Vapor pressure of water at the inlet in bars
P20 = 0.01;
%*************************************************************************
for j= 1:2
%The inlet pressure of oxygen and nitrogen in bars
if j == 1
   P10 = .2;
else
   P10 = 1-P20;
end
P30 = Pt - P10 - P20;
%*************************************************************************
step_i = 15;
for i=1:step_i
%Current of cell (A/cm^2)
Itot = 0.01 + 0.01*(i-1)
%Oxygen flux (mol/(cm^2*sec))
%Itot is positive
N1 = Itot/(4*F);
%Tolerance
tol = 0.1;
%*************************************************************************
%Properties of Platinum Film
%Specific Area of Pt Film (cm^2_Pt/mg)
SA = 250;
%Pt Loading (mg/cm^2)
Pt_loading = 40.2/1000;
%Total Pt area;
```

```
Area_tot = SA*Pt_loading;
%Exchange Current Density @ 1 bar Oxygen and 298 K
io_298 = 1*10^-7;
%Tafel Slope
TF = 0.1184/2.3;
%Activation Enthalpy (J/mol)
E_act = 25000;
%*************************************************************************
%mass fraction of electrolyte is assumed to be constant
w_e_0 = 0.30;
%*************************************************************************
%first iteration
heat_flux
if Q_kin >= Q_tot
%must increase temperature to increase evaporation rate
T_old = T;
p = -1;
temp_converge = 1;
while (abs(Q_kin - Q_tot)/Q_kin)*100 >= tol
   T = T_old;
   heat_flux
   temp_converge = temp_converge + 1
   p = p + 1;
   while (abs(Q_kin - Q_tot)/Q_kin)*100 >= tol
  T_old = T;
  T = T + (10/(10^p));
   heat_flux
  if (abs(Q_kin - Q_tot)/Q_kin)*100 >= tol & Q_kin <= Q_tot
     break
  end
  end
error = (abs(Q_kin - Q_tot)/Q_kin)*100;
if temp_converge >= 10
   break
end
end
%*************************************************************************
else
%*************************************************************************
%must decrease temperature to decrease evaporation rate
T_old = T;
p = -1;
temp_converge = 1;
while (abs(Q_kin - Q_tot)/Q_kin)*100 >= tol
   T = T_old;
   heat_flux
   temp_converge = temp_converge + 1
   p = p + 1;
   while (abs(Q_kin - Q_tot)/Q_kin)*100 >= tol
  T_old = T;
   T = T - (10/(10^p));
   heat_flux
  if (abs(Q_kin - Q_tot)/Q_kin)*100 >= tol & Q_kin >= Q_tot
     break
  end
  end
```

```
error = (abs(Q_kin - Q_tot)/Q_kin)*100;
if temp_converge >= 10
  break
end
end
%*************************************************************************
end
%*************************************************************************
%Pressure of liquid electrolyte at Pt film
liquid_properties
%mass flux at the liquid-gas interface
m_dot_tot = (N2_guess*N1*mw_2) - (N1*mw_1);
%Saturated permeability of substrate [cm^2].
k_sat = 1.42*10^-15;
%thickness of membrane (cm)
Lm = 112e-4;
%mass average velocity
velocity = m_dot_tot/den_e;
PL_final = 1 -(visc_e*velocity*Lm)/(k_sat);
%*************************************************************************
%Temperature of film
T_f(j,i) = T;
%Overpotential
OVP_f(j,i) = OVP;
%Potential of elecrode
potential_f(j,i) = 1.23 - OVP ;
%Current density
Itot_f(j,i) = Itot;
%Electrolyte Pressure at Pt film
PL_final_f(j,i) = PL_final;
%Partial Pressure of water
P2_water_f(j,i) = P2_water;
%Error for energy balance
error_f(j,i) = error
%*************************************************************************
end
end
%*************************************************************************
figure(1)
plot(T_f(1,:))
hold
plot(T_f(2,:))
hold
Ox_Gain = potential_f(2,:) - potential_f(1,:);
figure(2)
plot(Ox_Gain)
Axis([1 10 0.075 0.1])
```

heat_flux.m

```
%Initial guess for gas flux of water out of half cell.
%It is weighted with respect to oxygen flux.
N2_guess = 1;
%*************************************************************************
%Pressure of water at film
P2_water = exp( -1*(0.0001808*(T^2) - 0.16803*T + 37.773) );
```

```
%*************************************************************************
%First interation
  [x,y]=ode23('diffusion',[0:0.01:1],[P10 P20]);
  P1_final = y(101,1);
  P2_final = y(101,2);
%Solve for flux (over shoot method is used)
  if P2_final >= P2_water
  %Then the flux is greater than it should be.  It will be systematically reduced
  lower_flux
  else
  increase_flux
  end
%*************************************************************************
%effective exchange current density @ given temperature
io_eff = io_298*Area_tot*exp((-E_act/R)*( (1/T) - (1/298) ));
%overpotential
OVP = TF*( log(Itot/io_eff) + log(1/P1_final) );
%Heat produced due to irreversibility of electrochemical reaction (W/cm^2),
%ignoring heat generated due to reversible change in entropy.
Q_kin = OVP*Itot;
%latent Heat of vaporizaiton of water (assume to be that of pure water)
%in kJ/mole
delta_H = -3.0126*10^-5*(T^2) - 2.4201*10^-2*(T) + 53.880;
%Flux of water
N2 = N2_guess*N1;
%Heat removed by evaporation of water (W/cm^2) multiplied expression by
%1000 inorder to change delta_H from kJ/mol to J/mol
Q_evap = delta_H*1000*N2;
%Total heat removed from the system
Q_tot = Q_evap;
```

diffusion.m

```
function f = diffusion(x,y)
global Pt Itot L N2_guess N1
% Defining Local state variables.
%Pressure of oxygen in bars
P1  = y(1,:);
%Pressure of water in bars
P2 = y(2,:);
%Define Parameter
%Universal Constants;
R = 8.3;
F = 96485;
%molecular wieghts of gases (oxygen, water, nitrogen)
mw_1 = 32;
mw_2 = 18;
mw_3 = 28;
%Temperature of gas
T = 298;
%Binary diffusion coefficients. Equations obtained from Bird and Lightfoot pg
%505 (in cm^2/s)
%Oxygen and Water
D12 = (0.3022/Pt)*((T/323.83)^2.334);
%Oxygen and Nitrogen
D13 = (0.0544/Pt)*((T/143.01)^1.823);
```

```
%Nitrogen and Water
D23 = (0.2526/Pt)*((T/292.77)^2.334);
%Effective binary Diffusion coefficients
D12_eff=D12;
D13_eff=D13;
D23_eff=D23;
%*************************************************************************
%Equations for ODE
N2 = -N2_guess*N1;
%Note the dimension for length is cm and pressure is in bars.
%Thus, the necessary conversion factor is (10). So in the equaitons below 10 is a
%conversion factor
oxygen = ((10*R*T)/Pt)*( ((N2*P1)/D12_eff) - ((1*Pt + ((D13_eff/D12_eff)-1)*P2 - P1)/D13_eff)*N1 );
water  = ((10*R*T)/Pt)*( ((N1*P2)/D12_eff) - ((1*Pt + ((D23_eff/D12_eff)-1)*P1 - P2)/D23_eff)*N2 );
%Ode (non-dimensionalize the length)
P1_dot = L*oxygen;
P2_dot = L*water;
%%%%%%%%%%%%%%%%%%%%%%%%%%%%%%%%%%%%%%%%%%%%%%%%%%%%%%%%%5
% Creating f vector
f(1,:) = P1_dot ;
f(2,:) = P2_dot;
```

increase_flux.m

```
%iteration for converging to desired vapor pressure of water
N2_guess = 1;
N2_guess_old = N2_guess;
m = -1;
flux_converge = 1;

while (abs(P2_final - P2_water)/P2_final)*100 >= tol

   N2_guess = N2_guess_old;

   [x,y]=ode23('diffusion',[0:0.01:1],[P10 P20]);
   P1_final = y(101,1);
   P2_final = y(101,2);

   flux_converge = flux_converge + 1;
   m = m + 1;

   while (abs(P2_final - P2_water)/P2_final)*100 >= tol

   N2_guess_old = N2_guess;

   N2_guess = N2_guess + (.1/(10^m));

   [x,y]=ode23('diffusion',[0:0.01:1],[P10 P20]);
   P1_final = y(101,1);
   P2_final = y(101,2);


   if (abs(P2_final - P2_water)/P2_final)*100 >= tol & P2_final <= P2_water
      break
   end
```

```
  end
%*************************************************************************

end
%*************************************************************************
```

Lower_flux.m

```
%iteration for converging to desired vapor pressure of water
N2_guess = 1;
N2_guess_old = N2_guess;
m = -1;
flux_converge = 1;

while (abs(P2_final - P2_water)/P2_final)*100 >= tol

   N2_guess = N2_guess_old;

   [x,y]=ode23('diffusion',[0:0.01:1],[P10 P20]);
   P1_final = y(101,1);
   P2_final = y(101,2);

   flux_converge = flux_converge + 1;
   m = m + 1;

   while (abs(P2_final - P2_water)/P2_final)*100 >= tol

   N2_guess_old = N2_guess;

   N2_guess = N2_guess - (.1/(10^m));

   [x,y]=ode23('diffusion',[0:0.01:1],[P10 P20]);
   P1_final = y(101,1);
   P2_final = y(101,2);


  if (abs(P2_final - P2_water)/P2_final)*100 >= tol & P2_final <= P2_water
     break
  end

  end
%*************************************************************************

end
%*************************************************************************
```

Liquid_properties.m

```
%Liquid water and sulfuric acid properties.

%Temperature of the membrane. This temperature is different from the
%temperature at the surface of the substrate.
%T_L in [K]. All sulfuric acid properties are obtained for this temperature.
T_L = 273 + 25;
%*************************************************************************
%The concentration of the electrolyte is assumed to remain constant
%The potential of the electrolyte is assumed to remain constant
```

```
% A detail concentrated solution theory model of the membrane showed that
% these assumptions are valid for the range of current densities studied.
%Defining constant mass fraction and potential
w_e = w_e_0;
n_e = 0;
%**************************************************************************
%Define Parameter
%Unversal Constants;
R = 8.3;
F = 96485;
%molecular wieghts ( water, and sulfuric acid)
mw_w = 18.016;
mw_2 = mw_w;
mw_e = 98.076;
mw_o = 32;
mw_1 = mw_o;
%**************************************************************************
%Properties of pure liquid water
%Note: Density, viscosity and surface tension are fuctions of
%temperature. The expression given below are obtained from Weber's paper
%JES 152 A677 (2005)
%density of water [g/cm^3]
den_w_P = 1.1603 - 0.0005371*T_L;
%specific molar volume of water [cm^3/mol]
v_w_P = (1/den_w_P)*mw_w;
%surface tension of water [N/m]
surface_w_P = 0.12398 - 0.00017393*T_L;
%dynamic viscosity of water [bar*sec]
visc_w_P = (2695.3 - 6.6*T_L)*10^-11;
%**************************************************************************
%Transport and thermodynamic properties of electrolyte as function of electrolyte mass fraction. All
%properties were obtained by performing a polynomial regression on data
%obtained from. All properties are for an electrolyte temperature of T = 25 C
%Density of electrolyte [g/cm^3]
den_e = 0.29758*(w_e^2) + 0.63851*w_e + 0.99935;
%molar concentration of electrolyte [mol/cm^3]. This also the molar
%conentration of protons and sulfate ions.
mol_e = (w_e*den_e)/mw_e;
%molar concentration of water [mol/cm^3]
mol_w = (1-w_e)*den_e*(1/mw_w);
%density of sulfate ion
den_sulfate = mol_e*(mw_e-1.008);
%density of water
den_w = mol_w*mw_w;
%Slope of Density (Used to obtain the partial density and partial molar
%volume of electrolyte). Note partial density is different than density of
%each species. This is analagous to the fact that partial molar volume is
%different than concentration.
slope_den_e = 0.29758*2*(w_e^1) + 0.63851;
%partial density of electrolyte [g/cm^3]
den_e_partial = den_e + (1-w_e)*slope_den_e;
%partial molar volume of electrolyte [cm^3/mol]
v_e_partial = (1/den_e_partial)*mw_e;
%partial molar density of water [g/cm^3]
den_w_partial = den_e - (w_e*slope_den_e);
%relative viscosity of electrolyte [unitless]
```

```
r_visc_e = exp( 8.33785*w_e^4 - 11.17495*w_e^3 + 7.1826*w_e^2 + 0.74103*w_e - 0.0176);
%viscosity of electrolyte [bar*sec]
visc_e = r_visc_e*visc_w_P;
%Diffusion coefficient of electrolyte [cm^2/s]
diff_e = -0.000030765*(w_e^4) + 0.000081472*(w_e^3) - 0.000045373*(w_e^2) -0.000026002*w_e +
0.00002424;
%molar conductivity of electrolyte [s*cm^2/mol]
%At high electrolyte mass fraction w_e > 0.70 this correlation results in
%errors greater than 8%
molar_k_e = -6646.4657*(w_e^5) + 14202.4099*(w_e^4) - 11308.2673*(w_e^3) + 5032.3893*(w_e^2) -
2065.2415*(w_e) + 591.8387;
%conductivity of electrolyte [s/cm]
k_e = (molar_k_e)*(mol_e);
```

Appendix D

Half-Cell Model of Microfabricated Electrode in Concentrated Phosphoric Acid: MATLAB Scripts

vi_novel_1.m

```
%Written by Fritz Pierre
%This matlab script is used to produce an potential vs current plot for the
%novel electrode design concept. When platinum is deposited as a film in
%the macropores, the film experiences no oxygen transport losses.

clear all
close all

%begin time
tic

%Global variables - these variables are used in several of the electrode
%model '.m' files.
global T Pt Itot_Guess e_gas t_gas rk e_micro t_micro L k1 e_ion t_ion tr_anion k2_eff D1s D1s_eff delta
B_film H

global io A_gl a_pt U_rev r_agg e_type En P_ref U_pt TF k_BL_eff k_DL_eff

global k_sat Lm

%novel electrode model 1) for no oxygen transport losses within
%electrolyte.
e_type = 1;

%electrolyte film thickness
delta = 0*(1*10^-4);

%Define Parameter
%Universal Constants
R = 8.3;
F = 96485;
%*************************************************************************
%A typical operating condition of phosphoric acid fuel cell is acid
%concentration of 100%, pressure of 1 atm (with some water vapor), and a
%temperature of 190C.

%Temperature and Total Pressure of cell;
T = 273 + 200;
Pt = 1;
%Initial pressure of oxygen, water, and nitrogen in bars
%Assume high stoich flow so problem reduces to 1-D.
P10 = 0.1918;
P20 = 0.0866;
P30 = Pt - P10 - P20;
%*************************************************************************
```

```
%Pressure at the backside of matrix [bars]
PL_desired = 1;
%This pressure will be used at the first guess for the pressure at the
%diffusion layer-catalyst layer interface.  This pressure is higher than
%the actual pressure at this interface because the mass average velocity is
%positive.
PL_cat = PL_desired;
PL_cat_old = PL_cat;
%*************************************************************************
%reversible thermodynamic potential
%Value from Kunz and Gruver
U_rev=1.176;
%Tafel slop for oxygen reduction. Is assumed to remain unchange for the
%range of temperatures considered for phosphoric acid fuel cells. Refer to
%Kunz and Gruver. taken to by 90mV/decade.
TF = 0.090/2.3;
%exchange current density (A/cm^2)
%Approximation from Kunz and Gruver's work
io = 222*10^-9;
P_ref = 1;
%*************************************************************************
%Electronic conductivity of backing layer (s/cm)
k_BL_eff = 12.5;
%*************************************************************************
%Electronic conductivity of microporous layer (s/cm)
k_DL_eff = 1;
%*************************************************************************
%Geometric Parameters";
r = (5*10^-4);
s = r*(1/5);
rk = r;
%use an average value for diffusion length to approximate effective
%diffusion length in agglomerate. Average between mininum length
%and maximum length. For e_type = 1, r_agg value is not needed since there
%is no oxygen transport losses in a thin film.
r_agg = s*((1+sqrt(2))/2);
%porosity of microporous region of catalyst layer
e_micro = 0.77;
t_micro = 1;
e_agg = e_micro;
t_agg = 1;
%number of pores
Npores =(1/((2*r+2*s)^2));
%gas phase porosity and tortuosity of catalyst layer
e_gas = Npores*pi*r^2;
t_gas = 1;
%volume fraction of electrolyte in catalyst layer and tortuosity for ion
%transport
e_ion = (1-e_gas)*e_micro;
t_ion=1;
%Volume fraction of agglomerate in the catalyst layer
En=(1-e_gas);
%*************************************************************************
%electrolyte phase properties
%Saturated permeability of substrate [cm^2].
k_sat = 1.42*10^-15;
```

```
%conductivity and effective conductivity of electrolyte(S/cm)
k1 = 0.5;
%transfer number of anion [H2PO4]-. It is assumed that this is the only
%ion with a finite molar volume that moves under the the action of the
%potential field. Most of the current is carried by proton hopping.
%However, proton is assumed to have a negligible molar volume. So it does
%not contributie to volume flux (velocity).
tr_anion = 0.025;
%*************************************************************************
%Solid phase properties from experiments (S/cm)
k2= 2.5;
k2_eff = (1-e_gas)*k2;
%*************************************************************************
%Effective Conductivity
k1_eff = k1*(e_ion/t_ion);
%*************************************************************************
%Physical properties of platinun in catalyst layer
%Total platinum loading in (micrograms/cm^2).
PLTOT=500;

%platinum deposition specific laoding within the macropores and
Density=input('input platinum loading density in the macropores (micrograms/cm^2) (Density >= 20
ug/cm^2)----->');
%Density=60
%minimum loading for when specific area can be measured (micrograms/cm^2)
Density_min = 0.5;

%specify type of loading method to to determine how specific area
%varies with platinum loading.
den_type=input('input type of deposition 1 = electrodep, 2 = vapor_dep ---->');
%den_type=1;

%logic command to determine which paramater values to use.
if den_type == 1
   alpha = 0.3008;
   kappa = 0.7951;
else
   alpha = 0.4725;
   kappa = 0.654;
end
%Roughness factor
A_pt = alpha*( ((Density/Density_min)-1)^kappa );

%Calculate length of pores (thickness of catalyst layer) (cm)
L=(PLTOT-Density)/(2*pi*r*Npores*Density);
%Aspect ratio
Aspect_ratio  = L/(2*r);
%Total surface area of pores vs projected area
Area=(2*pi*r*L*Npores);
%Total area including geometric area where platinum is also deposited
Area_tot = Area + 1;
%total surface area pores per volume of catalyst layer (cm^2/cm^3). This is
%equivalent to A_gl the specific eletrolyte film area in catalyst layer.
%This assumes that the gas/electrolyte interface is not wavy. This term is
%not significant for novel electrode since experimental evidence shows that
%if an electrolyte film is present it does not hinder oxygen transport.
```

```
A_gl = Area/L;

%a_pt is specific reaction area in the catalyst layer
%(cm^2/cm^3). That is area of platinum per volume of agglomerate.
%in reality agglomerate model is not used for our electrode since platinum
%is not uniformly distributed within the micropores of catalyst layer.
a_pt=(A_pt)*(Area/L)*(1/En);
%area of platinum in the front face of catlayst layer (at the catalyst layer gas
%diffusion layer interface) cm^2pt/cm^2.
a_front = (A_pt)*(1-e_gas);
%area of platinum in the back of the catalyst layer. (at the catalyst
%layer/matrics interface)
a_back = (A_pt)*(e_gas);
%total platinum area per geometric area of electrode cm^2pt/cm^2
a_pt_tot = (A_pt)*Area_tot;
%platinum utilization
U_pt = 1;
%**************************************************************************
%Henry's Law constant for oxygen in electrolyte (mol/(cm^3*bar)and effective
%(see j.electrochem vol. 142 No. 6 June 1995 pg 1756 for reference)
H = 3*10^-7;
%**************************************************************************
%diffusion coefficient of oxygen in agglomerate (cm^2/s)(see j.electrochem vol. 142
%No. 6 June 1995 pg 1756 for reference)
D1s = 1*10^-5;
D1s_eff = D1s*(e_agg/t_agg);
%thin film paramater (unit of s): A_gl is the specific eletrolyte film area in
%catalyst layer (cm^2/cm^3).
B_film = delta/(A_gl*D1s);
%**************************************************************************
%thickness of matrix (cm)
Lm = 50e-4;
%**************************************************************************
%Additional parameters

%step size for ode of the catalyst layer model
step=0.05;

%toleranance in percent
tol =0.1;
tol_p = .5;

%inital guess currents
Itot_Guess = -.2;

Min_Pot=input('input desired minimum potential of the backing layer at x=0 ---->');

%initial potential of solid phase at x=0 to start program
pot_initial = .9;

step_i = 100*(pot_initial-Min_Pot);
%**************************************************************************
for i= 1:step_i

% potential decreases by 10mV increments
  pot= pot_initial - 0.01*i
```

```
current_converge

pressure_converge

Itot(i)=y(fin,2) - I_back;
potential(i)=pot-n1_m_fin;

Itot_Ideal(i)=-io*a_pt_tot*U_pt*(P10/P_ref)*exp((U_rev-potential(i))/TF);
ratio(i)=Itot(i)/Itot_Ideal(i);
Power(i)=abs(potential(i)*Itot(i));


%catalyst layer variables
n1_result(:,i) = y(:,1);
I1_result(:,i) = y(:,2);
n2_result(:,i) = y(:,3);
I2_result(:,i) = y(:,4);
P1_result(:,i) = y(:,5);
P2_result(:,i) = y(:,6);
N_gas_result(:,i) = y(:,7);
PL_result(:,i) = y(:,8);

%matrix variables
n1_m_result(:,i) = y_m(:,1);
PL_m_result(:,i) = y_m(:,2);

%************************************************************************
%ANALYTICAL SOLUTUION

Apam = ((io*U_pt)/(k1_eff))*(P10/P_ref)*(L^2*En*a_pt);

%note the two negative signs
OVP_o = -(pot-0-U_rev);
flux = (-L/k1_eff)*( -(a_front*io)*(P10/P_ref)*exp(OVP_o/TF) );

arctan_p = atan(flux/( (2*Apam*TF*exp(OVP_o/TF) - flux^2)^0.5 ));

sec_p = ( (2*Apam*TF*exp(OVP_o/TF) - flux^2)^0.5 )/(2*TF);

OVP_f = TF*log( ( (2*Apam*TF*exp(OVP_o/TF) - flux^2)*(sec(sec_p + arctan_p))^2 )/(2*Apam*TF));

%OVP_f = TF*log(exp(OVP_o/TF)*sec( (Apam*exp(OVP_o/TF))/(2*TF

A_potential(i) = U_rev - OVP_f;

A_Itot_1 = -(k1_eff/L)*(((2*Apam*TF*exp(OVP_o/TF) - flux^2)^0.5)*tan(sec_p + arctan_p));

A_Itot(i) = A_Itot_1 - (a_back*io)*(P10/P_ref)*exp(OVP_f/TF);

OVP_f_result(i) = OVP_f;

end
%************************************************************************
%plots
```

```
%figure(1)
%semilogx(-Itot,potential)
%xlabel('Currant (A/cm^2)')
%ylabel('Potential vs NHE (V)')

figure(2)
plot(-Itot,potential)
xlabel('Currant (A/cm^2)')
ylabel('Potential(V)')

hold

plot(-A_Itot,A_potential)

hold

figure(3)
plot(potential,ratio)
xlabel('Potential vs NHE (V)')
ylabel('Effectiveness')

%figure(5)
%semilogy(potential,ratio)
%xlabel('Potential vs NHE (V)')
%ylabel('Effectiveness')

%end time
toc
```

current_converge.m

```
Old_Itot_Guess = Itot_Guess;

n0_bl = pot;
[x_b,y_b]=ode23('backing_layer',[0:0.01:1],[P10 P20 n0_bl]);
P10_diff = y_b(101,1);
P20_diff = y_b(101,2);
n0_diff = y_b(101,3);

[x_d,y_d]=ode23(' microporous_layer ',[0:0.01:1],[P10_diff P20_diff n0_diff]);
P10_cat = y_d(101,1);
P20_cat = y_d(101,2);
n20 = y_d(101,3);

%fin inidicates the number for the final row of all matrix produced by the
%ode solver.
fin=(1/step)+1;

%ODE solver, used the stiff solver.
%other initial conditions
n10=0;
n20=n20;

I_front = (a_front*io)*(P10_cat/P_ref)*exp(-(n20-n10-U_rev)/TF);
```

```
%note that I_front is positive. Place close attention to signs!!!
%Itot_Guess has a negative sign

I10=-I_front;
I20=Itot_Guess + I_front;
N_gas0=(-Itot_Guess - I_front)/(4*F);

PL0=PL_cat;

Tol=1*10^-10;
ode_params=odeset('RelTol',Tol,'AbsTol',Tol/100);
[x,y]=ode15s('e_ode',[0:step:1],[n10 I10 n20 I20 P10_cat P20_cat N_gas0 PL0],ode_params);

n1_fin = y(fin,1);
n2_fin = y(fin,3);
I1_fin = y(fin,2);
P1_fin = y(fin,5);
PL_fin = y(fin,8);
I_back = (a_back*io)*(P1_fin/P_ref)*exp(-(n2_fin-n1_fin-U_rev)/TF);
%note that I_back is postive so must change sign
Itot(i)=y(fin,2) - I_back;

[x_m,y_m] = ode23('matrix',[0:0.01:1],[n1_fin PL_fin]);
n1_m_fin = y_m(101,1);
PL_m_fin = y_m(101,2);

if abs(Itot_Guess) <= abs(Itot(i))
   sign_c = -1;
else
   sign_c = 1;
end

count_first = 0;
count_second = 0;
c=-1;

while (abs((abs(Itot_Guess-Itot(i)))/Itot(i)))*100 >= tol

Itot_Guess=Old_Itot_Guess;

n0_bl = pot;
[x_b,y_b]=ode23('backing_layer',[0:0.01:1],[P10 P20 n0_bl]);
P10_diff = y_b(101,1);
P20_diff = y_b(101,2);
n0_diff = y_b(101,3);

[x_d,y_d]=ode23(' microporous_layer ',[0:0.01:1],[P10_diff P20_diff n0_diff]);
P10_cat = y_d(101,1);
P20_cat = y_d(101,2);
n20 = y_d(101,3);

if P10_cat <= 0
   P10_warning = P10_cat
   break
end
```

```
%ODE solver, used the stiff solver.
%other initial conditions
n10=0;
n20=n20;

I_front = (a_front*io)*(P10_cat/P_ref)*exp(-(n20-n10-U_rev)/TF);
%note that I_front is positive. Place close attention to signs!!!
%Itot_Guess has a negative sign

I10=-I_front;
I20=Itot_Guess + I_front;
N_gas0=(-Itot_Guess - I_front)/(4*F);

PL0=PL_cat;

Tol=1*10^-10;
ode_params=odeset('RelTol',Tol,'AbsTol',Tol/100);
[x,y]=ode15s('e_ode',[0:step:1],[n10 I10 n20 I20 P10_cat P20_cat N_gas0 PL0],ode_params);

n1_fin = y(fin,1);
n2_fin = y(fin,3);
I1_fin = y(fin,2);
P1_fin = y(fin,5);
PL_fin = y(fin,8);
I_back = (a_back*io)*(P1_fin/P_ref)*exp(-(n2_fin-n1_fin-U_rev)/TF);
%note that I_back is postive so must change sign
Itot(i)=y(fin,2) - I_back;

[x_m,y_m] = ode23('matrix',[0:0.01:1],[n1_fin PL_fin]);
n1_m_fin = y_m(101,1);
PL_m_fin = y_m(101,2);

c = c+1;

count_first = count_first +1;

count_second = 0;

while (abs((abs(Itot_Guess-Itot(i)))/Itot(i)))*100 >= tol

Old_Itot_Guess = Itot_Guess;

Itot_Guess = Itot_Guess + ((sign_c*.1)/(10^c));

n0_bl = pot;
[x_b,y_b]=ode23('backing_layer',[0:0.01:1],[P10 P20 n0_bl]);
P10_diff = y_b(101,1);
P20_diff = y_b(101,2);
n0_diff = y_b(101,3);

[x_d,y_d]=ode23(' microporous_layer ',[0:0.01:1],[P10_diff P20_diff n0_diff]);
P10_cat = y_d(101,1);
P20_cat = y_d(101,2);
n20 = y_d(101,3);

if P10_cat <= 0
```

```
    P10_warning = P10_cat
    break
  end

  %ODE solver, used the stiff solver.
  %other initial conditions
  n10=0;
  n20=n20;

  I_front = (a_front*io)*(P10_cat/P_ref)*exp(-(n20-n10-U_rev)/TF);
  %note that I_front is positive. Place close attention to signs!!!
  %Itot_Guess has a negative sign

  I10=-I_front;
  I20=Itot_Guess + I_front;
  N_gas0=(-Itot_Guess - I_front)/(4*F);

  PL0=PL_cat;

  Tol=1*10^-10;
  ode_params=odeset('RelTol',Tol,'AbsTol',Tol/100);
  [x,y]=ode15s('e_ode',[0:step:1],[n10 I10 n20 I20 P10_cat P20_cat N_gas0 PL0],ode_params);

  n1_fin = y(fin,1);
  n2_fin = y(fin,3);
  I1_fin = y(fin,2);
  P1_fin = y(fin,5);
  PL_fin = y(fin,8);
  I_back = (a_back*io)*(P1_fin/P_ref)*exp(-(n2_fin-n1_fin-U_rev)/TF);
  %note that I_back is postive so must change sign
  Itot(i)=y(fin,2) - I_back;

  [x_m,y_m] = ode23('matrix',[0:0.01:1],[n1_fin PL_fin]);
  n1_m_fin = y_m(101,1);
  PL_m_fin = y_m(101,2);

  count_second = count_second+1;

if sign_c == -1
  if ((abs((abs(Itot_Guess-Itot(i)))/Itot(i)))*100 >= tol) & (abs(Itot(i)) <= abs(Itot_Guess))
    break
  end
else
  if ((abs((abs(Itot_Guess-Itot(i)))/Itot(i)))*100 >= tol) & (abs(Itot(i)) >= abs(Itot_Guess))
    break
  end
end

end

end


  test(i) = (abs((abs(Itot_Guess-Itot(i))/Itot(i))))*100;

  %Potential difference between front of backing layer and back of matrix.
```

```
potential(i)=pot-n1_m_fin;

%Guess for Itot for next value of electrode potential (next value of i)
Itot_Guess = y(fin,2) - I_back;

PL_m(i) = PL_m_fin;
```

e_ode.m

```
function f = e_ode(x,y)

% Written by Fritz Pierre
%This .m file models ion, electron, gas phase transport in the catalyst
%layer.

% This .m file is used to solve for current genereated by several types of
% electrodes.

%Assumption
%1. The macrohomogenious approach with a film containing agglommerate
%effectiveness factor is used to model transport in the catalyst layer.
%This approach relies on the fact that the size of the agglommerate is
%much smaller than the thickness of the catalyst layer.
%2. Platinum is assumed to be uniformily distributed within the agglomerates
%3. Assume the total pressure of the gas is constant and use the
%stefan-maxwell equaiton with Knudsen diffusion to model gas transport.
%4. An effective Knudsen radius is used.

%Global variables - these variables are used in several of the electrode
%model '.m' files.

global T Pt e_gas t_gas rk L k1 e_ion t_ion tr_anion k2_eff D1s D1s_eff delta B_film H

global io A_gl a_pt U_rev r_agg e_type En P_ref U_pt TF

global k_sat

%*************************************************************************
% Defining Local state variables
% n1 is the potential of solution, I1 is ionic current, n2 potential of solid phase,
% I2 is electronic current, P1 is pressure of oxygen, and P2 is pressure of
% water, N_gas is oxygen flux in the gas phase, and PL is liquid
% electrolyte pressure in bars
n1 = y(1,:);
I1 = y(2,:);
n2 = y(3,:);
I2 = y(4,:);
P1 = y(5,:);
P2 = y(6,:);
N_gas = y(7,:);
PL = y(8,:);
%*************************************************************************
%Define Parameter
%Unversal Constants;
R = 8.3;
```

```
F = 96485;
%molecular wieghts of gases (oxygen, water, nitrogen, phosphoric acid)
mw_1 = 32;
mw_2 = 18;
mw_3 = 28;
mw_4 = 97;
%************************************************************************
%Properties of phosphoric acid
%density [g/cm^3]
den_L = 1.8;
%specific molar volume [cm^3/mol]
v_L = (1/den_L)*mw_4;
%dynamic viscosity [bar*sec] divide by 10^5 to turn viscosity from Pa*sec
%to bar*sec.
viscosity_L = 0.0021*(1/10^5);
%************************************************************************
%Gas Phase Properties
%Binary diffusion coefficients. Equations obtained from Bird and Lightfoot pg
%505 (in cm^2/s)
%Oxygen and Water
D12 = (0.3022/Pt)*((T/323.83)^2.334);
%Oxygen and Nitrogen
D13 = (0.0544/Pt)*((T/143.01)^1.823);
%Nitrogen and Water
D23 = (0.2526/Pt)*((T/292.77)^2.334);

%Knudsen diffusion coefficients in cm^2/s. rk is in meters, the molucular weight needs
%to be multiplied by 0.001 to go from g/mol to kg/mol. The
%entire expression is also multiplied by 100^2 to go from m^2/s to cm^2/s.

Dk_1=(100^2)*((2*rk)/3)*(((8*R*T)/(pi*mw_1*0.001))^0.5);
Dk_2=(100^2)*((2*rk)/3)*(((8*R*T)/(pi*mw_2*0.001))^0.5);
Dk_3=(100^2)*((2*rk)/3)*(((8*R*T)/(pi*mw_3*0.001))^0.5);

%Effective binary Diffusion coefficients
D12_eff=(e_gas/t_gas)*D12;
D13_eff=(e_gas/t_gas)*D13;
D23_eff=(e_gas/t_gas)*D23;
Dk_1_eff=(e_gas/t_gas)*Dk_1;
Dk_2_eff=(e_gas/t_gas)*Dk_2;
Dk_3_eff=(e_gas/t_gas)*Dk_3;
%************************************************************************
%The micropores of both the catalyst layer and matrix are assumed to remain
%flooded with electrolyte regardless of capillary pressure. That is
%Saturation = 1. Thus the relative permeability is always equal to 1.
k_rel=1;
%************************************************************************
%Effective Conductivity
k1_eff = k1*(e_ion/t_ion);
%************************************************************************
%Equations for ODE

%gas phase transport. the necessary conversion factor is (10). So in the equaitons below 10 is a
%conversion factor.  The flux of oxygen is proportional to the flux of
%water, so we solve for the flux of oxgyen (N_gas) and use that in the
%equation of "water".
```

```
oxygen=((10*R*T*N_gas)/Pt)*(((1/(D13_eff))-(2/D12_eff))*P1 - ((1/D12_eff)-(1/D13_eff))*P2 -
((1/D13_eff)+(1/Dk_1))*Pt);

water=((10*R*T*N_gas)/Pt)*(((1/D12_eff)-(2/D23_eff))*P2 + ((2/D12_eff)-(2/D13_eff))*P1 +
((2/D23_eff)+(2/Dk_2))*Pt);

%Reaction equation:  Using the the thin film - agglomerate model

%Thin film parameter defined in each electrode type .m file.
B_film = B_film;

%K is the reaction rate constant for consumption of oxygen in catalyst
%the layer. The electrochemcial reduction of oxygen is assumed to be
%a first order reaction therefore the rate constant has units of (s^-1)
%a_pt is specific reaction area in the catalyst layer
%(cm^2/cm^3)
K = ((a_pt*io)/(4*F*P_ref*H))*exp(-(n2-n1-U_rev)/TF);

%Thiele modulus
Thiele=(K*(r_agg^2)/D1s_eff)^(1/2);

%the effectiveness factor is found by assuming the oxygen diffusion through a
%rectangular agglomerate. The assumptionis valid if r >> s. This assumption leads
%to a lower bound estimate (a conservative estimate) of oxygen  diffusion. The local
%concentration gradients near each individual platinum particle is assumed
%neglible.  This assumption is valid for oxygen reduction since the local
%current density is small at typical operating potentials of the cell.

%e_type allows for the differention between the novel and conventional electrode design.
% For the novel design, experiments show that the thin platinum films deposited
%on a porous electrode does not experience concentration losses up to
%sufficiently high current densities.  Therefore the effectiveness factor is always equal to 1 for novel
electrode design

%effectiveness factor for agglomerate.

if e_type == 1
   E_agg = 1;
else
   E_agg = (tanh(Thiele))/Thiele;
end

%Reaction is the volumetric rate of production of oxygen (mole/(cm^3*s))
%At a given potential negative pressures may result while the equation are
%converging. To limit the effect that a physically imposible negative
%pressure has on the converging equaiton, the following condition is given.

if P1 <= 0
  Reaction = 0;
else
  Reaction=(P1*H*En*U_pt)/((1/(E_agg*K))+B_film);
end

%U_pt is platinum utilization
%En is the fraction of the catalyst layer volume made up of the agglomerates.
```

```
% Ode system of equaitons. The dot represents the differential with respect
% to the dimensionless position in the catalyst layer.

n1_dot  = -I1*(1/k1_eff)*L;
I1_dot = -4*F*Reaction*L;
n2_dot = -I2*(1/k2_eff)*L;
I2_dot = 4*F*Reaction*L;
P1_dot = oxygen*L;
P2_dot = water*L;
N_gas_dot = -Reaction*L;
%velocity of anioin due to electric field
v_anion = -((v_L*tr_anion)/F)*I1*(1/(1-e_gas));
%there is no negative sign since v_hydraulic = -v_anion. From volume
%conservation delta(v) = 0. and velocity of electrolyte at the boundaries
%is equal to zero.
PL_dot = ((viscosity_L*L)/(k_rel*k_sat))*v_anion;

%%%%%%%%%%%%%%%%%%%%%%%%%%%%%%%%%%%%%%%%%%%%%%%%%%%%%%%%5
% Creating f vector

f(1,:) = n1_dot ;
f(2,:) = I1_dot;
f(3,:) = n2_dot ;
f(4,:) = I2_dot;
f(5,:) = P1_dot ;
f(6,:) = P2_dot;
f(7,:) = N_gas_dot ;
f(8,:)=PL_dot;
```

backing_layer.m

```
function f_b = backing_layer(x_b,y_b)

% Written by Fritz Pierre (Start Date: 8/4/05)

%This function is used to solve for the oxygen and water pressure
%distribution in the backing layer of the phosphoric acid fuel cell.

%Assumptions:
%1. The gas porosity of the backing layer is assumed uniform and
%independent of current density.
%2. The gas pressure is constant. This assumption is completely valid due
%to the high permiability of the carbon paper that makes up the backing
%layer.
%3. Constant temperature

%Global variables - these variables are used in several of the electrode
%model '.m' files.

global T Pt Itot_Guess k_BL_eff


% Defining Local state variables.
%Pressure of oxygen in bars
```

```
P1  = y_b(1,:);
%Pressure of water in bars
P2 = y_b(2,:);
%Potential of solid phase
n = y_b(3,:);

%Define Parameter
%Universal Constants;
R = 8.3;
F = 96485;

%molecular wieghts of gases (oxygen, water, nitrogen)
mw_1 = 32;
mw_2 = 18;
mw_3 = 28;

%Binary diffusion coefficients. Equations obtained from Bird and Lightfoot pg
%505 (in cm^2/s)
%Oxygen and Water
D12 = (0.3022/Pt)*((T/323.83)^2.334);
%Oxygen and Nitrogen
D13 = (0.0544/Pt)*((T/143.01)^1.823);
%Nitrogen and Water
D23 = (0.2526/Pt)*((T/292.77)^2.334);

%Physical Parameters of Backing layer
%Porosity
e = 0.60;
%Tortuosity - We use here the Bruggeman expression for tortuosity
t_b=e^-0.5;
%average pore radius for Knudsen diffusion in meters
rk=20*10^-6;
%thickness of backing layer in cm
Lb=350*10^-4;

%Knudsen diffusion coefficients in cm^2/s. rk is in meters, the molucular weight needs
%to be multiplied by 0.001 to go from g/mol to kg/mol. The
%entire expression is also multiplied by 100^2 to go from m^2/s to cm^2/s.

Dk_1=(100^2)*((2*rk)/3)*(((8*R*T)/(pi*mw_1*0.001))^0.5);
Dk_2=(100^2)*((2*rk)/3)*(((8*R*T)/(pi*mw_2*0.001))^0.5);
Dk_3=(100^2)*((2*rk)/3)*(((8*R*T)/(pi*mw_3*0.001))^0.5);

%Effective binary Diffusion coefficients
D12_eff=(e/t_b)*D12;
D13_eff=(e/t_b)*D13;
D23_eff=(e/t_b)*D23;
Dk_1_eff=(e/t_b)*Dk_1;
Dk_2_eff=(e/t_b)*Dk_2;
Dk_3_eff=(e/t_b)*Dk_3;

%**************************************************************************
%Equations for ODE
%Oxygen flux (mol/(cm^2*sec))
%Itot_Guess is negative
N1 = -Itot_Guess/(4*F);
```

```
%Water  flux (mol/(cm^2*sec)). All water leaves cell as vapor
N2 = Itot_Guess/(2*F);

%Note the dimension for length is cm and pressure is in bars.
%Thus, the necessary conversion factor is (10). So in the equaitons below 10 is a
%conversion factor

oxygen = ((10*R*T)/Pt)*( ((N2*P1)/D12_eff) - (((1+(D13_eff/Dk_1_eff))*Pt + ((D13_eff/D12_eff)-1)*P2
- P1)/D13_eff)*N1 );

water = ((10*R*T)/Pt)*( ((N1*P2)/D12_eff) - (((1+(D23_eff/Dk_2_eff))*Pt + ((D23_eff/D12_eff)-1)*P1 -
P2)/D23_eff)*N2 );

%Ode (non-dimensionalize the length)

P1_dot = Lb*oxygen;

P2_dot = Lb*water;

n_dot = -Itot_Guess*(1/k_BL_eff)*Lb;
%%%%%%%%%%%%%%%%%%%%%%%%%%%%%%%%%%%%%%%%%%%%%%%%%%%%%%%%5
% Creating f vector

f_b(1,:) = P1_dot ;
f_b(2,:) = P2_dot;
f_b(3,:) = n_dot;
```

microporous_layer.m

```
function f_d = microporous_layer(x_d,y_d)

% Written by Fritz Pierre (Start Date: 8/4/05)

%This function is used to solve for the oxygen and water pressure
%distribution in the gas diffusion layer of the phosphoric acid fuel cell.

%The gas microporous layer is made up of uncatalyzed carbon black binded by
%teflon. The diffusion layer is used to reduce electrolyte movement, reduce
%contact resistance between the the backing layer and the catalyst layer, and
%improve gas distribution to the catalyst layer.

%Assumptions:
%1. The gas porosity of the backing layer is assumed uniform and
%independent of current density. .
%2. The gas pressure is constant. This assumption is completely valid due
%to the high permiability of the diffusion layer and due to the zero flux
%of the nitrogen, which makes up most of the air.
%3. Knudsen diffusion is taken into account. We will assume use an
%effective Knudsen radius to calculate the Knudsen diffusion coefficient.
%4. Constant temperature

%Global variables - these variables are used in several of the electrode
%model '.m' files.

global T Pt Itot_Guess k_DL_eff
```

```
%Defining Local state variables.
%Pressure of oxygen in bars
P1  = y_d(1,:);
%Pressure of water in bars
P2 = y_d(2,:);
%Potential of solid phase
n = y_d(3,:);

%Define Parameter
%Universal Constants;
R = 8.3;
F = 96485;

%molecular wieghts of gases (oxygen, water, nitrogen)
mw_1 = 32;
mw_2 = 18;
mw_3 = 28;

%Binary diffusion coefficients. Equations obtained from Bird and Lightfoot pg
%505 (in cm^2/s)
%Oxygen and Water
D12 = (0.3022/Pt)*((T/323.83)^2.334);
%Oxygen and Nitrogen
D13 = (0.0544/Pt)*((T/143.01)^1.823);
%Nitrogen and Water
D23 = (0.2526/Pt)*((T/292.77)^2.334);

%Physical Parameters of Backing layer
%Porosity
e = 0.40;
%Tortuosity - for now I will use the Bruggeman epxression for tortuosity
t_b=e^-0.5;
%average pore radius for Knudsen diffusion in meters (estimate 1 micron)
rk=1*10^-6;
%thickness of backing layer in cm
Ld=50*10^-4;

%Knudsen diffusion coefficients in cm^2/s. rk is in meters, the molucular weight needs
%to be multiplied by 0.001 to go from g/mol to kg/mol. The
%entire expression is also multiplied by 100^2 to go from m^2/s to cm^2/s.

Dk_1=(100^2)*((2*rk)/3)*(((8*R*T)/(pi*mw_1*0.001))^0.5);
Dk_2=(100^2)*((2*rk)/3)*(((8*R*T)/(pi*mw_2*0.001))^0.5);
Dk_3=(100^2)*((2*rk)/3)*(((8*R*T)/(pi*mw_3*0.001))^0.5);

%Effective binary Diffusion coefficients
D12_eff=(e/t_b)*D12;
D13_eff=(e/t_b)*D13;
D23_eff=(e/t_b)*D23;
Dk_1_eff=(e/t_b)*Dk_1;
Dk_2_eff=(e/t_b)*Dk_2;
Dk_3_eff=(e/t_b)*Dk_3;

%**************************************************************************
%Equations for ODE
```

```
%Oxygen flux (mol/(cm^2*sec))
%Itot_Guess is negative
N1 = -Itot_Guess/(4*F);
%Water  flux (mol/(cm^2*sec)). All water leaves cell as vapor
N2 = Itot_Guess/(2*F);

%Note the dimension for length is cm and pressure is in bars.
%Thus, the necessary conversion factor is (10). So in the equaitons below 10 is a
%conversion factor

oxygen = ((10*R*T)/Pt)*( ((N2*P1)/D12_eff) - (((1+(D13_eff/Dk_1_eff))*Pt + ((D13_eff/D12_eff)-1)*P2
- P1)/D13_eff)*N1 );

water = ((10*R*T)/Pt)*( ((N1*P2)/D12_eff) - (((1+(D23_eff/Dk_2_eff))*Pt + ((D23_eff/D12_eff)-1)*P1 -
P2)/D23_eff)*N2 );

%Ode (non-dimensionalize the length)

P1_dot = Ld*oxygen;

P2_dot = Ld*water;

n_dot = -Itot_Guess*(1/k_DL_eff)*Ld;

%%%%%%%%%%%%%%%%%%%%%%%%%%%%%%%%%%%%%%%%%%%%%%%%%%%%%%%%%%%%%%%%%%%%%%%%%%%%
% Creating f vector

f_d(1,:) = P1_dot ;
f_d(2,:) = P2_dot;
f_d(3,:) = n_dot;
```

matrix.m

```
function f = matrix(x,y)

% Written by Fritz Pierre
%This .m file models ion, and liquid electrolyte transport in the matrix.
%In the novel electrode design the matrix is mostly made of the same
%material as the catalyst layer.  A thin silicon carbide film is used to
%electronically isolate the cathode from the anode.


%Assumption
%1.  The macrohomogenious approach with a film containing agglommerate
%effectiveness factor is used to model transport in the matriz layer
%This approach relies on the fact that the size of the pores within the matrix is
%much smaller than the thickness of the layer

%Global variables - these variables are used in several of the electrode
%model '.m' files.

global T Pt Lm k1 e_micro t_micro tr_anion Itot_Guess

global k_sat
%*************************************************************************
```

```
% Defining Local state variables
% n1 is the potential of solution, and PL is liquid
% electrolyte  pressure in bars
n1 = y(1,:);
PL = y(2,:);
%*************************************************************************
%Define Parameter
%Unversal Constants;
R = 8.3;
F = 96485;
%molecular wieghts of gases (oxygen, water, nitrogen, phosphoric acid)
mw_1 = 32;
mw_2 = 18;
mw_3 = 28;
mw_4 = 97;
%*************************************************************************
%Properties of phosphoric acid
%density [g/cm^3]
den_L = 1.8;
%specific molar volume [cm^3/mol]
v_L = (1/den_L)*mw_4;
%dynamic viscosity [bar*sec] divide by 10^5 to turn viscosity from Pa*sec
%to bar*sec.
viscosity_L = 0.0021*(1/10^5);
%*************************************************************************
%The micropores of both the catalyst layer and matrix are assumed to remain
%flooded with electrolyte regardless of capillary pressure. That is
%Saturation = 1. Thus the relative permeability is always equal to 1.
k_rel=1;
%*************************************************************************
%Effective Conductivity
k1_eff = k1*(e_micro/t_micro);
%*************************************************************************
%Equations for ODE

% Ode system of equaitons. The dot represents the differential with respect
% to the dimensionless position in the catalyst layer.

n1_dot = -Itot_Guess*(1/k1_eff)*Lm;
%velocity of anioin due to electric field
v_anion = -((v_L*tr_anion)/F)*Itot_Guess;
%there is no negative sign since v_hydraulic = -v_anion. From volume
%conservation delta(v) = 0. and velocity of electrolyte at the boundaries
%is equal to zero.
PL_dot = ((viscosity_L*Lm)/(k_rel*k_sat))*v_anion;

%%%%%%%%%%%%%%%%%%%%%%%%%%%%%%%%%%%%%%%%%%%%%%%%%%%%%%%%5
% Creating f vector

f(1,:) = n1_dot ;
f(2,:)=PL_dot;
```

pressure_converge.m

```
%iteration for converging to desired pressure at the backside of the matrix
PL_cat = PL_desired;
PL_cat_old = PL_cat;
m = -1;
P_converge = 1;

while (abs(PL_m(i) - PL_desired)/PL_m(i))*100 >= tol_p

   PL_cat = PL_cat_old;

current_converge

   P_converge = P_converge+ 1;

   m = m + 1;

   while (abs(PL_m(i) - PL_desired)/PL_m(i))*100 >= tol_p

  PL_cat_old = PL_cat;

  PL_cat = PL_cat - (.1/(10^m));

current_converge

  if (abs(PL_m(i) - PL_desired)/PL_m(i))*100 >= tol_p & PL_desired >= PL_m(i)
     break
  end

  end
%*************************************************************************

end
%*************************************************************************
```